Ludwig-Maximilians-Universität München

Radial velocity measurements for white-dwarf/brown-dwarf binarie candidates and development of an active mirror control for the 11 m Hobby-Eberly-Telescope.

Dissertation
Marco Häuser

Ludwig-Maximilians-Universität München

Dissertation:

Radial velocity measurements for white-dwarf/brown-dwarf binarie candidates and development of an active mirror control for the 11 m Hobby-Eberly-Telescope.

Candidate:	Date:	Reviewer:
Marco Häuser	27th of June 2019	Supervisor: Prof. Dr. Ralf Bender *Ludwig-Maximilians-Universität*
		2nd Referee: Prof. Gary Hill Ph.D. *University of Texas at Austin*

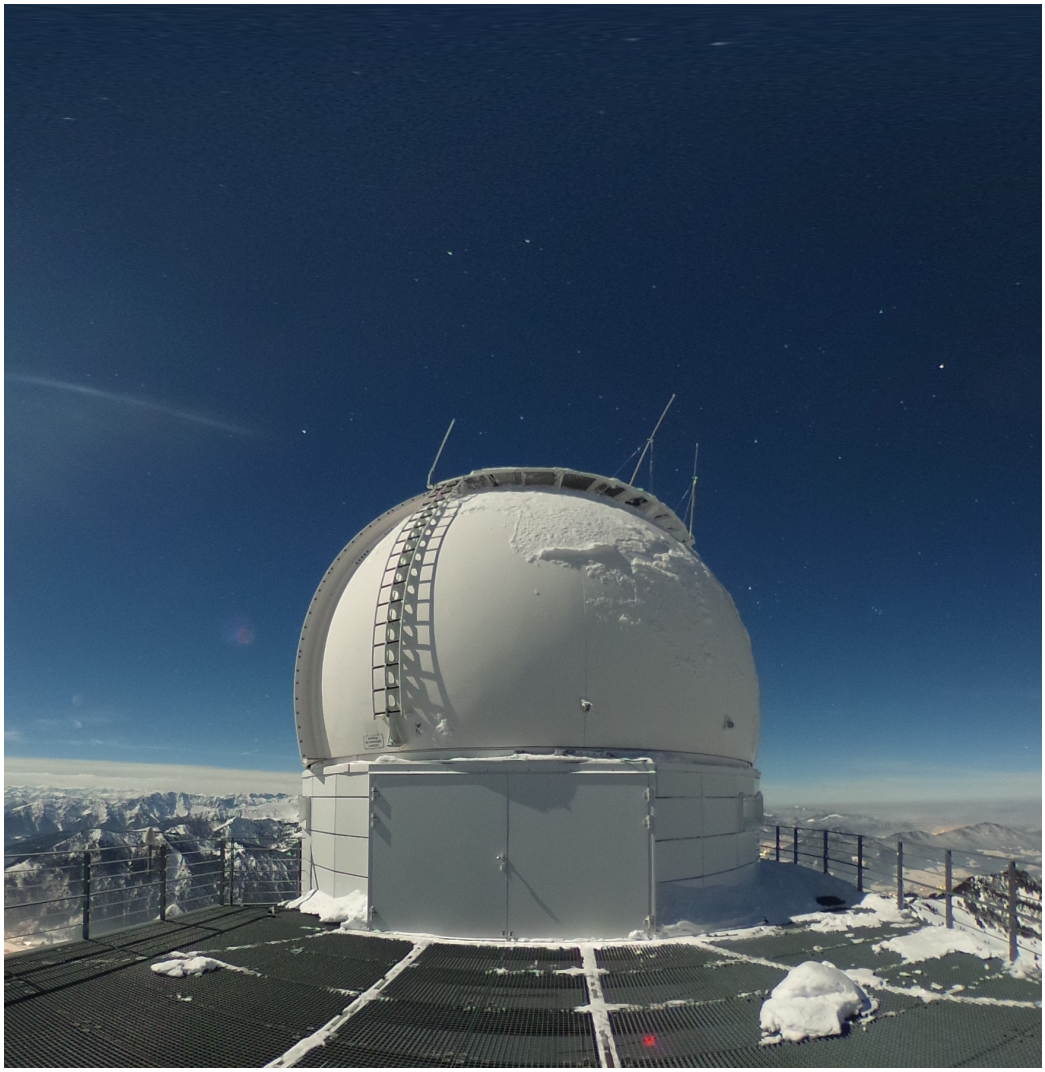

Wendelstein Observatorium: Where it all began....

Credit: M. Kluge

"Der Ziellose erleidet sein Schicksal - der Zielbewusste gestaltet es."

Immanuel Kant

Dissertation an der Fakultät für Physik der Ludwig-Maximilians-Universität München

Radialgeschwindigkeitsmessungen von Weißer-Zwerg/Brauner-Zwerg Binärsystem Kandidaten und Entwicklung einer aktiven Primärspiegelkontrolle für das 11 m Hobby-Eberly-Telescope.

Vorgelegt von Marco Häuser
München, 27 Juni 2019

Erstgutachter:	Prof. Dr. Ralf Bender
Zweitgutachter:	Prof. Gary Hill Ph.D.
Datum der mündlichen Prüfung:	6. August 2019

Zusammenfassung

Diese Dissertation präsentiert die Ergebnisse von Radialgeschwindigkeitsmessungen für potentielle Weißer-Zwerg (WD) / Brauner-Zwerg (BD) Binärsysteme. Weiterhin wird im zweiten Teil dieser Arbeit das Upgrade der Primärspiegelkontrolle des 11m Hobby-Eberly-Telescope (*HET*) des McDonald Observatories in Texas geschildert.

Als methodisches Fazit unserer Arbeit stellen zeigt sich, dass die getestete Methode zur Bestätigung von WD-BD unter Nutzung von nieder auflösender Spektroskopie bedingt funktionsfähig ist.

Die Auswahl der Testkandidaten beruht auf den nicht klassifizierten Objekten einer ursprünglichen Kandidatenliste von Steele et al. [86], welcher einen Kandidaten als WD-BD bestätigen konnte. Zunächst zeigt sich, dass die reale Leistungsfähigkeit und Stabilität des *ES2* Spektrograhen unter Berücksichtigung aller notwendigen Kalibrationen nicht zur sicheren Klassifikation von WD-BD Binärsystemen ausreicht. Dem gegenüber erreicht der deutlich modernere *LRS2* Spektrograph grundsätzlich seine Spezifikationen und ist somit für die Selektion von Kandidatenlisten für die Nachverfolgung mit noch aufwendigeren Instrumenten geeignet.

Alle Kandidaten werden durch Ihre Spektren als Spezialfälle von F-Sternkonstallationen und nicht als als WD-BD Binärsystem klassifiziert. Diese Einschätzung wird durch die inzwischen verfügbaren Distanzmessungen der *Gaia*-Satellitenmission [30] [29] bestätigt.

Diese Studie zeigt, dass niederauflösende und somit kostengünstige Spektroskopie ein probates Mittel zur Vorselektion von deutlich aufwendigeren Multi-Instrument Beobachtungen sein kann.

Der zweite Teil dieser Dissertation behandelt das Design der neuen aktiven Hauptspiegelsteuerung des optischen Großteleskopes *HET*. Ziel dieses Upgrade ist die Langzeitperformance sowie die Gesamteffizienz des *HET* nachhaltig zu steigern. Die verbesserte Systemleistung in Hinsicht auf die Stabilität und Abwärme sind in Form eines verbesserten Seeings Gegenstand aktueller und zukünftiger Messungen.

Zunächst wird die Vorgänger Studie in welcher für das *4MOST*-Projekt der Prototyp eines Glasfaserpositionierer mit 27 μm absoluter Positioniergenauigkeit bei $1\sigma = 14$ μm Standardabweichung entwickelt wurde, präsentiert.

Aufbauend auf dieser Entwicklung wurde die Hauptspiegelsteuerung des *HET* durch unseren maßgeschneiderte *HET Segment Motion Controller* ersetzt und in Zusammenarbeit mit dem technischen Team des *HET* die Inbetriebnahme begonnen. Seit dem 5 Juni 2019 wird der Hauptspiegel des *HET* nun im wissenschaftlichem Betrieb von SCS2 gesteuert.

Summary

In a nutshell: The work presented in this thesis observationally tests the evolutionary scenarios which can yield a binary system, consisting of a highly evolved stellar remnant of an intermediate to low mass star and an almost unevolved very low mass star, which most probably formed together. The parts I and II of this thesis each cover their individual aspects independently and can be read and understood separately from each other.

Detailed abstract: This thesis is separated into two major parts. Both, the radial velocity measurements of WD-BD candidates in part I as well as the detailed design of the active mirror control for the *HET* in part II can be read independently, since the *HET* hardware upgrade is not directly linked to the scientific study presented in this work. The telescope upgrade rather improves the whole facility, which hence benefits all research aided by *HET* data, such as this radial velocity measurements of binary systems.

We present the follow-up study for candidates, resulting from the *WFCAM Transit Survey* [80]. The targets have been proposed by a P. Steele as binaries, consisting of a White-Dwarf (WD) with a Brown-Dwarf (BD) companion. In 2013, Steele et al. [86] published his only confirmation NLTT 5306, which they characterized as the shortest period detached WD-BD binary known at that time and also being the fourth of only seven confirmed such binary systems until today. In contrast to these cases, we try to confirm the remaining targets which were not ruled out by Steele, using lower resolution spectroscopy. Generally surveys leave plenty of targets of unclear nature, which in order to confirm them, have to be followed up extensively. We make use of time efficient but less resolving spectroscopy to see if the technique is feasible to reduce the observation time for this and further targets like those three which we test:

- For our first target SDSS193144, the spectra disproved the WD-BD theory and the major component is classified as F8 star with around $T_{eff.} \approx 6000\ K$. However the gathered radial velocity data allowed to compare the real performance of two used low resolution spectrographs, for the specific task of faint rv follow up observations.

- For the second target SDSS70433, we find a upper limit for the targets radial velocity semiamplitude of $K = 35.0\ km/s$. The primary partner is identified as a F6 star ($T_{eff.} \approx 6400$) in a distance of about $r = 2.6\ kpc$. The measured 4 % transit as well as the period of $p \approx 4.6\ d$ are consistent with a M-dwarf companion, which would cause a maximum radial velocity variability of $\Delta v_{app.} = 22.7\ km/s$.

- The nature of our third target SDSS070428 remains unknown as we did not get enough data to derive a proper limit to the radial velocity variability. The measured spectra hint a F5 V host star with $T_{eff.} = 6380\ K$, which is either orbitally affected by a companion or composed of a blended, eclipsing binary. While, additional observations could shed some light on the true nature on the target, this thesis' assumption has been to refute.

In conclusion, we show that our low resolution attempt is a reasonable first step of a follow up study. Short exposure time campaigns with resolution $R \leq 2000$, using unassigned schedule holes or mediocre weather periodes during a night can hence be of value for the community by prefiltering such follow up samples. In our case, none of the targets ends up as the rare WD-BD type, as it is consistent with the little known number of such binaries. Finally, the most recent data release of the *Gaia*-project has delivered inevitable indication against WD-BD binaries as all three targets have proven to be too far away for the expected combined luminosity and thereby supports our stellar classifications.

Nowadays, most results of observational astrophysics are gained via the data of a few, outstanding observatories respectively surveys. Each of these projects and facilities, such as the Very Large Telescope, requires enormous initial financial investments, as well as enough budget for instruments, long term maintenance and the according staff. Thus, only a few such leading research facilities exist and the available observation time is limited. Therefore, it is important to test the lower limits of required instrumentation power for follow up observations such as presented in this work.

The technical part of the thesis starts with the proof of concept for a fiber-positioner, which was proposed to ESO for their upcoming multi object spectrograph *4MOST*. Hence, we present a *CAN-Bus*-controlled, $\Theta - \Phi$-style fiber-positioner prototype, which points without iterations or a metrology system. This design provides an overlapping patrol disc of 17.3 mm diameter and reaches a filling factor of 100 %. Given a mechanical reference point measured by stall detection, the absolute accuracy is 27 μm ($1\sigma = 14\ \mu m$) and pointings are repeatable with 7 μm ($1\sigma = 4\ \mu m$). Better positioning is reachable with optional calibration. This precursor laid the foundation for the later SCS2 upgrade of the primary mirror control for the 11m Hobby-Eberly-Telescope (*HET*), which is presented in the second project in this thesis.

Together with the ongoing major instrument upgrade, we present the upgrade of the *HET* Segment Control System (SCS) to SCS2. Because *HET*'s primary mirror is segmented into 91 individual 1-meter hexagonal mirrors the SCS is essential to maintain the mirror alignment throughout an entire night of observations. The new motion control for SCS2 further increases the systems efficiency, precision and reliability.

HET's 91 mirror segments are aligned to micron precision using inductive edge sensors to probe the relative position on a sub-micron level. The system corrects for external influences, such as steep temperature changes and mechanical stress, while tracking the telescope on sky. SCS2 uses initially an optical alignment system and afterwards commands corrections for every segment in a closed 30s loop based on the edge sensor feedback.

The segment actuators are controlled by the custom developed *HET* **S**egment **MO**tion **CO**ntroller (SMOCO). To preserve the existing *HET* hardware layout, each SMOCO will control four adjacent mirror segments, being able to drive all twelve axes simultaneously.

Ultimately, the facility upgrade SCS2 allows for sub-arcsecond precision in tip and tilt as well as sub-micron precision in piston.

After an extended phase of onsite *HET* software adaptation, the 5th of June 2019 was the first night of operation including SCS2. As expected the brief transition from SCS towards SCS2 caused no telescope downtime and boosted the active mirror performance. The SCS2 Lead Software Engineer at *HET*, described the upgrades performance as "*visually apparent and impressive.*" (Chris Robison 14th of June 2019)

Summarizing this thesis, we cleared the open cases of the potential WD-BD target list using low-cost, low-priority observation time. The project was our test case for providing fall back targets to boost *HET*'s observational efficiency during times of mediocre weather. A typical application for our method can be the ever larger candidate lists from exoplanet surveys. While filtering the targets via independent *Gaia*-distance measurements [30] [29] already reduces the number of potential targets, there are still too many to investigate each of them in detail with high resolving power instruments. Hence, the unique combination of the *LRS2*-spectrograph's resolving power mounted to one of the largest optical telescopes on earth, can not only produce competitive data to study galaxy dynamics but also be of good use to preselect candidates within very short exposure times and less then optimal conditions. Finally, the development of SCS2 is a relevant contribution to the long term efficiency of the *HET* in general.

Contents

II Development of an active mirror control

Preamble

Modern text books of astronomy imply that due to the accomplishments of roughly the last century, an excellent understanding of the evolution of isolated stars was developed, while their formation is still a central topic of scientific studies. Indeed, most proposed formation schemes mostly see the formation in multiple systems and star cluster, including the coeval formation of their planetary systems. Observationally, it is meanwhile an established result (e.g. Eggleton et al. [21]) that the majority of stars, young as well as old ones, live in binary or even multi-stellar systems. While member stars of wide binaries might follow the scheme for isolated stellar evolution closely, this is certainly not true for closer pairs which can impact each other by exchange of radiation, momentum, and even matter.

The evolutionary scenarios get significantly more complicated given the additional free parameters of mass ratio and separation between the components and the amount of interaction. To test these theories, good statistical samples of the various binary system types are required. Especially, rare cases need a reliable data base to allow the deduction of constraints for the theoretical predictions. The approach of this thesis is consequently:

A) *To use follow-up data on candidates derived by a NIR survey to verify the nature of a list of candidates for a thus far rather rare kind of binaries, namely those consisting of a white and a brown dwarf.*

In order to enlarge the small data base of only seven known targets as shown in section 1, a follow up study on potential binary systems consisting of a White-Dwarf companioned by a Brown-Dwarf is provided in part I.

B) *To improve the hardware used for observations, especially for survey and follow-up telescopes.*

This goal is achieved by an integral facility upgrade of the *HET*, as described in part II.

In a nutshell, the work presented in this thesis observationally tests the evolutionary scenarios which can yield a binary system, consisting of a highly evolved stellar remnant of an intermediate to low mass star and an almost unevolved very low mass star, which most probably formed together. The parts I and II of this thesis each cover their individual aspect independent and can be read and understood separately from each other.

Observing in Texas: *Getting ready for the long night...*

Credit: C. Obermeier

"There is a way out of every box, a solution to every puzzle;
it's just a matter of finding it."

Jean-Luc Picard

Part I

White Dwarf - Brown Dwarf - Binaries

Chapter 1

Introduction

We study potential binary targets, which may consist of White-Dwarfs (WD) with low mass Brown-Dwarf (BD) companions. Due to the vast difference in density, the gravitationally dominating WD is small compared to the orbiting BD. Binary systems in general are very common. In fact the majority of all stars is expected to be part of a binary or multiple star system. E.g. Eggleton et al. [21] provide a local survey of almost 6971 stars distributed within 4559 systems. It shows that just over a third of all stars (39%) form as single stars. Hence, the complementary fraction of stellar objects exists within multiple systems. From an observers point of view, this means, that about 40% of all sources are actually composed multi-star-targets.

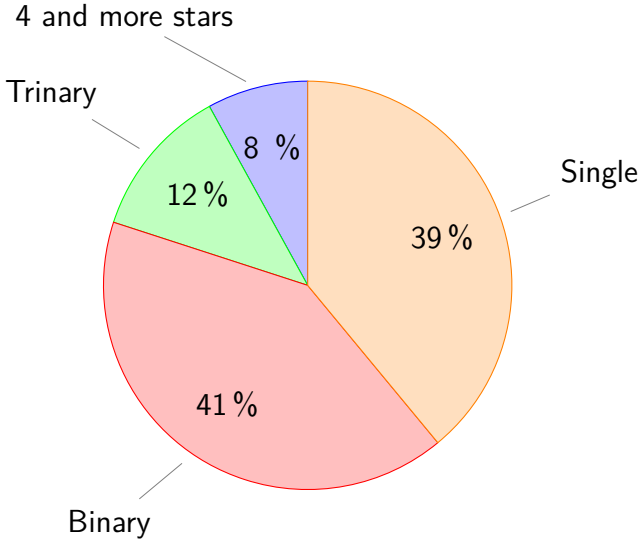

Bright Stellar Systems
Eggleton et al. [21]

#	Stars	Systems
1	2718	2718
2	2874	1437
3	855	285
4	344	86
5	100	20
6	66	11
7	14	2
Σ	6971	4559

Figure 1.1: Stellar distribution in bright stellar systems.
Data taken from **Eggleton et al. 2013** [21]

The composition of binaries varies from low-mass-ratio binaries, consisting of two main sequence stars, all the way to high-mass-ratio binaries. In this case, the high mass partner ($\leq$ 8 $M_{\odot}$) is likely to end up as WD, while the lightest possible stellar-mass companions are BDs. On the one hand, binaries composed of two main sequence companions are common and known very well. In fact, the stellar distribution from Eggleton et al. [21] is based on such systems. High-mass-ratio binaries on the other hand are harder to confirm as they feature less signal to noise, hence only few are known today. In 2011 Girven et al. [31] and Steele et al. [85] estimated that only 0.5% of all detached WD companions are BD. WD-BD binaries can generally be classified into two distinct groups, wide and close pairs.

Wide pairs: The secondary BD has potentially migrated outwards due to the friction based loss of angular momentum. The additional friction between the BD and the mass ejected during the WDs formation, causes this migration process as investigated by Nordhaus et al. [65]

Close pairs: Both companions are not only orbiting each other, but also directly affect each others evolution. Such systems are in general called post-common-envelope binaries (PCEB) and occur with all kind of partners. In our case, this group only consists of post-common-envelope WD-BD binaries. Hence, the number of known systems shrinks to only 7 so far:

Sample of known WD-BD PCEB

Author	year	cite	Author	year	cite
Dobbie et al. WD2359-434	2005	[20]	Littlefair et al. SDSS J141126.20+200911.1	2014	[61]
Burleigh et al. WD0137-349	2006	[6]	Farihi et al. SDSS J155720.77+091624.6	2017	[27]
Casewell et al. WD0837+185	2012	[9]	Parsons et al. SDSS J1205-0242	2017	[67]
Steele et al. NLTT 5306	2013	[86]			

Table 1.1: Sample of known post-common-envelope binaries (PCEB) consisting of White-Dwarf (WD) with a close Brown-Dwarf (BD) companion.

Due to the rarity of these systems, only large surveys are likely to encounter them. In our case, the starting point were results of the *WFCAM Transit Survey*, which delivered target-specific light curves. Intrinsically, all photometric surveys are biased to detect eclipsing binaries, as such system show

measurable flux variations. As the spectroscopic follow up of transit systems allow to neglect the typical $\sin(i)$ uncertainty of regular spectroscopic binaries, our approach allows for detailed characterization of these systems.

The light curves gained by the *WFCAM Transit Survey* indicated binary systems, while the analysis of the spectral energy distribution (SED) classified the primary as WD. Hence the photometric characteristic rather leads to a stellar class companion like a BD. As SED analyses were not accurate enough to detail the nature of this systems, spectroscopic follow up had to be done.

This thesis provides a follow up study of this target sample. All of the targets are fainter than 14 mag_i and therefore only observable for low to mid resolution spectrographs at mid-sized telescopes.[1] The project began with observations at Mc Donald observatory in Texas in 2015. The 2.1m Otto Struve Telescope (see section 3.1) and its *ES2*-spectrograph were available for a reasonable amount of nights. Nevertheless the real instrument stability never met the expected values, subsequently additional observations became necessary.

In 2017 *HET*'s *LRS2*-spectrograph (see section 3.2) started scientific operation and can also be used to follow up these systems. Due to the vast difference in primary mirror surface between effective 2m class aperture and *HET*'s 9m aperture, exposure times become rather short and low level priority observation time became available.

Additionally to the spectroscopic follow up observations, photometric, multi-band observations were obtained, using the *Wendelstein three channel imager (3KK)* (see 3.3), which allows simultaneous observations in two optical and one near infrared channel.

As already explained, all light curves are results of the *The WFCAM Transit Survey* (see section 1.1), from which all photometric observations are taken. The actual photometric data reduction and analysis is not part of this thesis but was the foundation for the target selection. In order to understand the survey data, we first take in section 1.1 a brief look at the actual survey instrument. Afterwards the remaining targets, which are the foundation for this work are shown in section 1.2.

[1] At same sized telescopes, higher resolutions simply requires longer exposure times, as the available amount of light gets distributed over a larger detector surface.

1.1 The WFCAM Transit Survey

The UKIRT Wide-Field Camera (WFCAM) is a facility instrument at the 3.8 m United Kingdom Infrared Telescope (UKIRT), located on Mauna-Kea, Hawaii. WFCAM includes 4 IR detectors with each $2048 \cdot 2048$ pixel, operating from 1.0 μm until 2.5 μm. [38]

In picture 1.2 WFCAM can be seen on the right picture, mounted in its novel 'Foward-Cassegrain' position.[44]

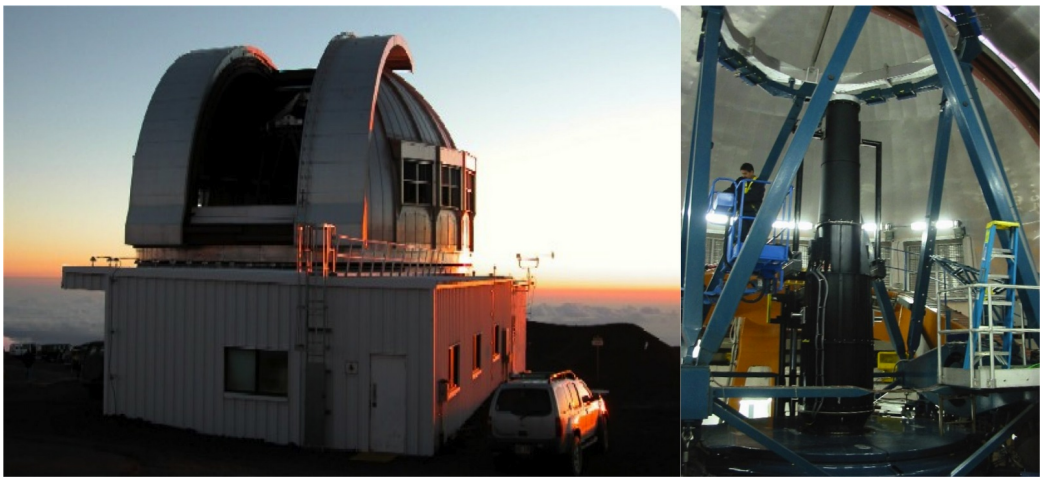

Figure 1.2: *"Left: The UK Infrared Telescope (UKIRT) on Mauna Kea, Hawaii. Right: The Wide-Field Camera (WFCAM) which is being used to observe the Ultra Deep Survey (along with four other major surveys)."*
Credit: Joint Astronomy Center, Hawaii
Taken from **McLure et al 2012** [63]

Starting in 2007, WFCAM executed the *WFCAM Transit Survey*, which is best described by the original paper:

The WFCAM Transit Survey by **Sipőcz et al. 2011** [80]

> *"The WFCAM Transit Survey (WTS) has been obtaining data on the United Kingdom Infrared Telescope since 2007. The WTS targets about 8,000 M dwarfs over several square degrees of sky, and aims to find low-mass eclipsing binaries and planets, down to the size of the Earth, transiting M dwarf stars with periods up to a few days."*[80]

1.2 Potential WD-BD target systems

The targets for this thesis were selected using light curves, gained by the WFCAM transit survey, as mentioned above. Following the initial WFCAM WTS data acquisition, P.R. Steele was working with this data from 2011 until 2013 in our scientific group: *Optical and Interpretative Astronomy (OPINAS)*.[2] A remnant of his work is a minor sample of three potential WD-BD binary systems which showed periodical flux variations.
Initially Steele et al. [85] provided in 2011 an overview of potential WD candidates with substellar companions. Furthermore, Kovács et al. [55] showed in 2013 that the obtained data is sensitivity to such short periodic binary systems. Meanwhile, Steele et al. [86] published in 2013 the first confirmed WD-BD binary system from the initial WFCAM WTS data sample. For references on the published WD-BD system (NLTT5306) please see table 1.1.
Table 1.2 lists our targets, which we try to confirm as WD-BD binaries:

Target list

Target ID	RA hh:mm:ss.s	DEC ±dd:mm:ss.s	m_i [mag]	p [d]	t_0 [JD]
SDSS070428	07:04:28.2	+13:12:53.5	16.5	0.371	2454526.845
SDSS070433	07:04:33.6	+13:22:16.3	16.0	4.660	2454527.598
SDSS193144	19:31:44.0	+36:17:26.4	14.0	0.228	2454317.876

Table 1.2: WD-BD target list, as it origins from Steele et al. The periods are results from the initial light curve analyses done by P.R. Steele.

As usual, t_0 is given as Julian Date (JD).[3] In defining an absolute date and henceforward counting days, one gets rid of special cases such as leap years and others. During the course of this project, the *Gaia* mission [30] [29] released astrometric data, which allowed us to independently measure the distance of each our target using the geometrical parallax method.[4]

[2] The *Optical and Interpretative Astronomy (OPINAS)* group is shared among the Max Planck Institute for extraterrestrial physics (MPE) and the University Observatory of the Ludwigs-Maximilians-University Munich(USM-LMU)

[3] Julian Date (JD) counts the days passed, after the 1st of January, 4713 BC and we used the standard python library *jdcal* [25] to calculate them.

[4] The parallax π is the apparent change of position over the course of half a year. The distance $r = 1\ pc$ is accordingly defined as $r = \frac{1" \cdot 1\ pc}{\pi}$; the distance in which a given target appears to move due to the Earth's orbit motion around the Sun.

The listed targets all show indication of binary systems as it is shown in the following figures 1.3 through 1.5. The black circles mark normalized and the red ones the binned flux data, vertical bars indicate the error bars. The green line shows the automatically fitted light curve assuming v-shaped transients, which not always meets the data well and can hence be ignored.
The first target SDSS070428 shows a clear periodic variability with a period of $p = 0.371\ d$, a time offset of $t_0 = 2454526.84456\ JD$.

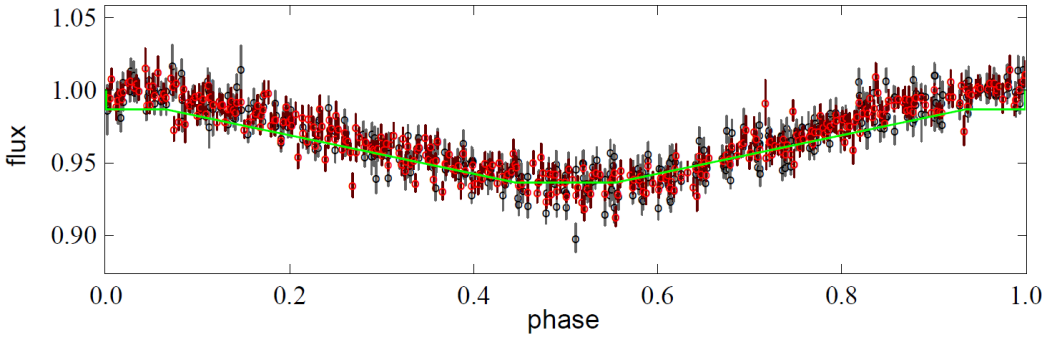

Figure 1.3: Light curve: SDSS070428. Circles mark flux with vertical error bars and the green line shows an automated fit assuming v-shaped transients.

The second target SDSS070433 shows an obvious transit with a period of $p = 4.660\ d$, a time offset of $t_0 = 2454527.59773\ JD$.

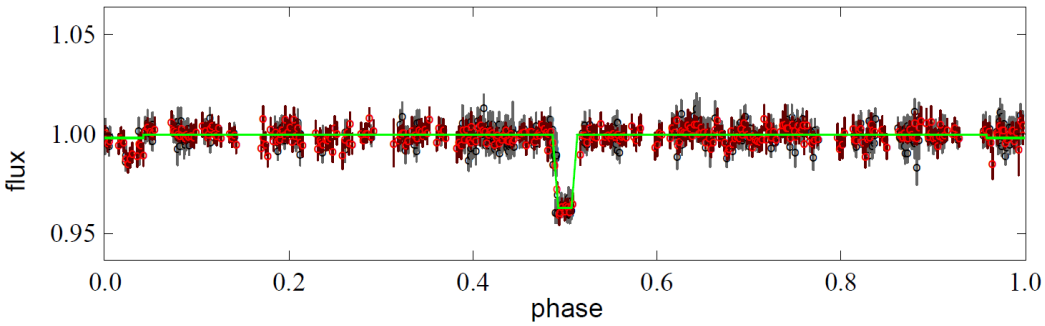

Figure 1.4: Light curve: SDSS070433. Circles mark flux with vertical error bars and the green line shows an automated fit assuming v-shaped transients.

These light curves all contain an automatically fitted theoretical model as provided by Steele et al. Nevertheless, this fit is not perfect in all cases, as it for example only finds the primary 4%-transit of SDSS070433, but not perfectly traces the 1%-occultation at phase 0.025, which indicates a minor eccentricity e as we will discuss it later in the thesis.

The last target SDSS193144 shows again a strong periodic variation, similar to the one of SDSS070428. The period is $p = 0.228\ d$ and a time offset of $t_0 = 2454317.87646\ JD$.

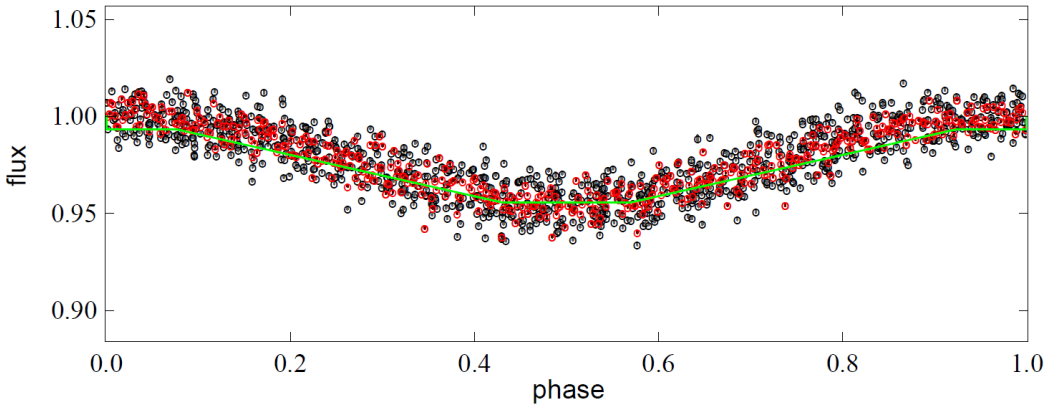

Figure 1.5: Light curve: SDSS193144. Circles mark flux with vertical error bars and the green line shows an automated fit assuming v-shaped transients.

In addition to the light curves, the following picture provides the finder charts as they have been used through out the project. The data for the finder charts origin from the *SDSS*-(DR7) [3] (SDSS070428 and SDSS070433) and the *2MASS* [81] (SDSS193144) catalog.

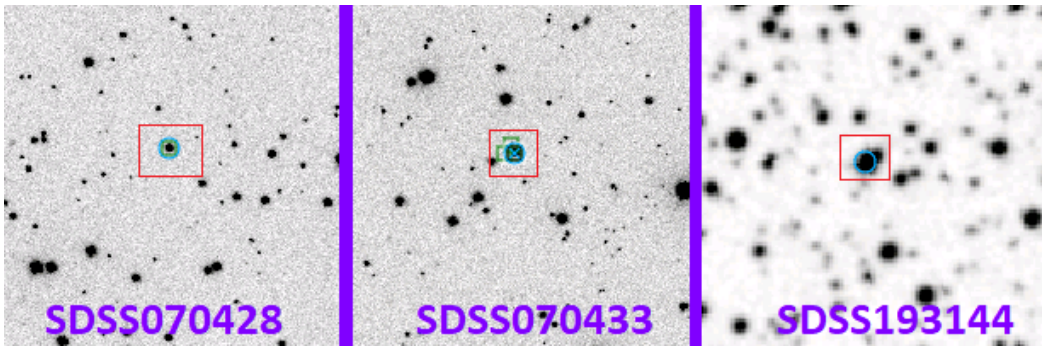

Figure 1.6: Finder charts for all targets as annotated and highlighted in the red box. The field of view is roughly $2,5 \cdot 2,5\ arcmin^2$ and all these finder charts have been produced using the *Caltech* finder chart tool *IRSA* [25]. Note: SDSS193144 only appears crowded in this finder chart data and is clearly separated from its neighbor in our spectra.

The finder chart for SDSS193144 shows an neighboring source which seems to blend the actual target. Checking with our photometric *3KK* follow up showed, that both targets are clearly separated and just look blended within the *2MASS* data.

Figure 1.7: RGB picture composed from our own g', r' and J-band *3KK* observations of our target SDSS193144. As marked by the red arrow, it shows that this target is not blended as it seemed within the *2MASS*-finder chart.

In addition our early *ES2* observations (see figure 1.8) prooved as well that we are able to separate both targets also within our spectra.

Figure 1.8: Fits file of a SDSS193144 test pointing spectra. The two horizontal line show the actual scientific target as well as a neighboring source. The prominent emission towards the right edge of the spectra is the 5577.34 Å Oxygen emission. Details on the spectroscopic data reduction and analysis follow later in chapter 5 and following.

Before we now start to analyze these targets in detail, we first investigate theoretically the nature of our target companions in the next subsections.

1.3 WD - White dwarfs

White dwarfs (WDs) are generally considered to be the final evolution stage of the majority of all main sequence stars. Literature commonly agrees on a WD progenitor initial-mass ($M_{Progenitor}$) which is less than 8 $M_{\odot}$.[5] [18]

Observationally, WDs are generally characterized by their densities and vary in color and mass. They are located in the lower left section of the well known *Hertzsprung-Russell* diagram.

1.3.1 Evolution

When a star with $M_{initial} \leq 8\ M_{\odot}$ reaches the end of its hydrogen core burning phase, its core starts to collapse, since no more energy is released to counter play the outer shells gravitational pressure. In consequence, the cores density reaches a regime where the gravitational pressure p_{grav} becomes greater than the Fermi pressure p_{Fermi} of the electrons.

From now on, the core is degenerated as $p_{core} \geq p_{Fermi-Electron}$ and mostly consists of degenerate electron-gas and bare helium cores. The stars is from now on stabilized by Electron-Fermi pressure $p_{Fermi-Electron}$.
The following evolution is determined by the initial progenitors mass and falls in either of the three scenarios[18]:

- $\mathbf{2.5\ M_{\odot} \leq M_{Progenitor} \leq 8.0\ M_{\odot}}$: The heaviest WD progenitors manage to ignite helium fusion in shells around their main sequence hydrogen fusion core, hence these stars skip the helium flash but still end up with to less mass to fusion carbon, thus the resulting core structure is equivalent to the former case. Still the WDs core and crust composition is influenced as described in the following subsection 1.3.2.
- $\mathbf{0.26\ M_{\odot} \leq M_{Progenitor} \leq 2.5\ M_{\odot}}$: Such lighter progenitors heat up until the helium fusion starts. As helium fusion is less efficient than hydrogen fusion, the released energy only heats the core because stabilizing Proton Fermi pressure $p_{Fermi-Proton}$ still can not be overcome. Subsequent the first helium fusion leads to a immediate chain reaction, in which most of the helium gets burned instantly. This event is called helium flash and fusions the helium cores into mostly carbon and partly oxygen cores, surrounded by degenerated electron-gas, still stabilized by $p_{Fermi-Proton}$. The following carbon fusion can not ignite due to the

[5] $M_{\odot}$: Mass of our Sun

missing thermal energy based on the low WD progenitor mass. Once the helium flash has happened and the degenerated carbon core has formed, the outer shells start to cool and contract since the cores energy release almost dropped to zero. The in falling shells release their gravitational energy, which further heats the core and also leads to the ejection of the shells.

- $\boldsymbol{M_{Progenitor} \leq 0.26\ M_{\odot}}$: Due to the gravitational energy released by the cores contraction, which became possible by $p_{grav} \geq p_{Fermi-Electron}$, the cores temperature rises. For WDs, with initial masses less than 0.26 $M_{\odot}$, the further evolution stops here with the release of their shells and the bare core remains as WD.

The star now consists of a degenerate hot carbon core (up to $10^7 K$) with a thin non degenerated crust and a giant outer shell which will form a planetary nebula once finally ejected.

1.3.2 Spectral Classification

Based on the abundances and prior evolution, most WDs have either a thin hydrogen crust (DA) or are covered by helium (DB/DO). In rare cases, the atmosphere is contaminated by carbon (DQ) or even higher elements (DZ). This classification as for example proposed by Edward et al. in 1983 [79] is based on historic roots and follows overall no deeper logic, while the proposed subclasses only contain targets of specific temperature ranges.

The common characteristic which clearly distinguishes WDs from other objects is their large surface gravity $log(g)$ which indicates dense, degenerated matter. As mentioned before, WDs are extreme hot cores of post-main sequence stars and slowly cool over time.
While also young and massive O-stars could reach similar temperatures, their bolometric surface would be way to big, so their resulting apparent luminosity would exceed a WDs luminosity by many magnitudes for local sources. In case of a distant O-star one has to investigate the details of its spectral composition to differentiate between both stellar classes.

1.3.3 Equation of state

Like all stable stars, WDs are characterized by an equilibrium of pressure. The gravitational pressure p_{grav} is defined by their spherical geometry and Newtons theory of gravitation as show in the following equation, with G being the Gravitational constant, M the objects mass and R its radius:

$$p_{grav} = -\frac{3}{8}\frac{GM^2}{\pi R^4} \tag{1.3.3.1}$$

Regular main sequence stars compensate the gravitational pressure by their internal thermal pressure. Even main sequence stars can be heavier by a factor of 100 times and more, their mass is still distributed over a large volume. As WDs evolve from the dense core of stars, their progenitors are only kept stable by the enormous amount of thermal pressure due to the internal energy production by fusion. With the loss of this energy source, the core collapses and becomes even denser.

WDs consist of degenerated electron gas and atomic cores, which means that its electrons behave like non-interacting particles with pressure. As the quantum mechanical derivation of this state is covered in standard literature like Griffiths - *Introduction to quantum mechanics* [34] and beyond the focus of this thesis, we skip it and directly start with equation 5.46 from Griffiths [34] as it is shown here:

$$p_{fermi} = \frac{(3\pi^2)^{\frac{2}{3}}\hbar^2}{5m} n^{\frac{5}{3}} \tag{1.3.3.2}$$

m and n represent the mass and number density of the particles for which the Fermi pressure is calculated. While the densities of electrons and atomic cores are similar, the electrons mass is roughly a factor 2000 times smaller than the one of a proton. Hence the Fermi pressure of an electron is about 2000 times higher as the one of protons. The Fermi pressure of electrons becomes relevant, once the electrons are compressed into such small volume, that by *Heisenbergs uncertainty-principle* their quantum mechanical impulse exceeds their thermal based impuls. This Fermi pressure $p_{Fermi-Electron}$ is the stabilizing counterpart to gravity, until gravity exceeds it. The critical mass for which $p_{Fermi-Electron} \leq p_{grav}$ is called *Chandrasekhar limit* and discussed in detail in subsection 1.3.5.
Further details on the equation of state can be found in the recent paper of Boshkayev et al. [5].

1.3.4 Mass-Radius relation

In consequence of their equation of state, WDs show an reciprocal relation between mass and radius, so increasing mass leads to smaller and smaller radii. A general formula for WDs mass radius relation can not be given since the many factors like the WDs core temperature, its abundance and other properties influence the individual WDs structure. Still, the mass-radius relation can be approximated for non relativistic WDs as adapted from Koester et al. [54] (see equation 3.20): $R_{WD} \propto M_{WD}^{-\frac{1}{3}}$

Boshkayev et al. [5] recently published a paper on the *Equilibrium structure of white dwarfs at finite temperatures.* They conclude on plot 1.9, which merges observational data with their theoretical results on WDs equation of states.

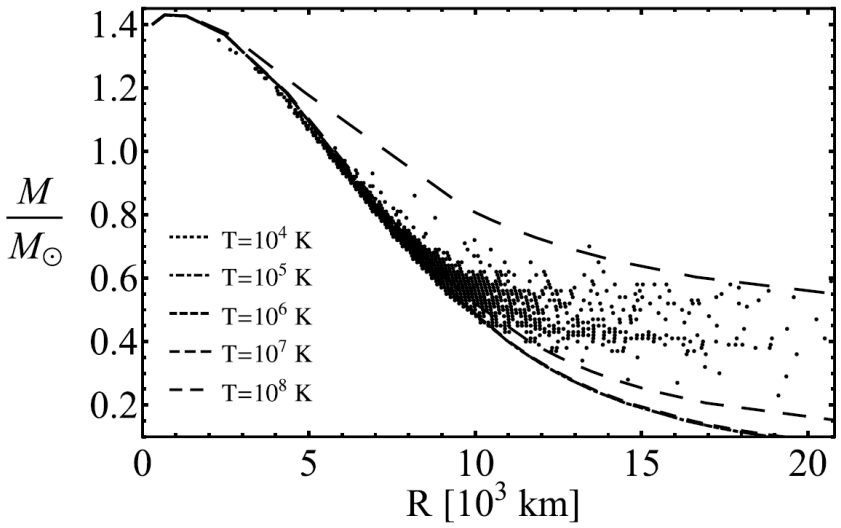

Figure 1.9: *"Mass-radius relations of white dwarfs obtained with the Chandrasekhar EoS (dashed black lines) for selected finite temperatures from $T = 10^4 K$ to $T = 10^8 K$ and their comparison with the masses and radii of white dwarfs taken from the Sloan Digital Sky Survey Data Release 4 (black dots)."* Taken from **Boshkayev et al. 2016** [5]

Note: The plotted Chandrasekhar Equations-of-State (EoS) account also for general relativity and are functions of the core temperatures.

One can see that the masses and radii of WDs, observed by the *Sloan Digital Sky Survey Data Release 4* [2] are mostly consistent with the Chandrasekhar equation of state, as proposed by Boshkayev et al. [5]. Most of the observed

WDs seem to agree with internal core temperatures of up to $10^7 K$ and slightly above. These core temperatures are not to be confused with the much cooler surface temperature of the observable crust.
For a detailed study of the WDs structure one has to take into account, that WD-cores are isothermal, non conductive and their effective temperature depends on the heat flux between the core and the thin outer layer, from which photons finally escape.

1.3.5 Chandrasekhar limit

As mentioned above, the radii of a WD shrinks with increasing mass. This leads naturally to the question: *Is there a limit to WD masses?*

The Indian astrophysicist Subrahmanyan Chandrasekhar calculated in 1930 that WDs above roughly $M_{WD} \geq 1.4\ M_\odot$ can not stabilize themselves any more. Gravitational pressure now forces the free electrons to merge with the bare atomic cores and form neutrons. Typically within binary systems, the accretion happens via a steady mass transfer from the donating binary partner. As this process is slow enough, almost all such binary WDs reach the exact Chandrasekhars mass and therefore collapse equally. This kind of standardized events are called supernova 1a (SN1a) and are used to probe intergalactic distances beyond the limits of Cepheid variables and parallax measurements. The remanent of such a SN1a is a neutron star.

Chandrasekhars limit got refined over the decades based on details like the WDs spin, its magnetic field and the various possible abundances. Still its rough value of $M_{Chand} \approx 1.4\ M_\odot$ is still good enough for most applications, especially since the majority of WDs has masses around $M_{WD} \approx 0.6\ M_\odot$ as is shown in section 2.5.

1.4 BD - Brown dwarfs

Brown dwarfs (BDs) have first been theorized in the 1960s by e.g. Kumar S. 1967 *On planets and black dwarfs* [56]. The name has changed to brown dwarfs, since the term black dwarf was also used to refer to cold white dwarfs. In 1975, Jill Tarter finally suggested the name brown dwarf as reference to the expected color of these objects. Still, it took another 20 years until the first BD (Gliese 229B) was finally observed by Nakajima et al. 1995 [64]. BDs are characterized by their color respectively temperature in combination with their low mass and density. They are located in the lower right part of the *Hertzsprung-Russell* diagram, where they represent all protostars which failed to accumulate enough mass to ignite their hydrogen fusion.

1.4.1 Formation by gravitational collapse

Commonly stars are assumed to form from gravitationally collapsing clouds composed of cold interstellar matter. Without reviewing stellar evolution in detail, the gravitational collapse of such interstellar clouds is characterized by the *Jeans-Mass* (M_{Jeans}) as adapted from standard literature [18] (see equation 11.16b), where ρ is the density, k_B the *Boltzmann constant* and $\bar{\mu}$ the average atomic mass [$M_{Hydrogen}$] (e.g. 2 for pure H_2):

$$M_{Jeans} \propto \frac{1}{\sqrt{\rho}} \cdot \left(\frac{k_B T}{G\bar{\mu}}\right)^{\frac{3}{2}} \tag{1.4.1.1}$$

Whenever a cloud of interstellar matter reaches this limit, it collapses and hence forms a protostar, which mass is depending on the initial conditions. The actual *Jeans-Mass* from (1.4.1.1) is defined taking into account the typical dimensions of such clouds and considering intrinsic density fluctuations. However, we like to follow a slightly more obvious approach which leads to a more intuitive understanding of the process but still provides a close result in reference to M_{Jeans}. To describe a stable interstellar cloud we consequently use the Ansatz to equalize the internal gas- and the gravitational-pressure:

$$|p_{gas}| = |p_{grav}| \tag{1.4.1.2}$$

p_{grav} is given by equation (1.3.3.1). In contrast to WDs, gas clouds are stabilized by the gas pressure p_{gas}, which is given by the ideal gas law $pV = Nk_BT$, such that the initial density ρ and the mean particle mass $\bar{\mu}$ are directly included.

$$p_{gas} = \frac{\rho k_B T}{\bar{\mu}} \tag{1.4.1.3}$$

The average particle mass $\bar{\mu}$ is usually slightly larger than the mass of a hydrogen atom M_H. In an exemplary cloud, composed of $70\%H$, $10\%H_2$ and $20\%He$ atoms, $\bar{\mu}$ ends up to be:

$$\bar{\mu} = 0.7 \cdot 1\ M_H + 0.1 \cdot 2\ M_H + 0.2 \cdot 4\ M_H = 1,7\ M_H$$

As p_{grav} is defined by the radius R, we rewrite ρ using basic geometry. Hence the density ρ is replaced by the clouds mass and volume respectively radius. Using $\rho = M/V = \frac{3}{4\pi}\frac{M}{R^3}$ equation (1.4.1.3) can be rewritten to:

$$p_{gas} = \frac{3k_B}{4\pi}\frac{MT}{R^3\bar{\mu}} \tag{1.4.1.4}$$

As soon as p_{grav} exceeds p_{gas} the could starts to collapse. Hence we can calculate the according $M_{critical}$ using equations (1.3.3.1) and (1.4.1.4):

$$p_{grav} = \frac{3G}{8\pi}\frac{M^2}{R^4} \geq p_{gas} = \frac{3k_B}{4\pi}\frac{MT}{R^3\bar{\mu}} \tag{1.4.1.5}$$

$$\Rightarrow M_{critical} \simeq \frac{2k_B}{G}\frac{TR}{\bar{\mu}} \tag{1.4.1.6}$$

In order to compare our result with M_{Jeans} we rewrite (1.4.1.6) using the spherical radius-density relation $\rho = \frac{3}{4\pi}\frac{M}{R^3}$ again. Of course we could have converted R right away into ρ but using R for those intermediate steps make the calculations easier and more elegant. After some minor equivalent transformations we finally end up with our Jeans-like inequality for the critical mass of an interstellar cloud:

$$\Rightarrow M_{critical} \simeq \sqrt{\frac{6}{\pi}} \cdot \frac{1}{\sqrt{\rho}} \cdot \left(\frac{k_B}{G}\frac{T}{\bar{\mu}}\right)^{\frac{3}{2}} \tag{1.4.1.7}$$

1.4.2 Stable BDs

Based on the simplified *Jeans* approach for the critical mass we understand the initial conditions for the formation of BDs. The forming BD now starts to heat up along the ongoing contraction.
During their contraction phase, the temperature rises enough so the limited p_{grav} is compensated by $p_{gas} \propto T$. In the case of regular stars the collapse is first stopped by the energy released due to hydrogen fusion. The difference is the initial mass, which either can or can not be compensated by the thermal gas pressure p_{gas}.

Instead, BDs are inherently too lightweight to reach hydrogen fusion. Chabrier et al. 2005 [10] states a Hydrogen Burning Minimum core Mass of $m_{\text{HBMM}} \simeq 0.07\ M_{\odot} \approx 73\ M_{Jupiter}$. Accordingly, core temperatures range from $T_c = 10^4\ K$ to $10^7\ K$ and densities from $\rho_c = 10^1\ \frac{g}{cm^3}$ to $10^3\ \frac{g}{cm^3}$.

In contrast to large gas planets BD are heavy enough to ignite deuterium and thereby produce enough energy to stop an otherwise ongoing collapse. Deuterium mainly burns via the $p\ +\ d\ \rightarrow\ \gamma\ +\ {}^3He$ reaction and begins around $\approx\ 13\ M_{Jupiter}$. Higher mass BDs can even begin to burn lithium either via the $p\ +\ {}^7Li \rightarrow\ 2\alpha$ or the $p\ +\ {}^6Li \rightarrow\ \alpha\ +\ {}^3He$ reaction.[7] Still the amount of released energy is way less than the one produced by hydrogen fusion and hence barely sufficient to prevent the BDs further collapse.

However, due to the lack of produced energy, the overall temperature and the externally visible temperature of the BD atmosphere is typically below $T_{BD} \leq 2000\ K$. The BDs evolution is furthermore dominated by a passive cooling phase in which it slowly contracts due to ongoing thermal emission. This phase is actually not unlike a WDs cooling phase, but the BDs initial temperature and matter densities are magnitudes lower.

1.4.3 Spectral Classification

Generally stars are classified by their spectral type, which is a historic color scale. BDs are commonly addressed by the following spectral classes:

Brown Dwarf spectral classes

Class:	Y	T	L
T_{eff}	500 K ... 900 K	900 K ... 1600 K	1600 K ... 2300 K

Table 1.3: Brown Dwarf spectral classes as commonly defined by their T_{eff}, following the nomenclature as motivated by Kirckpatrick et al. [51].

These spectral classes define the color range which clearly indicate targets as BDs. To avoid confusion, commonly only L, T and Y-class objects are typically named BDs. However, for the slightly hotter M-class objects the situation is not such clear, which will be discussed in the following subsection. Due to the low surface temperature of BDs, their spectral energy distribution peaks in the near infra-red. In fact about 90% of the energy gets emitted at wavelengths longward of $1\mu m$ and peaks between $1-2\mu m$.[10]

While on the one end, high mass main sequence stars can in first order be spectrally approximated by their black-body continuum radiation, which, based on the abundances and mass, is in the visible mostly superposed by the *Balmer*-series [6] and few other absorption lines.
On the other end, low mass stars like M-dwarf and especially for BDs this approximation does not hold anymore. The black-body continuum is overlapped by evermore absorption lines, until it is hardly recognizable any more as Chabrier et al. 2002 showed in figure 1 of their paper [10].
BD spectra are intrinsically dominated by many strong absorption lines of heavier elements and molecules due to two effects:

1. The abundance of heavier elements in the visible atmosphere increases with lower temperatures as well as the first molecules become stable.

2. These absorption lines are located in the near infra-red which is the only observable section of the emitted spectrum due to the dwarfs limited luminosity.

1.4.4 BDs vs. M-class, S-class and Planets

Various kinds of stellar objects can appear within the same color range and hence simple color characterizations are not good enough to confirm BDs. The following three paragraphs just briefly introduce the three main classes which may appear in the same color regime as BDs.

M-class dwarfs vs. BDs - *Lithium*-test: As the lower end of the main sequence is represented by so called M-class dwarfs with $T = 2300 - 3650\ K$ it is not quite clear if young BDs could also reach such temperatures and appear in this class. Due to the similar low density of very low mass, hydrogen burning M-dwarfs and BDs, it is hard to distinguish both objects. To solve this problem, Rebolo et al. [72] first presented in 1998 the idea to use Lithium to distinguish such objects.

> *"The lithium surface abundance is widely used as a probe of conditions inside the stars. This light element burns at temperatures of about* $2.5 \cdot 10^6 K$*, easily attained even in the interiors of very low mass M stars. In fact, as far as we know, no detection of lithium in main-sequence M stars has been reported, ..."*[72]

The so called *Lithium-test* separates BDs featuring lithium absorption lines from hydrogen burning M-class stars without lithium lines in their spectra.

[6] *Balmer*-series: All absorption lines of the hydrogen atom, named after Johann Jakob Balmer, which first mathematically described them in 1885.

S-class giants vs. BDs: Due to extreme differences in densities various kinds of stellar objects can appear within the same color range. Even very high mass stars like some variants of red giants appear with similar colors and temperatures, such as S-class giants: $T = 2200 - 3800\ K$.
Luckily such giants show significant differences in other parameters like their density, so they are distinguishable from BDs.

BDs vs. Planets: Planets are considered as a by-product of regular star formation and hence mostly stay gravitationally bound to their hosting star. Still, BDs are sometimes considered to represent the upper end of the planet mass function, since they are the largest possible objects without hydrogen fusion.

While this statement is true, the formation of BDs still supports the argument that BDs are the lowest end of star formation as for example Whitworth et al. 2007 [91] states. Another strong argument, BD fuse deuterium and sometimes lithium, which clearly separates them from gas planets like Jupiter.

If we further consider that the only difference between regular stars and BDs is the lack of hydrogen fusion, we have to take into account that higher mass objects like O, B and A stars also fuse heavier elements than hydrogen during their main sequence phase. Some high mass classes even find short but stable phases without central hydrogen fusion. In contrast, many main sequence stars fail to burn helium, and the vast majority fails to fusion carbon until the very end of their regular lifetime.

All those stars are not forfeiting their right to be named stars. Furthermore, BD are often enough found without any companion so based on literature like Raghavan et al. 2010 [71] which reported the majority of BDs to exist in single systems, we estimate them to form on their own just like regular stars. Hence it seems odd to consider BD not as stars, as the only difference is the lack of hydrogen fusion. Even BDs miss to burn hydrogen they are still formed by the same mechanism as regular main sequence stars and surveys like Raghavan et al. 2010 [71] support this theory by the high percentage of single BDs.

1.5 WD-BD Binaries

So far, only few WD-BD binary candidate systems have been observed and even less of such systems have been confirmed. One cause for this are the rather low masses and the resulting dim binary luminosities as discussed in subsection 1.5.3. Hence, it is reasonable to review and compare the mass ranges of both parties side by side.

1.5.1 Mass ranges

WD masses: We already discussed the physical upper limit for WD masses in section 1.3.5. Beyond the Chandrasekhar limit at $M_{Chand} \approx 1.4 M_{\odot}$, WDs collapse as supernova.
The lower end of the mass range are so called extremly low-mass (ELM) WDs. In 2013, Althaus et al. [4] provided new evolutionary sequences for such ELM WDs, which range from 0.15 until 0.20 $M_{\odot}$. ELM WDs represent the currently known lower limit for WD mass at 0.15 $M_{\odot}$.
Histogram 1.10 is taken from Kepler et al. [50] and shows the mass distribution within the above defined range. Based on this distribution function, a typical DA WD can be assumed with $M_{WD} = 0.6\ M_{\odot}$.

BD masses: On the one hand, the lightest possible BD one can think of is characterized by the onset of deuterium burning. In order to fuse deuterium the BD needs a minimal mass of about 13 $M_{Jupiter}$.[7]
The upper end of the weight regime of BDs is on the other hand given by the onset of hydrogen burning and starts dependent on the abundances between 0.07 $M_{\odot}$ and 0.09 $M_{\odot}$.[74]

Binary comparison: In conclusion of the former statements we find in extreme cases theoretical ratios between 1/1400 until 1/2. Mass ratios for a common WD ($\approx 0.6 M_{\odot}$) - BD ($\in [13 M_{Jupiter}, 0.06 M_{\odot}]$) binary range from 1/100 until 1/10. They are significantly higher than any exoplanet systems mass ratio and hence cause stronger radial velocity signals.

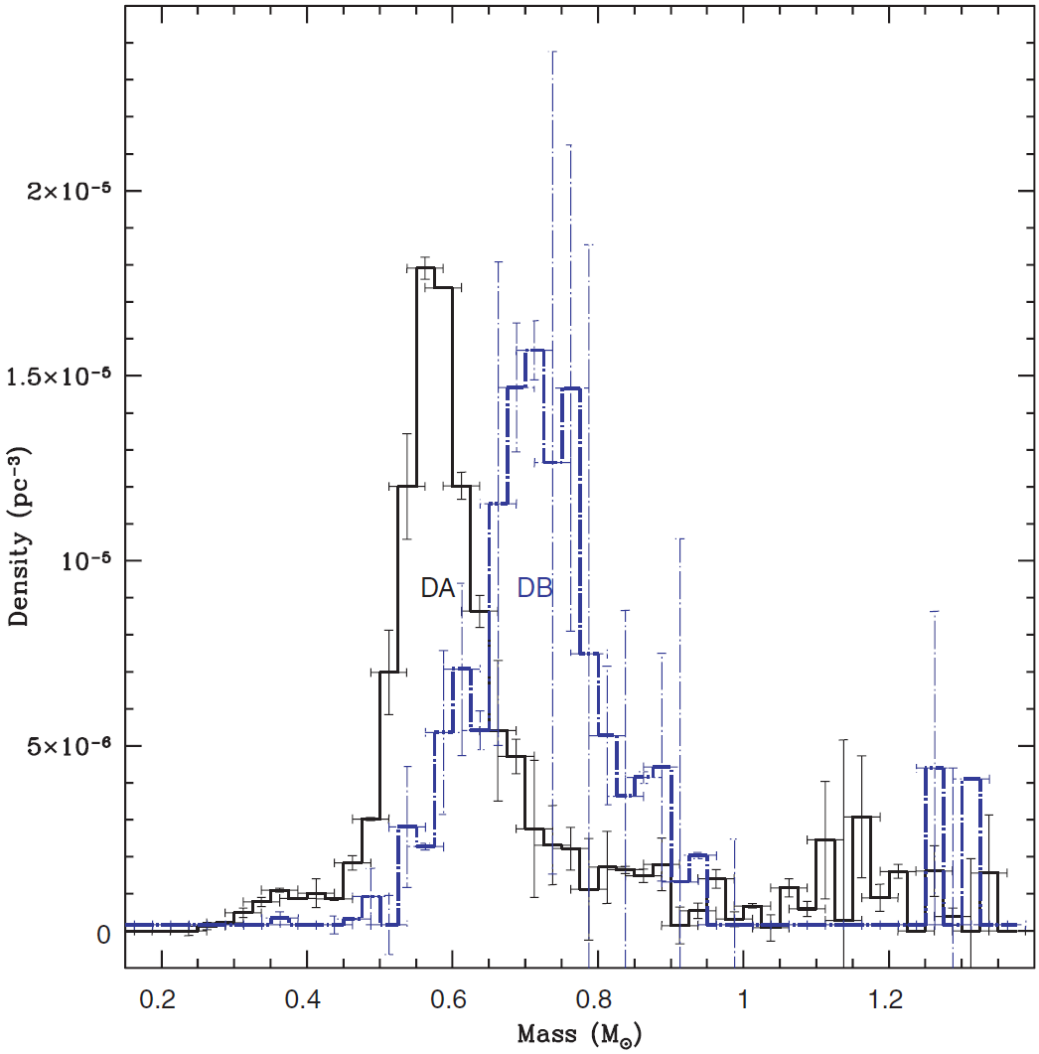

Figure 1.10: Histogram of WD masses: *"DA and DB histograms corrected by observed volume for comparison. The DB histogram has been renormalized to the DA maximum for display."* Taken from **Kepler et al. 2007** [50]

1.5.2 Object radii

WD radii: As the mass radius relation for WDs depends also on other parameters like the temperature, we rather choose a heuristic approach. In plot 1.9 we find data from Boshkayev et al. 2016 [5], which also contains SDSSDR4 data.[7]

In agreement with Kepler et al. 2007 [50], the masses peak around $M_{WD} = 0.6\ M_\odot$ and we find WD radii in the order of $R_{WD} = 10 \cdot 10^3\ km$.

BD radii: The precise function for a BDs radius is dependent on many factors like the mass, the temperature, the abundance and age. A simple mass radius relation as for higher mass stellar objects is hence not sufficient as the stabilizing physical processes are less obvious. Early BD feature a monotonically increasing radius function $R_{BD}(M_{BD})$. But for a given mass, the radius is always a decreasing function of age. For late BD, the mass-dependence of the radius inverts, hence less massive BD have larger radii.[7]

One of the largest and also lightest BD (CT Chamaeleontis B) was reported in 2008 by Schmidt et al. [75], who stated:

$$M_{CT\ Cham\ B} = 17 \pm\ 6\ M_J \qquad R_{CT\ Cham\ B} = 2.2^{+0.81}_{-0.60}\ R_J \approx 1.5 \cdot 10^5\ km$$

In 2017, Boetticher et al. [88] published the smallest BD known until then, designated as EBLM J0555-57, with a mass and radius as follows:

$$M_{J0555-57} = 85 \pm 4\ M_J \qquad R_{J0555-57} = 0.84^{+0.14}_{-0.04}\ R_J \approx 5.9 \cdot 10^4\ km$$

Note that the smallest BD found is already at the upper mass limit for BD. Hence this radius, which is roughly Saturn sized, can be used as a minimal size for BDs.

Still, in a rough first order approximation we can follow Burrows et al. 2001[7], which theorized that the radius for BD is over almost two orders of magnitudes in mass constant in the order of $R_{Jupiter}$. Hence we assume:

$$R_{BD} \in [0.84\ R_J, 2.2\ R_J] = [5.9 \cdot 10^4\ km, 1.5 \cdot 10^5\ km]$$

Hence the BD is always 10 to 100 times larger as its WD primary, while being significantly lighter.

[7]SDSSDR4: Sloan Digital Sky Survey - Data Release 4

1.5.3 Temperature ranges - spectral continuum

In order to understand the light curves of WD BD binaries one has to realize the huge temperature differences of both partners, which dictate their spectral continuum.

Integral radiation emission: The first approach to the spectral continuum is to calculate the integral sum of emitted radiation. To do so, we follow the Stefan-Boltzmann-Law $P = \sigma_B \cdot A \cdot T^4$ [17] and insert the spherical surface:

$$L = \sigma_B \cdot 4\pi \cdot R^2 \cdot T^4 \tag{1.5.3.1}$$

Using the rewritten form, we can directly calculate the power emission based on the objects temperature and radii, alongside the Stefan-Boltzmann-Constant σ_B.[8] The following table 1.4 shows the results for some exemplary WD and BDs.

Full spectrum - Blackbody radiation L [W] for exemplary objects

WDs:	$R = 5000\ km$	$R = 10000\ km$	$R = 15000\ km$
$T_{eff} = 10000\ K$	$1.78 \cdot 10^{23}$	$7.13 \cdot 10^{23}$	$1.60 \cdot 10^{24}$
$T_{eff} = 25000\ K$	$6.96 \cdot 10^{24}$	$2.78 \cdot 10^{25}$	$6.26 \cdot 10^{25}$
$T_{eff} = 50000\ K$	$1.11 \cdot 10^{26}$	$4.45 \cdot 10^{26}$	$1.00 \cdot 10^{27}$
BDs:	$R = 60000\ km$	$R = 100000\ km$	$R = 150000\ km$
$T_{eff} = 400\ K$	$6.57 \cdot 10^{19}$	$1.82 \cdot 10^{20}$	$4.10 \cdot 10^{20}$
$T_{eff} = 1000\ K$	$2.57 \cdot 10^{21}$	$7.13 \cdot 10^{21}$	$1.60 \cdot 10^{22}$
$T_{eff} = 1750\ K$	$2.41 \cdot 10^{22}$	$6.68 \cdot 10^{22}$	$1.50 \cdot 10^{23}$

Table 1.4: Full spectrum - Blackbody radiation L [W] for exemplary WDs (Top) and BDs (Bottom) as resulting from equation 1.5.3.1. Note that the total emission can be in the same order of magnitude, dependent on the stellar parameters.

In conclusion, when taking into account the bolometric luminosity, cold WDs and hot BDs may emit a similar amount of energy as highlighted in green within table 1.4. But this picture changes dramatically if we investigate the black body approximation of a specific and narrow wavelength range exclusively.

[8] The Stefan-Boltzmann-Constant σ_B is a combination of the following natural constants[17]: $\sigma_B = \frac{2\pi^5 k_B^4}{15h^3c^2} \approx 5.67 \cdot 10^{-8} \frac{W}{m^2 K^4}$

Planck emission: As we show in chapter 3, we use spectroscopy to follow up the photometric *WFCAM Transit Survey* (see sub-section 1.1), which observed in J-band.[9] To calculate the wavelength dependent target brightness, we use Planck's-Law in as shown in the following equation (1.5.3.2):

$$\omega_\lambda(\lambda)\, d\lambda \;=\; \frac{8\pi hc}{\lambda^5}\frac{1}{e^{\frac{hc}{\lambda k_b T}}-1}\, d\lambda \qquad (1.5.3.2)$$

The resulting Planck-curves represent the blackbody radiation for different temperatures. Mathematically these curves never cross each other and their λ_{peak}, which is different from their λ_{median}, shifts for decreasing temperatures towards longer wavelengths, as described by *Wien's displacement law*.
When we now compare two of such curves for typical WD-BD temperatures e.g. 15000 K for a cool WD vs. 1500 K for a BD, we find a difference in radiation of roughly five orders of magnitude.
From this aspect, one could assume the WD to absolutely dominate the picture in all wavelength regimes, but so far we only calculated $\omega_\lambda(\lambda)$ which ignores the physical size of the emitter.

Total emission: To get the full amount of emitted radiation per wavelength we have to consider: $P \;=\; \iint \omega_\lambda(\lambda) \cdot d\lambda dA$

Wavelength-depended radiation for WD and BD

Band:	g'	i'	J
Wavelength:	475 nm	750 nm	1250 nm
WD:	$6.2 \cdot 10^{29}\frac{W}{nm}$	$2.1 \cdot 10^{28}\frac{W}{nm}$	$4.4 \cdot 10^{27}\frac{W}{nm}$
BD:	$3.3 \cdot 10^{25}\frac{W}{nm}$	$1.9 \cdot 10^{27}\frac{W}{nm}$	$1.2 \cdot 10^{28}\frac{W}{nm}$
Sum:	$1.9 \cdot 10^{29}\frac{W}{nm}$	$2.3 \cdot 10^{28}\frac{W}{nm}$	$1.6 \cdot 10^{28}\frac{W}{nm}$

Table 1.5: WD: $T_{WD} = 10,000\ K$, $R_{WD} = 5,000\ km$
BD: $T_{BD} = 1,750\ K$, $R_{BD} = 150,000\ km$

Usually the Integral covers the full spherical surface, but we are only interested in the amount of light emitted by the projected, observable surface. In first order approximation we can forget about direction dependencies and simply approximate using πR^2. The values for each object in table 1.5 consider the objects actual physical size, which leads to comparable emission in the infrared.

[9] J-band: 1166 nm until 1332 nm (see: sub-section 3.3)

Resulting binary continuum: Now that we understand the impact of the physical size, we can calculate a combined binary continuum assuming both partners are fully visible (see plot 1.11). The resulting continuum mostly follows the WD spectrum for the visible regime but approaches the BD spectrum for $\lambda \geq 1\mu m$. This behavior is generally called infrared-excess.

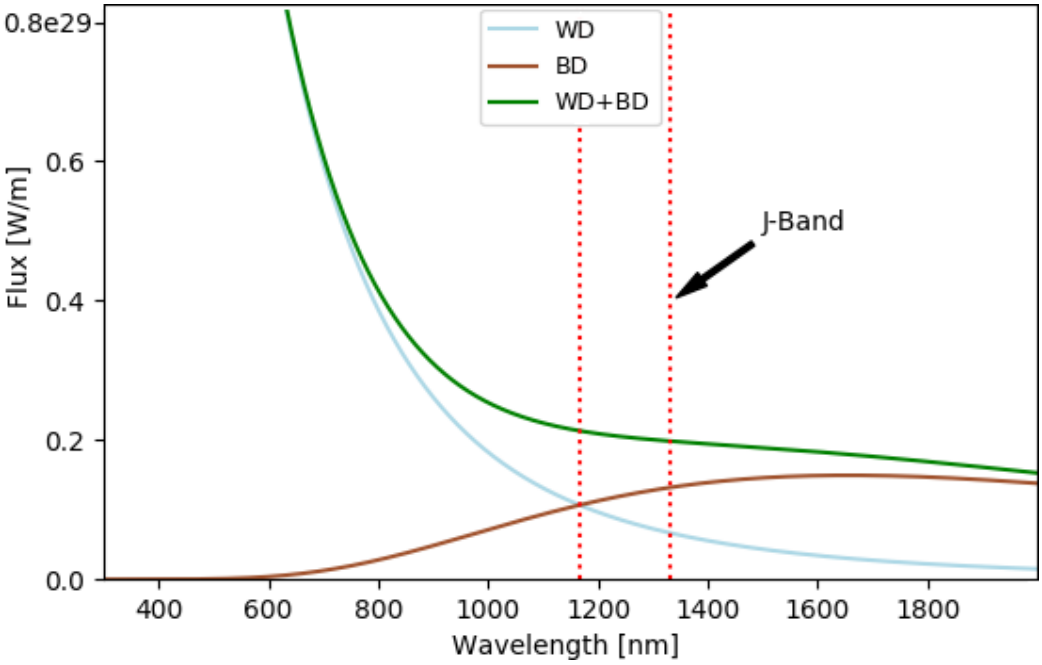

Figure 1.11: Combined continuum for a WD-BD binary. In this example the BD becomes dominant to the WD in the J-Band (1166 nm until 1332 nm). WD: $T = 15 \cdot 10^3 K$, $R = 5 \cdot 10^6 m$ | BD: $T = 1,75 \cdot 10^3 K$, $R = 150 \cdot 10^6 m$

Note: We plotted the most extreme case of a cold WD vs. a hot BD. In most cases the BD will start to affect the combined spectral energy distribution only at much longer wavelengths.

1.5.4 Binary effects

Intrinsically all monitoring photometric surveys have a strong detection-bias for eclipsing binaries, as such system show measurable flux variations. In order to understand such transiting binary effects we recall illustration 1.12 which is taken from Obermeier 2016.[66]
The transit is clearly visible and defines the time when the minor partner partly shades the dominant one, versus the occultation during which the major companion completely conceals the minor.

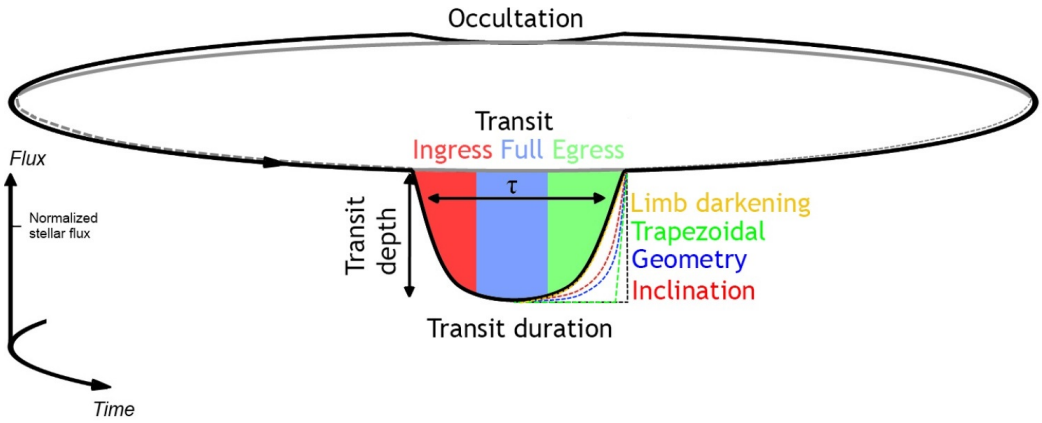

Figure 1.12: Illustration of the normalized flux over time for an eclipsing binary system. Taken from **Obermeier 2016** [66]

Inclination uncertainty: Generally all binaries follow their internal two-body dynamics such as theoretically described by Hilditch et al. (2001) [39] based on their semi major axis a: $a_{WD} \cdot m_{WD} = a_{BD} \cdot m_{BD}$. When we now assume a circular orbit with transit period P, we find: $v_{WD} = 2\pi a_{WD}/P$. Combining both geometrical results with Keplers 3rd law we can follow standard literature and end up with the apparent amplitude $v_{app.}$ for binary systems:

$$v_{app.} = v_{binary} \cdot \sin(i) \tag{1.5.4.1}$$

This $\sin(i)$ factor represents the viewing angle of the system. In a face-on system ($i = 0°$), both partners are all the time visible and the radial velocity shift as described in section 2.4 vanishes due to $\sin(0°) = 0$. An edge-on system with $i = 90°$ shows maximum radial velocity shift as $\sin(90°) = 1$. As we can only detect transits for systems which we see from an edge on angle we can neglect the impact of $\sin(i)$ and assume $v_{app.} = v_{binary}$, which allows for detailed characterization of the system.

Selection bias: In diagram 1.12 we can see light curve features, like transit and occultation which only eclipsing binary provide. Hence such light curves are easier to detect, as they strongly differ from stellar variability.
Not only eclipsing binaries are found by such studies. Also periodic light curves which may reveal significant differences between the day and night side of the BD can be found by such surveys.
Even such non eclipsing binary systems are also detectable, also their signal vanishes when the inclination angle i approaches 0°, as both partners then are visible almost all the time with equal illumination phases.

Chapter 2

Spectral shifting effects

Binary systems consist of two companions, which orbit a common barycenter. Neither of the companions should be of negligible mass with respect to the other, so the system follows internal 2-body dynamics. It can be defined by the motion of the common barycenter and the individual orbits of both stellar objects. Dependent on the mass and size distribution as well as on the distance between both partners, the relative velocity within the binary system ranges over several magnitudes.

However, only very nearby binary systems can actually be verified by imaging. The majority of binaries is either to far away or its dynamics only features minor separation, which can not be resolved directly. These systems have to be analyzed by time resolved spectroscopy or photometry. Both verification methods rely on the systems dynamical parameters and tend to higher detection efficiencies for shorter orbit periods.
Binary systems in general and WD-BD binaries in specific suffer from the following spectral shifting effects:

• Section 2.1: Earth's rotation • Section 2.2: Earth's orbit motion • Section 2.3: Relative target motion • Section 2.4: Binary orbit wobble	Doppler effect
• Section 2.5: Gravitational red shift	General relativity

On the one hand, the first four effects can all be combined to the resulting relative motion along the line of site (radial velocity). All of them together cause the spectral shift via the Doppler effect. On the other hand, the gravitational red shift is based on the local gravitational potential of the WD, which causes measurable spectral shift due to the high escape velocity.

2.1 Earth's rotation

The effect of Earth's rotation on our measured spectra is a combination of geometrical considerations.

1. Earth's geometry
2. Relative target position
3. Time of observation

Earth's geometry: The Earth's rotation around its own axis is the reason for our day-night cycle. Starting from this fact, we can roughly estimate the according angular velocity ω.

$$\omega_{Earth,\ rot.} = \frac{2\pi}{t_{Earth,\ rot.}} = \frac{2\pi}{23,934h} \approx 7.3 \cdot 10^{-5}\ \frac{rad}{s} \tag{2.1.0.1}$$

As for all spherical objects, the actual rotation speed $v_{rot.}$ at a given location depends not only on the angular velocity ω, but also on the latitude φ and the Earth's radius R.

$$\begin{aligned} v_{rot.} &= \cos(\varphi) \cdot R_{Earth} \cdot \omega_{Earth\ rot.} \\ &\approx \cos(\varphi) \cdot 6.371 \cdot 10^6\ m \cdot 7.3 \cdot 10^{-5}\ \tfrac{rad}{s} \\ &\approx \cos(\varphi) \cdot 465\ \tfrac{m}{s} \end{aligned} \tag{2.1.0.2}$$

Relative target position: The actual effect on the measured star spectra is even smaller, as we further have to take the relative target position in relation to the orientation of Earth's rotation into account. Any astronomical target can be located using the equatorial or the RA-DEC coordinate system.

DEC: Declination (DEC or δ) is the celestial equivalent to the geographic latitude and aligned with the Earths rotation plane. Hence we account for the declination using a $\cos(DEC)$ factor.

RA: Right ascension (RA or α) is the celestial equivalent to the geographic longitude and is measured relative to the March equinox of the Sun.[10] As the spectral effect is based on relative motion, the RA only has indirect impact as it determines at which local time an object is visible. The relative position along the RA axis is defined by the so called

[10] March equinox: The point in time, when the Sun crosses the celestial equator from south to north.

hour angle (HA). The local meridian transit (upper culmination) defines HA = 0:00:00 h and HA from there on is measured as the elapsed time since this transit. We can easily realise that the meridian transit also defines the moment when the Earths rotation causes us to move exactly orthogonal to the line of sight towards the target. Hence we account for the right ascension respectively the targets hour angle, using a $\sin(HA)$ factor.

Adding those two effects to the prior formula 2.1.0.2 we end up with the resulting imprint of the Earth's rotation on the apparent velocity $v_{app.}$ as shown in the following equation:

$$v_{rot.} \approx \underbrace{465\ m/s}_{Earth\ rot.} \cdot \underbrace{\cos(\varphi)}_{Obs.\ latitude} \cdot \underbrace{\cos(DEC)}_{Declination} \cdot \underbrace{\sin(HA)}_{Hour\ Angle} \tag{2.1.0.3}$$

Time of observation: We can estimate the effect to be always less then $\approx 465\ m/s$. Furthermore, astronomical observations are preferably done around culmination,[11] to minimize the included air mass. In consequence the $\sin(HA)$ term ends up close to 0, as the hour angle HA is 0:00:00 during culmination.
All in all the impact of the Earth's rotation can be calculated using equation 2.1.0.3, but is usually closer to $0\ m/s$ than to its maximum value $\approx 465\ m/s$.

Conclusion: In general this estimation is important for radial velocity studies like the search for exoplantes. For example an earth-like planet around a star like our Sun would lead to a measurable radial velocity less than $1\ m/s$. Hence such effects become crucial.
This thesis aims to measure typical radial velocities for stellar binary systems. As our WD targets are dim and rare, we hence have to use low resolution spectroscopy[12] to gain reasonable Signal-to-Noise (S/N). So our spectrographs are designed to measure effects in the order of $10\ km/s$ and above.
In conclusion, we can ignore the imprint ($v_{rot.max.} = 465\ m/s$) of Earth's rotation, as our spectral resolution is at least 20 times rougher then this effect.

[11] Culmination: Highest point on sky for a given object.
[12] In this thesis, we us low resolution spectroscopy, with a resolving power between 2.000 and 4.000

2.2 Earth's orbit motion

The first relevant component for the apparent velocity of the observed WDs is the Earth's orbital motion around our Sun.

As for the Earth's rotation, it's orbit impact is again a combination of several effects:

1. Orbit geometry
2. Relative target position
3. Time of observation

Orbit geometry: Similar to equation 2.1.0.2 we can define the Earth's angular velocity around the Sun by substituting $t_{Earth\ rot.} \approx 24h$ with $t_{Earth\ orb.} \approx 365d$.

$$\omega_{Earth\ orb.} = \frac{2\pi}{t_{Earth,\ orb.}} = \frac{2\pi}{365d} \approx 2 \cdot 10^{-7}\ \frac{rad}{s} \tag{2.2.0.1}$$

In contrast to the former section 2.2 the angular velocity is not reduced by a latitude factor $\cos(\varphi)$. The Earth follows its orbit around the Sun in a fixed plane, so we can handle it like an observatory at the equator, which always encounters the full angular velocity of Earth's rotation.

$$\begin{aligned} v_{orb.} &= R_{Earth\ orb.} &\cdot\ & \omega_{Earth\ orb.} \\ &\approx 1\ AU &\cdot\ & 2 \cdot 10^{-7}\ \tfrac{rad}{s} \\ &\approx 1.5 \cdot 10^{11}\ m &\cdot\ & 2 \cdot 10^{-7}\ \tfrac{rad}{s} \\ &\approx 30\ \tfrac{km}{s} \end{aligned} \tag{2.2.0.2}$$

The slow angular velocity is more than compensated by the huge average distance from the rotation axis.

Relative target position: Again we find that the projection of the Earth's orbit is similar to the projection of it's rotation relative to the targets position.

Ecliptic latitude: This time we have to convert the target DEC to the actual relative declination above the Earth's orbit, called ecliptic latitude (b). While DEC is defined as the angle above the equator, the ecliptic latitude needs some further conversion. As the Earth's rotational axis is tilted by $\Delta\phi \approx 23.4\ deg$ from it's orbital plane, we subtract 23.4 *deg*

from the targets DEC. So instead of $\cos(DEC)$ we have to account for $\cos(b) = \cos(DEC - 23.4\ deg)$.

Nevertheless, $\cos(b)$ may be individual for each target, but is still constant over time. Hence the individual maximal velocity $v_{orb.\ max}$ can be approximated:

$$v_{orb.\ max} \approx 30\ \frac{km}{s} \cdot \cos(b) \tag{2.2.0.3}$$

Ecliptic longitude: The targets RA has an ecliptic counter part called ecliptic longitude (l). The precise mathematical derivation is rather lengthy so we fall back to the rotational analogon.

Similar to the hour angle HA we can define an azimuthal angle AA for each target at each given point in time. This AA defines the relative location within the orbit in relation to the targets position and hence is compensated by $\sin(AA)$:

$$v_{rot.} \approx \underbrace{30\ km/s}_{Earth\ orb.} \cdot \underbrace{\cos(b)}_{Ecliptic\ latitude} \cdot \underbrace{\sin(AA)}_{Azimuthal\ Angle} \tag{2.2.0.4}$$

Time of observation: In contrast to the rotation, we can theoretically observe the target during each phase of our orbit, based on its ecliptic latitude. Hence $\sin(AA)$ is not negligible. In fact the azimuthal angle has major impact on the spectral shift due to the Earth's orbit around the Sun.

Conclusion: With a maximum velocity of $v_{orb.\ max} \approx 30\ km/s$, we have to consider the Earth's orbit effect for each individual observation. Due to the variable azimuthal angle ($\sin(AA)$), the apparent velocity $v_{app.}$ may alter within the following range:

$$v_{app.} \in \left[-\left(30\ \frac{km}{s} \cdot \cos(b)\right), +\left(30\ \frac{km}{s} \cdot \cos(b)\right)\right] \Rightarrow \left[-30\ \frac{km}{s}, +30\ \frac{km}{s}\right]$$

2.3 Relative target motion

The second component of the apparent velocity of the observed WDs is the relative motion between our Sun and the target system.

Relative solar motion: Our Sun is located within the Local Bubble, which is part the Orion arm of the Milky Way. Due to the Suns age, it completed several revolutions around the galactic center. Which led to a minor relative motion with respect to the local surroundings so it likely drifted far away of it's birth region. The general motion of stars in the local neighbourhood is referred to as local standard of rest (LSR). The measurement of our relative motion to the LSR is a long-standing challenge, since 1886 (Homann). Generally the LSR is expressed as $(U, V, W)_\odot$, with $U_\odot$ the spherical, $W_\odot$ the vertical and $V_\odot$ the radial component towards the galactic center. While it sounds like an easy task to measure the relative motion, it still is not clear how reliable those values really are. Even recent studies, deviated more than the authors error margins. While Coşkunoğlu et al. [13] 2011 suggested values in the range of $V_\odot = 13 \pm 0.5 \frac{km}{s}$, Huang et al. [47] published $V_\odot = 10 \pm 0.1 \frac{km}{s}$ in 2015. The insecurity is an expression for the systematic biases of the used methods.

Relative target motion: While our Suns relative motion within the local framework is measured imprecisely, the task is even harder for the target. But it seams reasonable to estimate effects in the same order of magnitude. Hence the systematic uncertainty doubles. While the Suns motion and the targets motion relative to LSR can not be measured precisely, we can measure the individual relative motion between the target and our Sun. Furthermore, we know that our Sun smoothly rotates around the galactic center and gravitational interactions with other stars are negligible. Due to the WDs limited luminosity, we study WDs until distances in the order of a few 100 *pc*. Consequently the WD can be assumed to reside in a similar environment with a flat gravitational gradient, so the resulting motion is neither accelerated nor deviated.

Conclusion: The effect of the relative motion between the Sun and the target is stable in a way that it's not changing on human time scales. Therefore $v_{rel.\ mot.}$ can be handled as an individual but constant offset for each target.

2.4 Binary orbit wobble

The third relevant component for the $v_{app.}$ is the orbit motion around the binary barycenter. In order to estimate the expected v_{wobble} (Binary Wobble), we consider the following aspects: angular velocity, mass distribution and barycenter distance.

Angular velocity: Similar to the effect of Earth's orbital rotation (2.2) the WDs wobble leaves its imprint on the spectra. Based on the same geometrical argument we calculate the targets angular velocity using the following equation:

$$\omega_{WD\ orb.} = \frac{2\pi}{t_{WD\ orb.}} \tag{2.4.0.1}$$

Mass ratio: The mass ratio of Sun and Earth is rather extreme. In contrast WD-BD binaries can be expected to be more balanced. In the case of Earth-Sun the mass ratio is roughly $M_{\odot} : M_{Earth} \approx 330.000 : 1$. Hence the Earth's orbit can be approximated as a test-particle within the Sun's gravitational potential.
Assuming an average WD mass $M_{WD} \in [0.1\ M_{\odot}, 1.4\ M_{\odot}]$ and a typical mass for a BD in the order of $M_{BD} \approx 50\ M_{Jupiter}$ or $\approx 0.05\ M_{\odot}$, we can not argue for the test-particle assumption any more. As shown in section 1.5, the actual mass ratio may vary from $M_{WD} : M_{BD} \approx 100 : 1$ to almost $1 : 1$.

Barycenter distance. Following the standard literature [17], the distance $r_{WD\ bary.\ dist.}$ between the center of the WD and the common barycenter is calculated as shown in equation (2.4.0.2).

$$r_{WD\ bary.\ dist.} = \frac{(M_{WD} \cdot r_{WD}) + (M_{BD} \cdot r_{BD})}{M_{WD} + M_{BD}} \Rightarrow \frac{M_{BD} \cdot r_{BD}}{M_{WD} + M_{BD}} \tag{2.4.0.2}$$

Note: In our initial system $r_{WD} = 0$, as the WD center is defined as origin.

Conclusion: v_{wobble} can be consequently calculated as follows:

$$v_{orb.} = r_{WD\ bary.\ dist.} \cdot \omega_{WD\ orb.} = \frac{M_{BD} \cdot r_{BD}}{M_{WD} + M_{BD}} \cdot \frac{2\pi}{t_{WD\ orb.}} \tag{2.4.0.3}$$

2.5 Gravitational red shift

Commonly redshift (z) is a term which is used to measure the cosmological distance of an object. It commonly is defined as the relative shift of an observed wavelength:

$$z = \frac{\lambda_{observed} - \lambda_{emitted}}{\lambda_{emitted}} \tag{2.5.0.1}$$

In a cosmological context, the redshift is caused by the expansion of space time it self, which is driven by dark energy.[13] The analog effect occurs when light is leaving the gravitational potential of its emitting object. For most stellar sources, this effect is negligible small.
The following calculations reveal, that the mass of the object and the location of emission are the crucial factors which determine the power of this effect. Beginning with white dwarfs, gravitational redshift becomes an important factor for the spectral analyses of objects with such high matter densities.
Starting with the energy E of a photon with a given wavelength λ one can express redshift as the energy loss due to the photons escape of the dwarfs gravitational potential, divided by the overall energy.

$$z = \frac{-\Delta E}{E} \tag{2.5.0.2}$$

When we now consider $E = \frac{hc}{\lambda}$ and furthermore rewrite $\Delta E = h\Delta\nu$ using $\frac{\Delta\nu}{\Delta\lambda} = \frac{c}{\lambda^2}$, we get $\Delta E = \frac{hc\Delta\lambda}{\lambda^2}$, which leads us to:

$$z = \frac{-\Delta E}{E} = \frac{hc\Delta\lambda}{\lambda^2} \cdot \frac{\lambda}{hc} = \frac{-\Delta\lambda}{\lambda} \tag{2.5.0.3}$$

The partial change in energy can be expressed as a fractional change in observed wavelength $-\Delta E/E = \lambda/\Delta\lambda$ as can be seen in (2.5.0.3).
For a white dwarf, the gravitational potential at the surface at radius (R_{WD}) of a WD of mass (M_{WD}) defines the escape potential which the photons have to overcome.

Velocity interpretation: As spectroscopic shifts are typically expressed as velocity, we use $\Phi = \frac{G \cdot M_{WD}}{R_{WD}}$ to rewrite the gravitational redshift (v_{grav}) to:

$$v_{grav} = \frac{c\Delta\lambda}{\lambda} = c\frac{\Delta E}{E} = c\frac{\Phi}{c^2} = \frac{G}{c} \cdot \frac{M_{WD}}{R_{WD}} \tag{2.5.0.4}$$

As mentioned in section 1.3, the range for WD masses and radii is limited. Hence the resulting gravitational redshift can be estimated within a certain range. The following subsection presents the according literature results.

[13] This statement quietly assumes the common ΛCDM interpretation of the accelerated expansion of the universe.

Literature results: In 2012, Falcon et al. [26] published a reasonable sized survey of local WDs, focusing on the gravitational redshift of the observed non-binary WDs which they assumed co-moving. Histogram 2.1 shows that the distribution of a subsample of 326 from Falcon et al. is consistent with the assumption of local WDs which can be assumed to be in general co-moving.

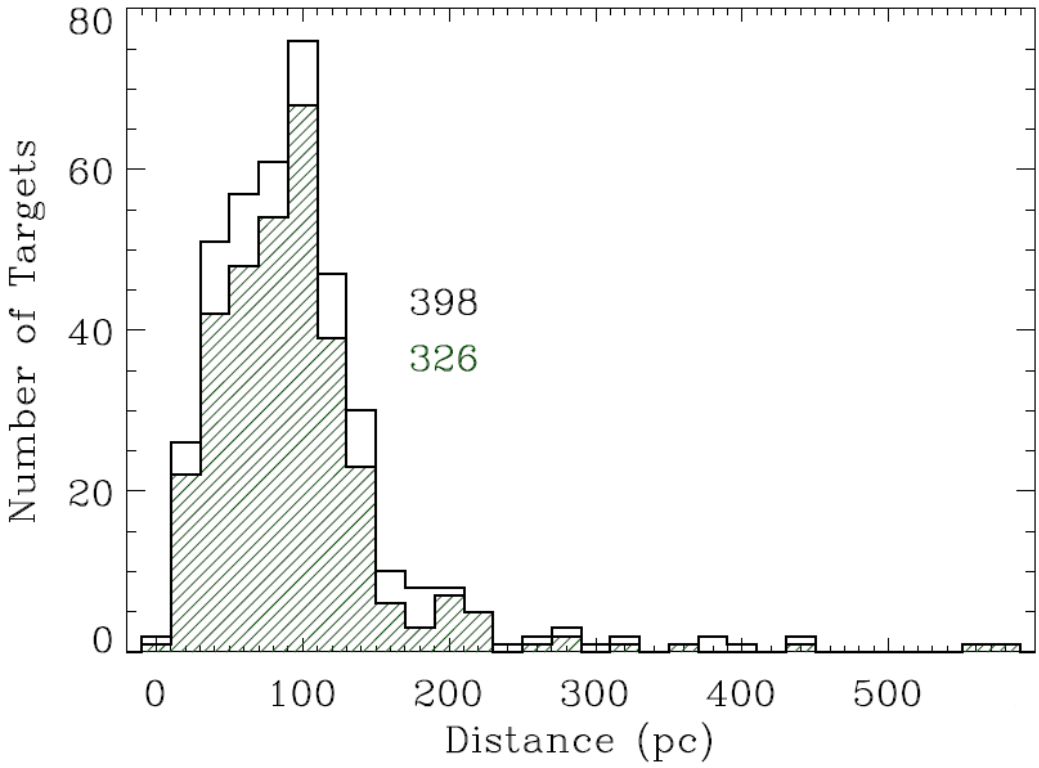

Figure 2.1: *"Distribution of distances (from spectroscopic parallax) of SPY-WDs from Pauli et al. (2006). The shaded, green histogram shows the targets in our sample. The mean is 94.5 pc; the median is 89.2 pc. These distances are short enough to support our co-moving approximation. We list the number of targets in each distribution."*

Taken from **Falcon et al. 2010** [26]

Note: The 329 WDs measured by Falcon et al. [26] confirm the co-moving assumption of the 398 WDs sample from Pauli et al. 2006 [68].

Even the co-moving assumption is right for the sample median, individual WDs still have relative motions. Subsequent a Gaussian distribution for the observed apparent velocities of the WDs can be seen in figure 2.2:
Falcon et al. shows, that the majority of WDs are redshifted following a Gaussian distribution which peaks at $\approx 32\ km/s$. Based on the distance

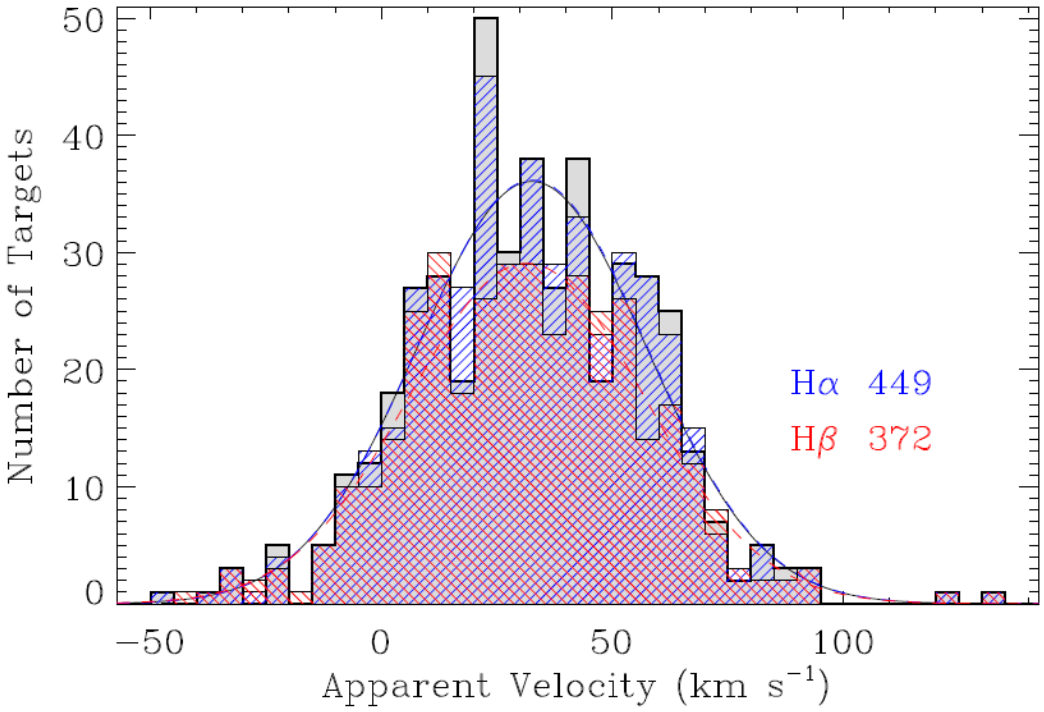

Figure 2.2: *"Histograms of measured apparent velocities v_{app} with a bin size of* 5 *km/s. The mean v_{app} for all targets in our sample (shaded) is* 32.57 ± 1.17 *km/s; the median is* 31.94 *km/s; the standard deviation is* 24.84 *km/s."* Taken from **Falcon et al. 2010** [26]

information from figure 2.1, we assume the majority of targets within a radius of 100 *pc* and hence to be co-moving. The measured peak at 32.57 *km/s* hence reflects the mean v_{grav} within this sample.

Conclusion: The result from Falcon et al. gives us a rough estimate of $v_{grav} \approx 32$ *km/s* for the gravitational redshift which we can expect for our target. As the redshift only depends on the mass and radius of the WD, it can be assumed constant with a value in the order of 30 *km/s*.

It is worth noting that the actual value of our WDs gravitational redshifts is not needed for the research of this thesis, as it is stable over time. The argument is the same, as in section 2.3 and hence $v_{grav.}$ is not crucial for the analysis of WD-BD binaries.

2.6 Summary of spectral shifts

All the effects mentioned above, merge during an individual spectral observation of the target. Hence we need to make sure that our exposure times are reasonably small compared to the expected periods of our targets, so the binary imprint is still resolved. In conclusion we classify all spectral shifting effects into static or variable effects.

Static effects: Relative Target motion (2.3) and Gravitational redshift (2.5) are both static but still individual for each target. On the one hand, the relative motion of any given target may randomly vary within some constrains due to typical relative velocities inside our galaxy. On the other hand, the gravitational redshift can be determined rather well, as the mass of WDs has some limits. The gravitational redshift is clearly constrained and causes shifts in the order of $32.5 km/s$[26].

Typically both effects can not be disentangled and lead to a uniform offset. Nevertheless, both effects are static and can therefore be ignored for the radial velocity measurements.

Variable effects: As shown in section 2.1, we can neglect the actual effect of Earth's rotation on our observations. The used low resolving spectroscopy is simply not able to resolve such small spectral shifts at all.

The spectral shift due to the Earth's orbit around the Sun is clearly limited to roughly $30 km/s$ and obviously correlates with the date in relation to the target position. So we can actually analytically correct for this effect.

All those variable effects leave their imprint based on the specific periodicity. But as one effect is negligible (rotation) and the other (orbit) can be analytically subtracted we are left with the binary wobble of which we have a know periodicity from the light curves of each target. So we are finally left with the binary wobble of the target, which we use to probe the system characteristics and confirm its binary nature.

In diagram 2.3 all those effects are displayed with their according range and weight. To assume a proper range for the relative target motion, we assume that the binary travels with a similar speed as the Sun in relation to the local standard of rest. However our galaxies dynamics also allow for much higher velocities up to an escape velocity of approximately $450 km/s$. But as we can ignore this effect anyhow, we for now assume the targets relative motion to be in the range of $\pm 15 km/s$ for our targets relative velocity.

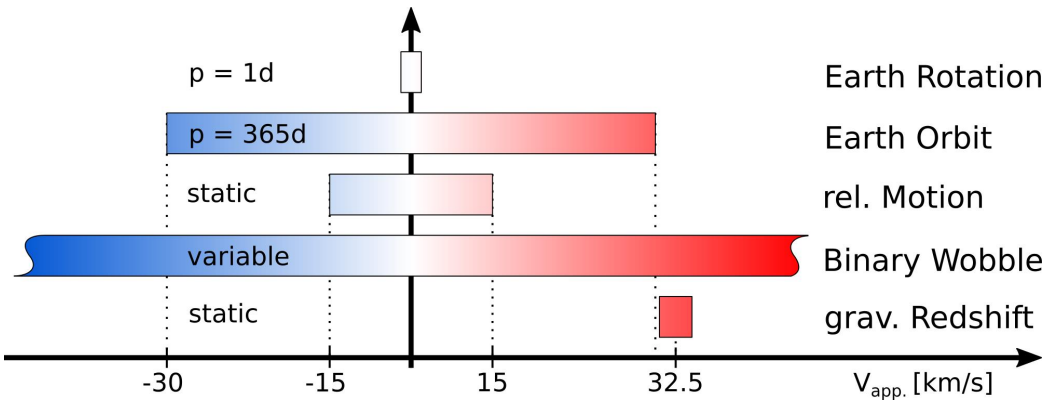

Figure 2.3: Summary of spectral shifting effects as discussed in the subsections 2.1 until 2.5. All those five effects contribute to the overall apparent radial velocity $v_{app.}$ as measured from the absolute spectral shift $\Delta\lambda$ [Å].
Variable effects: Earth rotation and orbit and binary wobble.
Static offsets: grav. redshift and rel. target motion.
Credit: H. Kellermann

Note: The effect of Earth's rotation is exaggerated for the lack of enhanced visibility.

Concluding the former subsections, we can mathematically formulate our measured apparent velocity as follows:

$$v_{app.} = \underbrace{v_{orb.}}_{\substack{Earth\ \ orb. \\ 2.2}} + \underbrace{v_{rel.\ mot.}}_{\substack{Relative\ \ Motion \\ 2.3}} + \underbrace{v_{wobble}}_{\substack{Binary\ \ Wobble \\ 2.4}} + \underbrace{v_{grav.}}_{\substack{Grav.\ \ Redshift \\ 2.5}} \tag{2.6.0.1}$$

2.7 Delayed time of observation

In addition to the spectral shifting effects as discussed in sections 2.1 until 2.5, we further have to take into account another effect which impacts our radial velocity study. As we intend to measure periodic oscillations in $v_{app.}$ the time when a spectra is observed is crucial for the analysis.

To find the binary characteristics of our WD-BD targets, we plot the dynamical part of the apparent radial velocity $v_{app.}$ over the time of observation, folded to the assumed binary period as gained from the photometric survey. Hence a minor offset in time between individual observations equivalently results in wrong binary characteristics, as wrong $v_{app.}$ would shift our result. Consequently we briefly review the shift in time, as introduced by the Earth's orbit.

If we recall, that the Sun's light needs roughly 8 minutes to reach Earth, we intimately know that light needs up to 16 additional minutes to reach Earth, compared to the diametral orbital location. The effect is related to the Earth's orbit as discussed in section 2.2.

Even this effect sounds minor, it still has to be taken into account since the periodicities of our WD-BD binaries are less then a day. Details on this corrections are considered in the results section 9.

Chapter 3

Instruments of choice

All observations used in this work have been done with one of the following three instruments.

1. The focus of this thesis is the follow up study of this minor sample of targets, as shown in chapter 1. A first campaign has started in 2015 using the *ES2*-spectrograph which is a resident instrument at the 2.1 m Otto Struve Telescope (see section 3.1). As the *ES2*-spectrograph data quality was not high enough, additional observations became necessary.

2. In 2017, *HET*'s *LRS2*-spectrograph (see section 3.2) started scientific operation and could be used to follow up our targets. Due to the vast difference[14] in effective primary mirror surface, exposure times are rather short compared to *ES2*. In late 2017 and mid 2018 we got in total 5 hours of low-priority observation time allocated.

3. In 2018, we used the *3KK* imager (see section 3.3) of the 2.0 m *Fraunhofer Telescope* located at the *Wendelstein Observatory* to get final SED data for the remaining targets.

The following three sections cover the telescope and instrument details of the used facilities.
Further chapters deal with the according data reduction (see chapter 5) and analysis (see chapter 7).

[14]Effective 2.1 m vs. *HET*'s 9.2 m aperture

3.1 ES2 at 2.1 m Otto Struve Telescope

The *ES2* is a resident spectrograph at the 2.1 m Otto Struve Telescope.

Otto Struve Telescope: According to its mirror size of 82 inches, the Otto Struve telescope is commonly referred too as *"The 82-Inch"*. It is the initial telescope of the Mc Donald Observatory and started operation in 1939. Nevertheless, due to extensive maintenance it is still in good condition and often used with a variety of instruments. Although bigger telescopes are available nowadays its 2.1 m mirror size is still big enough to support various science cases.

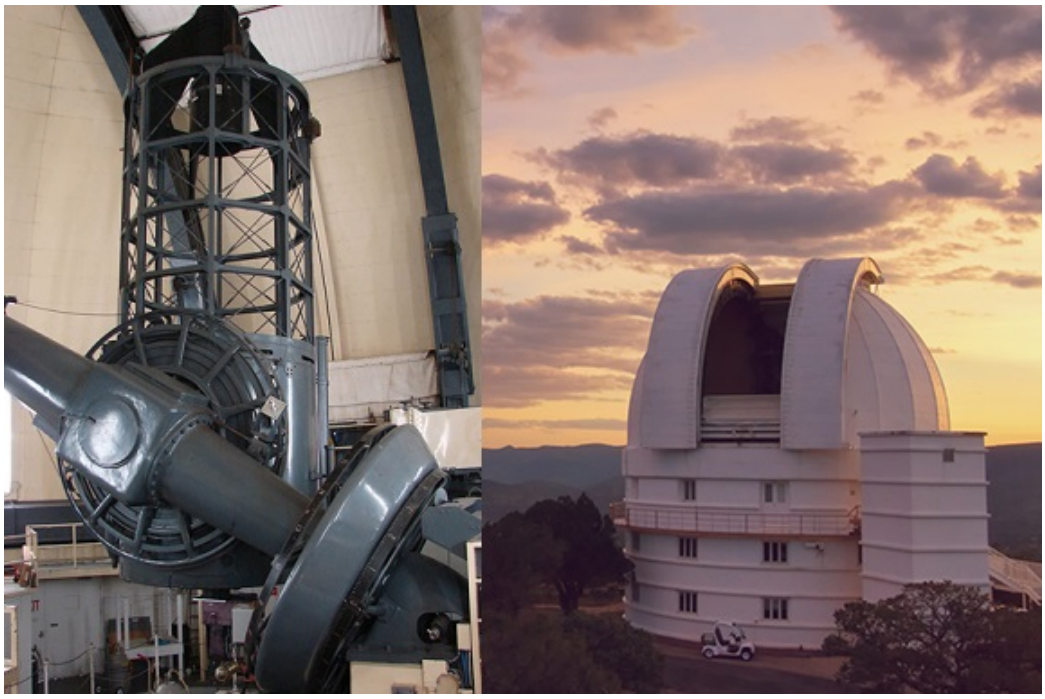

Figure 3.1: Picture of the 82" Otto Struve telescope. Left: Telescope in zenith park position. Right: 19 m dome of the Otto Struve Telescope.
Credit: MC Donald Observatory

Observation time at Otto Struve telescope can only be requested from the Telescope Allocation Committee (**TAC**) of the University of Texas. Observing at Otto Struve telescope is only possible in visiting mode. Hence the observer has to physically travel to Mc Donald Observatory and takes responsibility over the whole telescope facility, usually for several days in a row. Scientists which like to utilize the 82-Inch have to be trained by experienced observers to be allowed to operate the facility. Even though parts like

the weather station or the telescope guiding have been updated during the decades, many things still have to be done manually without computer or script support. Hence observing has a real hands-on feeling, which is a great experience for observers and instrument builders.

***ES2*-spectrograph:** The Electronic Spectrograph Number 2 - *ES2* is a cassegrain spectrograph build in the 1990's. The following description contains many facts which are all taken from the instruments users' manual [62] and will not be cited explicitly until the end of this chapter. *ES2* is a classic slit-spectrograph with several different gratings[15] and two different detectors (TI1 and CC1) available. Each of the detectors is mounted inside its own housing including the cooling cycle and dewar[16]. Hence switching the detector can be done with relative low risk and reasonably high repeatability. Still, switching from detector TI1 towards CC1 and vice versa is done only during daytime by a local staff member. Detector TI1 is optimized for the blue region of the observable spectrum, while CC1 covers the red part of the visible spectrum. We decided to utilize TI1 as CC1 only provides coverage of the H_α *Balmer*-line, while TI1 provides H_β and H_γ.

- TI1: *"This is an* $800 \cdot 800$ *pixel device manufactured by Texas Instruments. Each pixel is* $15 \cdot 15$ *microns on a side with no gaps between pixels. The projection on the sky is* $0.9 \cdot 0.9$ *arcsec (assuming a projection factor of 8.16, which changes with grating angle). This detector has the higher quantum efficiency of the two at all wavelengths but suffers from severe fringing in the red."* [62]

All of the observations used in this thesis have been done with the TI1 detector and the specific grating 22. It has 600 *groves/mm* which allows roughly a spectral resolution of $\Delta\lambda \approx 2.8$ Å$/bin$. *ES2* features a wide variety of filters which have not been used for the observations in this thesis, hence the details are skipped but can be found in the users' manual [62].

[15] A grating is an optical component with periodic groves to diffract light.
[16] A dewar is an insulated vessel, which is used to locally store cold liquids like nitrogen in order to cool the detectors.

3.2 LRS2 at 11 m Hobby-Eberly-Telescope

LRS2-spectrograph is the second generation low resolution facility spectrograph of the Hobby-Eberly-Telescope (*HET*).

Hobby-Eberly-Telescope: The *HET* has an 11m primary mirror and is one of the largest optical telescopes in the world. It is located at the McDonald Observatory in Texas and exclusively operated by *HET*'s own staff. The telescope and its operation are funded by the following five universities: The University of Texas at Austin, the Pennsylvania State University, the Ludwig Maximilians University Munich, the Georg August University of Goettingen and until 2011 the Stanford University.

Figure 3.2: Panoramic twilight picture of the *HET* facility with open dome and cooling vents. Credit: MC Donald Observatory

Observation time at *HET* can only be requested from the Telescope Allocation Committees (**TAC**) of the funding Universities. The request has to be supported by one of the funding universities or a partner institute of a specific instrument. In our case the obeservation time was granted by the *Munich-**TAC***. Observing at *HET* is generally only available via a sophisticated queueing system. Hence observations have to be described in detailed proposals and be documented in a specific online-form. The execution is handled locally and data is subsequently available via *HET*'s data server.

More details on *HET*'s technical details can be found in chapter 11, which discusses in detail the SCS2 hardware upgrade of the *HET* and hence features an extensive hardware description.

***LRS2*-spectrograph:** The second generation Low Resolution Spectrograph *LRS2* is one of *HET*'s facility instruments and replaces the first generation *LRS* instrument. The following description contains many facts which are all based on the following paper and will not be cited explicitly until the end of this chapter:

LRS2: The new facility low resolution integral field spectrograph for the Hobby-Eberly telescope

by **Chonis et al. 2014** [11]

> *"The second generation Low Resolution Spectrograph (LRS2) is a new facility instrument for the Hobby-Eberly Telescope (HET). Based on the design of the Visible Integralfield Replicable Unit Spectrograph (VIRUS), which is the new flagship instrument for carrying out the HET Dark Energy Experiment (HETDEX), LRS2 provides integral-field spectroscopy for a seeing-limited field of 12"x6". For LRS2, the replicable design of VIRUS has been leveraged to gain broad wavelength coverage from* 370 *nm to* 1.0 *μm, spread between two fiber-fed dualchannel spectrographs, each of which can operate as an independent instrument. The blue spectrograph, LRS2-B, covers* $370 \leq \lambda(nm) \leq 470$ *and* $470 \leq \lambda(nm) \leq 700$ *at fixed resolving powers of* $R = \frac{\lambda}{\delta\lambda} \approx$ *1900 and 1100, respectively, while the red spectrograph, LRS2-R, covers* $650 \leq \lambda(nm) \leq 842$ *and* $818 \leq \lambda(nm) \leq 1050$ *with both of its channels having* $R \approx$ *1800."*[11]

In contrast to the former explained ES2 slit-spectrograph 3.1, *LRS2* is an integral field spectrograph. The following schematic 3.3 shows the basic concept of integral field spectroscopy.

As can be seen in picture 3.4, the fiber cables (green) guide each lenslet-pixel's light towards the actual spectrograph unit (blue box).

Both *LRS2* detectors are each fed with a individual fiber bundle called Integral Field Unit (*IFU*). According to their wavelength coverage they are called *LRS2*-B and *LRS2*-R. As feeding by individual IFUs causes

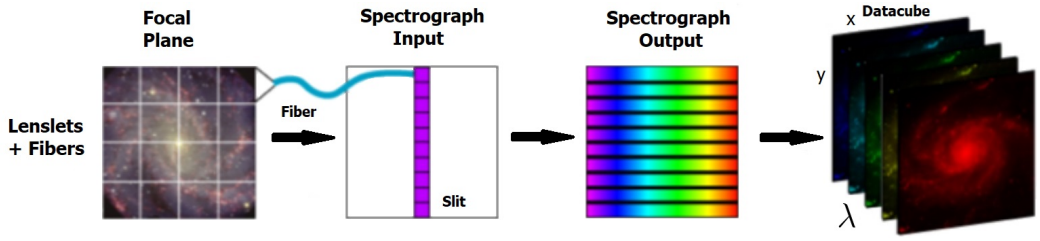

Figure 3.3: Concept scheme for integral field spectrography. Each section of the focal plane gets imaged by an individual fiber and results in an individual spectrum. Credit: B. Indahl

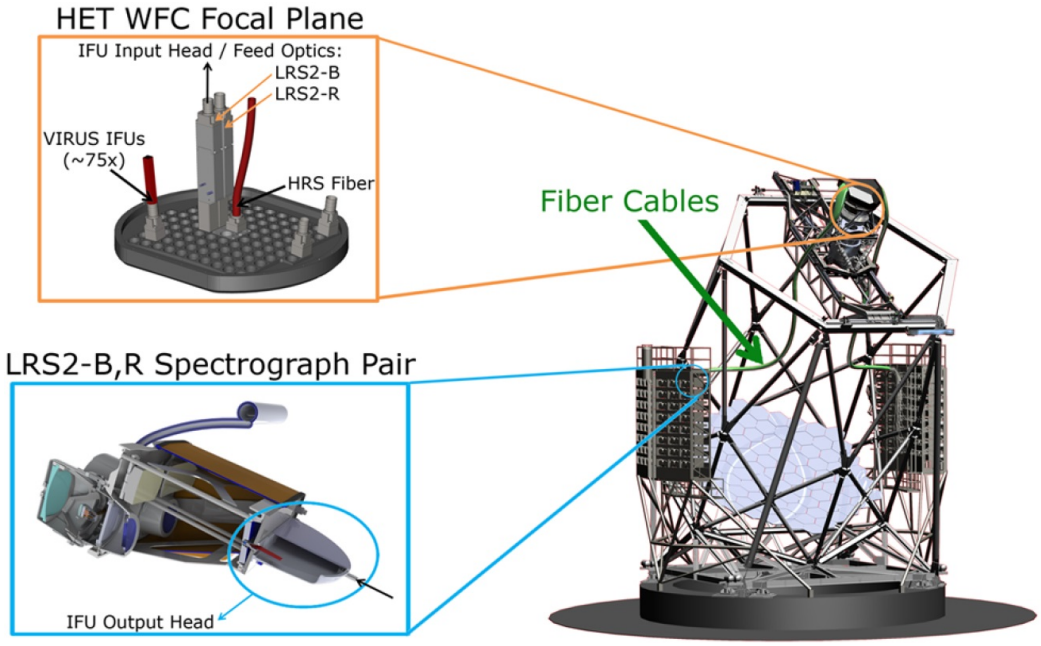

Figure 3.4: *"A schematic of the LRS2 fiber light path. The HET WFC focal plane is located at the top of the telescope inside the PFIP assembly (orange circle). The arrangement of VIRUS IFUs, fiber feeds for other HET facility instruments, and the LRS2 IFUs on the fiber feed mounting plate at the WFC focal plane is shown in the orange inset. At the other end of the fiber cable is a spectrograph pair (shown in the blue inset) where the fibers are arranged into two linear slits within the IFU output head to feed each spectrograph channel."* Taken from **Chonis et al. 2014** [11]

an offset between the targeted sky region of both channels. Hence a full coverage (Blue- and Red-Channel) observation of a single point like source can only be done in a sequence of two individual observations with an offset

correction for the guiding. Nevertheless, both detectors are read for each exposure and can be used as each others sky frame.

When reducing *LRS2* data, one has to keep in mind the wavelength depended system throughput which in contrast to a regular slit-spectrograph is not continuous any more. The following *LRS2* throughput diagram 3.5 provides insight in the expectable system performance.

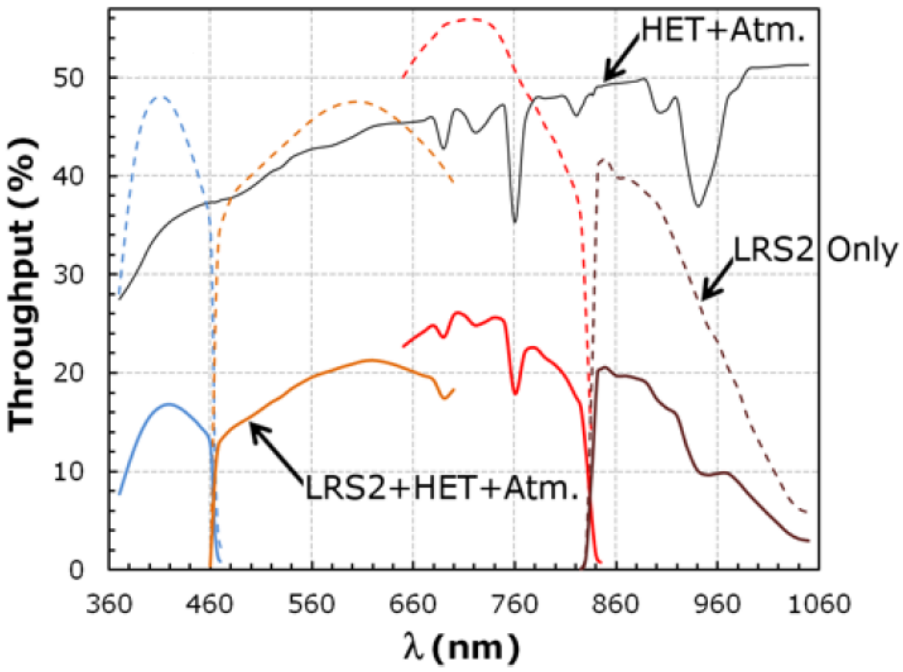

Figure 3.5: *"The throughput of the instrument using the most recent data on all of the optical components. The solid black curve shows the combined throughput of the HET and the sky at an airmass of 1.22, but does not include atmospheric or Galactic extinction or account for the mean illumination of the HET primary mirror during a track. The dashed colored curves are the throughput of the four LRS2 spectrograph channels, while the solid colored curves give the total sky-to-detector throughput."*

Taken from **Chonis et al. 2014** [11]

3.3 3KK at 2.0 m Fraunhofer Telescope

The *Wendelstein three channel imager (3KK)* is a first generation resident instrument at the 2.1 m Fraunhofer telescope.

Wendelstein Observatory: The observatory is located on the summit of *Mount Wendelstein* (1838 m) at the Alps north ridge. Consequently, the light pollution and weather stability are worse then for the prominent locations for example in Chile or Texas, but the exposed location (see 3.6) leads to superb seeing conditions (median ≤ 0.8").[57] The proximity to Munich is another advantage, even though the observatory is only accessible via cable car or rack railway.

Figure 3.6: Panoramic picture of the observatory located on top of *Mount Wendelstein* (1838 m).[46] Credit: Wendelstein Observatory

Fraunhofer Telescope: Commissioned in 2013, the new 2.1 m Fraunhofer telescope replaced the old 0.8 m telescope used at the observatory from 1988 until 2008. The upgrade from 0.8 m to a 2.1 m telescope required major facility construction work, due to the exposed location of the observatory right at the top of *Mount Wendelstein* as it can be seen in picture 3.7.

Figure 3.7: Facility picture of the Fraunhofer telescope seen through the open dome. The telescope was build by OHB (former Kayser-Threde GmbH). It resides in the 8.5 m dome, which can also be seen in picture 3.6 in the center of the upper picture. [46]

Credit: Matthias Kluge/Wendelstein Observatory

The whole observatory is exclusively owned by the University Observatory Munich [17] and operated by its staff members. Hence, observation time with all available instruments is based on appropriate proposals and allocated by the local science team.

[17] The University Observatory Munich is part of the physics department of the Ludwigs-Maximilians-University Munich (LMU).

***3KK*-imager:** *3KK* is specifically designed to fit the 2.1 m Fraunhofer Nasmyth ports, which delivers a Field of View (FoV) of 60 $arcmin^2$. Its wavelength coverage reaches from 340 nm to $\approx$ 2300 nm, distributed over three channels: blue, red and near infrared (NIR). Using a dichroic beamsplitters, first the blue part of the light gets redirected towards an Apogee ALTA E3041 camera with a blue coated Fairchild CCD 3041, used for the blue channel. Another beamsplitter redirects the visible red light towards a second Apogee camera, which is equipped with a red coated Fairchild CCD 3041. Finally the remaining NIR light heads on to the cold optics, leading to the HAWAII-2RG detector. The details of the optical design can be seen in figure 3.8.

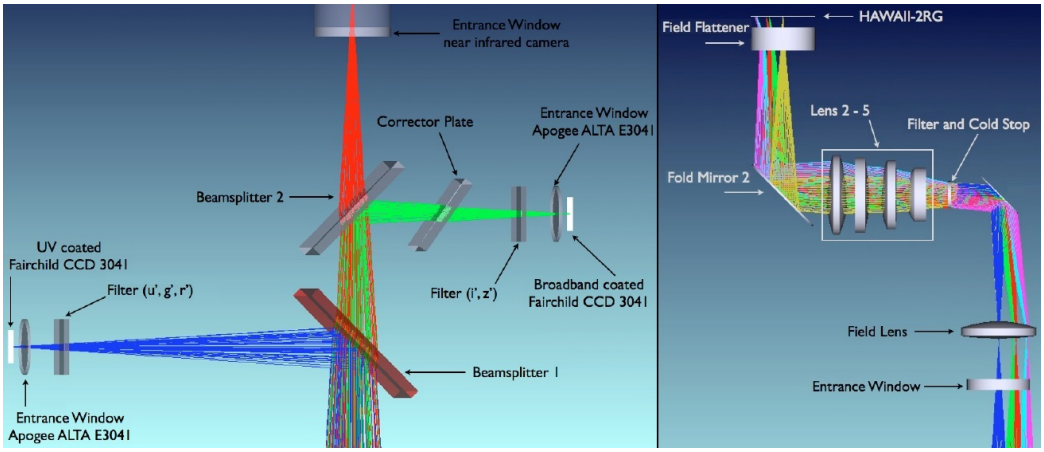

Figure 3.8: *"**Left:** Layout of the optical part of the 3kk. Beamsplitter 1 (BS1) reflects wavelengths shorter than 695 nm, beamsplitter 2 (BS2) all wavelength below 970 nm. The remaining light is transmitted to the near infrared channel. The fully transparent corrector plate in front of the red optical channels corrects for aberrations introduced by BS1.*
***Right:** Design of the near infared part of the 3KK. After the entrance window, light is reimaged using six lenses without changing the plate scale. A cold stop masking the obstruction of the secondary mirror and filters are placed near the pupil image. The design is folded two times to keep the dimension of the camera small."* Taken from **Lang-Bardl et al. 2010** [59]

Scientifically 3KK is designed to observe targets of opportunity at multiple wavelengths at once, which are variable on short time scales. Another science case is the efficient measurement of photometric redshifts as follow up for example for projects like PanSTARRS or Planck.

3KK furthermore provides broad-band photometry of stellar targets within brief exposure times, which makes it perfect for spectral energy distribution (SED) analysis. Table 3.1 features the optical details of each of *3KK*'s channels.

3KK design parameters
Data taken from Lang-Bardl et al. [57]

	Blue Channel	Red Channel	NIR Channel
Filter	$u', g', r', [OI], H_\alpha, [SII]$	i', z'	$Y, J, H, K_S, H_2, Br_\gamma$
Pixel scale	0.2 arcsec/px	0.2 arcsec/px	0.24 arcsec/px
λ-range	$340 - 695$ $[nm]$	$695 - 970$ $[nm]$	$970 - 2310$ $[nm]$
Field of View	6.8 $arcmin$	6.8 $arcmin$	8.2 $arcmin$

Table 3.1: 3KK Final design parameters.
Taken from **Lang-Bardl et al. 2016** [57]

As the various science cases require more specific wavelength band than the rough three channel distribution, all channels feature a variety of filters. For any observation, each channel can be equipped with one suitable filter.

3KK filters
Data taken from Lang-Bardl et al. [59]

Channel	Blue			Red			NIR				
Filter	u'	g'	r'	i'	z'	Y	J	H	K_S	Br_γ	H_2
cut-on	327	409	555	695	850	972	1166	1481	1989	2141	2113
cut-off	383	546	692	831	970	1071	1332	1780	2313	2187	2139
ZP mag	n/a	25.0	24.9	24.7	23.5	n/a	23.2	23.2	23.2	n/a	n/a

Table 3.2: 3KK Filters, including cut-on and cut-off wavelengths. All wavelengths are given in nm. The filter width is indicated by richness of the according cell colors. Zeropoints (ZP) are given for wideband filters only. Visible ZP are in good agreement with the second facility imager of the 2.1 m Fraunhofer telescope, which is optimised for wide field observations. The ZP were measured using M53 target data.
Data taken from **Lang-Bardl et al. 2010** [59]

In this thesis we use broad-band filter data from *3KK* to gain comprehensive photometric data for SED analysis. This provides us with independent temperature measurements for the WD targets. Based on the companion, the data can be used to reveal a NIR excess.

As we now have a good overview on the used instruments and their characteristics, the following section 4 discusses the application process for these facilities, the according proposals and provide a brief summary on the observational conditions.

Chapter 4

Observation campaigns

This chapter provides insight in the conditions of all observation campaigns which are analysed in this thesis. In total, we gather observational data with the three instruments described in section 3. For each of them, the observation time application process is different and also the observation mode varies. The following sections list each instruments observational mode and proposal process, as well as the observational conditions.

4.1 *ES2* campaigns

In the case of *ES2*, each observer needs to submit a scientific observational proposal for one of the three submission deadlines for the according trimester.

Observation mode: As the *Mc Donald Observatory* focuses their man power on the facility maintenance. Generally all instruments at the *2.1 m Otto Struve Telescope* are only available in visitor mode. Consequently the observer has to travel to *Mc Donald Observatory* in West-Texas and operates the whole telescope for several nights in a row on his own.

The observers of the two other large telescopes (2.7 m and 2.1 m) at the observatory are expected to run their telescope and instrument fully autonomous. The night time support is typically limited to emergency support and a brief, voluntary visit of a technical crew member in the early phase of the night. As a consequence, new observers are asked to be practically trained by a skilled observer to operate the facility for at least one observation run. In general, observing in small teams is appreciated.

Proposals: Instead of discussing all proposals here in detail, we just add one in the appendix for the sake of completeness. Given the visitor observation mode, the observers experience and facility knowledge is a relevant factor for the Telescope Allocation Committee. Therefore, a brief description of former observational experience at the McDonald Observatory has to be included in each observational proposal. Aside of this safety critical aspect the proposal has to contain the following details:

1. Science justification
2. Description of observations and justification of exposure times
3. Description and justification of special constraints
4. Results from previous observing time at McDonald

Observation runs: In total, we submitted the following observation proposals, which were mostly granted as applied:

ES2-spectrograph observation run

Trimester	Requested	Assigned
3-2015	4 nights	3 nights* (September 2015)
1-2016	6 nights	6 nights* (January 2016)
2-2016	2 x 6 nights	7 nights* (June 2016) 6 nights* (July 2016)
1-2017	6 nights	4 nights (March 2017)
2-2017	6 nights	5 nights (August 2017)
3-2017	6 nights	6 nights (September 2017)

Table 4.1: Applied and assigned observation time. Until 2016 the allotted observation periods are used in collaboration with the data acquisition for Obermeier 2016 [66] as indicated by *.

Instrumental Instability: During the runs we faced a row of technical problems, of which most could be resolved quickly. However, others lead to loss of data, as for example the *ES2* grism all of a sudden started to slide off the target while exposing. Hence, we especially lost data from our run in January 2016. Until today neither we nor the technical staff at *Mc Donald Observatory* could investigate what caused the problem. It only occurred during this run so we guess it was related to the *ES2* mounting procedure, as *ES2* is only mounted when it is used. Afterwards the complete instrument is removed from the telescope and stored separately which leaves plenty of room for mounting problems, which can not be investigated later.

For technical reasons all observations were done with a slit size of 1.6 arcsec. Hence occasionally the seeing was less than the slit size which makes the λ-calibration complicated.

Observational conditions: The following tables 4.2 and 4.3 list all our gathered *ES2* exposures and their observational conditions.

ES2 observation conditions 1/2
Target: SDSS193144

Exposure ID (Date & Time)	Air-mass	Moon alt.	Moon ill.	Moon sep.	Conditions Seeing/Clouds/etc.
20160606T082000	1.04	b.H.	2%	121°	clear
20160606T092500	1.01	b.H.	2%	122°	only 30 min
20160607T053000	1.55	b.H.	7%	125°	clear
20160608T065000	1.22	b.H.	13%	126°	minor clouds
20160608T075000	1.22	b.H.	13%	126°	minor clouds
20160608T085000	1.22	b.H.	13%	126°	minor clouds
20160610T055000	1.03	b.H.	31%	122°	cirrus
20160610T065000	1.02	b.H.	31%	122°	cirrus
20160611T082000	1.03	b.H.	40%	117°	cirrus
20160612T063000	1.22	5°	50%	111°	cirrus
20160712T064500	1.02	5°	53%	94°	clouds
20160712T080000	1.03	b.H.	53%	93°	clear
20160713T044500	1.35	40°	52%	87°	clear
20160714T051000	1.10	32°	71%	80°	clear
20160715T053500	1.08	34°	79%	73°	clouds
20160716T032000	1.35	42°	87%	67°	clear
20170802T045500	1.03	33°	75%	68°	cirrus
20170803T041500	1.06	40°	83%	63°	clear
20170805T064500	1.06	46°	94%	55°	clear
20170806T043000	1.04	38°	98%	54°	cirrus
20170830T035000	1.01	30°	59%	64°	clear
20170831T033000	1.01	36°	69%	60°	clear
20170903T024000	1.03	35°	91%	55°	clear
20170903T060000	1.15	38°	91%	55°	clear
20170904T034000	1.02	40°	96%	56°	clear

Table 4.2: Observational conditions for *ES2* exposures of SDSS193144. See figure 4.3 caption for details.

ES2 observation conditions 2/2
Targets: SDSS070428 and SDSS070433

Exposure ID (Date & Time)	Air-mass	Moon alt.	Moon ill.	Moon sep.	Conditions Seeing/Clouds/etc.
20160117T035000	1.35	48°	54%	76°	minor clouds
20160118T075500	1.13	10°	65%	62°	minor clouds
20160120T051000	1.09	65°	84%	34°	clear
20160120T070000	1.09	45°	84%	32°	clear
20170313T025000	1.07	18°	99%	74°	clear
20170316T033500	1.10	b.H.	87%	110°	clear
Target :	SDSS070433				
20160118T043000	1.15	50°	65%	62°	minor clouds
20160118T085500	1.35	b.H.	65%	62°	minor clouds
20160120T042000	1.15	75°	84%	34°	clear
20160120T061000	1.05	55°	84%	33°	clear
20160120T081000	1.20	25°	84%	32°	clear
20170315T033000	1.09	5°	83%	98°	clear
20170316T043500	1.20	5°	87%	111°	clear

Table 4.3: Observational conditions for *ES2* exposures of SDSS070428 and SDSS070433. Some observations where done while the Moon was still below the horizont (b. H.). Hence, neither the lunar separation (sep.) nor illumination (ill.) are relevant in these cases. The conditions color coding indicate the factors' impact, while the color of the exposure ID shows the estimated accumulated contamination.

Conclusion: One can see that we got only few dark time runs allotted, so we had to deal with various levels of Moon contamination. Hence we might find residuals of Moon light superposed on our targets spectra. This is even more likely for nights, with a bright Moon combined with minor or high-layer cirrus clouds. This is unfortunate as we detected other lines than typical for WD in our spectra, but it is difficult to disentangle the moon light contribution clearly enough to use those detections as tracer of the secondary object and its spectrum.
In terms of observation time loss due to weather, we had very different runs. As usual for *Mc Donald Observatory* many observation runs had mostly good and some minor amount of bad or contaminated nights. But, we also faced two runs in which we could not open the dome at all due to rain and wind.

4.2 *LRS2* campaigns

Observation time for all *HET* instruments such as the *LRS2*-spectrograph is either granted via the shareholders' programs of the funding institutions or via a scientific observational proposal, similar to the one in appendix *ES2-spectrograph Observation run proposal*.

Observation mode: All observations are explicitly executed by the local *HET* night time staff, which consists out of a resident astronomer and a telescope operator. Hence observing with *HET* in general is queue based and follows a strict prioritization scheme.

The shareholders' observation time is especially allotted, based on their financial contribution to the *HET* facility and grouped into the five levels of priority P0 through P4. P0 data is guaranteed to be executed as close as possible to the requested date and time. With decreasing priority the deviation in terms of exposure time and weather quality becomes larger. Usually observations with priority P2 and higher get rather well completed, while P3 and P4 typically fail their goals.

Proposals: In our case, we actually were able to use our own shareholder low-priority observation time. This P4 time is suitable for us, as we only required short exposure times of roughly 10 to 15 minutes, while typical *HET* *LRS2* exposure sequences are up to 90 minutes for single targets. Such kinds of sequences can also contain special sky nodding or dithering schemes depending on the astronomical question to be answered. Details on such methods for advanced sky subtraction are discussed in section 5.3.3 in context of the general data reduction. Our targets require none such sophisticated exposure sequences and furthermore ask for no specific observational conditions. So our targets are effortless for *HET* and can be observed on opportunity. However the downside of P4 time is the limitation in the predictability of the observations and hence we can not schedule our exposures to the targets period.

Therefore even our P4 targets get reasonable amounts of data, as they fit nicely in between larger observation blocks of higher priority. Usually higher priority observations try to request exposure times near the available maximum as the ratio between overhead time which is also charged and the exposure time is more favourable. The overhead or set-up time is in the order of several minutes, depended on the time which is needed to point and

confirm the target. Hence a typical observation night at *HET* consists of several larger high priority observations, with minor pause time in order to meet the next high priority target.

Consequently, our short, low priority blocks had an increased chance of observation, especially since the weather condition were less critical for our rather bright targets.

Observation runs: We got allotted P4 time at *HET* using *LRS2*, in 2017 and 2018. The completion rates of both our projects M-17-03-002 (60%) and M18-02-003 (57%) are well above the average for low-priority P4 observation programs. Therefore, our approach to utilize our share of cheap P4 time for short observations of bright targets is valid, as we make it easier for the telescope operators to efficiently fill their schedule and allow them to make use of short cloud gaps in mediocre nights. Hence the overall facility efficiency increases.

LRS2 programs

Trimester	Program	Requested	Completed
2017-03	M-17-03-002 compl. 60%	2.5 h P4	2 visits a 10 minutes SDSS193144 3 visits a 15 minutes SDSS070428 3 visits a 15 minutes SDSS070433
2018-02	M-18-02-003 compl. 57%	2.5 h P4	4 visits a 10 minutes SDSS193144 4 visits a 15 minutes SDSS070433

Table 4.4: *LRS2* programs, including requested and executed observations.

Observational conditions: The following table 4.5 shows the observational conditions for all *LRS2* exposures used in this thesis. In contrast to the former *ES2* exposures, all *HET* observations are executed at roughly the same air-mass of 1.22, as the telescope operates at a fixed elevation of 55°. Details can be found in section 3.2.

Conclusion: Having a look at the actual conditions we find that on the one hand our first two targets SDSS070428 and SDSS070433 had superb observational conditions, as the Moon was always below the horizon. On the other hand, our third target SDSS193144 suffered mediocre conditions most of the time, hence we have to handle this data carefully and might commonly find superposed spectral features. Nevertheless, the WDs strong

Balmer-lines should still dominate so the data is usable for our radial velocity analysis.

LRS2 observation conditions

Exposure ID (Date & Time)	Moon alt.	Moon ill.	Moon sep.	Conditions Seeing/Clouds/etc.
Target :	SDSS070428			
20171124T113502	b. H.	28%	156°	clear
20171125T113436	b. H.	37%	145°	clear
20171126T065819	b. H.	45%	133°	clear but windy
Target :	SDSS070433			
20171115T075444	b. H.	10%	92°	clear
20171116T073806	b. H.	5%	104°	clear
20180411T023105	b. H.	23%	142°	minor clouds
20180412T024445	b. H.	15%	130°	dust and windy
20180415T023212	b. H.	1%	91°	clear
20180416T023249	b. H.	0%	78°	clear but windy
Target :	SDSS193144			
20171120T014159	b. H.	3%	65°	thick cirrus
20171126T011653	45°	46%	60°	clear
20180408T102507	25°	50%	56°	clear but windy
20180409T103500	20°	40%	56°	clouds
20180411T100506	5°	23%	60°	minor clouds
20180411T101117	5°	23%	60°	minor clouds

Table 4.5: List of the observational conditions for all *LRS2* exposures. Some observations where done while the Moons altitude (alt.) was negative, it was still below the horizont (b. H.). Hence, neither the lunar separation (sep.) nor illumination (ill.) are relevant in this case. The conditions color coding indicate the factors impact, while the color of the exposure ID shows the estimated accumulated contamination. Since the *HET*s primary mirror is fixed at an elevation of 55°, all its targets are observed via airmass 1.22.

4.3 *3KK* campaign

As the *Wendelstein three channel imager (3KK)* is mounted at our own 2.1 *m* Fraunhofer telescope, applying for observation time is an internal process. The observatory and all its instruments are operated on 365 nights a year in a queue based fashion by a local observer, who usually operates the facility for several nights in a row. The two main telescope operators are both resident-observers and solely hired for this purpose. Consequently they cover the major fraction of the observation time. During, the remaining nights, the facility is operated by a small number of trained astronomers who mainly work at USM, but are still affiliated with the *Wendelstein Observatory*. Hence a few of the exposures are actually observed by ourselves.

In order to gather photometric data in additional bands, we set up an observation request with the following characteristics:

- Target: SDSS193144
- Coordinates: RA: 19:31:44.04 | DEC: +36:17:26.40
- Conditions: Seeing (max.): 2.00 arcs | Airmass (max.): 1.8
- Optical Filters: g, r, i and z (single exposure time = 30.0s)
- Near-Infrared Filters: H, J and K (single exposure time = 28.7s)

The observation campaign entered the queue on the 4th of April 2018 and stay queued the whole summer, until the target set for the winter. In total we gather 1384 exposures distributed as shown in table 4.6.

3KK observations

Channel	Blue		Red		NIR		
Filter	g'	r'	i'	z'	J	H	K_S
Observations	260	282	250	263	245	17	67
$\sum_{\text{Filter}}$	542		513		329		
$\sum_{\text{Total}}$	1384						

Table 4.6: *3KK* exposures separated in their respective filters, as gathered by the *Wendelstein Observatory*. Details on the filter characteristics and the general *3KK*-instrument design can be see in section 3.3.

The observations provided above have all been reduced using the new automated *3KK* data-pipeline, as developed by the *Wendelstein* staff, and especially Christian Obermeier. A paper describing all the details is planned, but yet not available, hence see Obermeier et al. in prep for further details. As it is obviously not reasonable to discuss the observational conditions for each exposure individually, we still have a look on the general airmass as it is shown in the following histogram 4.1. The airmass AM is defined as the actual path length l from the observatory until the outer edge of the atmosphere, normalized by the minimal path length l_0 for a zenith observation. Hence, the smaller the $AM = l/l_0$, the fewer atmospheric perturbations and contaminations the observation faced.

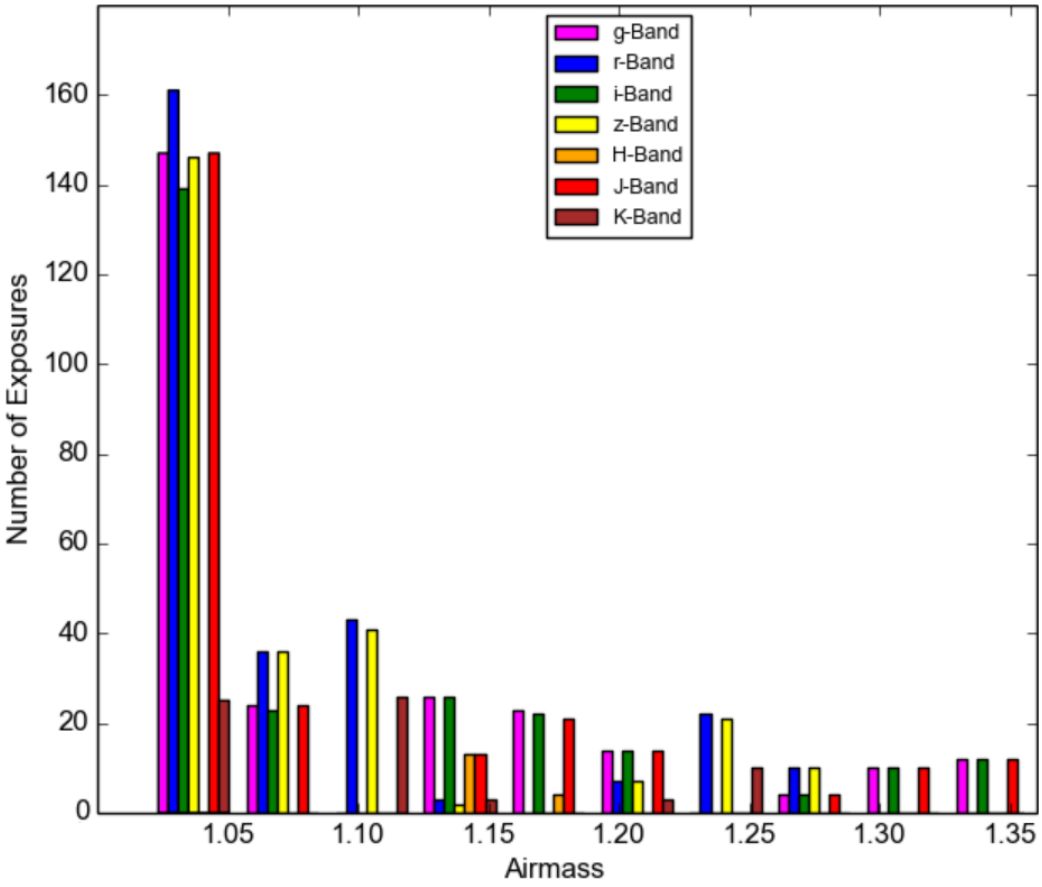

Figure 4.1: Histogram of the airmasses of all *3KK* exposures as listed in table 4.6. It can be seen that about 50% of all exposures where done at best possible airmasses (better than 1.05). In general all exposures were gathered at significantly better airmasses than the required 1.8.

Based on these numbers, we gathered in total about 11.4 hours of data photometric of SDSS193144. But, due to the explicit instrument design, we are only charged about 3.5 hours of telescope time. Taking in account the typical minimal overhead time for pointing and instrument setup, we may have consumed a little more than 4.0 hours, which is still great compared to the 11.4 hours of data which we collected.

The *3KK* observational campaign was added to the project at a rather late point in time. Consequently, we could only observe the target SDSS193144, as the other two were not visible to the *Wendelstein Observatory* for most of the time. Observing the two other targets for a very short period in time, would not have provided enough information to make proper use of such photometric observations. The follow-up of these two targets SDSS070428 and SDSS070433 hence remains to be done in the future.

As the observational conditions of all our observation campaigns have now been documented, we move the focus on the actual data reduction for both our spectrograph's as detailed in the following section 5.

Chapter 5

Spectroscopic follow up

This chapter describes the data reduction pipelines for *ES2* and *LRS2*. The spectrographic data first has to pass the basic astronomical reduction steps like bias subtraction, dark current correction and flat field division etc. These data reduction steps are covered once (see 5.1) in detail for the *ES2*-spectrograph and are applicable also to the LRS2 data. All of the related *ES2* reduction is executed by a self developed python script called: *82-es2-pipe.py*

The reduction of *LRS2* data is done analogue and consequently skipped. Details on this pipeline can be found in Indahl 2017 [48].

Once the basic data reduction steps are done, the spectra are stored as fits files mapping the y over the x axis. Spectral calibration lamps with usually well known spectral features were consequently observed each night and provide appropriate pixel to wavelength allocation on a nightly basis.
The wavelength calibration leads to a rebining from $X - Y$ to $\lambda - Y$ data. Hence this step defines the sampling scale for the data. Spectroscopic data can be either sampled to simple constant wavelength [Å]-bins (e.g. *ES2*), or logarithmic wavelength $ln(\lambda[\text{Å}])$ bins (e.g. *LRS2*).

When the data is finally converted and respectively rebined, the spectra are stored again as files. For simpler handling, the target spectra subsequently get extracted from these fits files and stored as tables.

5.1 ES2 data reduction

The *ES2* data reduction is mostly automated and executed by the *Python* -script *82-es2-pipe.py* . Table 5.1 provides an overview of the individual reduction steps, while the verbose description of the algorithms is outsourced to the appendix, as *ES2* is a classical slit spectrograph.

ES2 data reduction

#	Step:	Prefix:	Code:	Options:	Reference file:
1	Bias	b	biasredux	-b	masterbias.fits
2	Bias offset	ob	subtractfits	-c	
3	Extract slit	eob	extractfits	-r	
4	Flatfield	feob	dividefits	-f	masterflat.fits
5	Cosmics	cfeob	cosmicfits	-c -k	
6	Rotation	rcfeob	pymidas		
7	Rebinning	rrcfeob	multrebin	-1 -2 -c -i -w	

Table 5.1: Overview of the *ES2* data reduction pipeline.

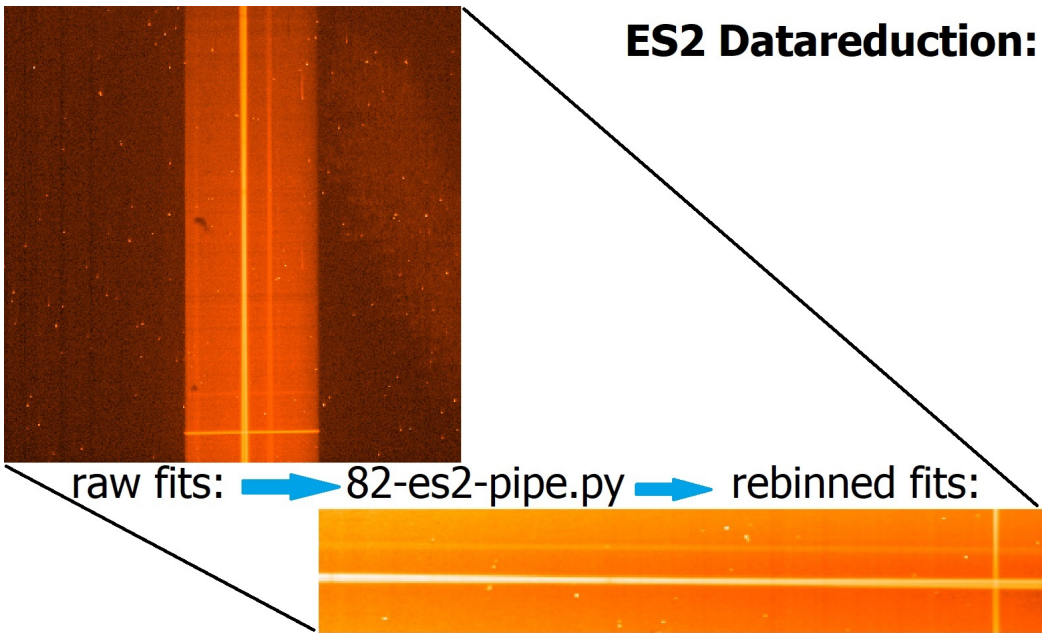

Figure 5.1: *ES2* pipeline. Left: Raw fits file as observed by the *ES2*-spectrograph. Bottom: Final fits file, ready for spectral data extraction.

5.2 ES2 λ-calibration

Once the basic data reduction (see section 5.1) is executed, the spectral fits files are still x-y mapped. A rebinning algorithm is used in order to convert the detectors x-axis pixels into λ-bins. However, the required calibration lamps for *ES2* are already rather old and show significant ageing effects (see section 5.2.1). Hence the Oxygen 5577 Åsky-line is used as an additional calibration anchor (see section 5.2.2).

5.2.1 Argon calibrations

ES2 features a minor set of three integrated spectral calibration lamps: an Argon penlight lamp, a Neon penlight lamp and a quartz incandescent lamp.[62]
Commonly, the *ES2*-spectrograph is designed such that all exposures which are taken with TI1 should be calibrated with the Argon and all CC1 detector exposures be calibrated with Neon, as these lamps show only a reasonable emission line distribution in the according wavelength regimes. As we mostly used the TI1 detector (see section 3.1), the only suitable calibration lamp for the wavelength regime between roughly 4300 Å till 5800 Å is consequently the Argon lamp. Figure 5.2 shows such an Argon calibration exposure, which is the starting point for the calibration.

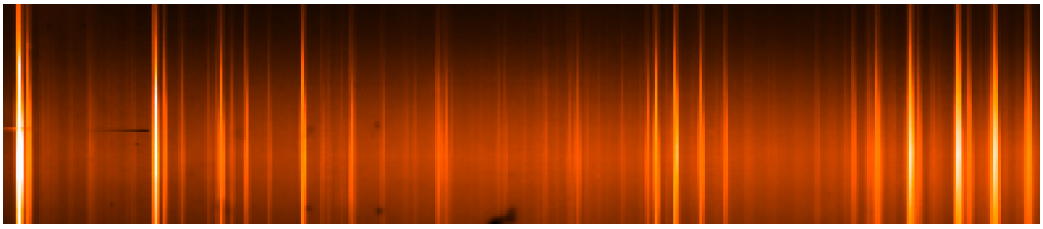

Figure 5.2: Fits file of a reduced Argon spectra. The dark artifacts are known and stable detector faults and the flat-field is not corrected here. Exposure time: 60 s; Date: 12 June 2016

Each calibration consists of the following steps:

1. Create a reference list of lines, to provide initial values.
2. Identify and refine these values for each daily calibration exposure.
3. Calculate a mapping polynomial.
4. Rebin the spectra accordingly.

Creating a reference line list: For each observation run, we need to generate a rough mapping of the pixel and the according λ values of the according emission line in order to provide the rebining algorithm with a starting value. On the one hand, the instrument stability during the typical duration of an observation run [18] is good enough, so that these mapping values are only needed once. On the other hand, the instrument mounting process including the grating adjustment ruins each set up and requires a new reference list of lines.
Initially the task of finding lines has to be done manually once, to provide the algorithm with reasonable starting values. Hence the measured spectra from figure 5.2 & 5.3 need to be compared to figure 5.3, which shows a low resolved, theoretical Argon spectrum as calculated by NOAO/IRAF V2.12.2.[19]

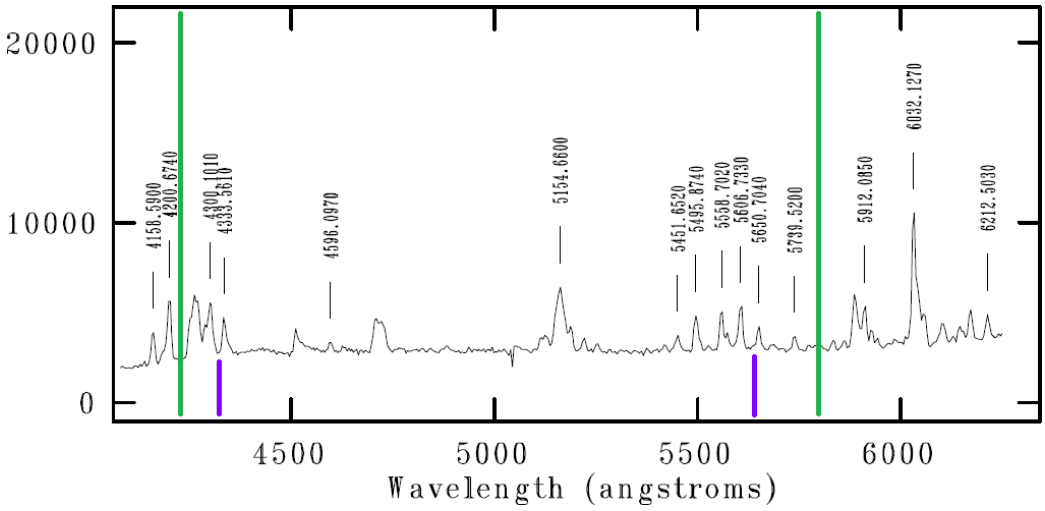

Figure 5.3: Theoretical Argon spectra. The y-axis just shows relative flux in units of arbitrary counts. Green markers indicate roughly the observation range. The purple marker frame the range as it is visible in our following exposure 5.3. Data: NOAO/IRAF V2.12.2

When we compare this to the line profile (figure 5.3) of the measured spectra we find several discrepancies. In the end, several of the theoretically clean emission lines seem to be blended with other emissions from either outgasing or contamination to the gas lamp. Consequently, only few lines are left to be used in order to calibrate and rebin the spectra. An exemplary reference list of lines including the according pixel mapping is given in table 5.2.

[18] Typical duration of an observation run with *ES2* Mc Donald Obs.: 3-10 days
[19] NOAO/IRAF V2.12.2: http://iraf.noao.edu/

Reference line list for *ES2* spectra rebining

λ [Å]:	4333.561	4702.309	5154.660	5451.652	5558.702	5606.733
Pixel:	390	282	150	63	31	18

Table 5.2: Exemplary, reference line list for *ES2* spectra rebinning. These calibration data translate to a 0.1 px precision of $v_{0.1px} \approx 20\ km/s$ given the mapping function of:

$$\lambda_x = 5663\text{Å} - 3.39\frac{\text{Å}}{px} \cdot x$$

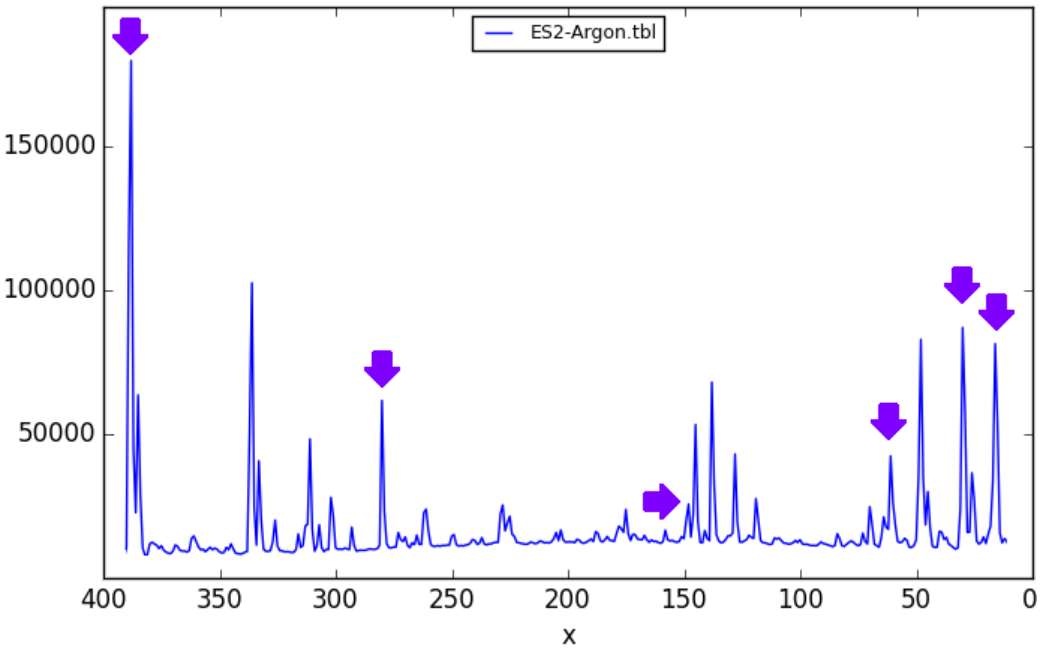

Table 5.3: Measured Argon spectra. The y-axis shows flux in counts and the x-axis is still binned as TI1 detector pixel. The purple arrows mark the used calibration lines as mapped in table 5.2.

Identify and refine line values: The above shown reference line list is just taken as starting values for individual location of each line. Assuming a given pixel value like 150, we have to consider a minor window around this value. Typically an extension of ± 2 pixel provides a reasonable sized box, which in our example reaches from pixel 148 until 152. We have three options to identify the actual line value:

1. The simplest approach is to use the pixel with the highest flux as theoretical line center. This leads to rather coarse line values, as the actual line center often lies between pixels.

2. The second approach is to fit a parabola to the data inside the window and use the resulting vertex. As the box only covers the center of the line, a parabolic fit is close enough to the physical shape of the emission line. This method is accurate enough but it may be confused be neighboring lines, which significantly offset the parabolic fit.

3. Finally the last method calculates the center of gravity for the window and assigns the theoretical λ value. This proved to be the most stable and accurate method available.

Starting with the identification of the actual line values, the following Argon wavelength calibration is automated, using the *Multrebin* code:

Multrebin options Code by: Johannes Koppenhöfer

#	Option:	Value:	Meaning:
1	-1	3	Rebining polynomial order
2	-2	1	Orthogonal line polynomial order
3	-c	2 (Gravity)	Center finding mode
4	-i	filename	Input file
5	-w	Argon filename	Calibration file

Calculate a mapping polynomial and rebin the spectra: Once the *Multrebin* code successfully fitted the center of the calibration lines, it fits a third order polynomial to them. While more lines would improve the robustness of the fit, the aged Argon lamp only provides the six lines shown in table 5.2, which provide enough information to find a proper solution. The solution is calculated for every nights spectral calibrations and slightly varies from day to day.

The rebined spectra seem to be calibrated properly. Nevertheless, when we rebin the Argon spectra itself, one would naively expect its lines to precisely meet the theoretical value. Obviously, a third order polynomial provides four degrees of freedom and hence can not fit all six lines perfectly, so each line will show sub-pixel deviations from the theoretical value, which leads to a minor uncertainty in the spectral offset. Still, the spectral distortion is mapped rather well and is compensated sufficiently.
For most science cases, this calibration is adequate. However, radial velocity studies inherently depend on the accuracy and long therm stability of the wavelength calibration. Hence we need further information in order to correct the calibration offset for each observation.

5.2.2 5577 Å - Oxygen anchor

In order to further improve the spectral calibration offset we utilize the telluric OI line at 5577.34 Å. This atmospheric emission line is just one of many airglow emissions, which exist throughout the upper atmosphere. Due to the narrow wavelength band covered by the *ES2*-spectrograph this is the only reasonable telluric emission line which is usable for its calibration.

This specific oxygen line at 5577.34 Å is generated by the atomic oxygen transition $O(^*S) \rightarrow O(^\prime D)$ and commonly referred to as green sky line.[19] Usually one tries to omit this spectral region within the targets' spectra in order to avoid data contamination from this local oxygen emission even after comprehensive sky subtraction. In our case we utilize the local nature of this emission line to further improve the absolute spectral offset.

Figure 5.4: Fits file of a SDSS193144 spectra. The two horizontal line show the actual scientific target as well as a neighboring source. The prominent emission towards the right edge of the spectra is the 5577.34 Å Oxygen emission.

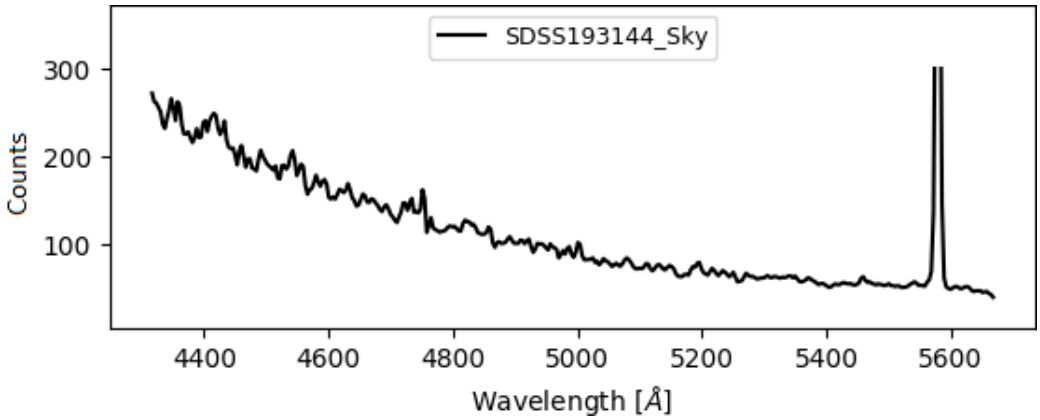

Figure 5.5: Extracted sky emission of a SDSS193144 spectra without flux calibration. The oxygen line is dominating the green part of the sky emission.

Looking at the spectrum in figure 5.4, the oxygen line clearly dominates the sky emission in its region. As it becomes clear in graph 5.5, the 5577.34 Å line is sufficiently bright, so we gain enough signal to noise to adequately fit the emission line using a Gaussian profile. In our case, the fit peaks at a slightly shifted wavelength of 5577.90 Å as it can be seen in graph 5.6.

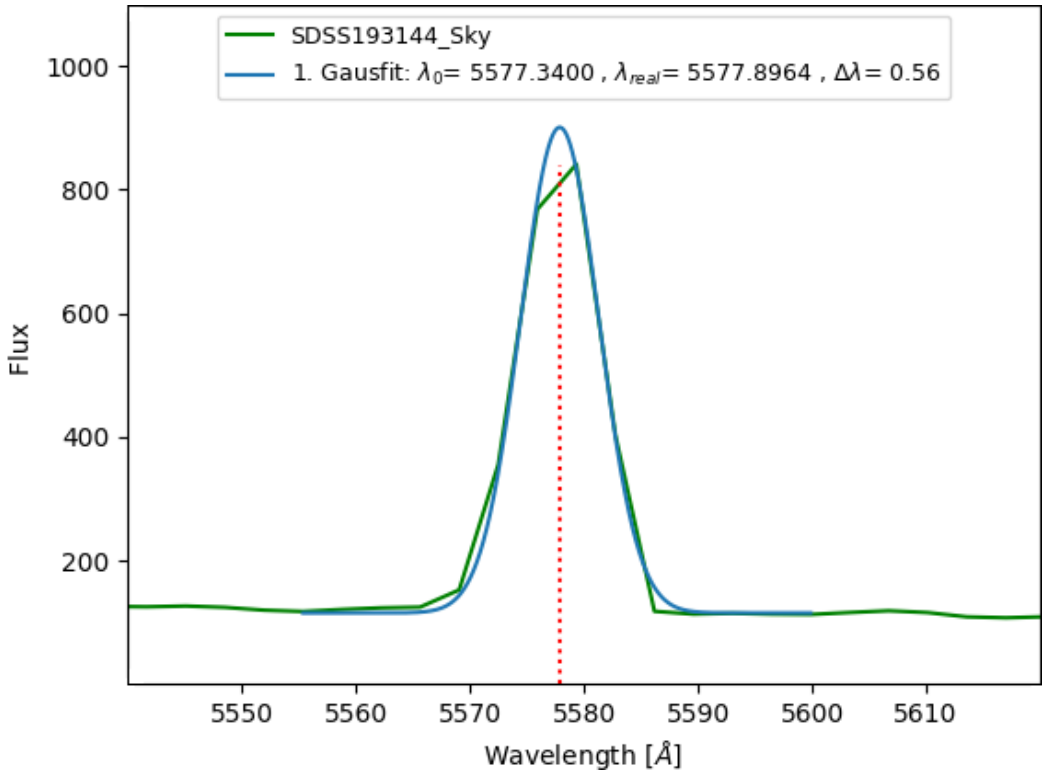

Figure 5.6: Fit of 5577.34 Å emission shown in figure 5.5. The best fitting Gaussian centers at 5577.90 Å which shows an displacement from the theoretical position of 0.56 Å. This translates to roughly 1/5 pixel inaccuracy of the former argon calibration.

The displacement of 0.56 Å can not be caused by astronomical effects, as the majority of this light is emitted in the terrestrial atmosphere. Hence we have independent information on the remaining wavelength calibration offset as left after the argon calibration. Here the 0.56 Å correlate to roughly 1/5 pixel deviation from its nominal, theoretical location.

For the sake of improved wavelength offset calibration, each extracted target spectrum gets shifted according to the displacement of its individual oxygen emission line.

5.3 LRS2 data reduction

As *LRS2* is currently one of *HET*s prime instruments, the data reduction pipeline is critical for its success. In contrast to *ES2*, the *LRS2* team provides a configurable data pipeline,[20] which is to some extent similar to the one described in section 5.1.
The *LRS2* specific pipeline as prepared by Briana Indahl, is separated into six more or less independent python-based sub-pipelines which partly require former reductions steps to be already executed, as it can be seen in table 5.4.

LRS2 Datareduction

#	Reduction step:	Reference section:	Dependency: 5.3.1	5.3.2	5.3.3	5.3.4	5.3.5
1	Basic reduction	5.3.1	○				
2	Deformer	5.3.2	●	○			
3	Sky Subtraction	5.3.3	●	●	○		
4	Fiber extraction	5.3.4	●	●		○	
5	Cube Creation	5.3.5	●	●		●	○

Table 5.4: Data reduction steps for *LRS2*, including the relative dependencies. It can be seen, that the sky subtraction is an optional part of the data reduction. Unlike the reduction of *ES2*, the *LRS2*-data might be used right after the fiber extraction or in form of a datacube with configurable parameters. ○ Self-reference, ● Dependency

All of the listed reduction steps are pre-selectable within the data reduction wrapper, which is provided by the *LRS2* team. This configuration file is capable of reducing a list of observations (different observation times) for a specific target and a specific configuration (e.g. *LRS2*-B or *LRS2*-R). In order to reduce several targets or different setups, one has to provide unique configuration files.
The modular approach of the reduction pipeline seems rather excessive for the amount of data in this thesis, but one has to keep in mind, that the underlying *CURE*-pipeline was designed to handle a large amount of spectroscopic data, originating from the massive blind survey *HETDEX*.

[20] The *LRS2* pipeline is a modified version of the CURE pipeline which was originally developed for the *HETDEX* project. This approach is reasonable, as the *LRS2*-spectrograph is an adopted version of the *VIRUS*-spectrograph, which is used for *HETDEX*. Details on the fundamental *CURE*-pipeline are published in 2014 by Snigula et al. Cure-WISE: *HETDEX Data Reduction with Astro-WISE*.[82]

5.3.1 Basic reduction

In the case of *LRS2*, the basic reduction steps like bias and dark current reduction are all handled completely autonomously and analog to section 5.1.

Basic reduction options Code by: Briana Indahl

#	Option:	Value:	Meaning:
1	subDarks	True	Optional dark frame correction
2	dividePixFlt	True	Optional flat field correction
3	rmCosmic	True	Optional cosmic correction
4	sigclip	5.0	Cosmic detection limit
5	sigfrac	0.3	Cosmic neighbouring fractional limit
6	objlim	5.0	Contrast limit between cosmic and object

Additionally, hot and cold pixels[21] are accounted for, by a bad pixel mask, from which a dark frame is subtracted as well as it is divided by a flat field. Next, the fits data gets flat field corrected on larger scales, using either lamp or twilight flats if available. Afterwards the data pipeline runs a detection algorithm for cosmics, similar to the one explained in section 11.7.2. In contrast to the simple single CCD setup of the *ES2*-spectrograph, each of the two *LRS2* channels red (LRS-R) and blue (*LRS2*-B), get further split on two CCD detector arms, which are accordingly called:

• ultra-violet arm	(UV)	[370nm; 470nm]	*LRS2*-B
• orange arm	(O)	[460nm; 700nm]	
• red arm	(R)	[650nm; 847nm]	*LRS2*-R
• far red arm	(FR)	[823nm; 1050nm]	

Consequentially, the raw fits data from two detector arms are handled separately but finally have to be combined in order to trace the emission of an individual source across the cut off wavelength of the detector arms. Figure 5.7 show such a raw fits data file of *LRS2*, which covers one of the four arms. As the zoomed region at the bottom of figure 5.7 shows, fibers illuminate the CCD in an array pattern as a result of the IFU based design. On the one hand, these gaps might seem like a waste of photons, but as all of the light, collected at the IFU pick off gets redistributed on the CCD, it rather just requires more detector surfaces. On the other hand, this additional detector surface allows for in-frame straylight measurements, which enhances the data reduction.

[21] Hot and cold pixels show significantly more or less quantum efficiency due to variations during the production process a the CCD. Hence these pixels' information are not reliable and usually flagged and neglected during data reduction.

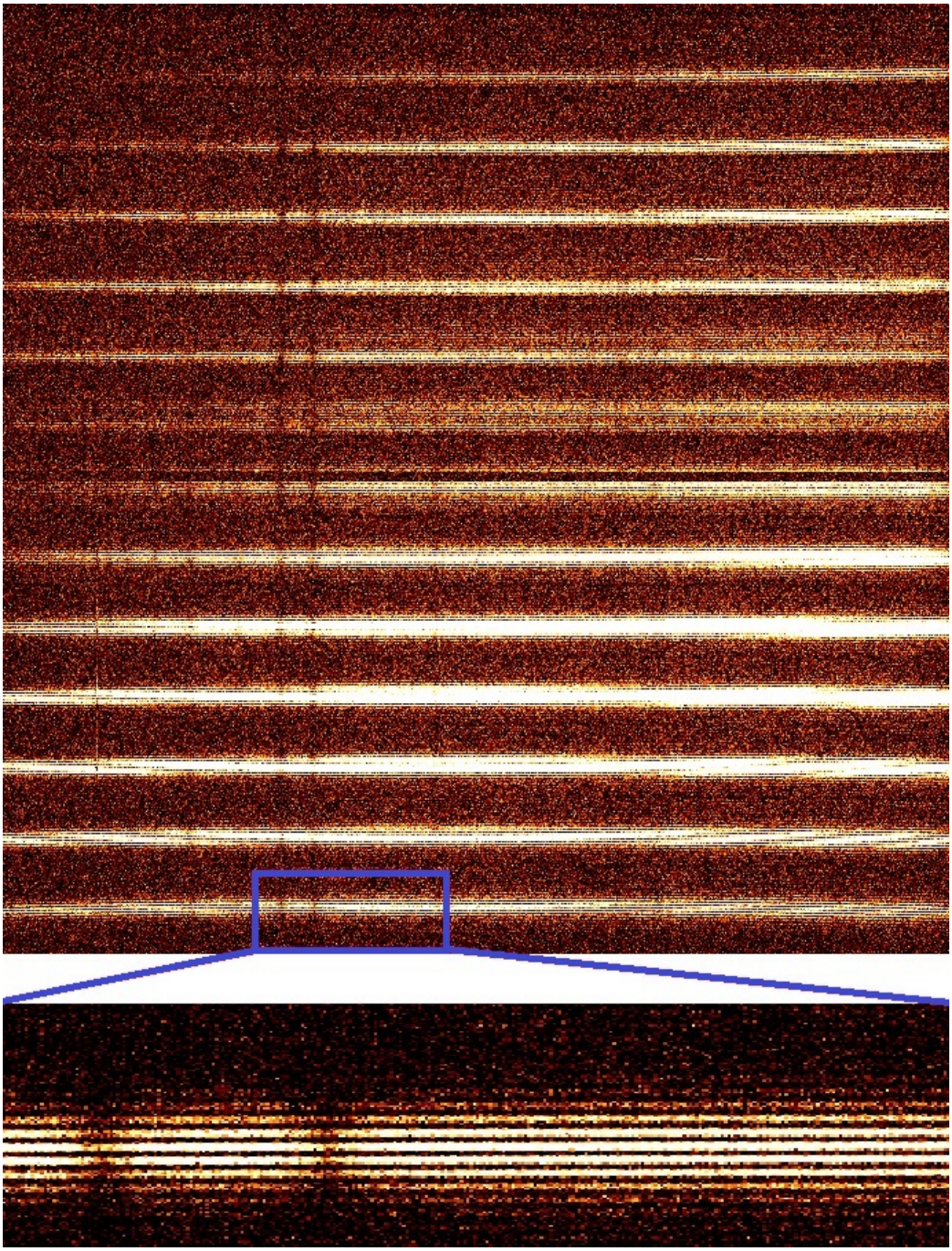

Figure 5.7: *LRS2* fits file after basic reduction. The bottom part shows a zoom of the blue box, highlighted in the general data frame. The zoomed region clearly shows the dedicated gaps between the CCD illumination from the IFUs individual fibers. These gaps allow an in-frame measurement and correction of the straylight, as these areas should never be illuminated by design.

5.3.2 Deformer

The deformer handles the two dimensional deformation of the basic fits files: (1) The fiber allocation dimension on the detector and (2) the orthogonal λ dimension. In order to deform the fiber positions on the detector, the pipeline assumes the basic fiber-gap pattern along the spatial dimension and as it can be seen in figure 5.8, which is taken from Koehler 2009 [52]. The solution along the λ dimension is aided by dedicated arc frames of various calibration lamps.

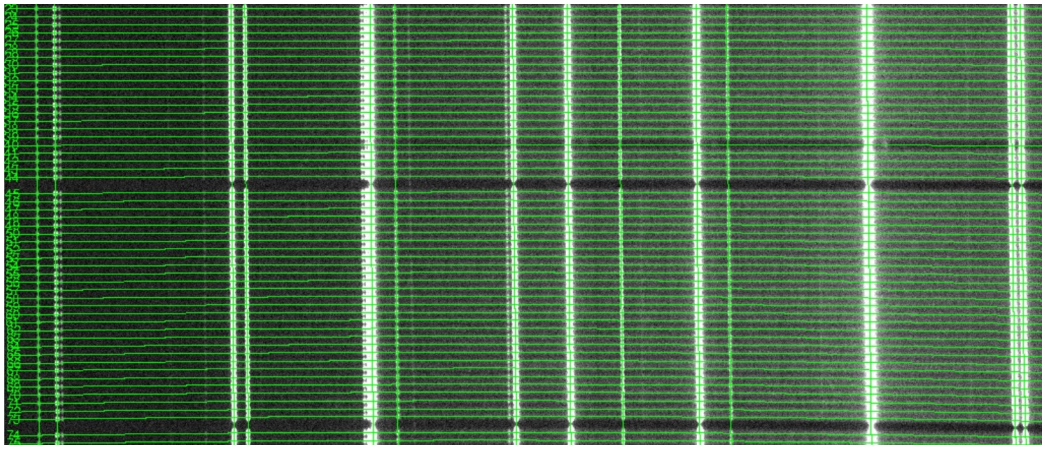

Figure 5.8: *"An arc frame used for calibration. The green lines show the position of fiber peaks and the position of the arc lights from the measured distortion model."* Taken from **Koehler 2009** [52]

While the actual algorithms behind the deformer code are rather complex, we will just cover the fundamental idea behind it. The fiber position f and the wavelength ω need to be correlated with the initial pixel positions x, y. Therefore the pipeline uses a polygon fit of order N, including its cross terms:

$$F = \sum_{j,i=0}^{N} A_{ij} x^i y^j \tag{5.3.2.1}$$

$$f = F_f(x, y) \quad \& \quad \omega = F_\omega(x, y) \tag{5.3.2.2}$$

The according wavelength solution is based on many individual calibration lines, which are fitted using Gaussians. The basic idea of a Nth order polynomial, supported by several lines is analog to the simpler version shown in section 5.2.1. Details can be found in Koehler 2009 [52].

5.3.3 Sky subtraction

The *LRS2* sky subtraction deviates from the *ES2* version, which only implemented in-frame sky subtraction via its data extraction tool. *LRS2* features three options for the sky subtraction: (1) Basic in-frame subtraction similar to *ES2* and an optional advanced correction, aided by either (2) dedicated sky nods or (3) simultaneous sky acquisition via the alternating *LRS2* channel.

Sky subtraction options Code by: Briana Indahl

#	Option:	Value:	Meaning:
1	window_size	200	Size of moving window for sky median
2	sky_kappa	3.5	Sky sigma-clipping limit
3	smoothing	2.0	Spline smoothing factor
4	sn_thresh	15.0	Signal to noise limit for sky detection
5	sky_scaling	1.0	Sky scaling factor prior to subtraction

In the simplest case, the pipeline uses in-frame sky subtraction, as well as shown in figure 5.9, which is adopted from Chonis 2015 [12]. It shows a mockup of two galaxies imaged by *LRS2*. The fiber allocation (small hexagons) of the scientific target is highlighted, while the remaining fibers shaded in blue provide the sky information. The sky subtraction algorithm uses the sn_thresh value to separate sky ($S/N \leq 15$) from target fibers.

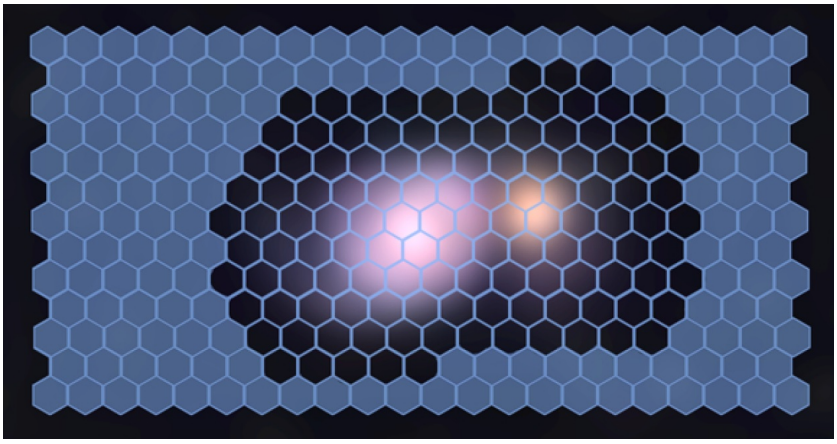

Figure 5.9: *"Illustrations of the observation of a small or unresolved object where sky signal can be obtained in-situ from IFU spatial elements that are sufficiently far from the target. In this figure, the shaded spatial elements indicate those that contain only sky flux and would be sufficient to use for sky subtraction."* Adapted from **Chonis 2015** [12]

The sky subtraction can be optionally aided by dedicated sky exposures which are either gained by sky nodding, in which case they are charged like normal scientific exposures, or are simultaneously recorded using the alternating *LRS2* channel. Sky nodding is the common mode for sky subtraction, when in-frame subtraction is either insufficient or impossible if the field of view is contaminated. Figure 5.10 shows the typical sky nodding offset as it is usually achieved by moving the telescope slightly off target.

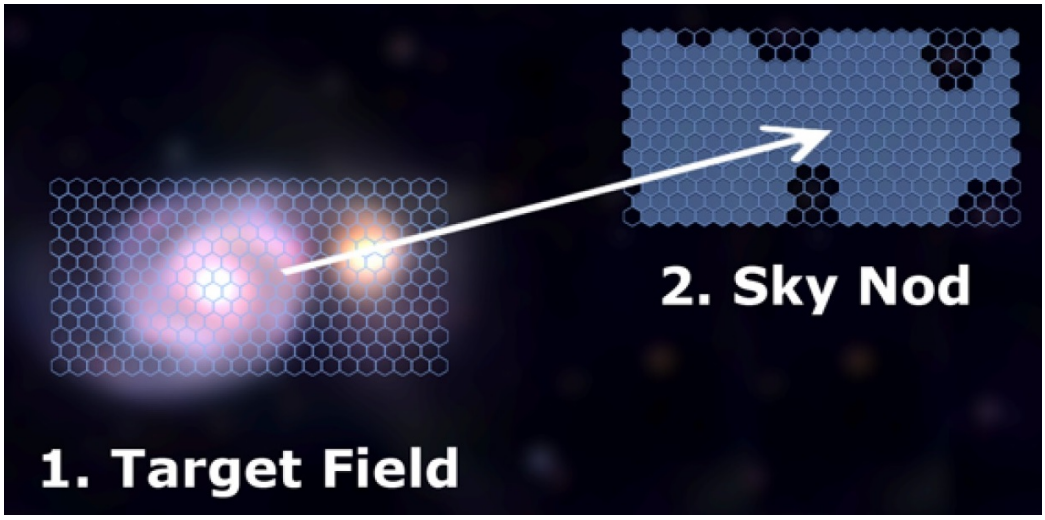

Figure 5.10: *"The panel shows the observation of a resolved object that fills the majority of the IFU. Sky signal is then obtained by nodding the telescope off-target and exposing the spectrograph on a relatively blank patch of sky."*
Adapted from **Chonis 2015** [12]

The second case of simultaneous sky frames is a mode which can only be done since *LRS2* features two independent spectrograph channels with slightly offset IFU heads. This becomes especially beneficial, when the observer requests full wavelength coverage, for which *LRS2* in any case sequentially records two exposures (e.g. *LRS2*-B then *LRS2*-R). The alternating exposure can hence be used as sky frame, as shown in figure 5.11 which is adopted from Chonis 2015 [12].

Both advanced sky subtraction methods allow for example the spectroscopy of the very faint outskirts of brightest cluster galaxies or similar science cases. However, in our case of roughly 16 mag stellar targets, the basic in-frame sky subtraction is yet good enough, since a large percentage of all fibers any ways point to clear sky, while only very few, meet our target.

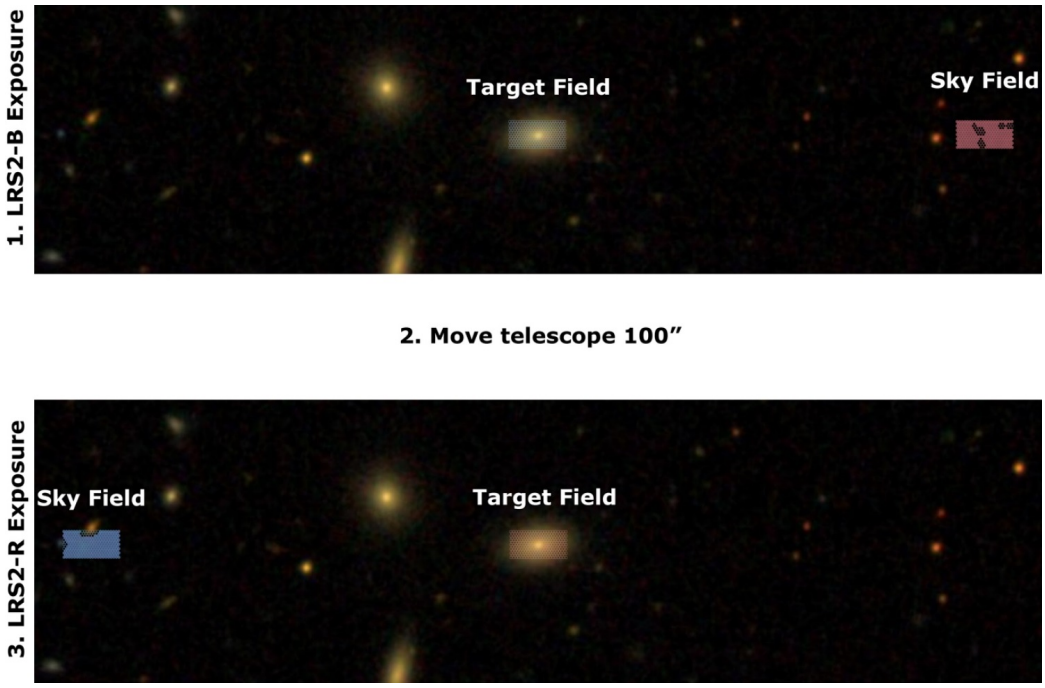

Figure 5.11: *“The panel shows the observation of an object for which the observer desires data over the entire LRS2 wavelength range. When this is the case, the two LRS2 IFUs are beam-switched between the target and blank-sky fields. The image is taken from the SDSS (Data Release 10; Ahn et al. 2014). [3]”* Adapted from **Chonis 2015** [12]

5.3.4 Fiber extraction

In the case of *LRS2*, the fiber spectra are extracted based on the distortion solution, which is calculated by the deformer as explained in section 5.3.2. The extraction algorithm collapses the spectra along the spatial axes, so the light of each fiber is re-binned and straightened according to the deformer solution into only one spatial pixel row. All of the gaps, which are visible in figure 5.7 are now cut. The resulting spectra is shown in figure 5.12.

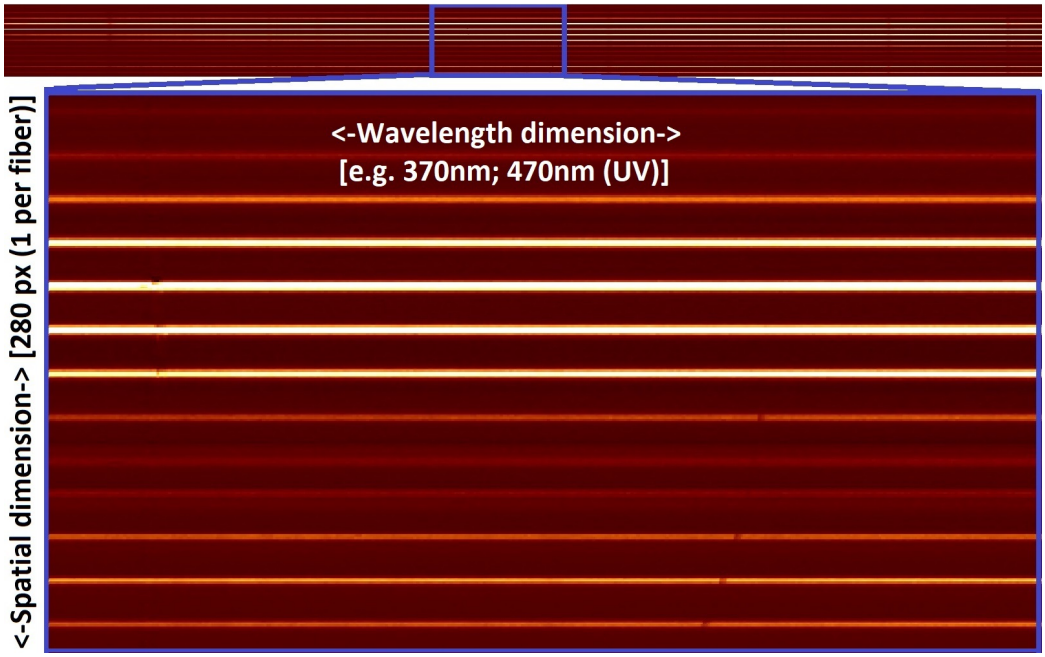

Figure 5.12: *LRS2* fits file after fiber extraction. Each pixel row contains the collapsed track of each individual fiber. The bright horizontal lines, visible in the zoomed box, are sliced fractions of the target star SDSS193144, which gets sampled by multiple pixels as it is systematically visible in figure 5.9.

The fiber extraction algorithm is less configurable as other parts, since all the configuration input has already been considered during the calculation of the deformer solution. Only in case of a very specific λ-calibration, the spectra are extractable without deforming the wavelength-dimension, so this could be done manually if needed. All of the data used in this thesis have been calibrated using the implemented λ-calibration.

Fiber extraction options Code by: Briana Indahl

#	Option:	Value:	Meaning:
1	wl_resample	True	Wavelength resample switch

5.3.5 Cube creation

Once the spectra are extracted to 1-dimension, the *LRS2* pipeline recreates a spatial image based on the known fiber pattern within the IFU heads as shown in section 3.2. The resulting spatial image is projected in figure 5.13.

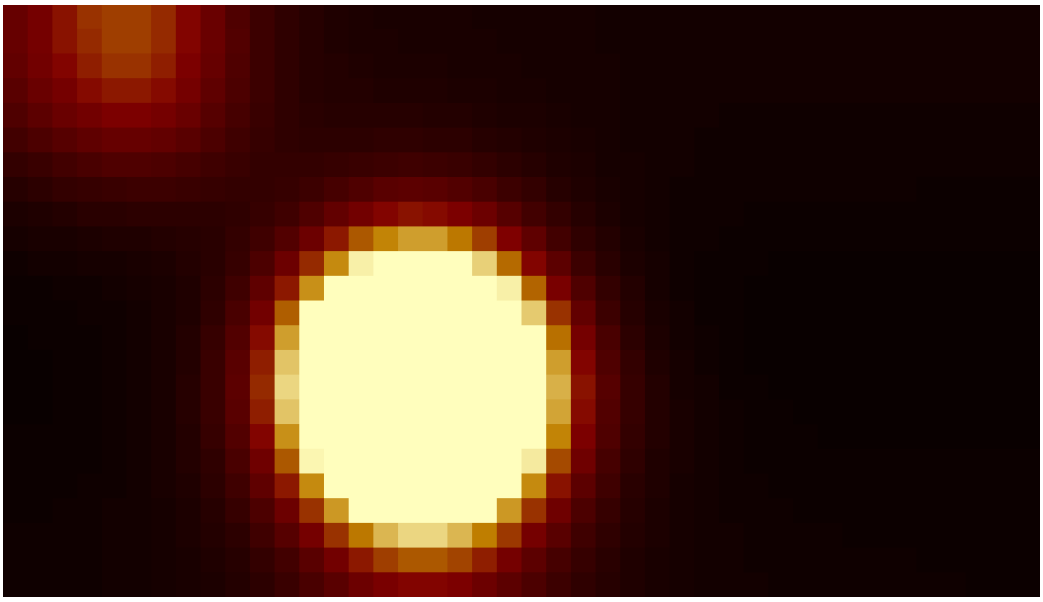

Figure 5.13: Projected view of an *LRS2* data cube, which is collapsed along the λ-dimension. The former individually extracted spectra are rebinned into a classical x,y image of the sky region which is sampled by the IFU as it is shown in figure 5.9. The central target clearly outshines the neighbouring source of minor luminosity, which is visible to the top left of the cube.

The cube creation code is to some extent configurable as it is reasonable within the context of the *HETDEX* project, for which the underlying *CURE* pipeline was created. The according code options are shown below:

Cube creation options Code by: Briana Indahl

#	Option:	Value:	Meaning:
1	sky_sampling	0.3	Regridded sample size on sky in arcsec.
2	max_distance	5.0	Samples further away will have weight=0
3	cube_sigma	0.75	Gaussian σ of the interpolation kernel
4	diffAtmRef	True	Differential atmospheric refraction

5.3.6 λ-calibration

Until the cube creation and the according spectral extraction all steps were automatically executed by the dedicated *LRS2* data pipeline. As we intend to measure relative radial velocities, we here check the quality of the wavelength solution for our calibration spectra within this subsection. Afterwards we apply a spectral offset correction using sky line anchors as already discussed in section 5.2.2 for *ES2*.

To check the wavelength calibration we turn to the reduced calibration files which contain rectified and collapsed arc exposures.[22] Analogous to our *ES2* pipeline, also the *LRS2* pipeline uses a set of well-known reference emission lines for each of its channels, as they are listed in table 5.5.

Reference line list for *LRS2* spectra rebining

UV-channel				Orange-channel		
λ [Å]	Pixel	Element		λ [Å]	Pixel	Element
3650.153	35	Hg		4678.149	117	Cd
3654.836	45	Hg		4799.912	218	Cd
3663.279	62	Hg		5085.822	456	Cd
4046.563	843	Hg		5460.735	766	Hg
4077.831	905	Hg		5769.598	1022	Hg
4358.327	1471	Hg		5790.663	1039	Hg
4404.751	1566	Fe		6438.470	1581	Cd
4412.989	1582	Cd		6965.430	2035	Ar
4481.811	1723	Ar				
4545.052	1853	Ar				
4579.350	1924	Ar				
4589.898	1945	Ar				
4609.567	1986	Ar				

Table 5.5: Reference line list for *LRS2* spectra rebining.

The following figure 5.14 shows an example plot of a calibration lamp exposure for the orange channel with applied *Gaussian*-fits for the individual reference lines, which are used to compute the wavelength solution. Note, that the last of the eight above listed reference lines is located just marginally outside of the nominal wavelength scale, to which all *LRS2* spectra are rebinned. Hence, it is omitted from the following plot.

[22] The arc exposures are collapsed to one line per fiber and rectified to the common wavelength solution setting of *LRS2*.

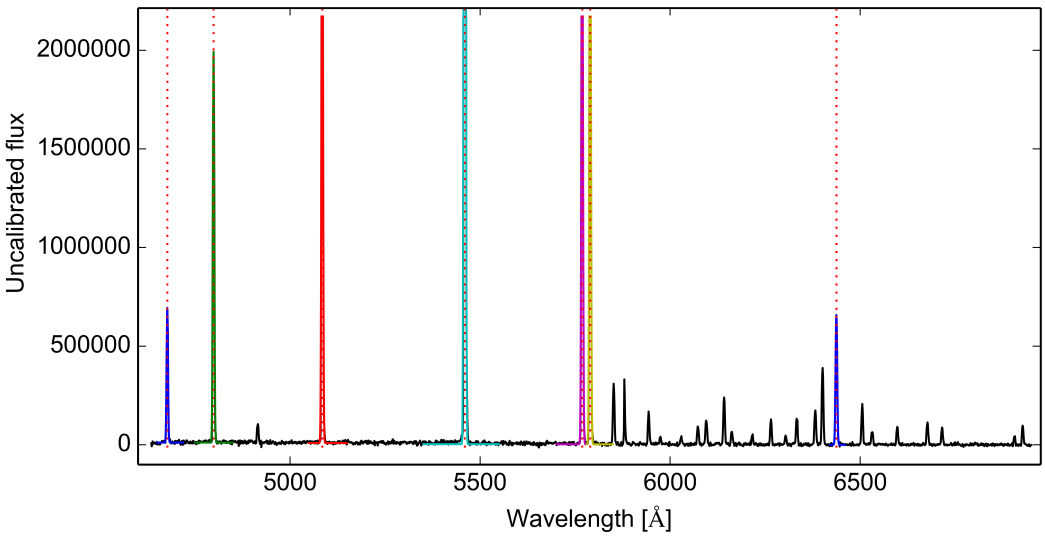

Figure 5.14: Extracted, rectified and collapsed calibration lamp spectrum for observation night 20171115. The applied *Gaussian*-fits are plotted in color, and the resulting center are indicated in red.

As all our *LRS2* data were observed within 12 nights, we hence investigate the reference line displacement $\Delta\lambda$ for each of those nights.

λ-calibration precision

	UV-channel	Orange-channel
Number of lines per spectrum:	10	7
Sample size:	120	84
$\overline{\Delta\lambda}$:	0.024 Å	-0.039 Å
$\sigma_{\overline{\Delta\lambda}}$:	0.095 Å	0.060 Å

Table 5.6: λ-calibration statistics for all 12 observation nights. $\Delta\lambda$ are measured within the calibration spectra, as plotted in figure 5.14.

Based on the results listed in table 5.6, we conclude that on the one hand the λ-calibration for the orange channel provides a precision down to 5% of a pixel. The UV channel on the other hand shows slightly worse performance, at 10% pixel size benchmark which we consider as our baseline.

During the former analysis we realize by how much the calibration changes and therefore took a closer look at the calculated 2d polynomial wavelength solution as it is calculated for the whole detector plane.
Usually, one would expect the wavelength solution to shift from night to

night mostly in a linear manner and also accept some minor variations in the general polynomial fit parameter space. Both effects are usually caused by small temperature differences of the spectrograph, its optical components in general, its dispersion element in particular and also its mechanical structure which sets the relative position of all those components. The following figure 5.15, shows a composition of two individual night's λ calibration solutions (left and center) as well as a difference image between both (right).

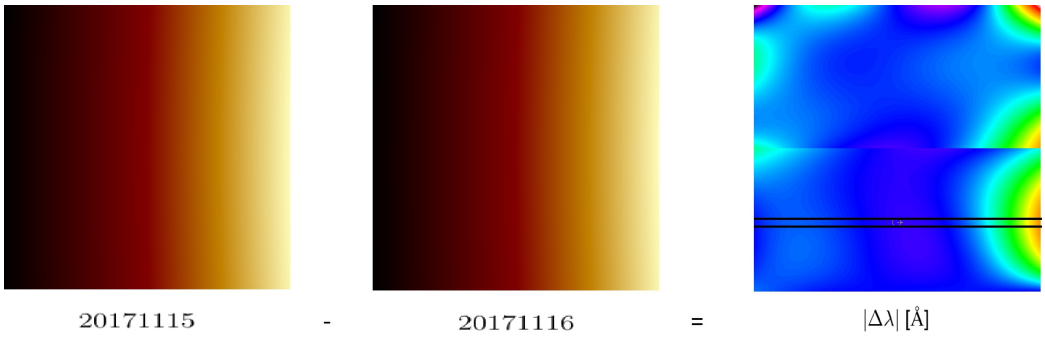

Figure 5.15: **Left and center:** λ calibration of both calibrations.
Right: Difference image of the two orange solutions.
Note: The black slice in the difference image highlights the section which we investigate in detail in plot 5.16.

For *LRS2*, we discovered that not only the wavelengths solution itself moves by almost 1 Å from night to night, but also the general shape of the solution varies drastically from night to night. Hence we investigated these difference images between two independent nights for all 2017 observations and subtracted each night from our first night's (20171115) wavelength solution. In order to avoid individual outliers, we calculated the mean from 50 pixel wide 2d-cuts, as they are already indicted in the right sub-figure of 5.15. The results for all the combinations are shown in plot 5.16.

Within 5.16 we mark the location of the first and last stable calibration arc line, which at least for the detector region from 1600 pixel upwards give a clear hint why the calibration might partly drift off. As usual these 2d fits of the wavelength calibration tend to loose their stability outwards of their enclosed range. It remains unclear, why the last calibration line, which is according to table 5.6 expected at around 2035 pixel, does not prevent the fit from occasionally running away.

However, in some exposures it seems that, due to te overall field curvature as it can be seen in figure 5.15, this calibration line might not be visible to all

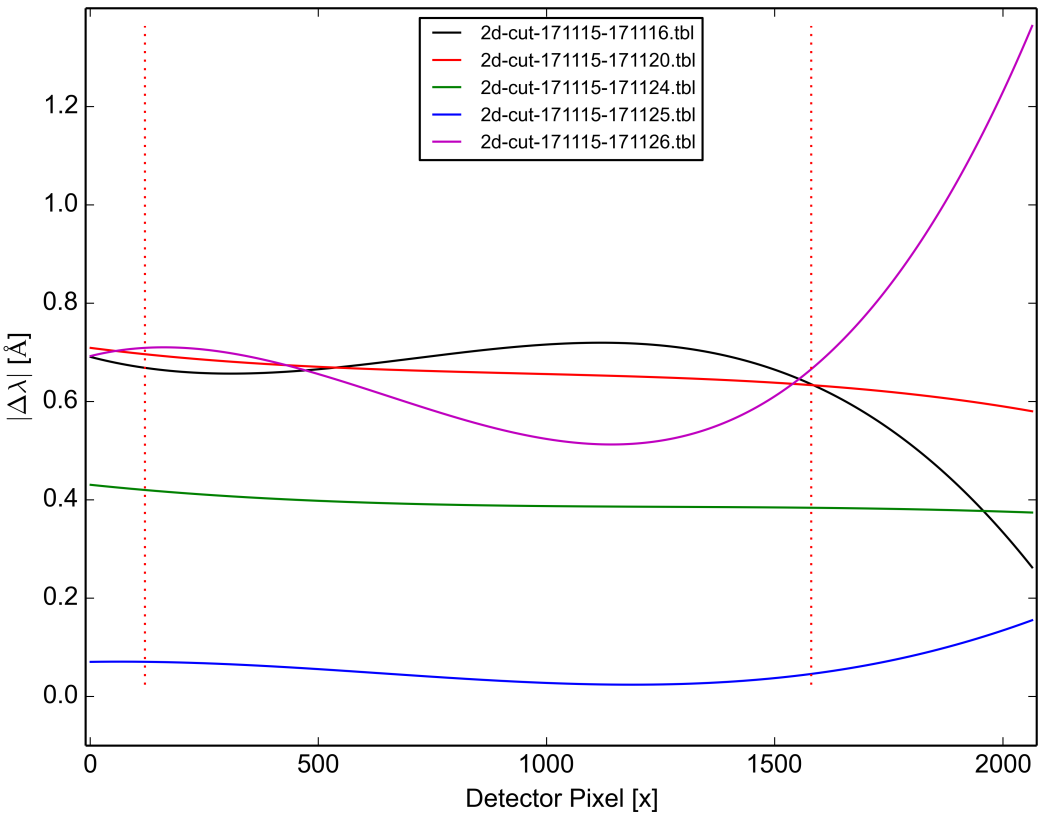

Figure 5.16: 50 pixel mean of 2d-cuts from all 2017 calibration observations wavelength calibration solutions as produced like shown in figure 5.15. The vertical red markers indicate the location of the last stable calibration line.

fibres and hence the provided data pipeline might have omitted it completely, which would be a reasonable explanation for the vastly different solutions for the nights 20171116 [23] and 20171126. [24]
In the end, we will check during our radial velocity analysis how much of an impact these λ-calibration variations might have. We have to be careful with the affected sections of the spectrum and might hence cut those regions from the analyzed data, even if it contains the prominent H_α absorption line.
Nevertheless, according to the results from table 5.6, the calibration passes our quality check and we proceed in the next section with the absolute offset correction, which should take care of the linear offset between exposures.

[23] Night Δ 20171115 - 20171116: Figure 5.16 black
[24] Night Δ 20171115 - 20171126: Figure 5.16 magenta

5.3.7 Sky anchors

In contrast to *ES2*, *LRS2* provides the two distinguished channels orange and UV, for which we consequently need to use different sky emission lines.

Orange *LRS2* channel: Within the orange channel, we utilize the known telluric O I line at 5577.34 Å as shown in figure 5.17 to correct the remaining spectral offset, analog to the *ES2* reduction from subsection 5.2.2. The overall mean displacement results in $\overline{\Delta\lambda}$ = -0.09 Å (σ = 0.24 Å), which is below 10% pixel size.

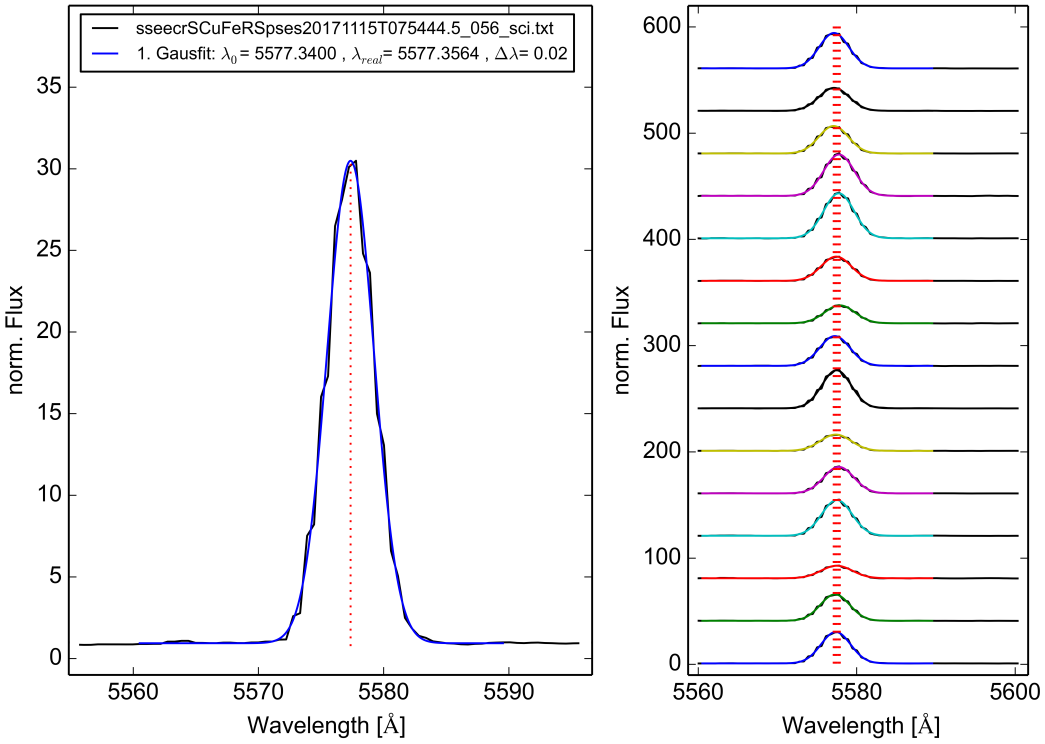

Figure 5.17: **Left:** Detailed sky line fit of exposure 20171115T075444 **Right:** Stacked O I sky line fits of all *LRS2* exposures.

UV *LRS2* channel: The UV band hardly offers any sky line which is as detectable as the O I line. However, we managed to identify the weak terrestrial Hg I emission line at 4358.33 Å.
For most exposures this line can be used, however three exposures provided almost no signal. One of these is marked in plot 5.18 by a red arrow and is hence shown in detail below. The attempted fit meets the given data

reasonably, but the Hg I line is almost missing entirely, so the fit is ignored and these three UV exposures can not be corrected.

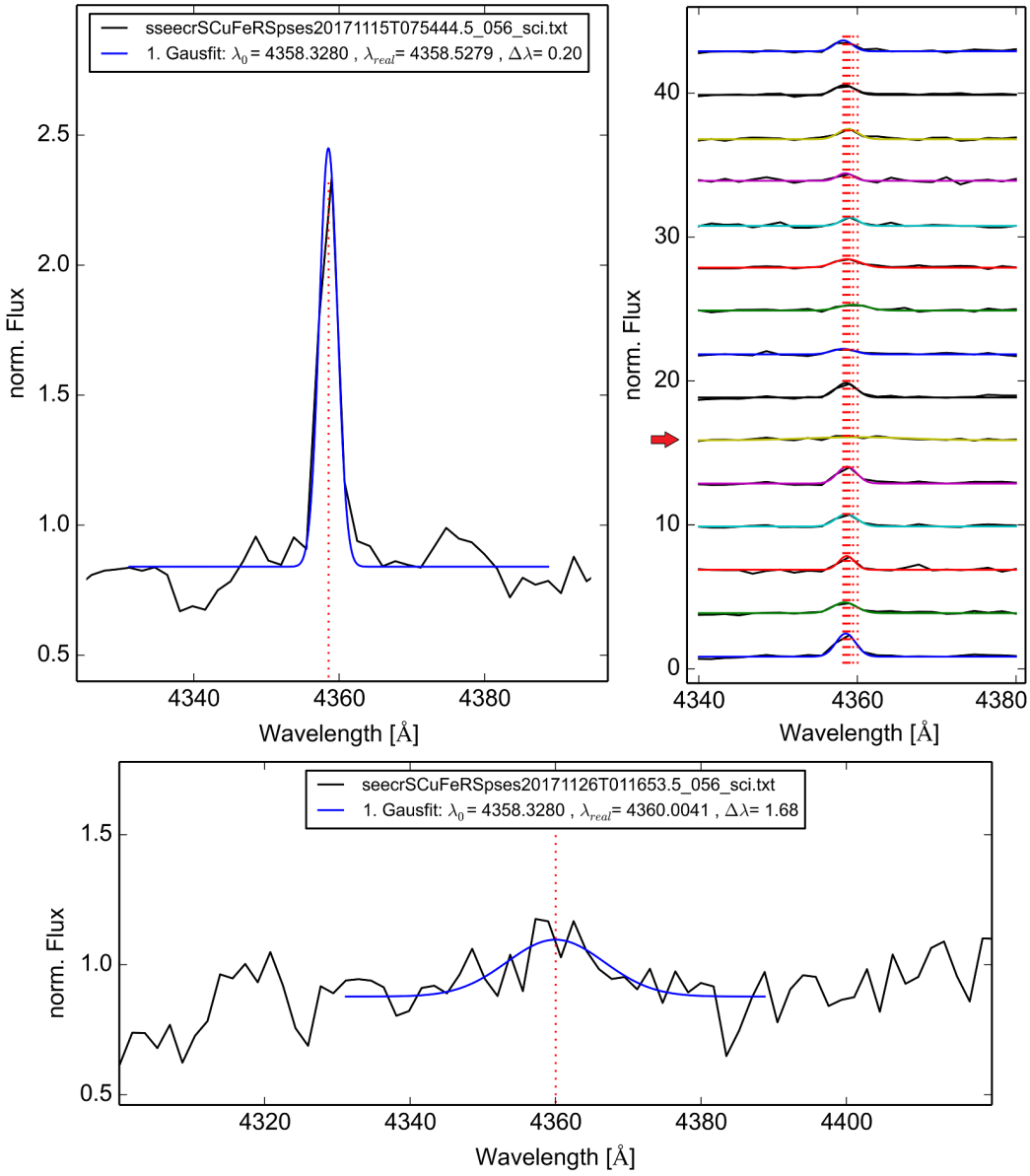

Figure 5.18: **Left:** Detailed sky line fit of exposure 20171115T075444 **Right:** Stacked Hg I sky line fits of all *LRS2* exposures. **Bottom:** Hg I Fit of exposure 20171126T011653, which lacks a traceable line profile and intensity.

The overall mean displacement results in $\overline{\Delta\lambda}$ = -0.24 Å (σ = 0.23 Å), which is still well in the sub-pixel domain ($\approx$ 20%).

5.3.8 Combined channel evaluation

In order to later combine the results from both channels, we here estimate the divergence of both given their individual precision.
The right section of figures 5.17 and 5.18, clearly shows a minor remaining displacement $\Delta\lambda$ of each individual spectra relative to each other. We measured a mean displacement within the orange channel at $\overline{\Delta\lambda}$ = -0.09 Å (σ = 0.24 Å), while the UV channel shows $\overline{\Delta\lambda}$ = -0.24 Å (σ = 0.23 Å). Calculating all the shifts show a maximum displacement between any two exposures of 0.78 Å (orange) and 0.81 Å (UV).
The following plot shows the individual displacement $\Delta\lambda$ from the literature value of Hg I (blue) and O I (red) respectively.

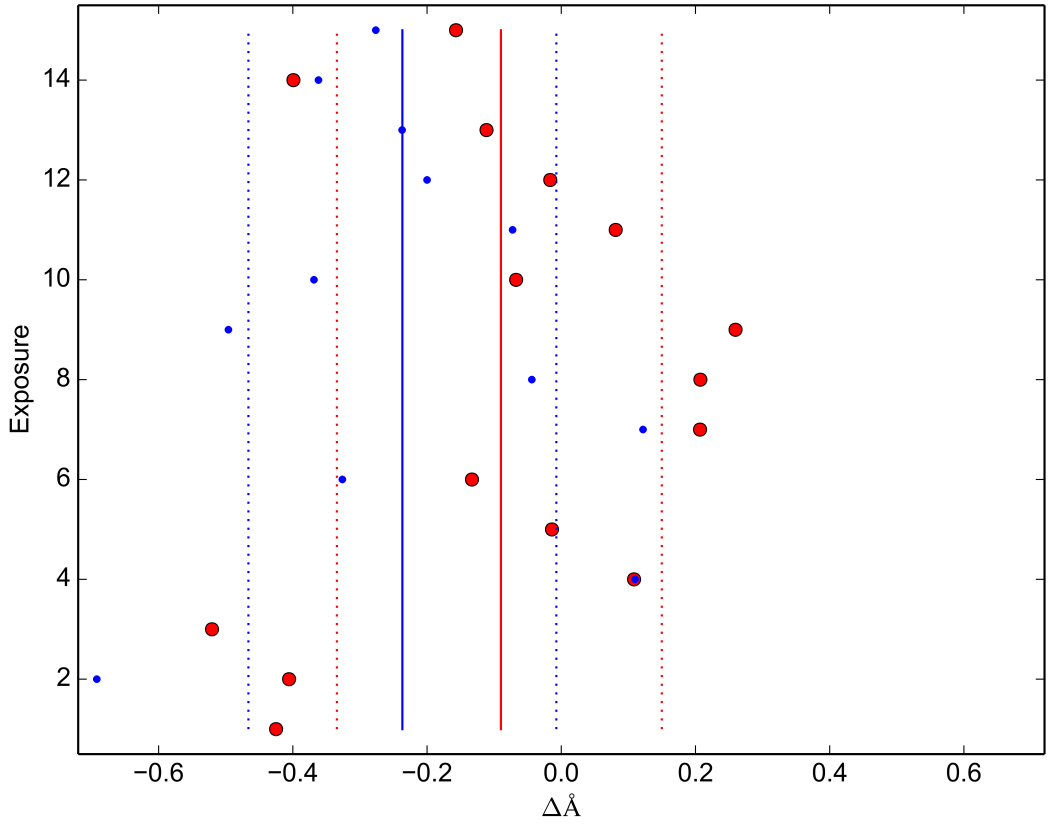

Figure 5.19: Sky line displacement $\Delta\lambda$ for *LRS2*. The UV channel is indicated by blue dots and orange observations by red circles. The according means $\overline{\Delta\lambda}$ (solid lines) and their σ (dashed lines) are also indicated by their according colors blue respectively red.
Note: Exp. 1-6: SDSS193144 (3 missing Hg I fits), exp. 7-12: SDSS070433 and exp. 13-15: SDSS070428.

The measured wavelength uncertainty of $\sigma_{UV} = 0.23$ Å and $\sigma_{orange} = 0.24$ Å at first seem comparably but according to equation (2.5.0.4), leads to the following radial velocity uncertainties:

- UV: $\Delta v_{app.} = c\ \frac{0.23\ \text{Å}}{4060\ \text{Å}} = 17.0\ \frac{km}{s}$
- Orange: $\Delta v_{app.} = c\ \frac{0.24\ \text{Å}}{5600\ \text{Å}} = 12.8\ \frac{km}{s}$

These channel dependent imprecisions allow us to estimate the two following statistical parameters:

1. **Inter-channel-mismatch (ICM):**
   The ICM between both *LRS2*-B channels can now be estimated using the following assumption: As the wavelength solutions result from different calibration exposures and furthermore independent sky lines have been used to correct the offset, both measurements are independent and hence according to the Gaussian propagation of error,[25] the overall consistency-level is expected to be:

   $$\sigma_{LRS2-B} = \sqrt{\left(17.0\ \frac{km}{s}\right)^2 + \left(12.8\ \frac{km}{s}\right)^2} = 21.3\ \frac{km}{s} \qquad (5.3.8.1)$$

   This statistical value will later be used to check the resulting $v_{app.}$ measurements for consistency.

2. **Combined radial velocity precession:**
   In addition to the above calculated inter-channel-mismatch, the individual channel precisions furthermore allow us to estimate the final 1σ-uncertainty of the combined $v_{app.}$ measurement.

   We combine the individual channels $v_{app.}$ results using their according σ_i to weight them by $w_i = \frac{1}{\sigma_i^2}$ as follows:

   $$v_{app.} = \sqrt{\frac{\sum w_i v_i}{\sum w_i}} \qquad (5.3.8.2)$$

[25] According to the Gaussian propagation of error, independent errors add up quadratically like: $\sigma_{total} = \sqrt{\sum \sigma_i^2}$

In contrast to the ICM, here the weighted, overall $\sigma_{v_{app.}}$ propagates not quadratically but also according to the weights w_i as follows:

$$\sigma_{v_{app.}} = \sqrt{\frac{\sum w_i \sigma_i^2}{\sum w_i}} = \sqrt{\frac{2}{\frac{1}{\sigma_{UV}^2} + \frac{1}{\sigma_{Orange}^2}}} = 14.5 \ \frac{km}{s} \tag{5.3.8.3}$$

While equation (5.3.8.2) will later be used during the radial velocity analysis, we can already conclude on the overall systematic rv-error of $\sigma_{v_{app.}} = 14.5 \ \frac{km}{s}$ as calculated above.

Concluding section 5 with these statistical estimations of the final radial velocity measurements, we can yet move on to work with our reduced spectroscopic data. All the instrument specific data reduction is now done and furthermore all spectra are wavelength and offset corrected using the available calibration lamps and sky lines Hg I resp. O I.

In the following section 6, we start the data analysis by investigating the extracted data and discussing the flux-normalization.

Chapter 6

Flux normalization

At this point, all data are reduced and λ-calibrated as discussed in chapter 5. Furthermore, the data are extracted from the fits files and are stored as ASCII files.

Such a spectrum, as it is the starting point for this chapters analysis, is plotted below in the following figure 6.1.

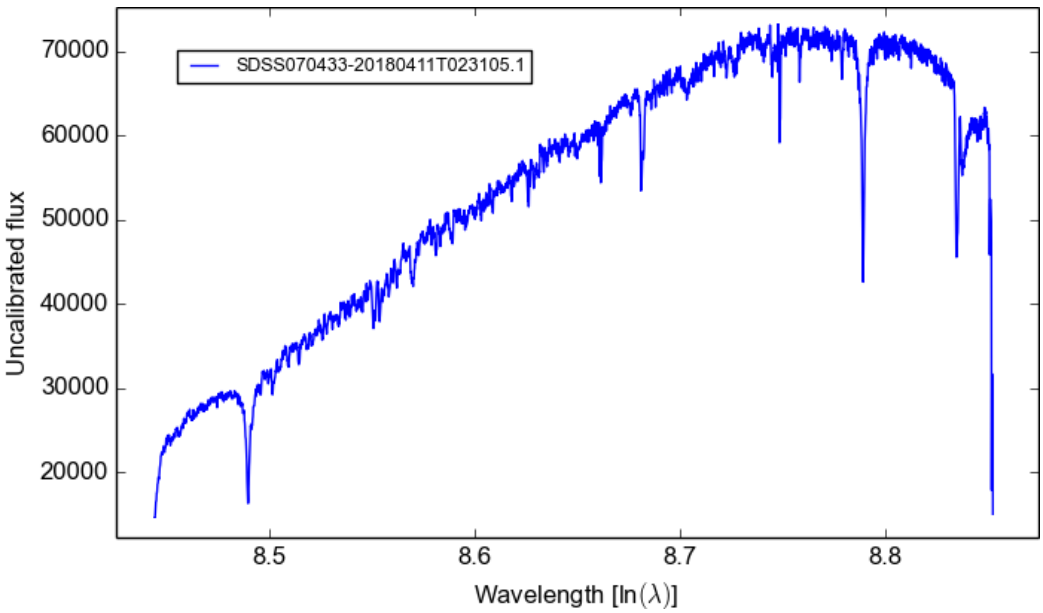

Figure 6.1: Unnormalized *LRS2* spectrum 20180411T023105.1, showing target SDSS070433. The continuum is here not dominated by the sources black body characteristics but rather by the instruments throughput curve in the according orange arm as shown in figure 3.5

We would need a flux calibrated spectrum in order to draw clear conclusions from the spectral continuum shape or λ_{peak}. We consequently rather use photometric *3KK* observations as discussed in chapter 8, to confirm the sources continuum characteristics.
Consequently, we will ignore the throughput dominated continuum and operate on flux normalized spectra. This approach is a standard method for many spectroscopic science cases in general and radial velocity studies in particular. Therefore, we first discuss the flux normalization and the used algorithm in this chapter, before we discuss the actual radial velocity analysis in the next chapter, in which we show the instrument specific results in the according subsections 7.1 and 7.2.
In order to analyze the spectral features for their radial velocity, we first have to normalize the basic spectral continuum, so our measurements become comparable in flux and the analysis is robust against flux variations, caused by the observation conditions as discussed in section 4.

In a nutshell, we have to find a mathematical fit, which follows the overall spectrum as well as possible, while ignoring all absorption and emission lines. Given this, one simply divides the spectrum by the fit and the resulting spectrum should nicely be normalized to 1, while only the spectral absorption lines deviate clearly.

In order to properly fit the spectral continuum we list four different approaches of increasing quality: Estimation of black-body radiation, combination of black-body radiation and instrument throughput, a general polynomial fit and finally a cubic splines algorithm.
Within this thesis we are using cubic splines to fit the stellar continuum and accordingly normalize the spectra. In order to keep this section brief we outsourced the motivation for this approach to the appendix. Furthermore, we assume the cubic spline algorithm to be known, so we also passed the brief mathematical discussion to the appendix.

6.1 Cubic spline normalization

The basic idea behind using cubic splines to normalize a continuum, is to mix the strength of former listed approaches to normalize data. As discussed, the continuum is a combination of many different effects, which all follow different mathematical functions. To disentangle them properly seems nearly impossible. But, we are manually able to identify minor wavelength bands in which we are not aware of any contaminations at all.

6.1.1 Finding suitable interpolation points

Given this, we now average the data within these small, approximately 15 Å wide bands, which should only be effected by a basic photon noise. We will discuss photon noise in the next section 6.2 in more detail, but for now it is enough to state that this is the most basic physical level of uncertainty within the spectrum. We now have a set of averaged interpolation points, which represent the continuum, while being independent of the majority of other data points. The remaining data points are potentially contaminated by any kind of absorption or emission line. Figure 6.2 shows a cubic spline fitted spectrum, with marked wavelength bands which where used to calculate the fit. The locations of the green probing bands are a manual input to the algorithm which only needs to be done once per instrument setup and is chosen conservatively in a way, so the bands have a margin of at least two times the bandwidth, to the next relevant absorption line.

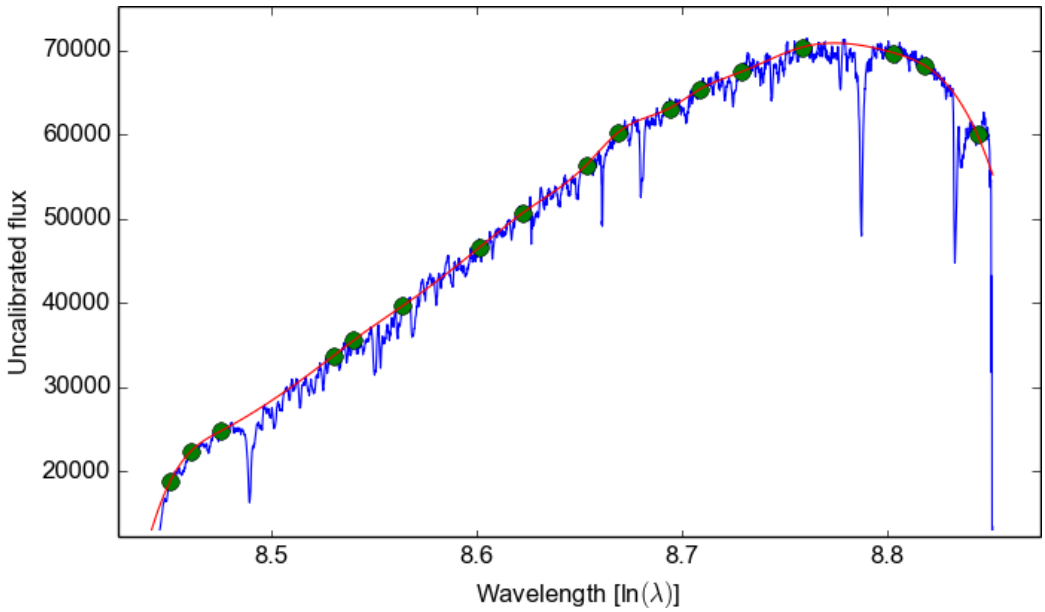

Figure 6.2: Random, cubic spline fitted *LRS2* spectrum, showing target SDSS193144. The blue continuum is probed at 17 minor wavelength bands which are marked with green circles. Based on this new data points, the algorithm calculates the red cubic spline, which meets all those abstract data points nicely.

6.1.2 Fitting the cubic spline

In order to calculate a proper fit, we use step wise defined spline functions as we show in the appendix *Cubic spline algorithm*. The resulting cubic spline function is plotted in as red line within figure 6.2 and meets all our requirements and fits the spectra very nicely.

6.1.3 Apply the cubic spline fit

Once we have the proper cubic spline solution, we can directly divide the measured spectrum by it. A resulting spectrum is plotted in figure 6.3. Ignoring the boundary effects, we find a nicely normalized continuum as required.

We can now see even better, that the cubic splines interpolation points avoid absorptions lines and are still evenly distributed over the whole spectrum. In the following subsection we will now check the quality of the flux normalization by comparing the result with the fundamental photon noise.

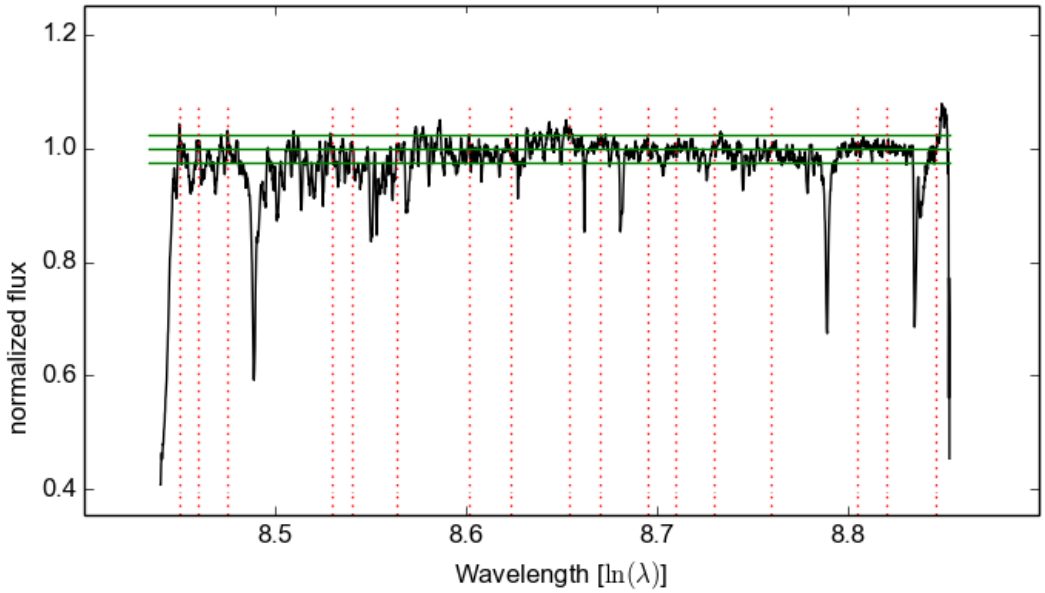

Figure 6.3: Normalized *LRS2* spectrum. The red dotted lines show the interpolation points for the cubic spline fit. The green lines mark the normalized flux level 1.00 while the upper and lower line indicate a ±2.5% margin.

6.2 Quality check via photon noise

Given the flux normalization as discussed in the last subsection, we now analyze our data to qualify the normalization. First, we pick the interval $\Delta \ln(\lambda)[8.805, 8.820]$ $\left(\approx 6.670 - 6.770\text{Å}\right)$ from the former figure 6.3 which is apparently not affected by absorption lines. The zoomed plot 6.4, shows the region, which contains 150 data points and is normalized to an error within 2.2 ‰. This deviation from the nominal is reasonable as we investigate a section of the spectrum, which was not included in the cubic spline interpolation. In addition to the acceptable average, we further calculate the standard deviation and find $\sigma = 0.0079$.

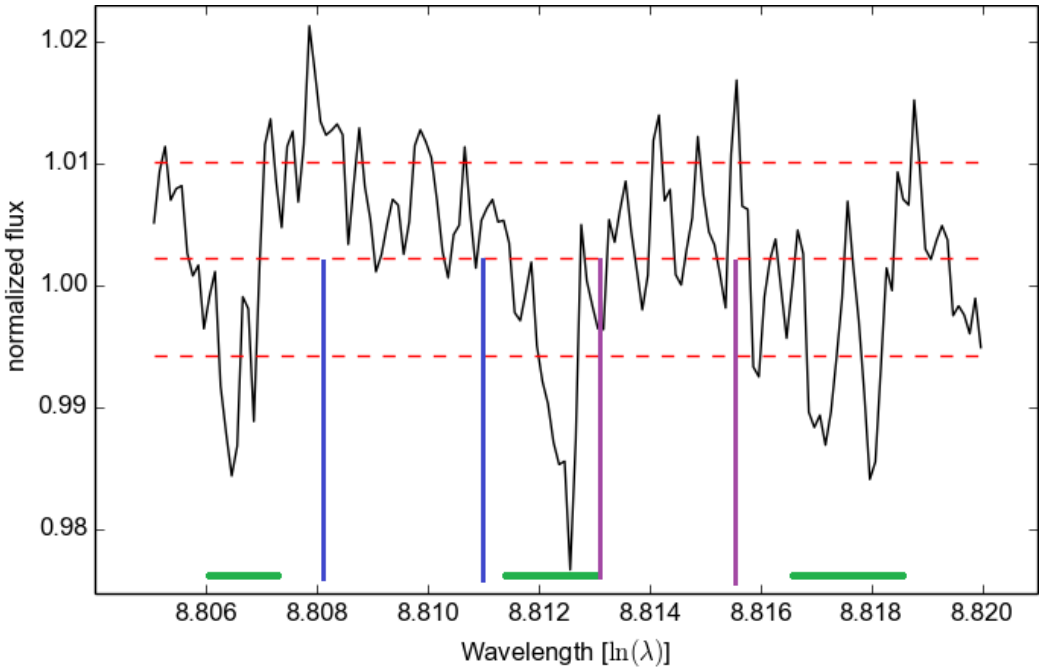

Figure 6.4: Extracted section from spectrum 6.3, from which we calculated the following statistical values. The red horizontal lines indicate the average flux as well as the $\pm 1\sigma$ thresholds. The green bars mark potential minor absorption lines and the purple vertical markers indicate the location of a sub-dataset consisting of 27 data points, in which σ drops to 0.0047. In the blue sub set, the standard deviation even drops to $\sigma = 0.0039$.
Sample statistics: •Average: 1.0022 •Median: 1.0032 •σ: 0.0079 •Samplesize: 150 values •Range: $8.805 - 8.820\,\ln(\lambda)$ $(\approx 6.670 - 6.770\text{Å})$

While this seams reasonable, we should briefly re-investigate the zoomed data region in plot 6.4. Taking a closer look we can clearly spot two, but potentially even three wavelengths, where the spectrum might actually contain minor absorption lines which we could not identify while looking at the whole spectrum earlier. Assuming, these features (8.8065, 8.8125 and 8.8170 [ln(λ)]) are indeed caused by physical absorption lines, we recalculate σ within the blue and the purple region exclusively and find even less noisy data with $\sigma_{blue} = 0.0039$ and $\sigma_{purple} = 0.0047$.
Following the former assumption, we can conclude that the standard deviation of our normalized data is less than 0.005.

In order to get an independent measurement of our initial data quality we now calculate the photon noise which should be the fundamental physical limit for our data normalization. Photon noise is a basic limit for the prediction of statistical values of *Poisson*-based emission processes. As for all *Poisson* distributions, we can estimate its standard deviation with $\sigma_{Photon} = \sqrt{N}$ while N in our case expresses the count of photons at a given wavelength.

To estimate the photon count, we also have to consider the detectors gain factor, which indicates the conversion efficiency from an electron, to the according analog digital unit (ADU). The ADU is commonly the actual unit of uncalibrated flux and needs to be scaled with a reference flux source in order to calculate flux calibrated data. In our case, the *LRS2* detector has an average gain of $g_{LRS2} = 0.84 \frac{e^-}{ADU}$. Consequently we can calculate the basic standard deviation as:

$$\sigma_{Photon} = \sqrt{g_{LRS2} \cdot ADU_{count}} \tag{6.2.0.1}$$

We now have an estimate for the fundamental noise within our unprocessed data, which we need to scale accordingly, as we like to verify our normalization result. Hence we find the normalized version photon noise estimation:

$$\sigma_{Photon} = \frac{\sqrt{g_{LRS2} \cdot ADU_{count}}}{g_{LRS2} \cdot scale} = \frac{1}{\sqrt{g_{LRS2} \cdot ADU_{count}}} \tag{6.2.0.2}$$

In our case, the scale factor reflects as well the mean local data value, so formula (6.2.0.2) can be simplified as shown in its last section. We find a basic photon noise level of $\sigma_{Photon} = 0.0026$.

When we now have again a closer look to the whole normalized spectrum from figure 6.3, we can see a trend within its noise. Independent from the absorption lines we find ever larger noise fluctuations towards shorter wavelengths. This is another systematic effect which we can conclude from formula (6.2.0.2). We find here the residue from the significantly lower flux level in this wavelength regimes, as it can be seen in figure 6.2, which here translates to larger statistical fluctuations.

This means that our flux normalization adds a measurable, but reasonable and minor statistic effect, by slightly increasing the noise. However, all non-linear transformations reduce the initial information content. Hence, we conclude that our flux normalization is valid, as the σ is still of the same order of the photon noise.

Concluding section 6, we now have proper flux-normalized spectra for both our instruments and can begin to measure the actual radial velocities in section 7.

Chapter 7

Radial velocity measurement

In this chapter we show the analysis of all gathered spectroscopic data and perform a radial velocity study of our targets. We start with brief step-by-step instructions on how we measured our targets apparent velocity $v_{app.}$, fold the results to the targets period and finally fit the periodic radial velocity profiles.

To do so, we first review our spectroscopic composition as shown in figure 7.1, in order to differentiate between features related to the target itself or to the observation process e.g. interstellar absorptions, cirrus or Moon contamination.

Spectrum composition

- Continuum:
  The continuum is the spectrum's substructure and approximately follows *Planck's law of black-body radiation*. As discussed in subsection 1.5.3, the continuum shape is mostly depended on the targets temperature, while the overall flux scales with the bolometric luminosity. But, as discussed above, the plotted, measured spectrum in figure 6.1 is dominated by the instruments throughput, so we need additional spectral flux standards in order to calibrate the absolute flux level. Although this would be possible, we rather use our photometric analysis to study the superposed spectrum. In figure 7.1 the normalized continuum is indicated as the dashed, magenta-colored horizontal marker.

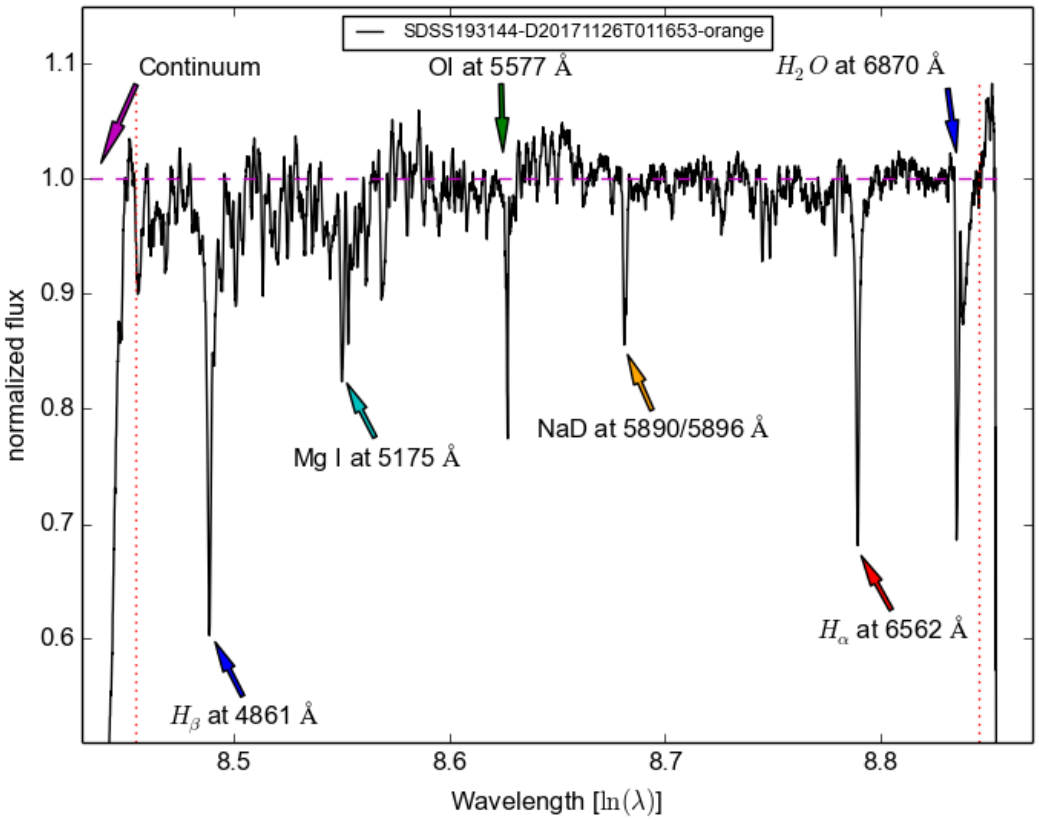

Figure 7.1: Reduced *LRS2* spectrum, showing target SDSS193144. The upper markers show the normalized continuum flux, a subtraction residuum of the telluric Oxygen sky emission OI at 5577 Å and the atmospheric water vapor absorption band from 6870 Å. The red, vertical markers indicate the limits of the normalization. In the lower section of the spectrum we find the two *Balmer*-absorptions H_α and H_β as typical for WDs.

- Stellar absorptions:
  With the exception of neutron stars and WD cores, all stellar objects are mostly composed of primordial hydrogen and helium. Based on the star's population[26], heavier elements become ever more abundant and tend to play a role in the stellar spectra. We can approximate, the more massive a star, the more heavy elements are shielded by outer shells, composed of hydrogen and helium which dominate such spectra.

[26]Stars are categorized based on their metal abundance into either population I, II or III, while population III stars formed earliest in the universe and hence show least metallicity.

- Interstellar absorptions:
  Another source of contamination is the interstellar material along the integral line of sight between the target and the observatory. Such features like for example the NaD doublet as indicated in figure 7.1, do not origin from a WDs atmosphere but are superposed on its spectrum while observation along the line of sight. We can ignore the affected bands, as they do not interfere with the *Balmer*-lines.

- Telluric absorptions:
  Like all ground based observations, our spectra of course suffer from telluric absorption lines. Within figure 7.1 we can see the known atmospheric water vapor absorption band starting at 6870 Å indicated by the blue marker. Just like the interstellar lines, we can ignore the affected wavelengths.

- Sky emissions:
  In addition to the several sources of absorption lines, all ground based observations additionally record so called sky emission lines. The most dominant oxygen line at 5577 Å is already discussed in subsection 5.2.2 and we utilized it as further independent calibration anchor. There are additional emissions, which originate from their according elements and molecules within Earth's atmosphere. Their positions are well-known and furthermore not affected by any spectral shifts. Additionally the data reduction usually identifies and corrects them by sky subtraction. Still minor non-physical residues might be left, hence we can ignore those wavelengths.

All of these sources or effects shown above, such as target-, interstellar- and atmospheric-absorptions or continuum- and sky-emissions all superpose each other and finally form the spectrum as we observe it. Understanding this structure and the inherent dependencies as well the features origin is crucial to identify the critical target absorption lines which carry the radial velocity information.

In addition to the components discussed above, the direct observational conditions as reported in section 4 impact the measurements in a more general fashion.
While it is obvious that on the one hand occasional clouds may block almost all starlight if they intersect the line of sight and additionally re-emit atmospheric straylight in the visible regime, the effect of thin, high-layer cirrus on the other hand is less drastic, but much harder to quantify and surely imprinted on the spectrum.

This uncertainty makes it problematic to deal with measurements which originate of nights with partly mediocre conditions as reported in section 4. It remains to be seen how conclusive the measurements of both of our instruments *ES2* and *LRS2* are.

In the end, the radial velocity analysis of the spectra is slightly different for both of our instruments, as well as for the two independent *LRS2*-channels *LRS2-UV* and *LRS2-Orange*. Consequently, the following list describes the individual steps of our radial velocity analyses as generically applied in this thesis. The instrument specific results are presented in the following subsections 7.1 and 7.2.

Radial velocity analysis in a nutshell:

1. Calculation of spectral shifting effects
2. Selection of correlation section
3. Cross-correlation of measured absorption line shifts
4. Folding measurements for target periodicity
5. analysis of the resulting radial velocity data

1. Calculation of spectral shifting effects:
   In a first step, we have to remember all the spectral shifting effects, which we discussed in chapter 5. Especially in section 2.6 we already identified the relevant dynamic effect of Earth's orbit. Here we now have to calculate the according dynamic spectral shifts as caused by Earth's orbit at the time of observation.

   Once the spectral shift is calculated we shift our spectral data accordingly. As discussed, we then still have a remaining static velocity offset, which is a composition of the relative target motion (see section 2.3) and the gravitational redshift (see section 2.5). As already concluded, these effects are for our observations time invariant and can thus be ignored.

2. Selection of correlation section:
   Once all the data are normalized and spectral shifts are accounted for, we cut the spectral regions which we like to cross-correlate in a 2nd step. Usually, one tries to cross-correlate the full spectra. Nevertheless, it is reasonable to exclude, cut or blank some parts of the spectra as they are for example corrupted by atmospheric absorptions such as the following examples:

   - Water vapor band at around 6870 Å: This band is dominated by atmospheric water absorption and hence the spectral features of this section must not be correlated all together with the remaining spectra as its terrestrial origin causes this band to host a neutral radial velocity. Therefore the spectra are cutoff prior to this band, which is marked in figure 7.1

   - Remanent sky line features: Within figure 7.1, we can also see a sharp artificial absorption which is located around the known O I sky emission line. During the data reduction, the pipeline removes the sky emissions as it is described in section 5.3.3. Due to the very high relative flux, the algorithm can not really distinguish between sky line and target. Hence, the over estimation of such strong sky lines occasionally lead to an unphysical flux subtracted from the target spectra, which is also hinted by the unnatural FWHM. Therefore, these sections are automatically set to exactly 1.00 nominal flux, which acts as the mathematical neutral element for the cross-correlation function.[27]

   - Reduction based cut offs: Another reason for exclusion of spectral regions are instrument and calibration specific issues of the data reduction. In our case we discussed in section 5.3.6 and especially figure 5.16, that the λ-calibration is on a very precise scale not homogeneous, which may cause non linear variations within our rv-analyses. Within the following analyses we will perform several different cross-correlation setups, from which one will investigate the difference between excluding such sections and keeping them active.

[27] Usually the mathematical neutral element for cross correlation is 0, but as we normalize our continuum to 1.00, we account for that, by subtracting flux 1.00 from the spectra within our algorithm.

Once the remaining spectral regions are extracted and masked, these data form tuples $\boldsymbol{f}(\lambda, \Phi)$ of length k, containing the relative flux Φ emitted at a given wavelength λ which might be handled in units of $\lambda[\text{Å}]$ or $ln\left(\frac{\lambda[\text{Å}]}{[1\text{Å}]}\right)$.

3. Cross-correlation of measured absorption line shifts:
As we find several absorption lines within a single spectrum, we calculate the cross-correlation between individual lines in order to enhance our stability and resolution. Generally the discrete cross-correlation $(\boldsymbol{a} \star \boldsymbol{b})[n]$ of the 1-tupel $\boldsymbol{a}$ and $\boldsymbol{b}$ is calculated as follows:

$$(\boldsymbol{a} \star \boldsymbol{b})[n] \equiv \sum_{m=-\infty}^{+\infty} \boldsymbol{a}^*[m] \cdot \boldsymbol{b}[m+n] \tag{7.0.0.1}$$

As mentioned above, the tupel length is limited to k components. Furthermore, we know the linear spacing in the wavelength dimension and therefore only need to cross-correlate the 1 dimensional subset $\boldsymbol{a}[\lambda] \Subset \boldsymbol{f_1}(\lambda, \Phi)$ of the reference spectrum and $\boldsymbol{b}[\lambda] \Subset \boldsymbol{f_2}(\lambda, \Phi)$ of the spectrum which we like to measure.

In addition, $\boldsymbol{f}$ is real, so the conjugation of $\boldsymbol{a}^*[\lambda]$ equals simply $\boldsymbol{a}[\lambda]$ and so the general equation (7.0.0.1) collapses to the following one:

$$(\boldsymbol{a} \star \boldsymbol{b})[\lambda] \equiv \sum_{m=-k}^{+k} \boldsymbol{a}[m] \cdot \boldsymbol{b}[m+\lambda] \tag{7.0.0.2}$$

As the cross-correlation is a common problem, we rely on well established and tested code such as *numpy.correlate (1.15)* which is included in the open-source *Python* library *numpy* [49]. However, it is important to realize that the correlation is calculated with a so called zero-padding. This means, that the second vector is padded with entries of value zero which hence suppresses the cross-correlation partner for this individual entry. To compensate for this behavior, we simply have to offset our normalized spectra to 0 such that the zero-padding adds neutral components to the anyhow small entries at the borders. Consequently the central spectral line dominates the cross-correlation, which now provides a further tupel c of length $2k-1$. The maximum within $\boldsymbol{c}$ can now be interpreted as the most likely spectral shift, while one can further define the statistical significance $\sigma_{\boldsymbol{c}}$ within $\boldsymbol{c}$.

Finally, we can conclude on a specific relative, apparent velocity $v_{app.}$ for each observation. As *ES2* and *LRS2* provide a different set of measurable lines, the statistical conclusion process is described in the according subsections 7.1 and 7.2. As discussed in section 2, the measured $v_{app.}$ is composed of a static and a dynamical part which we can separate by analyzing its time variation in the next step.

4. Folding measurements for target periodicity:
   The apparent velocity $v_{app.}$ measurements spans in time over many of the targets orbital periods. In order to find the proper periodic behavior we fold all this data points into a single orbit, using the known binary period, which is given by the photometric survey as discussed in subsection 1.2.

   The folding of individual time stamps hence follows the simple equation (7.0.0.3), which corrects for the time offset t_0 prior to the scaling with the target period. In order to calculate the proper t_0 [JD], we used the standard python library *jdcal* [25].[28] Finally the modulus provides us the actual $t^*_{obs.} \in [0, 1]$ of the observation which is expressed in unites of phase:

$$t^*_{obs.}(p, t_0) = \lfloor \frac{t_{exp} + 0.5 \cdot t_{shutter} - t_0}{p} \rfloor \Longrightarrow \lfloor \frac{t_{obs.} - t_0}{p} \rfloor \qquad (7.0.0.3)$$

5. Analysis of the resulting radial velocity data:
   Once the final radial velocity data is folded onto the binary period, the data can be analyzed using geometrical models in combination with the basic *Keplerian* laws. We follow the mathematical descriptions as presented by Hilditch et al. (2001) [39]. Further details on the analysis follow in subsection 7.3 as they are applied to the actual data.

The first three steps are handled separately for *ES2* and *LRS2* within the according two subsections 7.1 and 7.2 and show the intermediate results of the measured apparent velocities $v_{app.}$.

[28] As usual, t_0 is given in Julian Dates (JD) which counts the days passed, after the 1st of January, 4713 BC. In defining an absolute date and henceforward counting days, one gets rid of special cases such as leap years and others.

Finally the subsection 7.3 combines the information from both spectrographs *ES2* and *LRS2*. Folded radial velocity curves are hence generated as described in step 4 - *Fold measurements for target periodicity.*

Concluding the resulting velocity curves are furthermore investigated as discussed in step 5 - *Analysis of the resulting radial velocity data.*

7.1 *ES2* radial velocity measurement

Before we start with the radial velocity analysis we first screen our reduced data for quality and identified some major issues. Therefore we include here the following insertion *ES2 stability problems and faulty data*, providing a glimpse into these *ES2* specific problems. Ultimately, this forced us to switch the instrument as it is explained below.

Afterwards, we follow our method *Radial velocity analysis in a nutshell* from section 7, by calculating the dynamical spectral shifting effect of Earth's orbital motion for each individual observation. Next, we cut the available *Balmer*-lines H_β and H_γ which are visible in each spectrum for the *ES2*-spectrograph in the given setup.

Finally, we cross-correlate the *Balmer*-lines and conclude on a representative shift for the individual spectrum. Here, we now subtract the individual spectral shift as caused by the Earths orbital motion and calculated in *1. Spectral shift, caused by Earth's orbital motion.*

***ES2* stability problems and faulty data:** As mentioned in section 4.1, we faced several technical problems using *ES2*, which ultimately lead to the use of *LRS2*. The intrinsic stability of *ES2* simply never met the expected wavelength stability. Furthermore, the detector has several known faulty sections which occasionally aligned exactly with one of the *Balmer*-lines as shown in the following fits-file 7.2.
All affected spectra are removed from the data set so we only proceed with clean observations as listed in the following table 7.1.

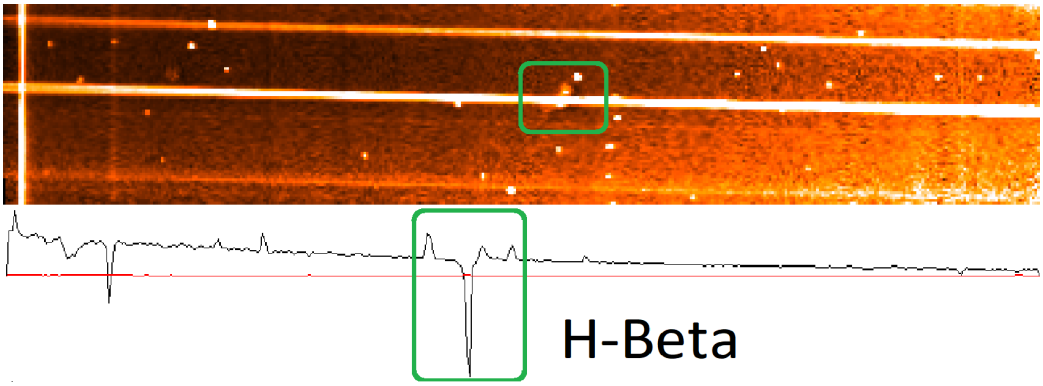

Figure 7.2: The green box marks the known faulty section of the detector. Due to lacking instrument stability, the observer is unable of fine-positioning the target within the slit, as he only sees the result after an hour long exposure. Hence, these observations are not usable, if the faulty section superposes a relevant *Balmer*-line.

In addition to these problems, we must consider the observation conditions, which where often mediocre. Therefore, the run in June 2016 was the only one which provided good enough conditions and by chance was the only dark time run, which we got assigned. All others where gray time observations with the Moon above the horizon and partly illuminated.

Furthermore, the longterm stability of *ES2* is not good enough to compare observations from various runs with each other, which was another reason why we decided to switch to *LRS2* as it became commissioned. In the end, we concluded to cross-correlate only these data sets to each other as listed in table 4.3.

7.1.1 Spectral shift, caused by Earth's orbital motion

Given the availability of proven codes, we chose the algorithm of Wright and Eastman (2014) [93], which claims increased precision of $\pm$ 1 cm/s. In the end, we aim to measure shifts significantly larger then $\pm$ 5 km/s, hence we truncated at $\pm$ 100 m/s. The following table 7.1 shows the resulting truncated orbital velocity shifts.

ES2 observations - Earth Orbit correction
Target: SDSS193144

Exposure ID (Date & Time)	Ecliptic		Shift
	Latitude	Longitude	Km/s
Target :	SDSS193144	$DEC \approx 36.3°$	
20160606T082000	0.967	+0.756	+21.8
20160606T092500	0.967	+0.755	+21.8
20160607T053000	0.967	+0.746	+21.5
20160608T065000	0.967	+0.734	+21.2
20160608T075000	0.967	+0.734	+21.2
20160608T085000	0.967	+0.734	+21.2
20160611T082000	0.967	+0.699	+20.1

Table 7.1: Earth Orbit correction for *ES2* exposures of SDSS193144. The static effect of the ecliptic longitude is calculated according to section 2.2 using: $\cos(DEC - \Delta\phi)$, with $\Delta\phi = 23.4°$.

As introduced in section 2.2, the correction of the Earth's orbital motion can be approximated using simple geometric angles in elliptical coordinates and is called heliocentric correction. However, in reality many additional effects like, Earth's nutation and precision, as well as general relativity effects like the *Shapiro delay*[29] affect the heliocentric correction.

Nevertheless, the amplitudes of all those effects are orders of magnitudes smaller as the Earth orbit. Hence we could follow the approximation given in section 2.2 equation 2.2.0.4; But as radial velocity analyses are nowadays primarily used to study exoplanets of ever smaller mass and semi major axis, the methods for heliocentric corrections consequently increased in precision and availability.

[29] *Shapiro delay*: Light which passes a strong gravitational potential propagates along the geodesic which makes it to pass the potential well slower as the light, passing a minor fraction of the potential. This effect is a prediction of general relativity and is fundamental for lensing effects.

7.1.2 Selection of correlation section

In preparation of the following cross-correlation we need to cut the *Balmer*-lines in such a way, that each data subset is clearly dominated by the shift of the actual line and not by surrounding noise. The following table shows the applied cut values for *ES2*.

ES2 observations - *Balmer*-line regions

Cut	$H\gamma$ at 4340 Å	$H\beta$ at 4861 Å
▲	8.383 ($\approx$ 4372.1 Å)	8.500 ($\approx$ 4914.8 Å)
▼	8.372 ($\approx$ 4324.3 Å)	8.477 ($\approx$ 4803.0 Å)

Table 7.2: *Balmer*-line regions and according upper (▲) and lower (▼) cut values as applied in logarithmic scale [ln(λ)].

7.1.3 Cross correlation of individual $v_{app.}$

As can be seen in figure 7.3, the result of the individual cross-correlations deliver Gaussian like results, as expected. Hence, each cross-correlation not only delivers the optimal shift, but we can even fit the resulting cross-correlation curve and thereby probe the σ of each individual measurement.

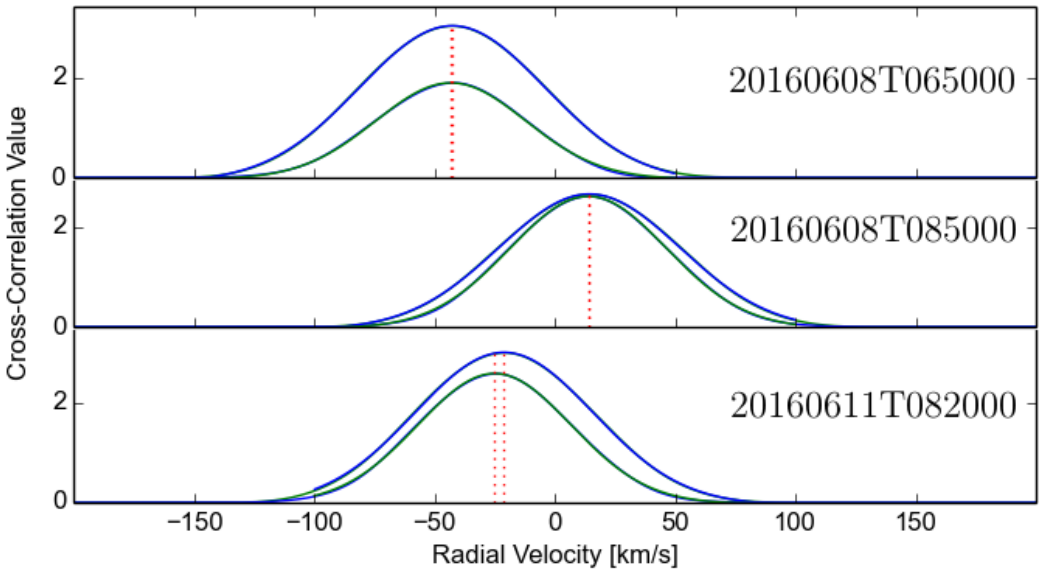

Figure 7.3: Cross-Correlation results for individual $H\beta$ and $H\gamma$ measurements of *ES2* spectra. Target: SDSS193144

In case of *ES2*, there are only two *Balmer*-lines within an exposure that can be measured. Hence, we conclude on the arithmetic mean as given by the two simultaneous measurements.

ES2 observations - Relative *Balmer*-line shifts
Targets: SDSS193144

Exposure ID (Date & Time)	$H\gamma$		$H\beta$		v	σ_v
	v	σ	v	σ	[km/s]	[km/s]
Target :	SDSS193144					
20160606T082000	0	0	0	0	0	0
20160606T092500	+84.2	78.9	+103.6	105.1	+93.9	92.0
20160607T053000	-239.8	85.2	-92.7	82.6	-166.3	83.9
20160608T065000	-42.0	30.6	-42.4	37.4	-42.2	34.0
20160608T075000	-149.9	88.4	-95.9	90.3	-122.9	178.7
20160608T085000	+14.4	32.1	+14.5	36.9	+14.5	34.5
20160611T082000	-24.2	31.5	-20.8	36.5	-22.8	34.0

Table 7.3: Measured *Balmer*-line cross-correlations for $H\beta$ and $H\gamma$ within all *ES2* exposures. The individual shifts are already given in km/s. The color of the exposure ID represents the observational conditions as categorized in section 4 in good (green), mediocre (yellow) or bad (red). The measured v are similarly marked to to their plausibility.

Inspecting the results from table 7.3, we can on the one hand spot three rather stable measurements with $\sigma \approx 34.0\ km/s$. This meets our expectations for the used instrument setup using the grism 22 with 600 groves/mm. Details on the setup can be found in appendix *ES2-spectrograph Observation run proposal*.
On the other hand, the remaining three measurements show significantly higher uncertainties:

1. 20160606T092500 ($\sigma = 92.0\ km/s$): In the case of the first measurement this maybe linked to the shorter exposure time of 30 min. vs. the nominal 60 min.

2. 20160607T053000 ($\sigma = 83.9\ km/s$): According to the observational logs this measurement had generally good conditions with the Moon below the horizon and clear sky. It is unclear, why the resulting radial velocity and the standard deviation vary that much within the spectra itself and in comparison to the other results.

3. 20160608T075000 ($\sigma = 178.7\ km/s$): The last result with bad stability is the second in a series of three exposures all taken consecutively. All faced acceptable Moon and sky conditions but minor clouds have been reported which may have especially affected this specific exposure.

In a last step, we now account for Earth's orbital motion around the Sun as previously explained in section 2.2.

Keeping the implausible data still highlighted using the former color coding, the resulting data are plotted in figure 7.4.

ES2 observations - Concluded radial velocity shifts
Targets: SDSS193144

Exposure ID (Date & Time)	$v_{Orbital}$ Km/s	v_{Balmer} Km/s	σ_{Balmer} Km/s	$v_{app.}$ Km/s	$\sigma_{v_{app.}}$ Km/s
Target :	SDSS193144				
20160606T082000	+21.8	0	0	-21.8	0.0
20160606T092500	+21.8	+93.9	92.0	+72.1	92.0
20160607T053000	+21.5	-166.3	83.9	-187.8	83.9
20160608T065000	+21.2	-42.2	34.0	-63.4	34.0
20160608T075000	+21.2	-122.9	178.7	-144.1	178.7
20160608T085000	+21.2	+14.5	34.5	-6.7	34.5
20160611T082000	+20.1	-22.8	34.0	-42.9	34.0

Table 7.4: The final radial velocity shifts are calculated as follows: $v_{app.} = v_{Balmer} - v_{Orbital}$. The first column is color coded according to the formerly agreed data plausibility.

Now, that we assigned each *ES2* spectrum an apparent radial velocity shift. In the following subsection, we repeat the steps 1 until 3 from our *Radial velocity analysis in a nutshell* method as explained above in section 7.

7.2 *LRS2* radial velocity measurement

In order to gain representative radial velocities for each *LRS2*-observations, we again follow the procedure from section 7.

7.2.1 Spectral shift, caused by Earth's orbital motion

The heliocentric correction for *LRS2* follows again Wright and Eastman (2014) [93], as described in 7.1. Table 7.5 shows the resulting truncated radial velocity shifts.

LRS2 observations - Earth Orbit correction
Targets: SDSS070428, SDSS070433 and SDSS193144

Exposure ID (Date & Time)	Ecliptic Latitude	Ecliptic Longitude	Shift Km/s
Target :	SDSS070428	$DEC \approx 13.2°$	
20171124T113502	0.985	+0.688	+20.2
20171125T113436	0.985	+0.676	+19.8
20171126T065819	0.985	+0.665	+19.5
Target :	SDSS070433	$DEC \approx 13.4°$	
20171115T075444	0.985	+0.796	+23.4
20171116T073806	0.985	+0.785	+23.0
20180411T023105	0.985	-0.996	-29.2
20180412T024445	0.985	-0.994	-29.2
20180415T023212	0.985	-0.987	-29.0
20180416T023249	0.985	-0.984	-28.9
Target :	SDSS193144	$DEC \approx 36.3°$	
20171120T014159	0.967	-0.922	-26.6
20171126T011653	0.967	-0.876	-25.2
20180408T102507	0.967	+0.958	+27.6
20180409T103500	0.967	+0.963	+27.7
20180411T100506	0.967	+0.972	+28.0
20180411T101117	0.967	+0.972	+28.0

Table 7.5: Earth Orbit correction for all *LRS2* exposures. The static effect of the ecliptic longitude is calculated according to section 2.2 using: $\cos(DEC - \Delta\phi)$, with $\Delta\phi = 23.4°$.

7.2.2 Selection of correlation section

In preparation of the cross-correlation we need to extract the relevant data interval from the gathered spectra. Given the analysis which we performed on the λ calibration in section 5.3.6, we have to review two cases:

1. Full spectrum correlation:
   For the basic analysis, containing the full remaining spectrum after the data reduction, we cross-correlate for the UV channel the interval $\lambda\left[\ln\left(\text{Å}\right)\right] \in [8.21,\ 8.43]$[30] and $\lambda\left[\ln\left(\text{Å}\right)\right] \in [8.46,\ 8.82]$[31] for the orange channel. Furthermore, we blanked the region around the O I emission line at 5577 Å, as it occasionally showed residuals from the sky subtraction.

2. Stable spectrum correlation:
   As discusses in section 5.3.6, we are unsure about the stability of the λ calibration from 6438.2 Å upwards. Therefore we prepare a second set of spectra which exclude the doubtful region.

As it is unclear how much of an effect the difference between the wavelength solutions of the orange spectra will have, we perform the cross-correlation for both setups individually.
In addition to these two cases, we also test to cross-correlate the data against some independent sample stellar spectra. We use the recent MILES catalog as published by Röck et. al in 2016 [73], to select the best matching spectral type within the catalog of 985 individually observed targets.

As we will discuss later, we use the data from the *Gaia* mission [30] to narrow down the $T_{eff.}$ for each of our targets and find good agreement with our own observation as presented in the following chapter 8. For the hereby selected spectra we performed a residual analysis to conclude on the best matching template spectrum for each individual target. We select the two best fitting templates, from which we plotted from bottom to top the residuum function in figure 7.4 and underline the best matching ones:

- SDSS193144: 1. 6000K-s0266, 2. 6083K-s0438
- SDSS070433: 3. 6298K-s0363, 4. 6493K-s0341
- SDSS070428: 5. 6556K-s0341, 6. 6799K-s0504

[30] UV channel: $\lambda\left[\ln\left(\text{Å}\right)\right] \in [8.21,\ 8.43] = [3677.5\ \text{Å},\ 4582.5\ \text{Å}]$
[31] Orange channel: $\lambda\left[\ln\left(\text{Å}\right)\right] \in [8.46,\ 8.82] = [4722.1\ \text{Å},\ 6768.3\ \text{Å}]$

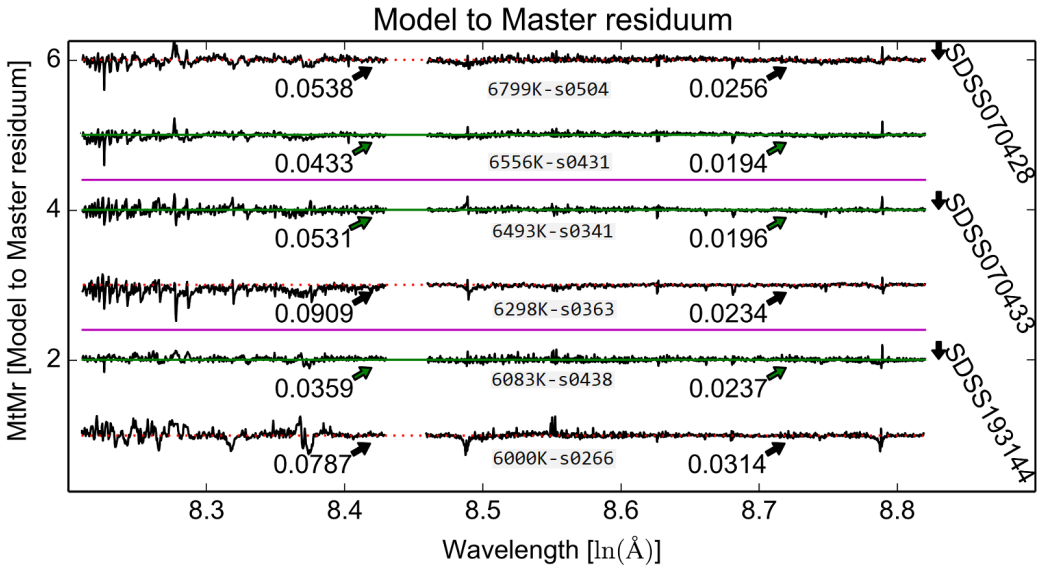

Figure 7.4: Master to model residuum for our targets. We calculate the residua between the model originating from Röck et. al [73] and the stacked master spectra which we create for each individual target. The model $T_{eff.}$ as well as the catalog ID are listed in gray.

Within figure 7.4, we highlight in green the best fitting model which we underline above and find the following matches:

LRS2 observations - Best fitting model parameter

RA $[hr:min:sec]$	DEC $[hr:min:sec]$	Extinction $[E_{B-V}]$	Spectral Type	$T_{eff.}$ [K]	$log(g)$ [1]
SDSS070428 ≈ MILES s0431: HD134083					
15:07:18	+24:52:09.1	0	F5 V	6556	4.32
SDSS070433 ≈ MILES s0341: HD089449					
10:19:44.2	+19:28:15.2	0	F6 IV	6493	4.06
SDSS193144 ≈ MILES s0438: HD136202					
15:19:18.7	+01:45:55.5	0.03	F8 III-IV	6083	3.85

Table 7.6: Model parameter as published online by Röck et. al. 2018 [1]

Here we find first evidence that our target might actually not be WD-BD binaries as we intended to proof. We will investigate this fact in detail within our conclusion in section 9 and for now continue to perform our radial velocity measurement in the following sub-section 7.2.3.

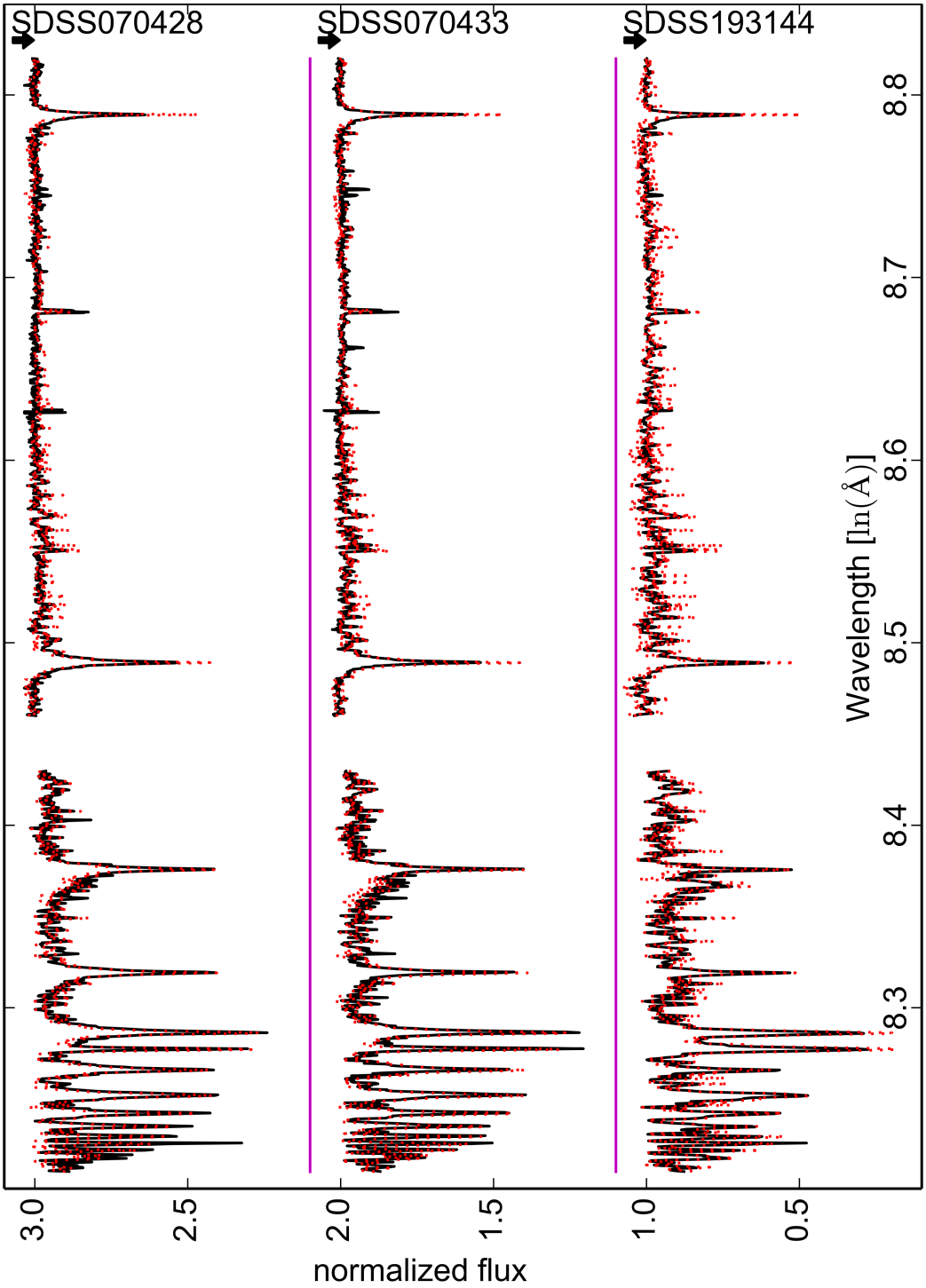

Figure 7.5: Our *LRS2* target spectra, plotted in black, are overplot in red by the best fitting MILES catalog target as published by Röck et. al. [73]

7.2.3 Cross correlation of individual $v_{app.}$

In contrast to the *ES2* analysis, *LRS2* provides enough signal to noise and a better spectral stability so we cross-correlate full *LRS2*-B-UV respectively *LRS2*-B-Orange spectra with each other. Similar to the *ES2* analysis, we reference all our cross-correlations to the first spectra of each target. As justified above in sub-section 7.2.2, we cross-correlate the data in the following four configurations and compare the according results.

- **Full:** Correlation of the full uv and orange channel
- **Stable:** Correlation of the full uv and most stable orange region
- **Model1:** Correlation with the best fitting model from MILES [1]
- **Model2:** Correlation with the second best model from MILES [1]

All the results are listed within table 7.7 and we find some relevant facts:

1. Averaging $\Delta v_{app.}$ for each method provides a test for systematic shifts between our UV and OR chan. analysis and the following results:
   Full: $-0.1\ \frac{km}{s}$ | Stable: $3.4\ \frac{km}{s}$ | Model1: $0.2\ \frac{km}{s}$ | Model2: $-2.0\ \frac{km}{s}$
   This small fluctuation is significantly below our radial velocity resolution, which we derivate in sub-section 5.3.8 and hence is a sign that our analysis strays on a small scale around 0.0 km/s. Therefore our algorithm shows no signs of systematic errors.

2. But when we investigate the two SDSS193144 observations which were both taken on the same night 180411, we find that all methods provide the same UV-results within the margin of $\Delta v_{app.} = 0.3\ km/s$, while the OR results vary up to 8.8 km/s for model2 and about 4.0 km/s for the other methods, which hints 10 times bigger intrinsic variations.

3. For each of the four models, the typical fluctuation within the UV measurements end up around 13 km/s, while the according orange measurements stray by at least 20 km/s. As a real radial velocity signal would affect both channels simultaneously, this result also points towards a worse performance of the orange channel. Hence, we find our expectation from point 1 confirmed within all our cross-correlations.

The facts two and three are indications, that the UV channel, despite the less S/N, might still perform better than the orange channel. The reason for this might be the larger amount of available calibration lines, which aid the intrinsic λ calibration and hence radial velocity analysis.
Thus we proceed with the UV channel results from the stable option as *LRS2* $v_{app.}$, since they provide the best systematical stability.

LRS2 observations - Cross-correlation results

ID	Full:			Stable:			Model1:			Model2:		
	v_{UV} $[\frac{km}{s}]$	v_{OR} $[\frac{km}{s}]$	$\Delta v_{app.}$ $[\frac{km}{s}]$	v_{UV} $[\frac{km}{s}]$	v_{OR} $[\frac{km}{s}]$	$\Delta v_{app.}$ $[\frac{km}{s}]$	v_{UV} $[\frac{km}{s}]$	v_{OR} $[\frac{km}{s}]$	$\Delta v_{app.}$ $[\frac{km}{s}]$	v_{UV} $[\frac{km}{s}]$	v_{OR} $[\frac{km}{s}]$	$\Delta v_{app.}$ $[\frac{km}{s}]$
SDSS070428:							S0431:			S0504:		
171124	0	0	0	0	0	0	0	0	0	0	0	0
171125	-18.5	-67.9	+49.4	-18.5	-61.6	+43.1	-20.0	-59.8	+39.8	-19.4	-56.5	+37.1
171126	-8.3	-31.7	+23.4	-8.0	-20.6	+12.6	-10.4	-21.2	+10.8	-10.1	-19.4	+9.3
SDSS070433:							S0341:			S0363:		
171115	0	0	0	0	0	0	0	0	0	0	0	0
171116	+16.4	+15.4	+1.0	+15.8	+8.5	+7.3	+17.6	+12.4	+5.2	+17.3	+14.2	+3.1
180411	-13.5	-34.2	+20.7	-13.8	-49.8	+36.0	-14.4	-47.2	+32.8	-13.2	-34.2	+21.0
180412	-34.8	-8.9	-25.9	-35.1	-17.0	-18.1	-34.5	-16.4	-18.1	-34.5	-11.6	-22.9
180415	+10.2	-1.8	+12.0	+10.2	-15.9	+26.1	+9.3	-19.8	29.1	+10.5	-10.5	+21.0
180416	+19.5	-11.1	+30.6	+19.5	-26.4	+45.9	+18.6	-27.6	46.2	+19.5	-16.2	+35.7
SDSS193144:							S0438:			S0266:		
171120	0	0	0	0	0	0	0	0	0	0	0	0
171126	-20.0	+21.7	-41.7	-20.0	+18.4	-38.4	-19.3	+30.1	-49.4	-18.1	+29.2	-47.3
180408	-14.0	+41.6	-55.6	-14.0	+46.7	-60.7	-12.4	+53.9	-66.3	-11.8	+52.1	-63.9
180409	-19.4	-22.4	+3.0	-19.4	-23.3	+3.9	-18.4	-15.5	-2.9	-16.9	-18.2	+1.3
180411	-19.1	-11.8	-7.3	-19.1	-12.4	-6.7	-18.4	-4.0	-14.4	-17.8	-4.3	-13.5
180411	-18.8	-7.7	-11.1	-18.8	-8.6	-10.2	-18.7	-8.6	-10.1	-17.8	-13.1	-4.7

Table 7.7: Cross-correlation results for the four configurations: full, stable, model1 and model2.

7.3 Common data analysis

The following subsection combines the radial velocity data, as they have been agreed on in the former subsections 7.1 and 7.2.

7.3.1 Fold observation results

As our data origins from a time period of several years and many hundreds respectively thousands of binary orbits, we fold our time axis to the binary periodicity, as it is commonly done for all radial velocity studies.

In order to get the proper phase information, we first offset the date and time t_{exp} as captured in the fits header, by half the exposure time $t_{shutter}$. This correction is already applied in the converted observation times given in JD in the following tables 7.9 and 7.10.

Afterwards we can calculate the target period using equation (7.0.0.3), as derived above. The therefore required informations on the target period and time offset are given in table 7.8.

Target - periodes and time offset

Target ID	p [days]	t_0 [JD]
SDSS070428	0.3713	2454526.8446
SDSS070433	4.6598	2454527.5977
SDSS193144	0.2282	2454317.8765

Table 7.8: Periods p and time offset t_0 as measured from the initial target selection light curves from section 1.2.

Nevertheless, for the better visual comparison and the sake of completeness we add them within the target headers of the tables 7.9 and 7.10. So we can now fold the *ES2* data, as given by table 7.9.

Given the general precision we now truncate all results at 4 digit precision, which correlates to about 1 minute resolution in units of our longest period target SDSS070433. For the other two targets, the precision, hence, is about 1s, which is anyway more precise than our observations themselves.

ES2 observations - Folded observation time
Targets: SDSS193144

Exposure ID (Date & Time)	$v_{app.}$ [Km/s]	$\sigma_{v_{app.}}$ [Km/s]	Obs. Time JD	$t^*_{obs.}$ phase
Target :	SDSS070428		t_0: 2454526.8446	p
20160606T082000	-21.8	0.0	2457545.8681	0.3717
20160606T092500	+72.1	92.0	2457545.9028	0.5239
20160607T053000	-187.8	83.9	2457546.7500	0.2368
20160608T065000	-63.4	34.0	2457547.8056	0.8627
20160608T075000	-144.1	178.7	2457547.8472	0.0452
20160608T085000	-6.7	34.5	2457547.8896	0.2309
20160611T082000	-42.9	34.0	2457550.8688	0.2868

Table 7.9: *ES2* exposures, folded to the nominal target periodicity as given by the photometric observations.

Following, we fold the *LRS2* data, as given in table 7.10.

LRS2 observations - Folded observation time
Targets: SDSS070428, SDSS070433 and SDSS193144

Exposure ID (Date & Time)	$v_{app.}$ [Km/s]	$\sigma_{v_{app.}}$ [Km/s]	Obs. Time JD	$t^*_{obs.}$ phase
Target :	SDSS070428		t_0: 2454526.8446	p: 0.228
20171124T113502	-20.2	0.0	2458081.9879	0.6449
20171125T113436	-38.3	17.0	2458082.9876	0.3370
20171126T065819	-27.5	17.0	2458083.7957	0.5132
Target :	SDSS070433		t_0: 2454527.5977	p: 4.660
20171115T075444	-23.4	0.0	2458072.8349	0.8084
20171116T073806	-7.2	17.0	2458073.8233	0.0205
20180411T023105	+15.4	17.0	2458219.6101	0.3064
20180412T024445	-5.9	17.0	2458220.6196	0.5230
20180415T023212	+39.2	17.0	2458223.6109	0.1650
20180416T023249	+48.4	17.0	2458224.6113	0.3797
Target :	SDSS193144		t_0: 2454317.8765	p: 0.371
20171120T014159	+26.6	0.0	2458077.5743	0.5246
20171126T011653	+5.2	17.0	2458083.5569	0.7427
20180408T102507	-41.6	17.0	2458216.9376	0.2712
20180409T103500	-47.1	17.0	2458217.9451	0.6868
20180411T100506	-47.1	17.0	2458219.9237	0.3575
20180411T101117	-46.8	17.0	2458219.9280	0.3763

Table 7.10: *LRS2* exposures, folded to the nominal target periodicity as given by the photometric observations.

7.3.2 Analysis of the resulting radial velocity data

We start the analysis by plotting the previously gathered data. The following series of data plots all share the same configuration as they all span 120 % of a full target period as estimated from the *WFCAM Transit Survey*. Furthermore all vertical error bars are set accordingly to cross correlation results from subsection 7.1 and 7.2 respectively, while the horizontal error bars reflect the relative exposure time as shown above in table 7.10.
In addition, each plot will show exactly one data point which so far shows no vertical error bar at all. This does not mean that this measurement is perfect, it rather reflects the systematic error, which is in this case intrinsically zero for the reference measurement since it is used as absolute anchor for all other data. While this seems arbitrary, it is actually acceptable as we are not interested in the total static offset of the radial velocity, but just intend to probe its dynamical component as plotted.

SDSS070428: Beginning with the first target SDSS070428, we have to consider the worse data return, as we got only three observations for this target in total. Hence the plot 7.6 provides not much information at all.

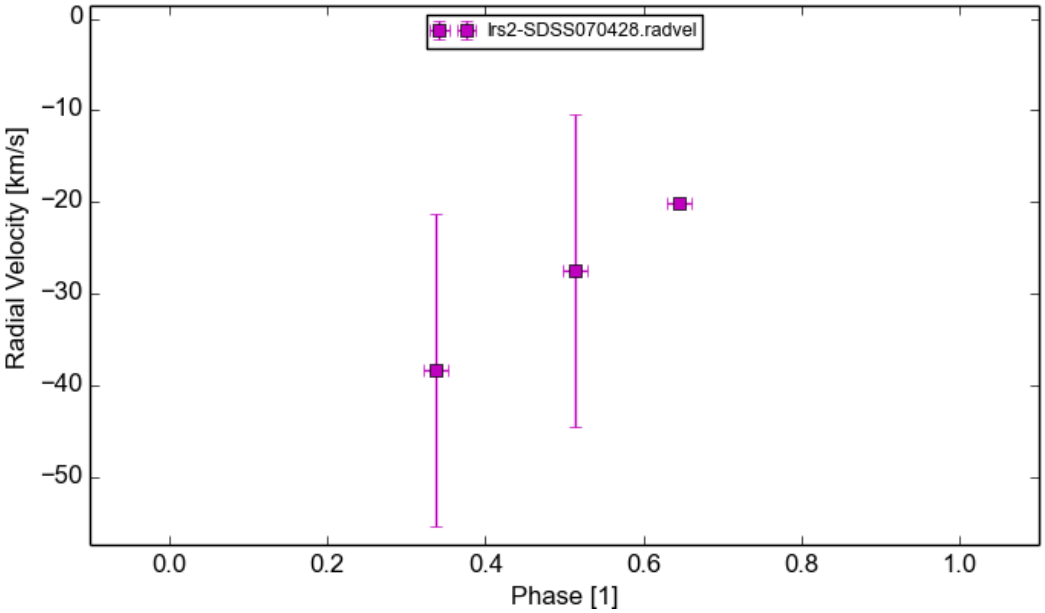

Figure 7.6: SDSS070428 - Radial velocity data as measured with *LRS2*. Folding period: $p = 0.3713\ d$

Accepting the amount of data we got provided with, further analysis is pointless. Hence, we move on to our second target.

SDSS070433: In contrast to SDSS070428, we gathered twice as much data for SDSS070433, due to prioritization.
For the initial *ES2* observations we were granted enough observation time, so we could observe both SDSS070433 and SDSS070428 equally, despite their close location. But in case of *LRS2*, we must prioritize one over the other, as we first of all only got little low priority *HET* observation time and secondly both targets move simultaneously through *HET*s special observational field of view. In doing so we could gather the data as it is shown below in figure 7.7.

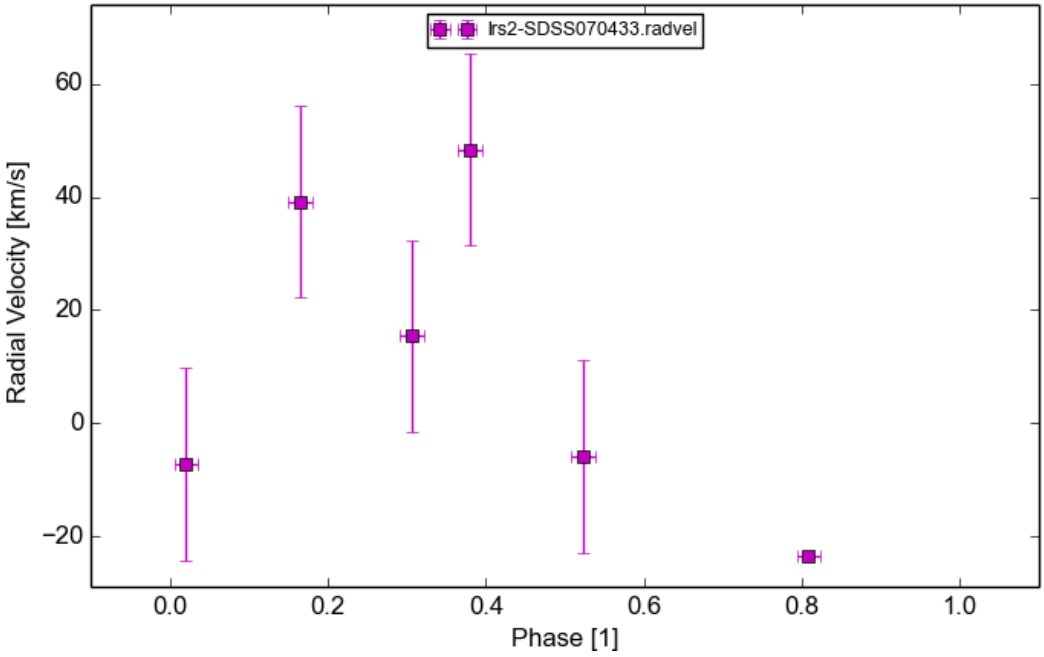

Figure 7.7: SDSS070433 - Radial velocity data as measured with *LRS2*. Folding period: $p = 4.6598\ d$

We prioritized SDSS070433 due to its light curve, which shows a clear transit instead of SDSS070428's periodic fluctuation. Hence, we decided to focus on SDSS070433, as the visible transit allows us to narrow down the range of the observational parameters. Details on this will follow in the later fit of the data.
Ignoring the third data point, we could potentially guess a sinusoidal like structure in the data, which would be in agreement with a transiting system of the given period. Nevertheless, considering all the given date, the system rather shows no clear rv signature or at least one at a significant faster periodicity.

SDSS193144: Unlike the former targets, SDSS193144 was the only one for which we gathered enough data within a single *ES2* observation run. Having a look at figure 7.8, we see no conclusive radial velocity pattern.

In addition to the few measurable *Balmer*-lines per exposure, the aged calibration lamp leads to large vertical error bars. Furthermore, the horizontal error bars are larger since a observation with *ES2* lasted one hour, which is a significant fraction of SDSS193144's total period.

For a clear separation between the better *LRS2* and the coarse *ES2* data, we assigned all *ES2* measurements with red diamonds instead of the purple squares which we exclusively use for *LRS2*.

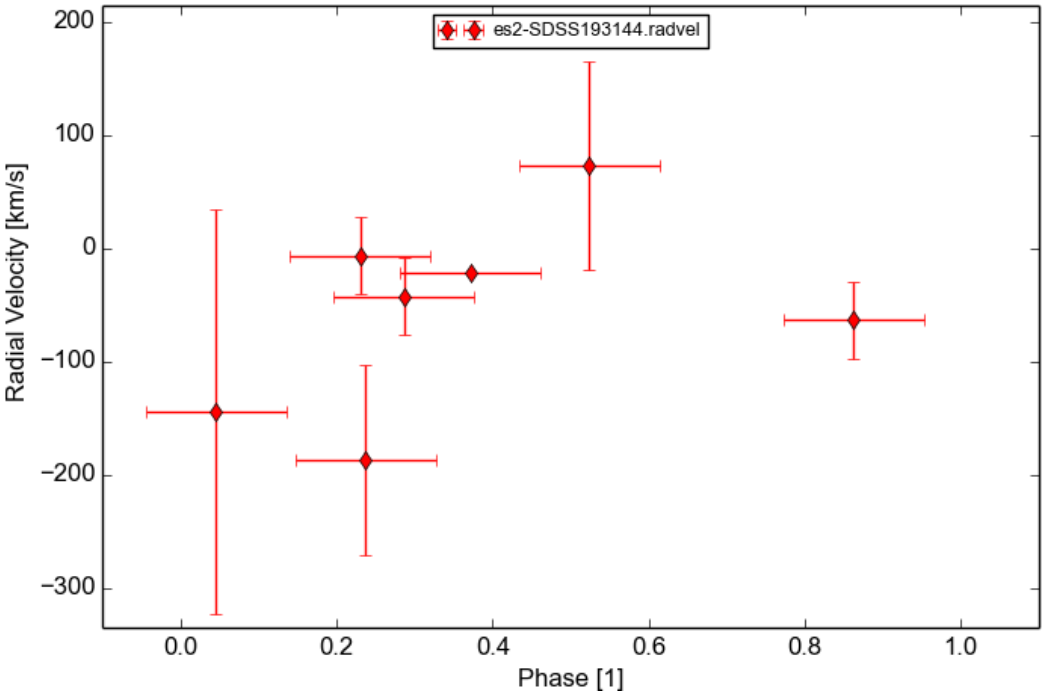

Figure 7.8: SDSS193144 - Radial velocity data as measured with *ES2*. Folding period: $p = 0.2282\ d$

It becomes clear, that we had to find an instrument to provide better long-therm stability and additional calibration lamps featuring more lines.

Consequently we switched to *LRS2*, which provides the following data set as it is shown in figure 7.9.

Comparing both results, we immediately recognize the reduced scatter velocity and improved resolution in phase precision as typically for *LRS2*. Still, SDSS193144 does not show an obvious structure as we would expect it.

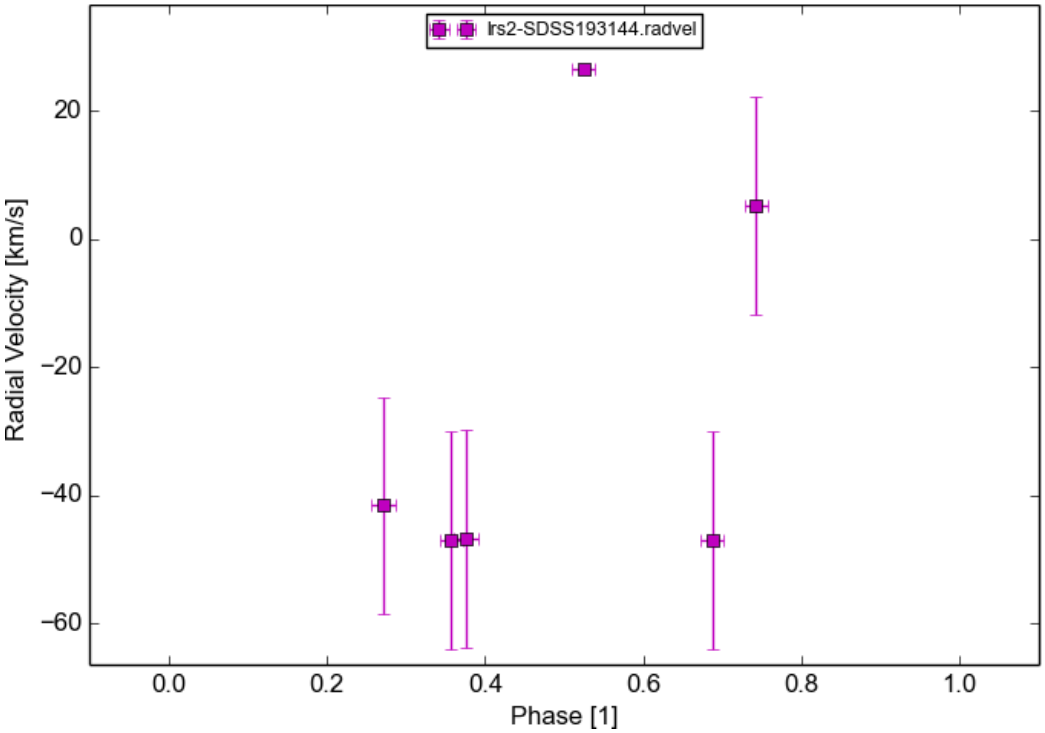

Figure 7.9: SDSS193144 - Radial velocity data as measured with *LRS2*. Folding period: $p = 0.2282\ d$

Therefore, we now relate the two data sets with each other. To do so, we first analyze the absolute data offset between both sets. As *LRS2*, is by far the more reliable instrument we re-calibrate the total offset of the *ES2* data.

Thus, we compare *ES2*'s primal measurement at $phase = 0.3717$ from table 7.9 with the two neighboring *LRS2* measurements at $phase = 0.3575$ and 0.3763 from table 7.10. By assuming, that this small fraction of the period can be approximated linearly we calculate the position of the *ES2* anchor to $phase = 0.3717$ and $v_{app.} \approx -46.9\ km/s$.

The resulting 25.1 km/s offset is hence handled as the actual velocity error and the uncertainty of all other *ES2* data points is accordingly quadratically enlarged due to the *Gaussian* propagation of uncertainty.

According to this procedure, we recalculated $v_{app.}$ for all *ES2* exposures and re-scaled their $\sigma_{v_{app.}}$ quadratically. The resulting data set can be seen in the following table 7.11, while the combined plot is shown in figure 7.10.

Rescaled *ES2* observations - Folded observation time
Targets: SDSS193144

Exposure ID (Date & Time)	$v_{app.}$ Km/s	$\sigma_{v_{app.}}$ Km/s	Obs. Time JD	$t^*_{obs.}$ phase
Target :	SDSS070428		*ES2*	
20160606T082000	-46.9	25.1	2457545.8681	0.3717
20160606T092500	+47.0	95.4	2457545.9028	0.5239
20160607T053000	-212.9	87.6	2457546.7500	0.2368
20160608T065000	-88.5	42.6	2457547.8056	0.8627
20160608T075000	-169.2	180.5	2457547.8472	0.0452
20160608T085000	-31.8	42.7	2457547.8896	0.2309
20160611T082000	-68.0	42.3	2457550.8688	0.2868

Table 7.11: Rescaled *ES2* exposures as discussed previously in the text. Hence $\sigma_{v_{app.}}$ has been enlarged quadratically and is as such been rendered in red, while the actual $v_{app.}$ should have improved to a better agreement with the *LRS2* data and is therefore marked green.

The combination of both data sets illustrates the clear advantage of *LRS2* over *ES2*. And while it seems beneficial to enlarge the count of data points by a factor of two, the additionally gathered information is still negligible as the errors of these data points are that much larger than these of the primal *LRS2* data.

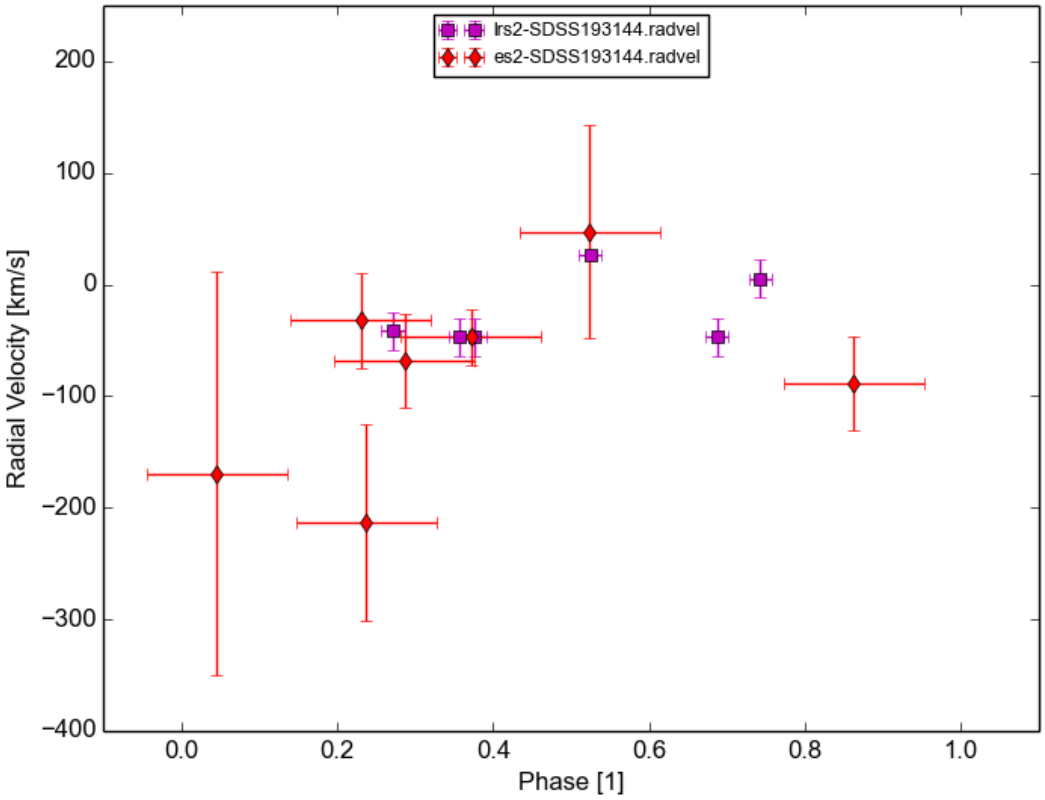

Figure 7.10: SDSS193144 - Combined *ES2* and *LRS2* radial velocity data. Folding period: $p = 0.2282\ d$

7.3.3 Fitting the radial velocity data

Probing radial velocity is one of the two major methods to find and confirm exo-planets. Hence, the mechanical orbit models have been investigated in such detail, that there are existing code-packages for this specific task.
Such libraries like the python code *radvel* [28] use state-of-the-art Markov Chain Monte Carlo (MCMC) sampling techniques and *Bayesian* statistical analysis to efficiently identify radial velocity signatures also for systems with multiple companions as for example exo-planets.
This capability to model and find such complicated signatures within a given data set is a clear advantage of such code. On the down side, such high dimensional phase spaces naturally require a minimal amount of data, which is significantly larger than our gathered data.
We therefore have to make use of the additional information which are not contained in our radial velocity data:

- First of all, the photometric light curves provide us with the targets system period p, which is usually unknown for pure radial velocity based targets.

- Second of all, we can make a reasonable guess for the viewing angle ω, as our target SDSS070433 shows a clear and periodic transit and both other targets SDSS070428 and SDSS193144 show periodic flux variations which indicate an eclipsing binary.

- Furthermore, such low mass-ratio binaries are gravitationally dominated by the common barycenter. Further system components like exo-planets should, if they exist at all, only be stable as circumbinary planets at significantly larger orbits[90] and hence be negligible. Exo-planets which approach the central region of such close binary system either get too close to one of the targets or are affected by both partners in a differential way, such they are ejected from the system. Already early theoretical studies like Wiegert et al. (1997) [92] show these restrictions of such non-circumbinary planets for the special case of the Alpha Centauri system and provide evidence that exo-plant orbits within close binary systems such as ours are intrinsically unstable.

Using these additional informations, we can choose an analytic approach based on the very simple example from our introduction section 2.

When first talking about radial velocities in subsection 2.4, we approximated binary systems, with circular orbits observed edge-on. However, reality usually is more complex than this first approach.

Starting with a simple two body system, the semi-major axes a and masses of both bodies follow $a_{WD} \cdot m_{WD} = a_{BD} \cdot m_{BD}$. For exo-planet studies, one usually proceeds with *Kepler's* third law and further approximates $m_\star >> m_{Planet}$ which is valid in this cases. However, this assumption is in our case not valid.
To model such orbits, we start from *Newtonian* gravitation and in extreme cases such as soon to be mergers also include general relativity. Following standard literature such as Hilditch et al. (2001) [39], this derivation leads to the following compact formula, which describes the most general case for the two body stellar motion:

$$v_{app} = \frac{2\pi a \cdot \sin(i)}{p \cdot \sqrt{(1-e^2)}} \cdot [\, \cos(\theta + \omega) + e \cdot \cos(\omega)] + \gamma \qquad (7.3.3.1)$$

with:

- θ: The phase θ defines the position within the folded radial velocity curve.
- ω: The longitude of the periastron[32] ω defines the relative orientation of the companions perihelion, relative to the sky plane which is tangential to the observers line of sight. We assume ω to be static within our observational timescales of a few years. Mathematically, ω leads to a phase shift of the resulting radial velocity curve.
- γ: The total static offset γ of the apparent radial velocity v_{app}. As previously argued, our cross correlation measurements intrinsically measures the dynamical fraction of v_{app}. Still the arbitrary selection of a reference observation causes an unknown offset of our data which relates to $\gamma \neq 0\ km/s$.

[32] Periastron is the term for the closest approach between two stellar objects, analog to the perihelion of a planet around the Sun.

- e: The orbits eccentricity e is defined relative to the barycenter. Perfect circular orbits are rather exceptional and especially systems with minor mass ratio tend to eccentric orbits, as it is the case for WD-BD binaries. The eccentricity e ranges from $e = 0$ for perfect circular orbits to $e < 1$, while $e = 1$ defines a parabolic trajectory. Values such as $e > 1$ indicate hyperbolic trajectories and describe fly-by interactions which are consequently irrelevant for our binary study.

- p: The targets system period p is static and in our case known by the photometric light curves.

- a: The semi-major axis a for the WD around the common barycenter.

- $\sin(i)$: The targets system inclination i is in the case of SDSS070433 case known, as the photometric light curve shows a transit ($i = 90°$). For the other two targets, an eclipsing binary can be expected, which causes an $\sin(i) \leq 90°$. We will provide an guess for the limiting $sin(i)$ in section 9.1.

The prefactor of equation (7.3.3.1) is commonly named semiamplitude K and can be directly measured in the radial velocity curve. Using our approximation $sin(i) = 1$ and the fact that we know p, we find the following formula for $a\ (K, p, e)$:

$$a\ (K, p, e) \ = \ \frac{Kp}{2\pi} \cdot \sqrt{(1 - e^2)} \tag{7.3.3.2}$$

After all we can reduce equation (7.3.3.1) to the following:

$$v_{app}\ (\theta, K, e, \omega) \ = \ K \cdot [\ \cos(\theta + \omega) \ + \ e \cdot \cos(\omega)] \tag{7.3.3.3}$$

To get an understanding for the resulting geometry of this kind of orbits we have a look at standard literature such as Perryman (2011) [69], which provided the following examples of radial velocity curves with various eccentricities.

In figure 7.11, we can see that small eccentricities like $e = 0.03$ in the left frame lead as expected to very sinusoidal curves. The central frame shows the case of $e = 0.53$ where it already is clearly distorted. The right case shows an extreme case of $e = 0.90$, which is extremely hard to detect precisely, as the peaks can only be measured during a very sharp transition.

Comparing these exemplary curves as presented by **Perryman 2011** [69] with our radial velocity measurements, the human eye tends to find some

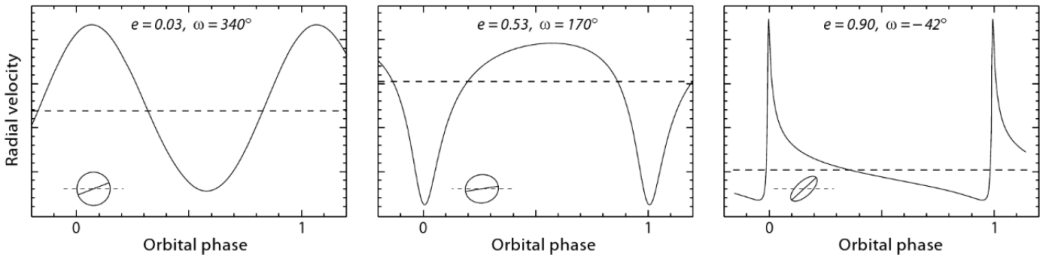

Figure 7.11: *"Example radial velocity curves with different eccentricities and orientation angles."*

Taken from **Perryman 2011** [69]

agreement between our SDSS070433 data and the left curve and potentially also between the SDSS193144 data and the central data from figure 7.11. While it is certainly tempting to assume such curve shape, looking at the bare data and especially the according error bars, we can not rule out a constant radial velocity. In addition, fitting the radial velocity function as we defined it in (7.3.3.3) will also only provide results with large error margins, as the amount of data points is in the same order as the free parameters of the fit.

Consequently, we need to narrow down the actual parameter space (K, e, θ, ω) even further, using assumptions and additional sources of information. Therefore we now investigate our photometric follow up data in section 8, before we combine all informations to conclude on our final results in section 9.

Chapter 8

Photometric follow up

*3KK*s general capabilities were already shown in section 3.3, and the observational campaign has been previously described in section 4.3. Hence the following subsections will focus on the relevant data analysis.

Using the available data, we create an illustrative RGB-composition of our target SDSS193144, which is shown in figure 8.1.

To create the RGB picture, we used all three *3KK* camera channels: blue (g' and r'), red (i' and z') and infrared (J, H and Ks). In order to match the exposures with the RGB color-frame, the near-infrared camera exposures have been interpreted as Red, the red camera data as Green and the blue channel has been assigned to Blue.
As mentioned previously, the only available target for the photometric follow up is SDSS193144. Unfortunately, all other targets are only observable during the winter months from the *Wendelstein Observatory*. The photometric follow up of the other targets SDSS070428 and SDSS070433 is a task which remains to be done in the future.

Within the following subsections we provide a brief overview on the covered wavelength bands, shed light on the data reduction process and discuss the measured light curves.

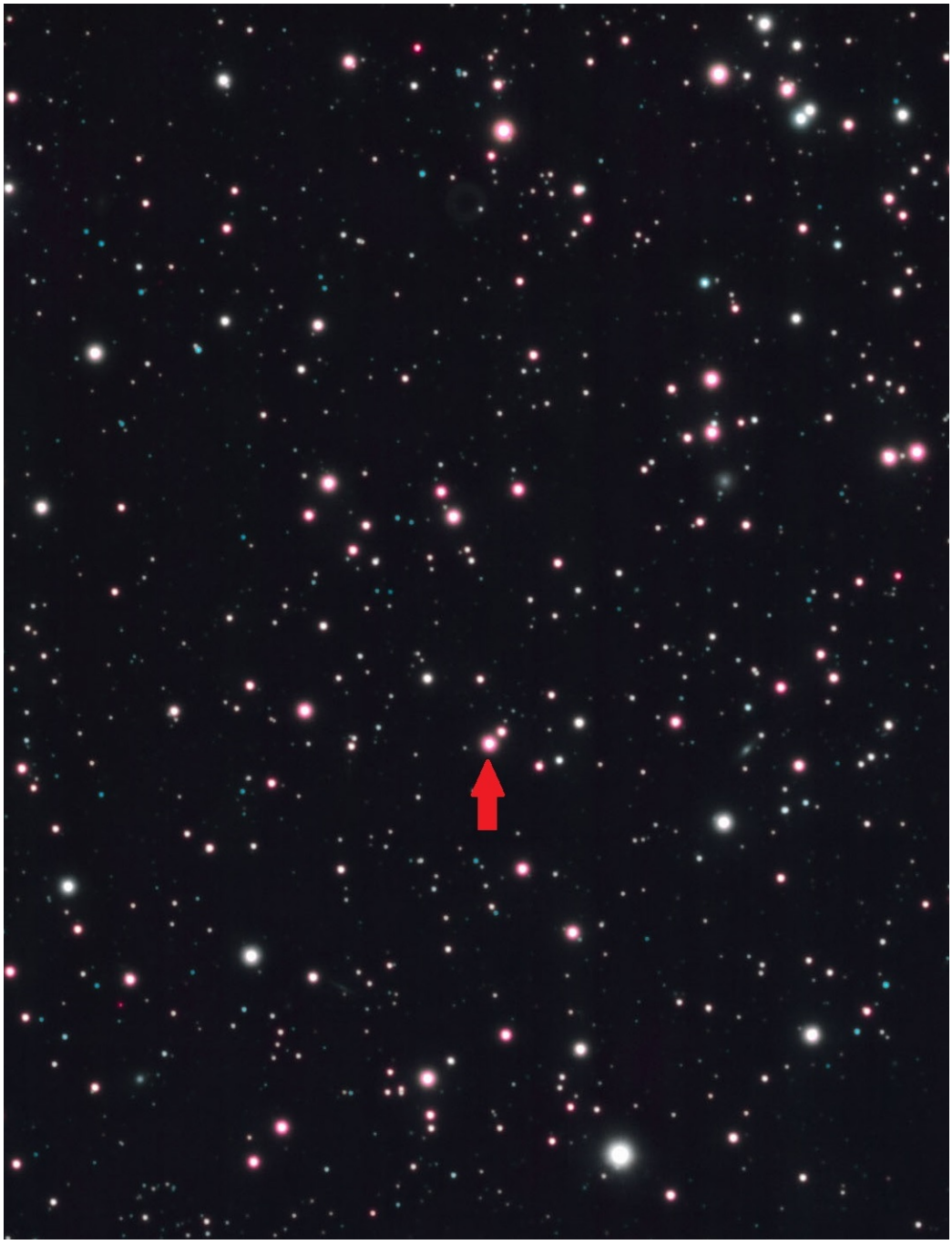

Figure 8.1: RGB composite of our target SDSS193144, using the photometric *3KK* exposures. SDSS193144 is indicated by the red arrow. The fainter star sitting just to the right of our target will be discussed later in this section, as it might have a systematic effect on the measurements.
Field of view: $\approx 4.0 \cdot 5.6\ arcmin^2$

Credit: C. Obermeier

8.1 Wavelength coverage

As outlined in table 3.2, each camera features an individual filter set. To get the maximum wavelength span, we observed the target using all available broad band filters. As it can be seen in the description of the *3KK* observational campaign (see 4.3), a typical setup of simultaneous observations contained either the filters g', i' and J; or the filters r', z' and H or Ks.
Both setups span from optical to near-infrared as it can be seen in figure 8.2 and 8.3, which are adapted version of a plot taken from Lang-Bardl et al. 2010 [59].

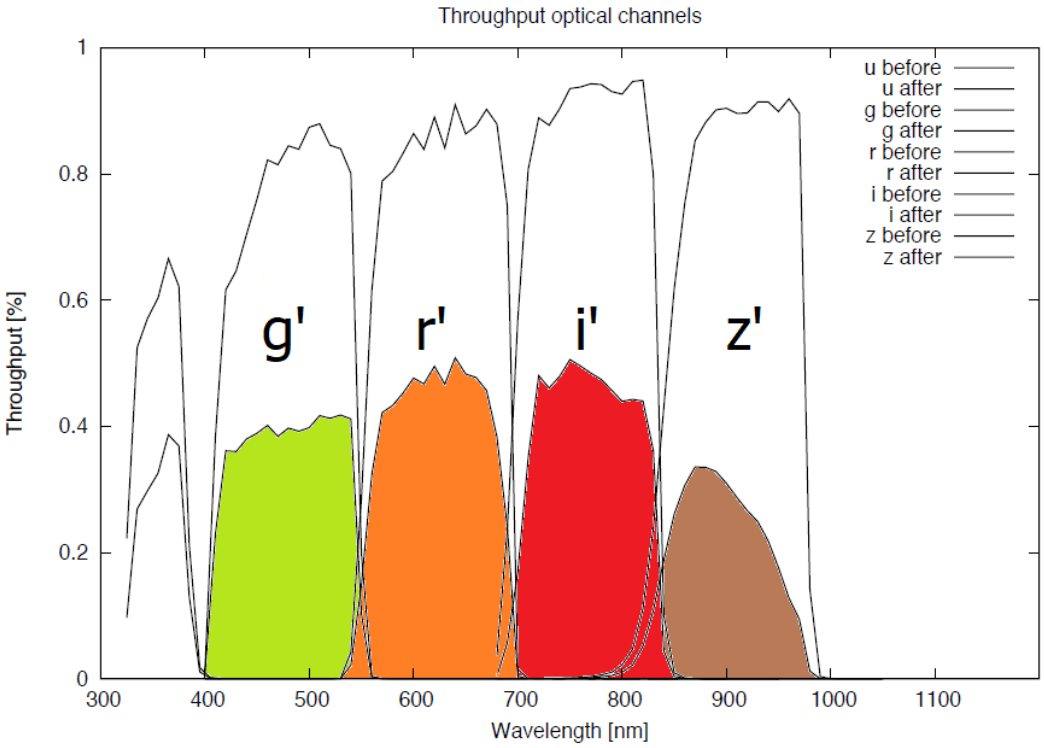

Figure 8.2: Efficiencies for the *Wendelstein three channel imager (3KK)* (3.3). *"Efficiency of the u', g', r', i' and z' filterbands. The efficiency includes reflectivity or transmission, respectively, of all optical surfaces, filter transmission curves and the quantum efficiency of the detectors."*
Adapted version, taken from **Lang-Bardl et al. 2010** [59]

Despite of the slightly different pixel scales[33] [57] and field of view[34] [57] all channels deliver comparable results for point sources such as ours.

[33]Pixel scales: 0.20 $\frac{arcsec}{px}$ for the optical and 0.24 $\frac{arcsec}{px}$ for the near-infrared channel
[34]Field of view: 6.8 *arcmin* for optical and 8.2 *arcmin* for the near-infrared channel

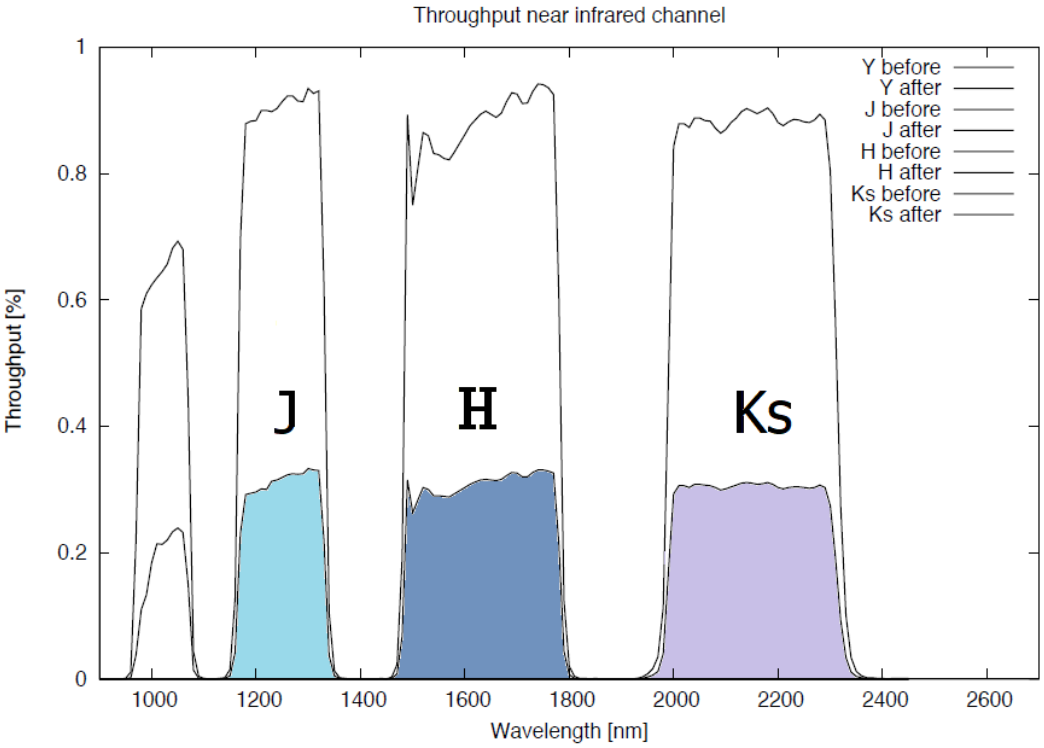

Figure 8.3: Efficiencies curves for the *Wendelstein three channel imager (3KK)* (3.3). *"Efficiency of the J,H,Ks filterbands. The efficiency includes reflectivity or transmission, respectively, of all optical surfaces, filter transmission curves and the quantum efficiency of the detectors."*
Adapted version, taken from **Lang-Bardl et al. 2010** [59]

If we now compare the bands, from which we expect reasonable results for our targets, we find that *3KK* is perfectly suitable to record light curves.

Nevertheless, the results from the analysis of the observation campaign as discussed in subsection 4.3 show that the rate of excluded exposures is significantly higher for the near-infrared channel than for both optical channels. As shown in table 4.6 the optical channels provide 542 (Blue) respectively 513 (Red) valid exposures of roughly 600 raw data frames per channel. In contrast, the near-infrared channel only provides 329 of 600 exposures.

This reduced efficiency of the near-infrared channel is in our case caused by the rejection of exposures due to their data quality, as reduced by the data pipeline which is discussed next.

8.2 Data reduction

The *3KK* data reduction process, as well as the actual pipeline are currently still being optimized and hence an according paper has not been published yet. Therefore, the following block schematic 8.4 illustrates the general data reduction steps as applied to *3KK* data used in this thesis.

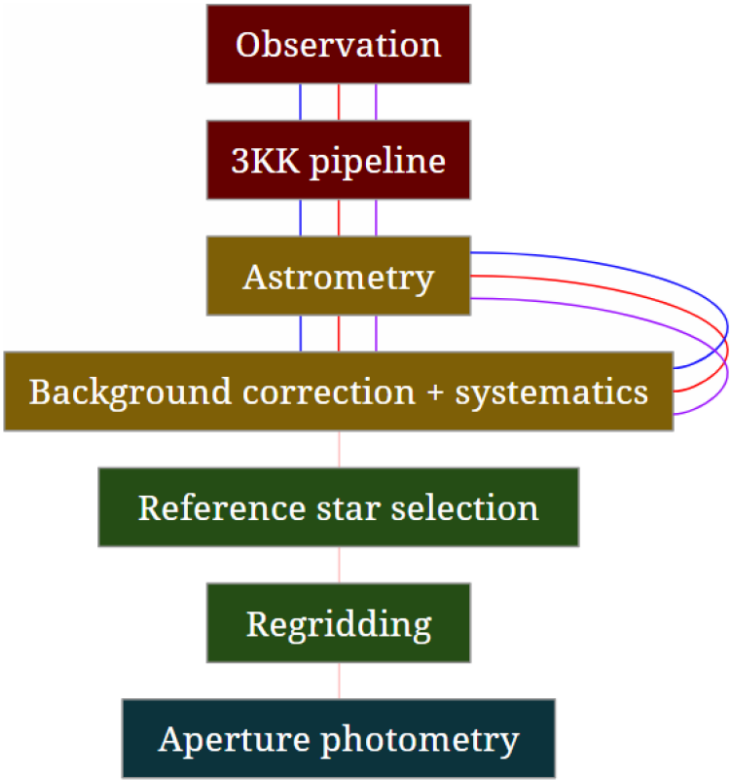

Figure 8.4: 3KK - Data pipeline block schematic. Credit: C. Obermeier

After the observation, first each individual channel exposure is run through a basic reduction pipeline handling the fundamental effects like dark current, bias offset and others. These steps are actually rather similar to those described in subsection 5.1. In case of the near-infrared channel this pipeline is rather different, as the camera uses a CMOS-detector which is being read out periodically every $1.4s$. Our exposures of about $28s$ integration time are therefore actually a combined frame which contains the information from all detector reads, as they happened in between. The frame composition follows the so called *sample up-the-ramp* mode which measures and fits the de-charging curve of the CMOS pixel. Further details on the CMOS

specific readout are published by the instrument designers in Lang-Bardl et al. (2016) [57]. We hence simplify the description of the data reduction as this lies beyond our focus.

In the second step of the pipeline, we calculate an astrometric solution for each individual channel. The most prominent stars in each exposure are correlated with according J-Band *2MASS*[35] observations, using the telescope pointing estimated as a starting point. Hence, the pipeline iterates the number of stars which could be identified in our exposures as well as in the catalog, until a proper parametrization from the initial (x,y) to the (RA,DEC) World Coordinate System (WCS) has been found.

This mapping is sometimes challenging, as there are a lot of systematics involved, which in addition get superposed and covered by various levels of stray light. Usually, stray light is avoided by the general instrument design and additional dedicated stray light covers. But while this program was ongoing, a second instrument was being integrated and commissioned at the very same telescope port and hence most stray light covers were detached to mount provisional equipment and to ease access.
Once the astrometric solution is individually found, the three channels get compared to each other in order to find a proper general background solution and to account for systematics. Given this solution, the exposures get individually corrected and a refined astrometric solution is being calculated. This process is iterative until the found solution is stable enough.

The exposures can now be combined to a single data set and furthermore processed as one. To do so, the exposures are now scanned for proper distributed reference stars, which should ideally be bright and isolated in all bands. The positions of these stars are now compared using the astrometric solution as previously calculated.
Nevertheless, the offset between individual channels may be small but not negligible. Hence the reference stars are analyzed with a fitted aperture and the according flux and centroid is measured. Now the relative spatial shift between each channels reference stars get calculated and the fits files get regridded in such a way, that the flux within the PSF is conserved.
Following this data reduction, the targets flux can now be measured within its PSF limit, using an according mask. To account for the local sky emissions, there is another annulus shaped region set around the target aperture,

[35]The *2MASS* catalog, as published by Skrutskie et al. (2006) [81], is used as reference data base in order to find a proper WCS solution for each independent exposure.

which is filtered by its median to avoid contamination from nearby objects. This local averaged sky background is now subtracted from our source and consequently we get the final flux of our target SDSS193144.

8.3 Results

Taking a look at the data, we conclude, that the gathered data within a single filter is yet not really conclusive enough in order to provide good light curves for each filter individually.
Hence, we combine the information of all exposures within a single channel in order to provide three more reliable light curves. They are shown in the following figure 8.6 for the blue channel, figure 8.7 for the red channel and figure 8.8 for the near-infrared channel. All plotted light curves provide the data average as plotted in red for bins of 0.04 phase width, while the fundamental data is plotted in gray.
In order to set our light curves into prospective, we recap the initial light curve 8.5 as derived from the *WFCAM Transit Survey* in subsection 1.1.

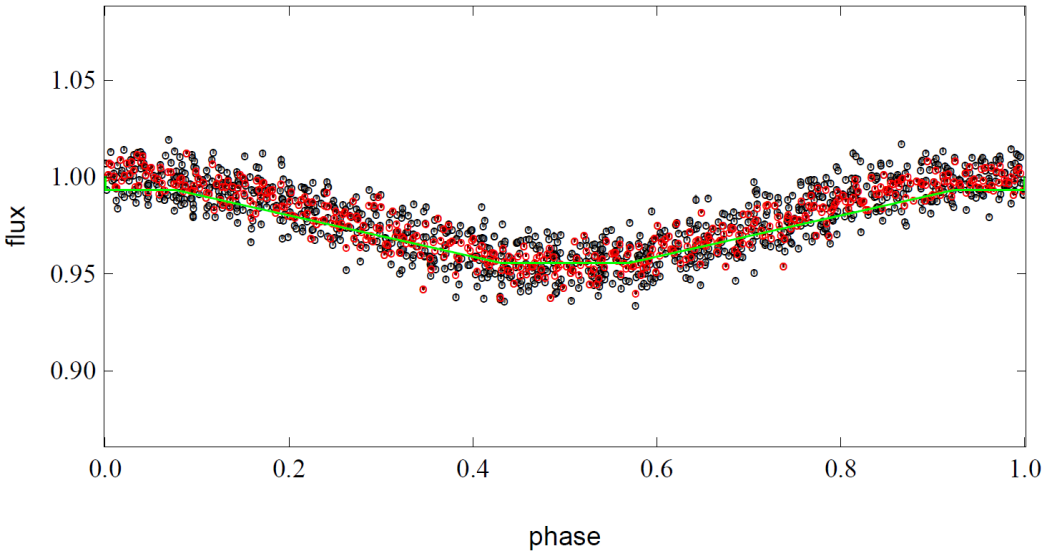

Figure 8.5: Light curves for the target SDSS193144. Circles mark normalized flux, vertical bars indicate the error bars and the green line shows the best fitting theoretical light curve. The photometric observations are folded to the best fitting period as listed in table 7.8.

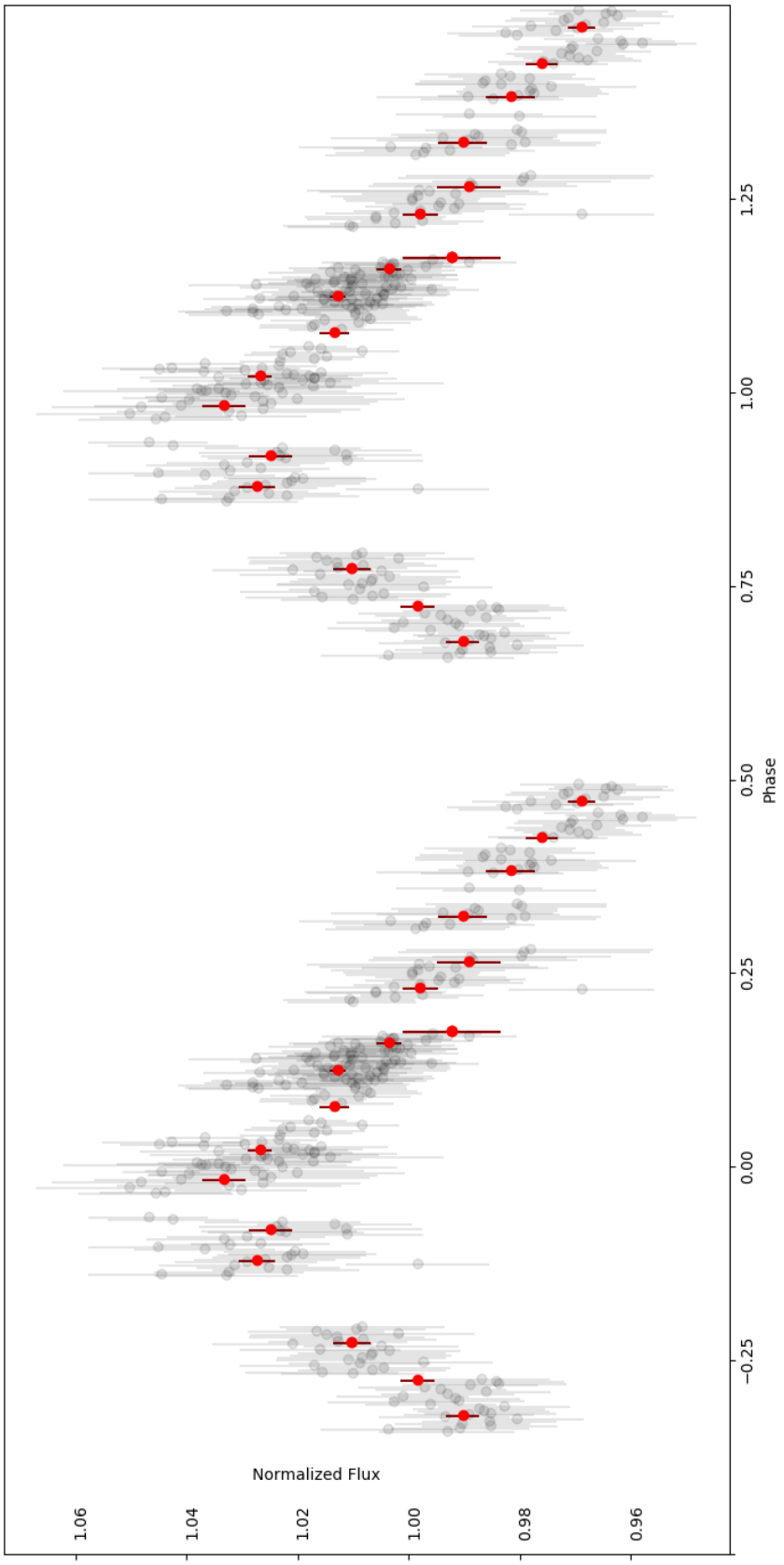

Figure 8.6: *3KK* - Light curve for g' and r'-band.

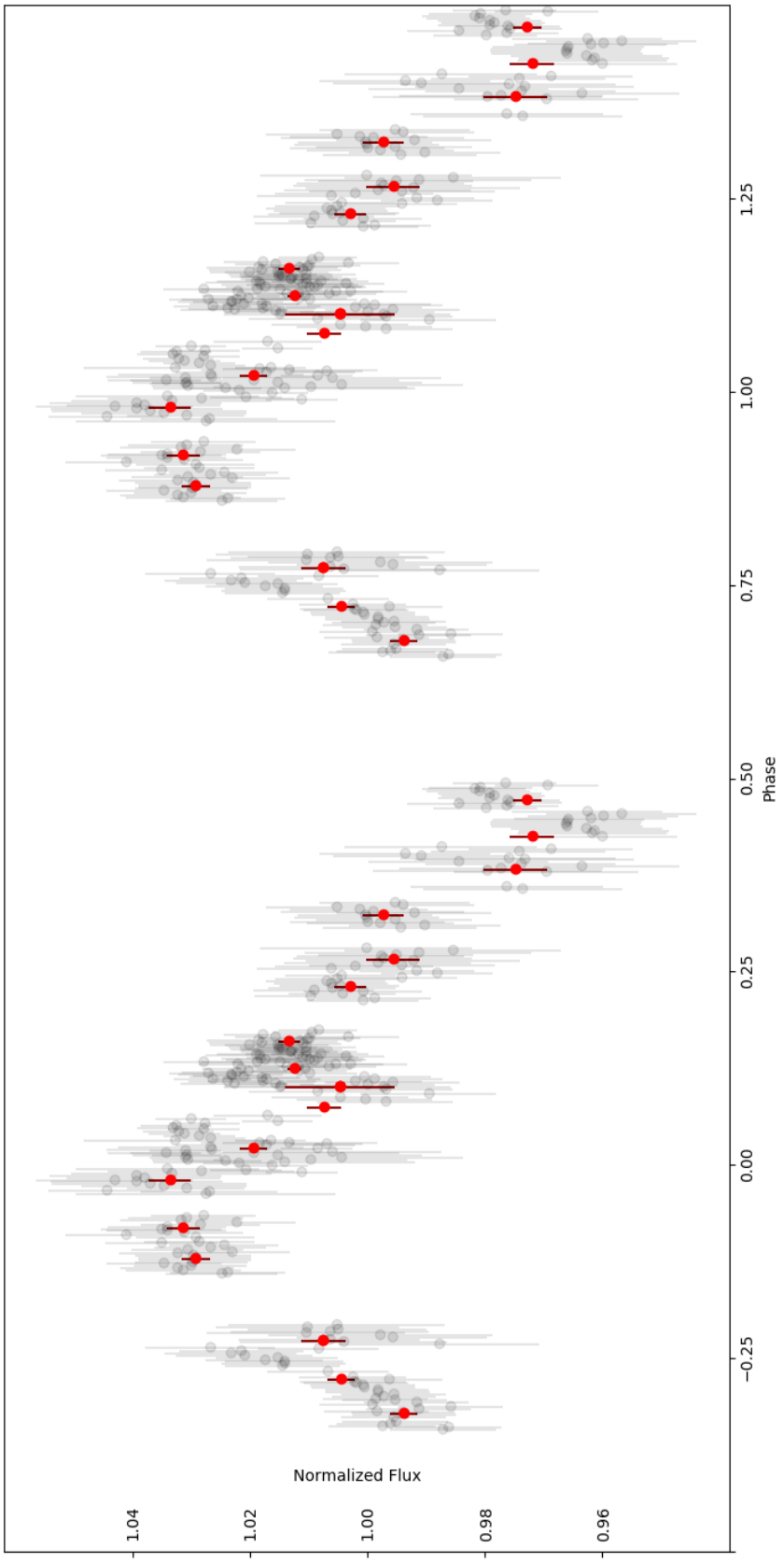

Figure 8.7: *3KK* - Light curve for i' and z'-band.

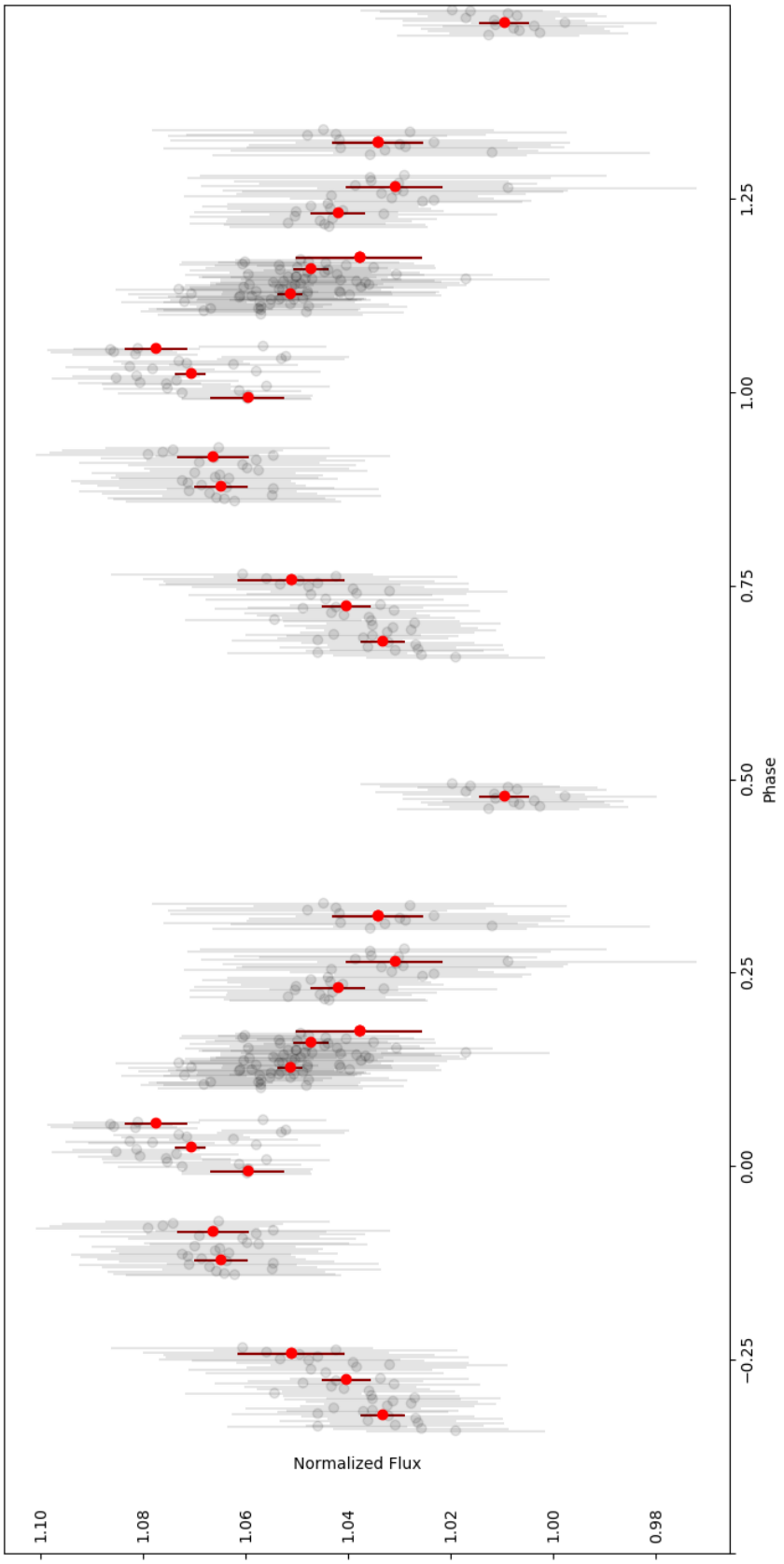

Figure 8.8: *3KK* - Light curve for J, H and Ks-band.

The shown light curves all agree with the period $p = 0.228\ days$ and time offset $t_0 = 2454317.87646\ JD$. Nevertheless they all show a slightly higher flux variation over the cause of a full period.
The initial measurements as gathered by the WFCAM Transit Survey data, reveals variations of roughly 4%-5% as shown in figure 8.5. In contrast, our curves show a variation of about 6.7% for the blue channel (see 8.6), 6.3% for the red (see 8.7) and still 6.0% for the near-infrared channel (see 8.8). Our extensive interpretation on the different flux variations within different filter bands follows in section 9.1.

Our explanation for this systematic offset between our and the WFCAM Transit Survey is not based on a bad flux calibration but rather the result of a crowding star, which seems from our perspective to be close to our target star. The following zoom 8.9 shows the central excerpt of our own RGB-composition of the target region.

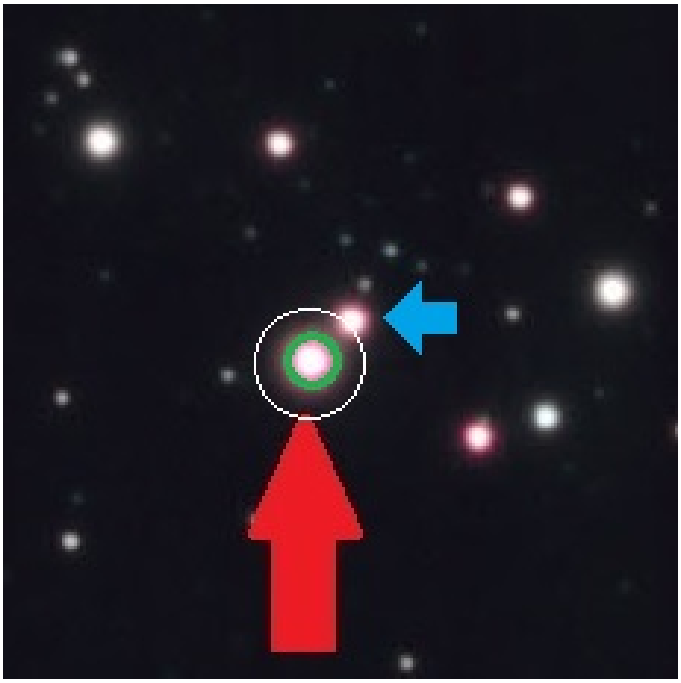

Figure 8.9: Zoomed view of figure 8.1, showing our target SDSS193144 marked by the red arrow and the neighboring star by the blue arrow. The white circle shows the typical size of an aperture for a photometric survey. The green circle shows the adapted aperture as we used it after we realized the contamination by the optically aligned, neighboring source.
Field of view: $\approx 1.0 \cdot 1.0\ arcmin^2$

It can be seen that the fainter neighbor star, as indicated by the blue arrow, is close enough to potentially contaminate the flux as measured within a typical aperture as indicated by white circle. In order to measure the actual flux of our target exclusively, we reduced the aperture towards the green circle, until the relative flux variations asymptotically settled and ended up at the values given above.

In reducing the aperture, we risk loosing valid flux especially for observations with bad conditions. Such observations are likely to build the very few, low flux outliers as they are present in our light curves.

In the end, the systematically larger flux variations as measured in our data can be very well explained by the minor flux contamination from the stable neighbor star, which is according to the *SDSS*-catalog about $1,5$ mag_z[36] fainter. Also the *2MASS*-catalog, which provides J-Band and longer wavelength measurements, lists the neighbor about $1,4$ mag_J[37] dimmer. Assuming the 1.4 mag difference, the combined flux from out target and the neighbor would accumulate to roughly 127 %. But as not all of the secondaries flux has been added to our measurement, we can estimate the combined flux to $\approx$ 115 %. This roughly correlates with a compression of 6.0 % variation as measured by us, to the 4.5 % as observed by the WFCAM Transit Survey.

Besides the systematic offset in variable flux, we confirm the initial period. The fact that the light curve shows the same periodicity and phase in all our bands confirms that we measured correct target.

[36] **SDSS** [3] | Target: $m = 13.80 \pm 0.02$ mag_z Neighbor: $m = 15.37 \pm 0.07$ mag_z

[37] **2MASS** [81] | Target: $m = 13.04 \pm 0.03$ mag_J Neighbor: $m = 14.48 \pm 0.05$ mag_J

Chapter 9

Conclusion

In this final section, we will draw a conclusion for each our targets.

9.1 Target: SDSS193144

As SDSS193144 is the only target with additional light curves, we start our conclusion with the investigation of the multi-band photometry data as implied earlier.

Looking at the initial light curve 9.1, we expect an eclipsing binary system with a periodic variation of roughly 4-5 % within $p = 0.228\ d$.

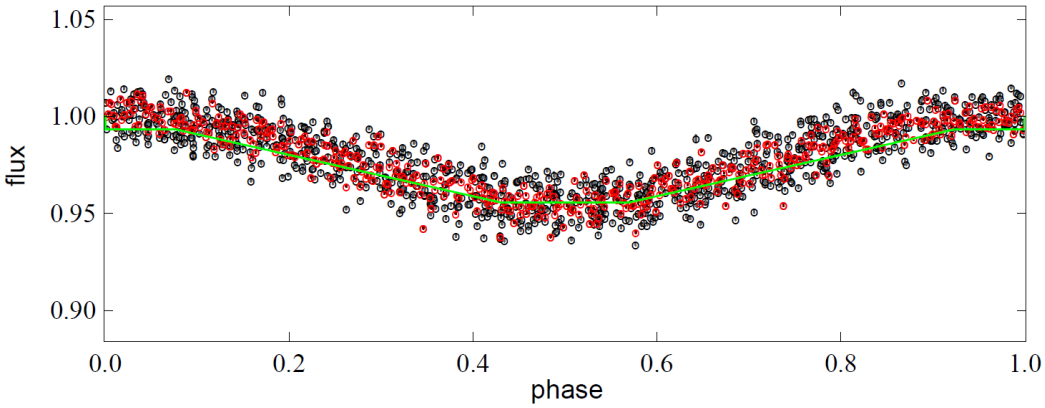

Figure 9.1: Light curve for the target SDSS193144. Circles mark normalized flux, vertical bars indicate the error bars and the green line shows the best fitting theoretical light curve.

Interpretation of multi-band photometry: In section 8.3, we confirmed the initial period as measured by the WFCAM Transit Survey. As previously discussed in section 8.3, the flux variation however, slightly differs due to the potential contamination by a nearby source. In addition, our curves show a periodic flux variation which differs from one band to the other in amplitude:

- 6.7% for the blue channel (see figure 8.6),
- 6.3% for the red channel (see figure 8.7) and
- 6.0% for the near-infrared channel (see figure 8.8).

Therefore we need to find a proper heuristic model, which can produce such a scenario for our target SDSS193144.
First of all, the most obvious feature in all light curves of SDSS193144 is the absence of a transit. The first conclusion which we can draw: Both companions never fully eclipse each other. As a second conclusion, we find the same target periodicity over an extensive period of time, which hints a binary based mechanism, as the light curve is unlike any known stellar-based periodic fluctuations, as it is for instance known for Cepheid variable stars.

Classification: Meanwhile we have an independent parallax measurement of $\phi = 0.70 \pm 0.07$ *mas* from *Gaia*, [29][30] which translates to a distance of $r = 1.4$ *kpc*. In addition, we find an estimated effective temperature of $T_{eff-Gaia} = 6021$ *K*, which is in good agreement with the best matching template from by Röck et. al. 2018 [1], that suggests a F8 III-IV star with $T_{eff.} = 6083$ *K* like *HD136202*.[38]
Combining the available parallax and the luminosity of *HD136202*, we find an absolute magnitude of $M \approx 3.1 \pm 0.05$ *mag*, from which we can calculate an apparent magnitude of SDSS193144. We find $m = M + 5 \cdot \log(r/10\ pc) = 13.8 \pm 0.9$ *mag* which meets perfectly our targets luminosity of 14.0 *mag*.

Interpretation of radial velocity results: In light of the former classification, we no longer expect a clear high amplitude radial velocity signal which we could measure with the given low resolving spectrograph's. Hence we stopped the data acquisition as it became clear, that 193144 is not a WD BD binary.
The available amount of *ES2*- and *LRS2*-data, as gathered in section 7.3.2 and plotted in the following figure 9.2, shows as we expect now, no strong

[38]HD136202 is the ID within the classical Henry Draper catalog as published in 1936 [8]

radial velocity variation for this target.

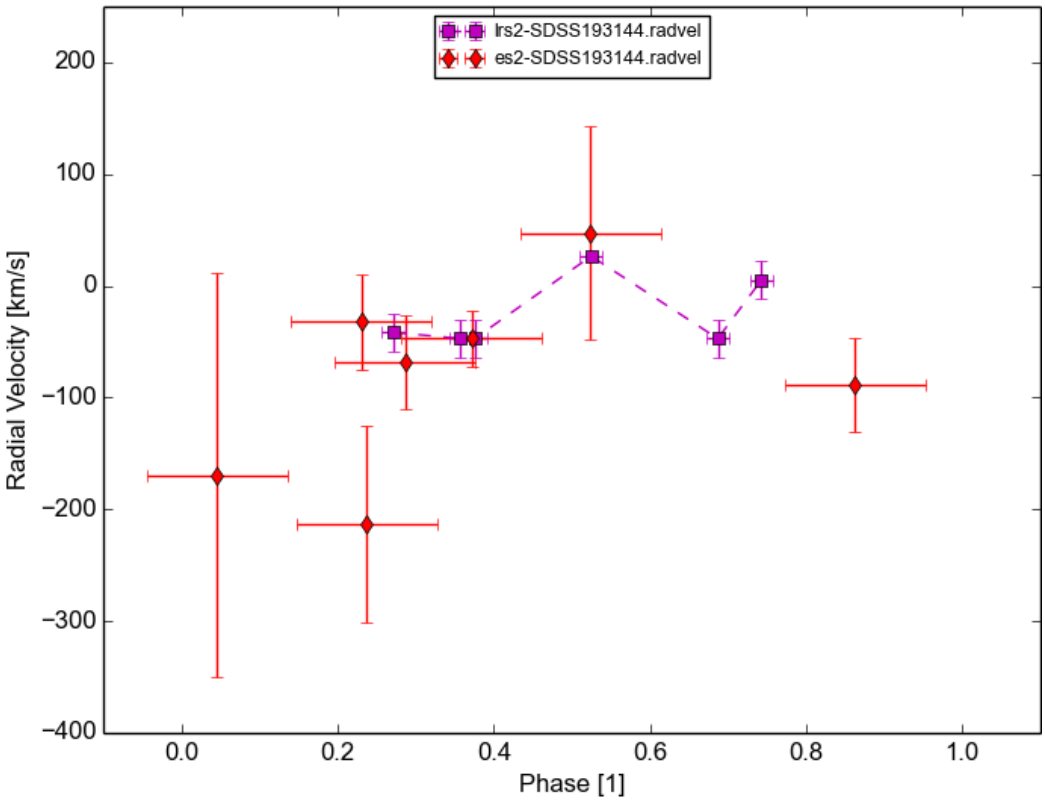

Figure 9.2: SDSS193144 - Combined *ES2* and *LRS2* radial velocity curve. In contrast to figure 7.10, the anchor point is now assigned with an average error bar as we expect it for *LRS2* exposures. Folding period: $p = 0.2282\,d$

Conclusion SDSS193144

Based on the strong agreement of the target spectra and the lack of a clear radial velocity variation, SDSS193144 is clearly not a WD BD binary. Nevertheless, the periodic stability and the shape of the flux variations still hint a geometric respectively orbital based origin, rather then a stellar physical cause. Potential candidates are either blended binaries or close contact binaries in which at least one partner has filled his *Roche*-limit.

9.2 Target: SDSS070433

In contrast to the former target, the story for SDSS070433 is slightly different, as we are missing our photometric multi-band follow up data. Otherwise, this target is the only system showing a clear transit in the initial light curve as it is given in figure 9.3. Given the 4 % transit depth, but only the minor 1 % occultation, this target is the most interesting one, but also the hardest to explain by a WD-BD binary.

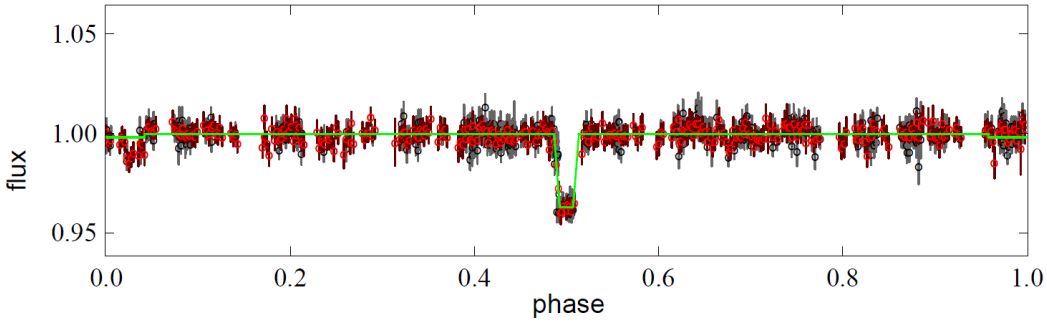

Figure 9.3: Light curve for the target SDSS070433. Circles mark normalized flux, vertical bars indicate the error bars and the green line shows the best fitting theoretical light curve. At a phase of 0.025 we can see a small occultation of 1%. Please note, that this is not sufficient to derive, but rather an indication that $e = 0.0$ can be estimated without making too much of an error.

Classification: Similar to SDSS193144, we meanwhile got an independent parallax measurement of $\phi = 0.38 \pm 0.07$ *mas* from *Gaia*, [29][30] which translates to a distance of $r = 2.6$ *kpc*. In addition, we find an estimated effective temperature of $T_{eff-Gaia} = 6381$ *K*, which is in good agreement with the best matching template from by Röck et. al. 2018 [1], that suggests a F6 IV star with $T_{eff.} = 6493$ *K* like *HD089449*.[39]

Combining the available parallax and the luminosity of *HD089449*, we find an absolute magnitude of $M \approx 3.2 \pm 0.02$ *mag*, from which we can calculate an apparent magnitude of SDSS070433. We find $m = M + 5 \cdot \log(r/10\ pc) = 15.3 \pm 0.9$ *mag* which just meets our targets luminosity of 16.0 *mag*.

[39]HD089449 is the ID within the classical Henry Draper catalog as published in 1936 [8]

Transit aided fit of radial velocity curve: The advantage of a transit within the light curve, is the certainty of the viewing angle i, which is hence very close to 90° as already discussed in section 7.3.3. Assuming our binary motion model is correct, this radial velocity data shows a significant trend towards a phase shift $\omega = 275.6 \pm 12.3°$, which we from now on fix to improve the other parameters quality.

While we hereby gain certainty for the other parameters, we still have not enough data to fit more then the semiamplitude K. Hence, we assume circular orbits using $e = 0.0$ as the light curves show no irregularities in the transit shape. Additionally, the light curves occultation at phase 0.025 indicates a very small eccentricity. In the end, this minor asymmetry is not conclusive enough to provide a better guess than $e = 0.0$. It rather assures us, that this assumption is good enough given the amount of available date. The resulting radial velocity curve is plotted in figure 9.4.

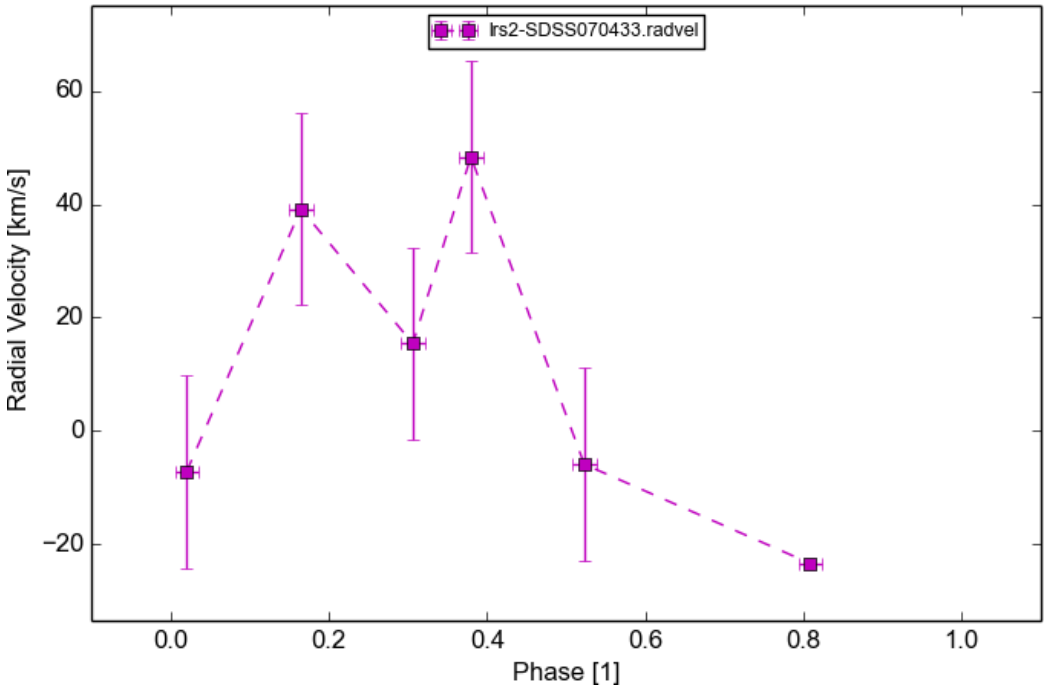

Figure 9.4: SDSS070433 - Radial velocity curve as measured with *LRS2*. Folding period: $p = 4.6598\ d$

As in this case we are sure about the expectable radial velocity periode, we find that the gathered data is not conclusive to probe a $v_{app.}$, but rather only provides an upper limit for the amplitude of $K \leq 35.0\ km/s$.

Resuming the 4 % transit depth, which hints an secondary radius of about 20% the primary radius, we can estimate the secondary to a red M3-5 V dwarf which has a mass in the order of 0.20 $M_{\odot}$. A F6 host star typically features a mass in the range of 1.20 $M_{\odot}$.

As already derived in section 7, using basic mechanics and the *Keplarian*-laws we can also write the semi amplitude K of the radial velocity $v_{app.}$ as follows:

$$K = \left(\frac{2\pi G}{p}\right)^{1/3} \cdot \frac{M_{F6}}{M_{M4}^{2/3}} \tag{9.2.0.1}$$

In our case this results in a maximum amplitude of $K \leq 22.7\ km/s$, which is in the order of our systematic error margin for the *LRS2* measurements. Therefore a fit of the few given data points is useless.

Further evidence, H_{α} deformations: During the cross-correlation of SDSS070433s data, we furthermore find that the peak of several *Balmer*-lines is significantly deformed as if it would consist of two components where one is sharper as the other as the overall width is still unchanged. Figure 9.5 shows the according H_{α} absorptions.

In contrast to the shape of the peak, the width of the deformed *Balmer*-line is constant. This relates to a secondary component with potential *Balmer*-emission from a smaller and colder companion. Such *Balmer*-emissions are known features of M dwarfs as for instance investigated by Stassun et al. in 2012 [84] and many others.
To make the width comparison easier, we plot the H_{α} absorptions also unstacked in figure 9.6. Furthermore, the relative luminosity can only be in the order of 1%, as it would agree with the light curves.

Given the fact, that the width is unchanged, there is also a certain likelihood for the shape to be formed by noise. But comparing the spectra indicates that these 2-3 pixel would all need to see the same systematic noise offset of several σ, which is less likely.

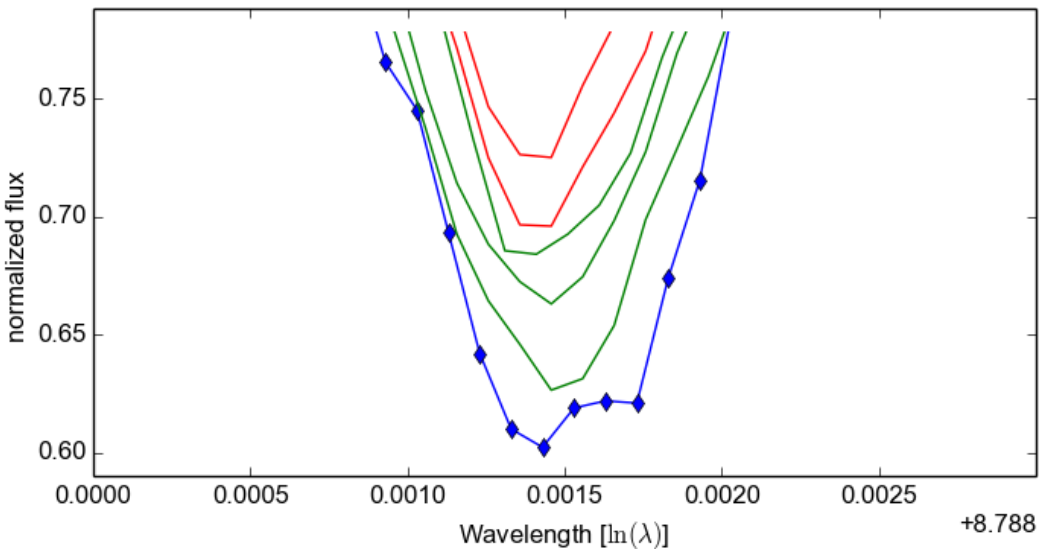

Figure 9.5: H_α deformations of SDSS070433. The spectra are distributed vertically for enhanced comparability. All spectra have been corrected for the helio centric motion and horizontally shifted so they peak at roughly the same position. The color coding of the spectra reflects their potential position on the radial velocity curve. Red spectra show higher red-shifts, while the blue spectrum reflects the smallest reds shift.

So if the hypothesis, that the H_α peak is deformed due to the contribution of the companion is right, we should see similar effects for further *Balmer*-lines. Investigating the other measurable lines, we find on the one hand similar effects just for this specific exposure for H_θ and H_ι.

On the other hand, these lines at the very blue end of the spectra provide significantly less S/N. Furthermore, the remaining lines show no clear deformation. We hence can not draw a clear conclusion from this deformation, but still it remains unclear what caused the systematic deformation of several *Balmer*-lines in a single exposure.

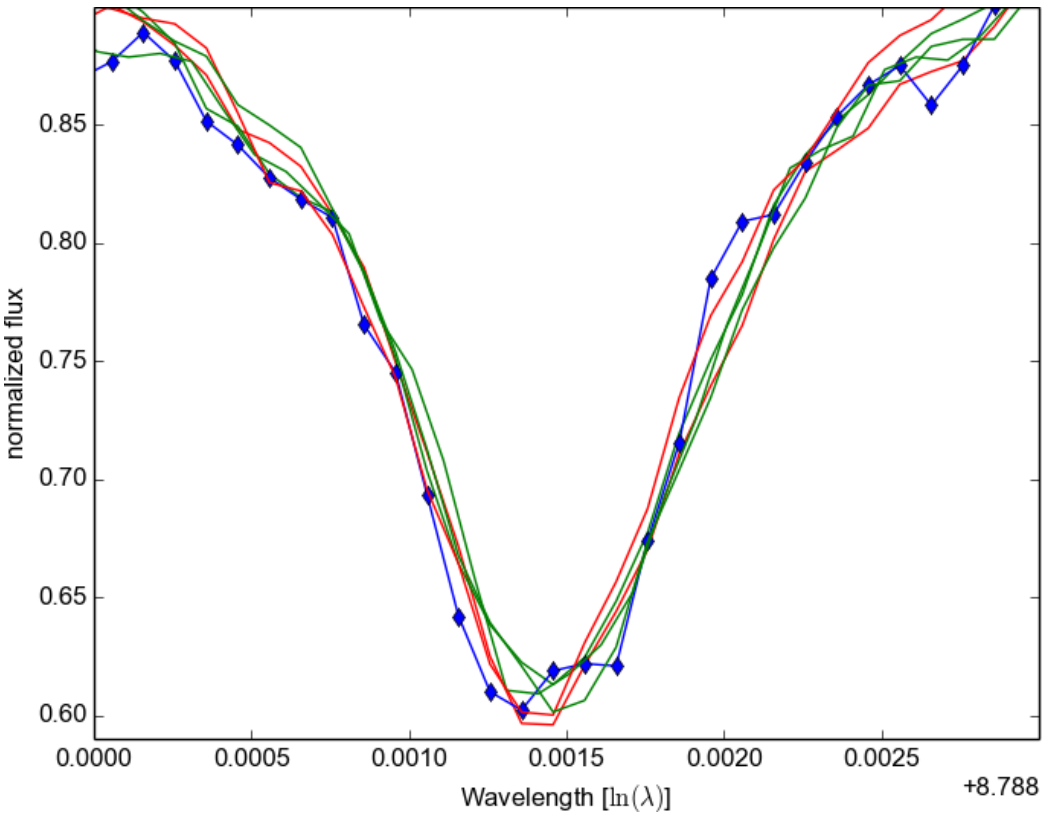

Figure 9.6: Shape deformation of SDSS070433s H_α-line. All spectra are distributed vertically for improved comparability of the absorption shapes. All spectra have been corrected for the heliocentric motion and horizontally shifted so they roughly peak at the same position. The color coding of the spectra reflects their potential position on the radial velocity curve. Red spectra show higher red-shifts, while the blue spectrum reflects the smallest reds shift.

Conclusion SDSS070433

Based on the sum of evidence SDSS070433 is clearly not a WD BD binary. The obvious transit within the light curve however is consistent with approximately a F6 - M4 binary. The according best fitting template s0341 from the *MILES* catalog [1] is in agreement with the hosting F6 star, and also matches the independent *Gaia* temperature measurement. The potential deformation of the H_α line due to an according sharp emission of lower intensity further aids this scenario.

9.3 Target: SDSS070428

Finally, we recap the radial velocity measurements of SDSS070428.

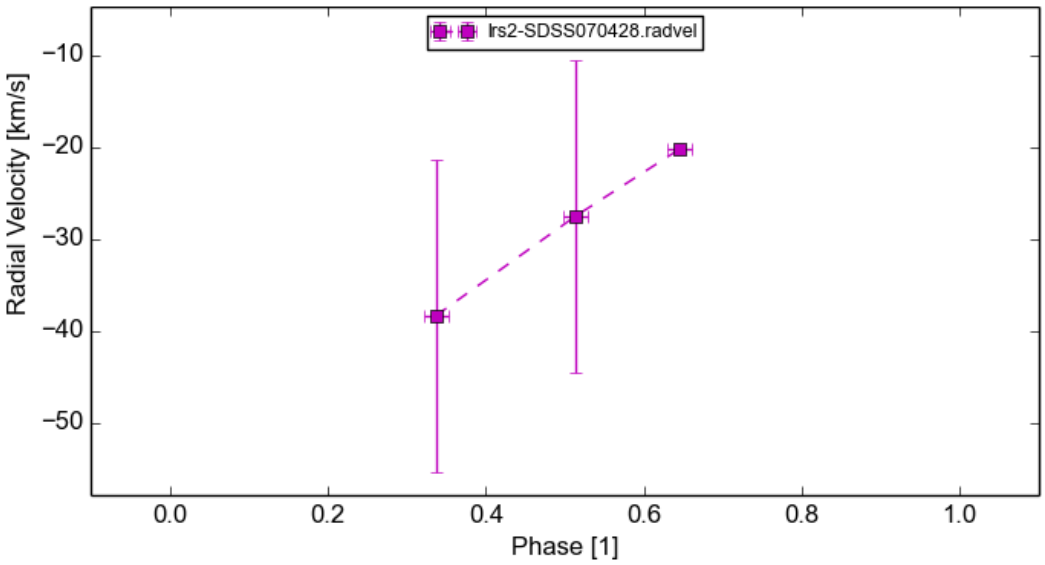

Figure 9.7: SDSS070428 - Radial velocity curve as measured with *LRS2*.

This target was assigned lower priority compared to the simultaneously observable target SDSS070433, which is located nearby.SDSS070433s light curve, simply provided more information on the system due to its transit and therefore was prioritized. Obviously, we can not reasonably conclude on any radial velocity parameters for this system as the 1σ-error bars still allow a constant velocity, as it can be seen within the radial velocity curve 9.7.

Classification: The given *Gaia*-parallax [29][30] of $\phi = 0.30 \pm 0.12$ translates to a distance of $r = 3.3\ kpc$ with an estimated effective temperature of $T_{eff-Gaia} = 6380\ K$. In addition, we provide the matching template s431 from the *MILES* catalog [1], which hints a F5 V like star with $T_{eff.} = 6556\ K$. The combination of this template luminosity and its parallax allows the derivation of an absolute magnitude $M \approx 3.5 \pm 0.05\ mag$, from which we can calculate an apparent magnitude of SDSS070428. We find of $m = M + 5 \cdot \log(r/10\ pc) = 16.1 \pm 0.9\ mag$ which meets perfectly our targets luminosity of 16.5 *mag*.

Conclusion SDSS070428

Based on our spectra and the astrometric data from *Gaia*, we can rule out SDSS070428 to be a WD BD binary, but rather a F5 V star like *HD134083*.

9.4 Methodic conclusion

Early comparison of our data with theoretical WD template spectra, as available for example from Koester 2010 [53], show similarity with WD of $\log(g) \approx 6.5$ and temperatures below $T_{eff.} \leq 10,000\ K$ in terms of *Balmer*-line widths and depths. In combination with the overall SED and the untypical shape of their light curves it is on the one hand clear why Steele et al. included this targets initially but later on focused on another target which actually ended up to be a WD BD binary. As we gathered enough data it became clear, that the targets primary components are rather F-stars, which afterwards got confirmed by the meanwhile published *Gaia* catalog. In addition to our spectra, it became therefore clear, that our targets are all too far away to be considered as WDs. We rather provided reasonable classifications based on the MILES data catalog.

Still, from a test case point of view, on the one hand we showed that *ES2* while still being useful to the community is not stable enough for such a rv survey. *LRS2* on the other hand, while it proved to have its little unknowns in the very details of its inter-night λ-calibration, seems to be a reasonable instrument to follow up faint potential WD BD targets, which can now be pre-selected much better based on their parallax.

To put things into a somewhat fair perspective, we have to keep in mind, that *ES2* is an instrument designed in the 1990's, mounted at an telescope, build in the 1930's. The fact, that this facility can still contribute to the community is remarkable on its own. Otherwise, *LRS2* is a state-of-the-art instrument, mounted and designed especially for one of the largest optical telescopes of the world. Nevertheless, *LRS2* was designed for a completely different science case. Given its fiber count of almost 300 fibers[11] and the according high spatial resolution, *LRS2* is greatly capable to probe for example galactic dynamics based on emission line diagnostics[11] and other tasks which benefit from a high count of spatially resolved spectra.

The approach to use lower resolving and better available instruments failed in the case of *ES2*, as the instrument stability never allowed to reliably correlate data from different observation runs with each other. In addition the S/N which one can gather within a reasonable observation time of 1 hour is too low, given the consequent spectral smearing for such short period targets. In case of *LRS2* we could at least show that low resolution can be a way to verify such binaries. However, the amount of data which is needed is significantly higher than what we could gather for this thesis.

In the end it seems possible to confirm such potential WD BD targets using *LRS2*. Our targets however, can all be ruled out to be WD BD targets as we meanwhile got access to the big *Gaia*-data catalog, which shows the strength of such large scale survey projects and the according state-of-the-art instrumentation in general.

An application for our method can be the ever larger candidates lists from exoplanet surveys. While filtering the targets via independent *Gaia*-distance measurements [30] [29] already reduces the amount of potential targets, there are still to many to investigate each of them in detail with high resolving first class instruments. Hence, the unique combination of the *LRS2*-spectrograph's resolving power mounted to one of the largest optical telescopes on earth, can not only produce competitive data to study galaxy dynamics but also be of good use to preselect candidates within very short exposure times and less then optimal conditions.

Conclusion

Summarizing this part, we cleared the open cases of the potential WD-BD target list using low-cost, low-priority observation time. The project was our test case for providing fall back targets to boost *HET*'s observational efficiency during times of mediocre weather. We show that our low resolution attempt is a reasonable first step of a follow up study. Short exposure time campaigns with resolution $R \leq 2000$, using unassigned schedule wholes or mediocre weather phases during a night can hence be of value for the community by prefiltering such follow up samples. In our case, none of the targets ends up as the rare WD-BD type.

Dawn over HET: *A long night ended; A new day began...*

Credit: C. Obermeier

"We live in a society exquisitely dependent on science and technology, in which hardly anyone knows anything about science and technology."

Carl Sagan

Part II

Development of an active mirror control

People involved: While the major work for this thesis and according projects has been done by myself, all of this has been achieved under the support of the *Universitäts-Sternwarte München* electronics division respectively the *Wendelstein Observatory* instrument staff. The following list of people have all provided valuable support:

Hans-Joachim Hess, Florian Lang-Bardl, Josef Richter, Hanna Kellermann, Claus Gössl, Arno Riffeser, Helmut Kravcar and Adolf Karasz

In order to make the contributions more obvious, the following sections just name the major contributors to the according project.

Context: The instrument part of this thesis focuses on the facility upgrade for Hobby-Eberly-Telescope's active primary mirror control, which is described in the second instrumentation chapter (see 11). The historic roots of this control system have been originally developed for an ESO project called 4MOST. Hence the first instrumentation chapter (see 10) provides insight on this precursor project. While on the first look both projects might not sound very familiar, they still show the evolution and advantages of modular and reusable technology designs.

Some of the technical details will reoccur along the road. Other aspects might have been solved differently in various situations. Consequently this chapters will each illuminate the reasons for such different solutions.

Publications & Citations: The following chapters document both projects in a hierarchic order. They are also meant to be used as brief functional and technical documentation. Hence, some of the content has already been published in the recent years. This will be stated clearly in the beginning of the according chapters. Since I am the responsible first author for all those publications, the content is an edited and more detailed version of the papers, posters and presentations and therefore is not cited explicitly besides this indication and the individual introduction section 10 and 11.

Chapter 10

Precursor project: A Fiber Positioner for 4MOST

The following chapter contains a detailed version of my published paper:

Presenting a high accuracy Theta-Phi-style fiber-positioner prototype with a 15 mm pitch. [36]

I especially want to point out the contributions from Florian Lang-Bardl, Josef Richter and Hans-Joachim Hess.

> *"4MOST is a wide-field, high-multiplex spectroscopic survey facility under development for the VISTA telescope of the European Southern Observatory (ESO). Its main science drivers are in the fields of galactic archeology, high-energy physics, galaxy evolution and cosmology. 4MOST will in particular provide the spectroscopic complements to the large area surveys coming from space missions like Gaia, eROSITA, Euclid, and PLATO and from ground-based facilities like VISTA, VST, DES, LSST and SKA. The 4MOST baseline concept features a 2.5 degree diameter field-of-view with ≈ 2400 fibres in the focal surface that are configured by a fibre positioner based on the tilting spine principle. The fibres feed two types of spectrographs; 1600 fibres go to two spectrographs with resolution R<5000 (λ ≈ 390-930 nm) and ≈ 800 fibres to a spectrograph with R>18,000 (λ ≈ 392-437 nm and 515-572 nm and 605-675 nm)."*[15]

Important note: Most of the content of the following chapter is similar or equal with the content of Häuser et al. [36]. Such content will hence not be cited any more until the end of this chapter.

10.1 Abstract

We present a $\Theta - \Phi$-style fiber-positioner prototype, which is controlled via the EMI-robust[40] *CAN-Bus*[41]. Our positioner points without iterations or a metrology system. Due to the overlapping patrol disc of 17.3 mm diameter, we reach a filling factor of 100 %. The positioners diameter is 14.6 mm, containing the control electronics on a contemporary PCB[42] of 13.5 mm width. While moving, the power consumption does not lead to a significant rise in temperature. Given a mechanical reference point measured by stall detection, the absolute accuracy is 27 μm ($1\sigma = 14$ μm) and pointings are repeatable with 7 μm ($1\sigma = 4$ μm). Better positioning may be reachable with upcoming calibration.

10.2 Introduction

In times of increasingly large survey projects, multi-object-spectrographs are a key technology to keep the duration of observation small enough to gather the huge amount of requested data. In the past, projects such as *KMOS* with its 24 individual selectable objects, have already years ago identified science targets that demand individually positionable light guides.[76]
Other approaches like the *HETDEX* experiment, which is a massive IFU based, blind survey, are already close to commissioning or in operation[87].

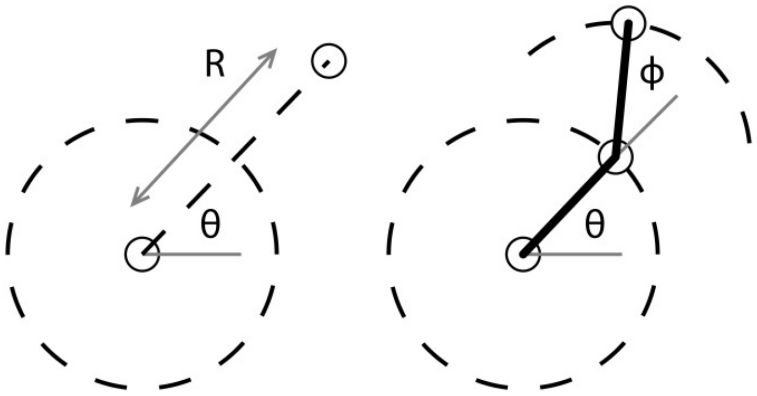

Figure 10.1: *BigBoss* $R-\Theta$ geometry (left) compared to $\Theta-\Phi$-style (right). Taken from **Silber et al. 2012** [78]

[40]EMI: Electro-Magnetic Interference
[41]CAN: Control Area Network
[42]PCB: Printed Circuit Board

In contrast to those either small numbered or big blind surveys, upcoming projects like *4MOST* or *BigBoss* require a high number of positionable fibers, to reach their science goals.
Especially the *BigBoss* design, presented in *Design and performance of an $R - \Theta$ fiber positioner for the BigBoss instrument* by **Silber et al. 2012** [78], is quite similar to our approach. Despite different moving characteristics as shown in figure 10.1, the precision reached by the *BigBoss* team is comparable to ours. Back in 2012, we presented an early design of our *4MOST* motivated $\Theta - \Phi$-style fiber positioner design.

It was initially developed to equip ESOs NTT with roughly 1500 fibers as a part of the *4MOST* project [58]. Now we have extended the scope of our design to a general fiber positioning solution, supporting the following key features:

- Temperature monitoring
- Electronic collision detection
- Adjustable starting and maximum speed
- Smart controlled movement of both axes
- Further reserve of local computation power
- No external referencing respectively metrology

The positioner is designed to reach any desired configuration within several seconds and remains controllable after a power loss. Furthermore, it is meant to be used within a huge array of identical units.
The *CAN* technology, which is robust to electromagnetic interference (EMI), is used to control the whole array of positioner units. A single unit has a diameter of less then 15.0 mm and is less then 200.0 mm long, including the control and power electronics on a printed circuit board (PCB) of 13.5 $\times$ 40.0 mm. Using state of the art electronics, we have minimized the size of the individual control electronics by a factor of roughly 15, making it more cost-efficient and robust to EMI.
While moving, the heat dissipation of the electronics does not lead to a significant temperature increase of the positioner. The power consumption in idle mode is even less and thus negligible.
Following, we will give an overview of our plans, towards a big array of such fiber-positioners, as well as a detailed review of the mechanical and electronic design. In addition we present the result of first performance tests of our existing prototype positioner.

10.3 Positioner Array

Our fiber-positioner's concept is based on a hexagonal tessellation of the focal plane, as shown in figure 10.2. Furthermore table 10.1 sums up the baseline design requests of our positioner.

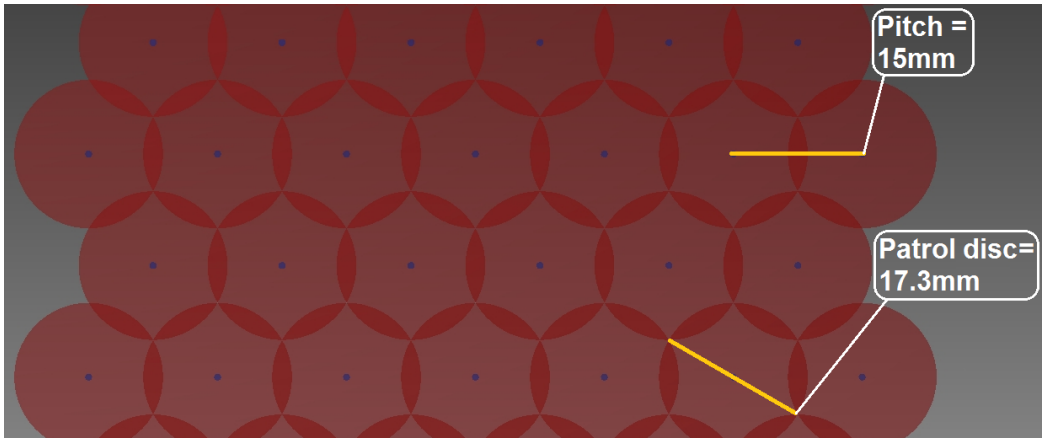

Figure 10.2: Geometry of positioner array in a hexagonal tesselation with a pitch of 15 mm and a patrol disc diameter of 17.3 mm.

Due to the disk shaped patrol area of an individual unit, overlapping areas are mandatory to be able to reach every single position within the field of view. This is the first of several, non trivial challenges, which need to be overcome. Also the sheer number of units requires special attention, so that all units are individually addressable.

#	Request:	Reference:
1	Center to center distance of two neighbouring units should not exceed 15 mm.	see section 10.4
2	The absolute positioning accuracy: 25 μm	see section 10.6
3	Filling factor of the focal plane: 100 %	see section 10.3
4	A control electronics, which is directly attached to every single positioner unit.	see section 10.4
5	The design should be self locking, so the motor power can be shut down after reaching the target.	see section 10.4
6	Provide a referencing system that is good enough, to position the fiber in the expected accuracy, without using a metrology system.	see section 10.3.3

Table 10.1: Baseline design requirements and their current status.

10.3.1 Detect and solve collisions between positioners

Since we want a filling factor of 100 %, our positioners patrol disks need to overlap. On the one side, the most obvious solution is a sophisticated software, that calculates all upcoming movements in advance and commands the positoners without collisions to their targets. On the other side, we learned from previous projects, that neither software can be perfect nor can a mechanical system's functionality, which may be affected by the environment, be guaranteed. While we expect to detect a non moving unit, either by its stall detection or even by a rise in temperature, we still needed a mechanism to detect the unlikely case of an unexpected movement of a unit.

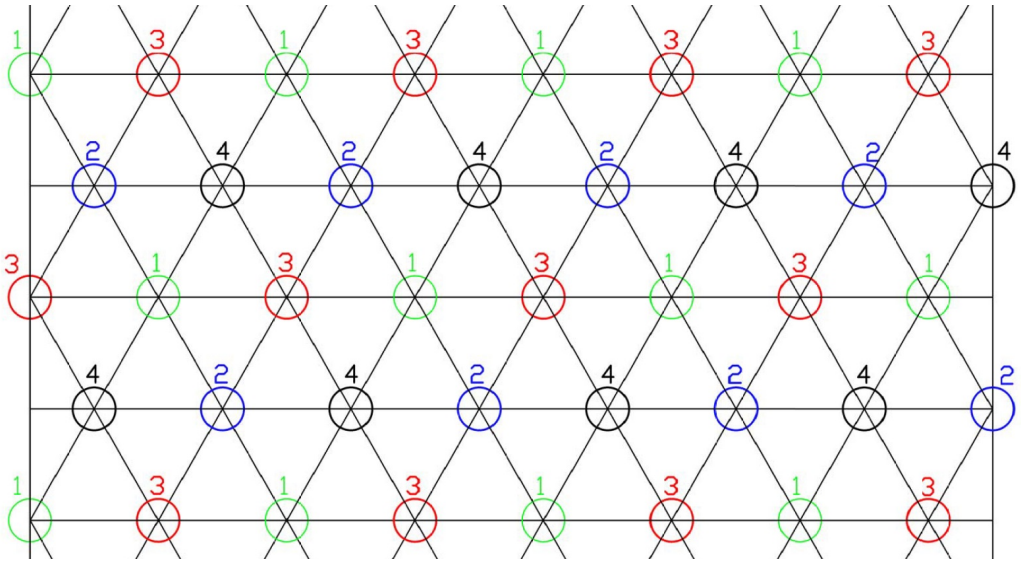

Figure 10.3: Tesselation pattern with periodical group definition.

Therefore we suggest to subdivide the array into four groups, as shown in figure 10.3. Hereby we utilize the geometrical fact, that our hexagonal like tesselation allows this grouping in a way, so no units of the same group are direct neighbours. Furthermore, all positioners are only rotated at the same time, while their Φ-stages are stowed and therefore can not collide. Once all units reached their final Θ-position, we trigger only one group at a time to move towards their Φ-stages target position. Hereby we can assure that a collision only occurs between a still standing and a moving positioner.

Using this grouping we present a mechanism that allows an independent detection of both colliding units as shown in figure 10.4.

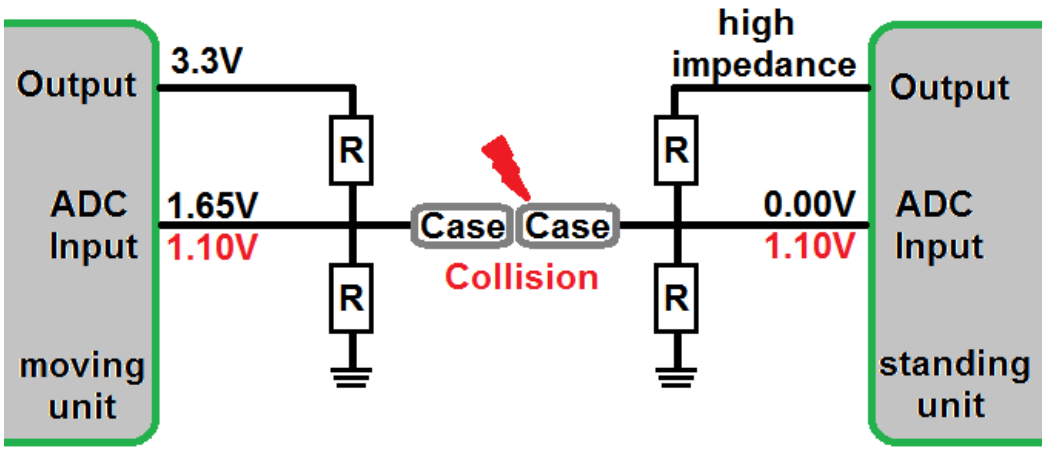

Figure 10.4: Concept of our emergency collision detection mechanism, based on the an electrical contact of both positioners. The black values represent the regular state without the collision, while the red indicate a detected collision.

While moving, each unit provides a 3.3 V signal, setting it's own case under this potential and measure's the resulting reference voltage (1.65 V) via a voltage divider. In the worst case the output still has a finite resistance towards ground causing a maximum current of 2.2 mA. The standing units equivalent output is left in a high impedance state and the resulting reference voltage (0.0 V) is monitored. If a collision occurs, both units can measure a shift to 1.1 V independently. The used 10-Bit ADC input has a resolution of 3.22 mV so a change from 1.65 V to 1.1 V causes its readout to shift significantly from about 512 to about 341.

In case of the standing unit, it even causes a bigger change, so both units can easily detect the collision. We further reach a sampling rate of 400 kHz, causing the units to detect collisions within $\sim$ 3 μs. If a collision is detected, both units trigger a high priority emergency stop via a *CAN* message containing their ID, the collision information and if they were standing or moving.

By this combination, we can uniquely identify the position of the collision, and know which positioner touched which. Now we can command both units to retreat their movement and trigger a new reference run. After a harmless collision, the array stays operational and can be reconfigured to a valid setup. If the collision caused damage, the according units can be ignored and stay at their position until they can get exchanged.

10.3.2 Unit addressing

The prototype we present is designed to operate in arrays up to several thousands of units. Since a direct communication between individual positioners and the control computer is not feasible any more on such a scale, we use the *CAN* technology as an array communication layer. The first big advantage of the *CAN* is the small number of signals needed to distribute the bus. Independent from the number of participating units, the *CAN-BUS* only needs a differential conductor pair and a third absolute reference ground. Another advantage is the availability of commercial hardware and it's common use in industry, which makes it cost effective and reliable. [43]

In our design we use the *CAN-BUS* with a bitrate of 500 $\frac{kbits}{s}$, allowing a maximal bus length of 130 m. Due to its bus topology, our *CAN* based network allows the replacement of individual units without the loss of communication. Furthermore, we use the 29-Bit extended frame identifier allowing us to define over $5.36 \cdot 10^8$ different messages. A worst case estimate of the longest message length in this configuration leads to 316 μs caused by 129 bits that need to be transmitted. To increase data security, *CAN* internally uses advanced features like bit stuffing and cyclic redundancy checks amongst others. So we can assume to transmit at least 3000 $\frac{messages}{s}$ with a 29 bit identifier and a maximum of 8 data bytes, while shorter messages will cause even less traffic on the bus.

Bit:	28 27 26	25 - 18	17 16	15 14 13	12 - 0
Allocation:	Priority	Commands	Axis	Groups	Identifier

Allocation:	Priority	Commands	Axis	Groups	Identifier
Count:	8	256	4	8	8192

Table 10.2: *CAN-BUS* bit assignment and number of attributes.

As can be seen in table 10.2 we suggest to reserve 8 possible priority levels within the identifier, which are shown in table 10.3. On the one side this allows the bus master to always keep control over the array and on the other side it gives the positioner units the opportunity to get heard even on a crowded bus.

[43] *CAN-BUS* was initially designed for the automotive industry and has become a standard system in wide parts of industry. Therefore, *CAN* components are easily available, strictly tested and thus reliable.

Prio.	Party:	Type:	Prio.	Party:	Type:
0	master	emergency stop	4	master	regular message
1	slave	emergency stop	5	slave	regular message
2	master	important message	6	master	status request
3	slave	important message	7	slave	status update

Table 10.3: Bit assignment of *CAN-BUS* messages and number of possible attribute per assignment.

Further, table 10.2 also shows that we can handle up to 256 commands. They can either be sent to a single unit, a certain subset or to all positioners at the same time. Especially commands like an emergency stop or a periodical status request are very efficient when sent with only one message to all participating units at the same time.

10.3.3 Array metrology

As already mentioned in the introduction, several other groups also work on similar designs. Most of these designs need an external metrology system like additional cameras. Usually they compare the reached position with the target position and cause small iterations to approximate the target as good as possible. In case of *BigBoss* [78] or the *COBRA* [77] positioner, even a backwards illumination of the fibers is required for those systems.

Unlike these projects our design does not require additional cameras or backwards illumination of the fibers. We rely on the accuracy of the stepper motors and gear boxes presented in section 10.4. As we show in the electronics section 10.5.1, each positioner has its own control electronics. To measure the actual position we count the number of steps which we commanded the steppers to execute.

Therefore we require a mechanical reference position which provides an initial set point. Also after a power loss or as part of the calibration a reference run is needed or strongly recommended. Since we use rather high scaled gear boxes, we need to make sure to not exceed their peak momentum of our motors. As the stepper motors and gear boxes are an inseparable unit, it is not possible to replace either the gear box or the motor without replacing the other.

Here the advanced motion controller starts to play a role. We measure the motor currents to calculate a stallguard value that changes linearly over a

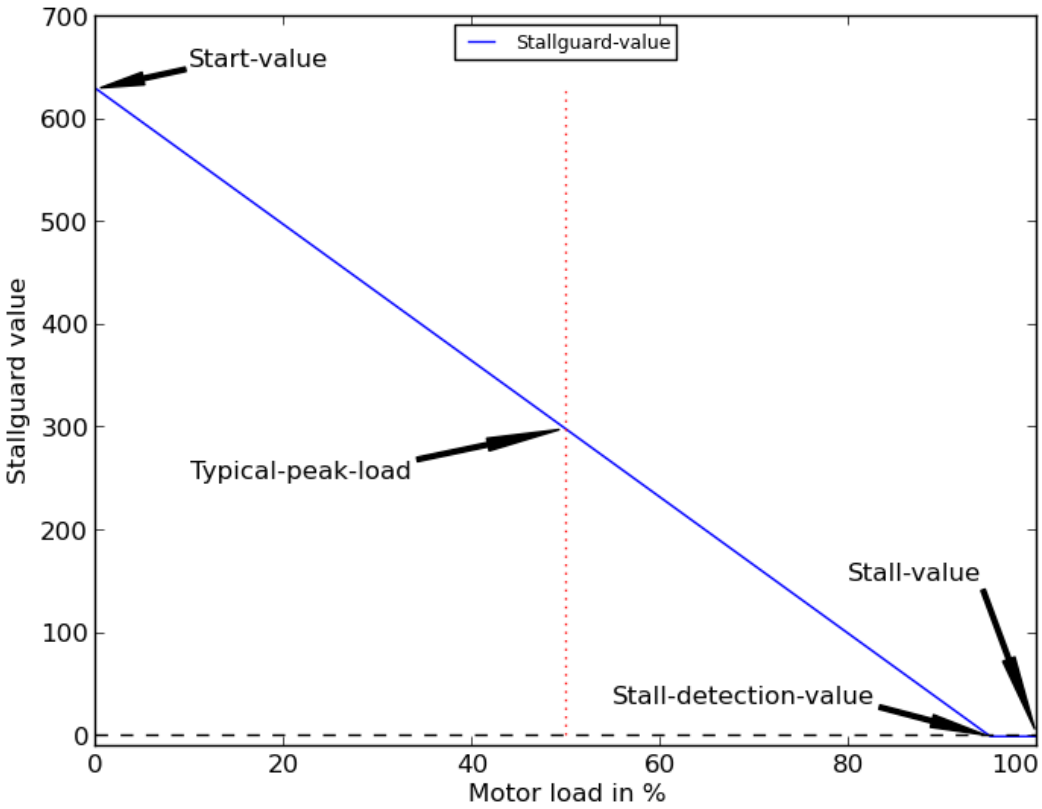

Figure 10.5: Conceptional definition of our stallguard value.

wide range of load, velocity and current settings. The stallguard value, as shown in figure 10.5, allows us to monitor the motor load of the steppers and define a secure load limit. In case a higher motor load is measured the motion controller shuts itself down immediately.

This stallguard value can be adjusted to a broad range of motor settings and other parameters. Right now this solution is supported by our control electronics, but it remains to be fully tested. Furthermore, the exact definition of the stallguard value and some adjustment also remain to be done. Even this work-package still includes risks, we are still confident that our next positioner version will feature this concept.

Keeping in mind, that we neither need iterations to reach our position, nor referencing for every single pointing, the effort put in this stall detection seems to be acceptable. So in contrast to other designs we will be able to operate without an additional metrology system. This can have a significant impact on the complexity and the costs of a big fiber-positioner array.

10.4 Mechanics

The mechanical design of our positioner is comparable to the $\Theta - \Phi$ type known from the *LAMOST* project[89]. Two rotational axes are used to position the fiber inside the patrol disc.

Detailed mechanical design: Figure 10.6 shows the current design of the built prototype. The red part on the left is used as cover and mount for the control electronics (not shown here). This electronics part is connected to the housing of the *Micro Harmonic Drive*® (MHD)-Stepper motor combination driving the center axis. To minimize bending we supported the drive shaft with an extra ball bearing inside this housing. The right part shows the mount of the gearbox-stepper motor combination of the second axis.

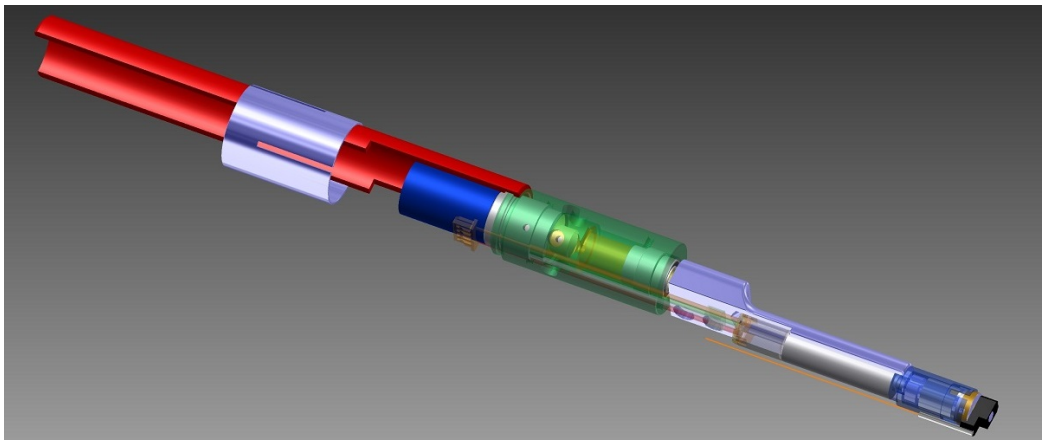

Figure 10.6: Current 3D Design of the positioner in an oblique viewing angle.

Because the planetary gear box is not backlash free like the MHD, it was necessary to preload it. The centric axis is driven by a *Faulhaber* stepper motor (AM1020-2R-A-0.25, Diameter 10 mm) directly attached to the *MHD* from *Micromotion* GmbH. The Motor needs 20 $\frac{steps}{revolution}$. The gear ratio of the *MHD* is 500:1. The excentric axis uses a Stepper Motor (0620-2R-V6-05, Diameter 6 mm)-Planetary Gear Box combination from *Faulhaber*.

The stepper motor also needs 20 $\frac{steps}{revolution}$, the ratio of the gear box is 1024:1. This leads to angular resolutions of 0.036 $\frac{deg}{step}$ for the centric and 0.016 $\frac{deg}{step}$ for the eccentric axes.
Up to now there is no mechanical stop implemented, so this work remains to be done.

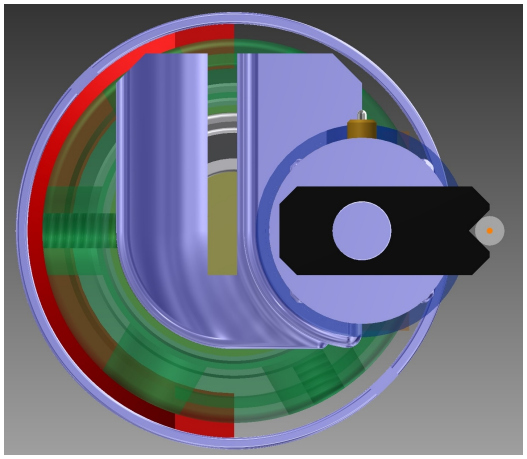

Figure 10.7: Current 3D Design of the positioner in the top view.

Geometry caused coordinate transformation: Due to our $\Theta - \Phi$ design, we have to transform the incoming xy information into the number of steps, needed to reach the target. Therefore we implement the following transformation, which provides the best possible stepper position for any given xy-coordinate:

$$n_{\Phi} = round\left(\frac{\Phi \cdot N_{\Phi} \cdot i_{\Phi}}{2\pi}\right) \tag{10.4.0.1}$$

With:

Φ-value:	$\Phi = arccos\left(\frac{r_{centric}^2 + r_{eccentric}^2 - x^2 - y^2}{2 \cdot r_{centric} \cdot r_{eccentric}}\right)$
Stepper resolution:	$N_{\Phi} = 20\frac{steps}{2\pi}$
Gear box ratio:	$i_{\Phi} = \frac{1024}{1}$

In our geometry only the Φ -stage determines the resulting radius. Consequently we first calculate the needed steps for the eccentric stepper and use the following formula, to get the offset corrected Θ stepper value.

$$n_{\Theta} = round\left(\frac{\Theta \cdot N_{\Theta} \cdot i_{\Theta}}{2\pi}\right) \tag{10.4.0.2}$$

With:

Θ-value:	$\Theta = atan2\,(x, y) + arccos\left(\frac{r_{centric}^2 - r_{eccentric}^2 + x^2 + y^2}{2 \cdot r_{centric} \cdot r_{eccentric}}\right)$
Stepper resolution:	$N_{\Theta} = 20\frac{steps}{2\pi}$
Gear box ratio:	$i_{\Theta} = \frac{500}{1}$

10.5 Electronics

As presented in the mechanical design, every single positioner includes its own control PCB. The following section will give a brief overview of the electronics concept of an individual positioner and possible electromagnetic interference (EMI).

10.5.1 Prototype electronics

The electronics prototype, we are presenting, has one *mini HDMI*[44] connector that provides incoming and outgoing signals, apart from the motor current. Further, the PCB has a standard 2x4 header to connect both stepper motors. Due to the specification of our semiconductors and missing isolation space, we need to restrict our design to a motor voltage of 16 V and a maximum motor current of 1.1 A, leading to a maximum driving power of 17.6 W per motor. Obviously, this is way more, than we can use to drive a single positioner, that is supposed to run in a big array.

Mode:	centric motor	eccentric motor	logic controller	motion controller	misc. parts	≈ Sum
Idle	0 mW	0 mW	6.6 mW	66 mW	5 mW	78 mW
Move	195 mW	180 mW	9.9 mW	132 mW	45 mW	562 mW

Table 10.4: Detailed power consumption per positioner, break down to single components. The values in the moving column, represent the worst case, when every component works at its maximum level, which is not the case during regular operation. Therefore we can estimate the power consumption of an individual positioner to ≈ 500 mW.

In fact we use a 2 V motor with 130 mA and 260 mW maximum power for the centric motion and a 6 V motor with 40 mA and 240 mW maximum power for the eccentric motion. During regular operation we even only use 75 % of this power to position our fibers. When the positioners are at rest they are even left powerless and only hold in position by self-locking gears. As shown in table 10.4 the PCB contains four major semiconductor devices, which are represented in block diagram 10.8.
First the *CAN* interface is handled by a 32-bit ARM® Cortex-M0® microcontroller (A). It interprets all incoming *CAN* commands and triggers the requested action via a serial peripheral interface (*SPI*). The movement and

[44] We decided to use this commercially available connector, due to its high number of conductors, paired with its small physical size. **Note**: We use a proprietary pin assignment!

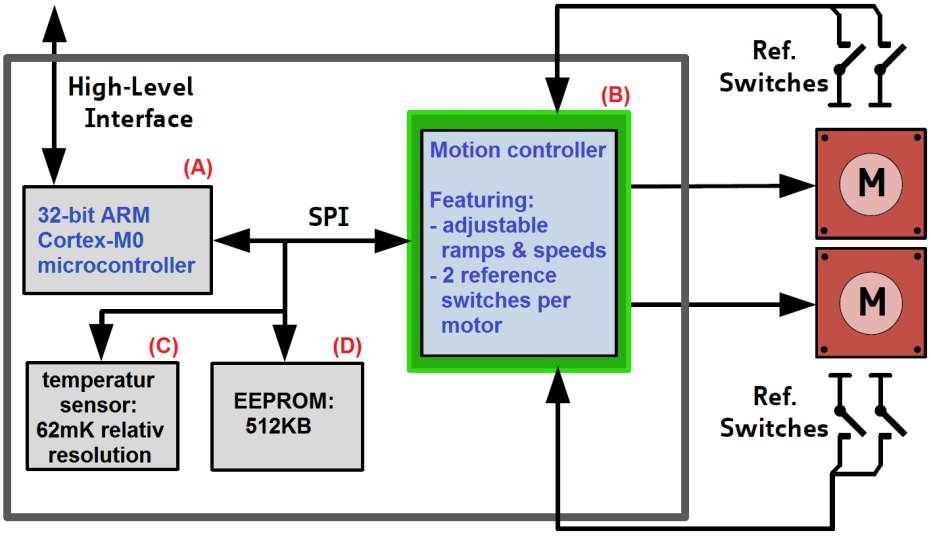

Figure 10.8: Positioner block diagram, including references (A,B,C,D).

the according current feed for the steppers, are handled via the motion controller (B). Monitoring the PCBs temperature is done by a semiconductor sensor (C) with a relative precision of 0.0625 K, linked to the *SPI-BUS* . It is further possible to save the motor configuration data on the nonvolatile 512 kB EEPROM (D). This device also opens the option to store calibration and other important data, so they are remanent.
Using state of the art technologies, we managed to shrink the electronics from our initial development PCB with roughly 80.0 mm × 100.0 mm as mentioned in section 10.2 down to only 13.5 mm × 40.0 mm, which is roughly 15 times smaller. By choosing the smallest available package sizes for both controllers we could limit the board width to 13.5 mm. Our first hand solder prototype can be seen in the pictures 10.9 and 10.10.

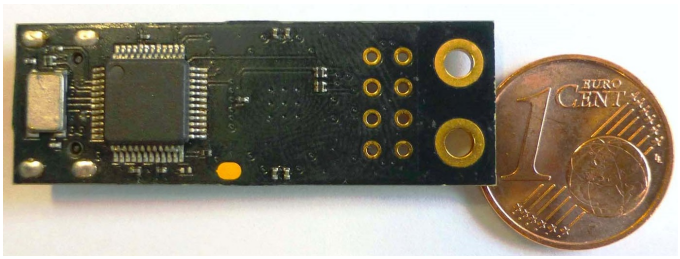

Figure 10.9: Bottom view of our prototype electronics, with an European cent coin (⌀16.25 *mm*) for reference. Only the microcontroller and its direct periphery is located on this side.

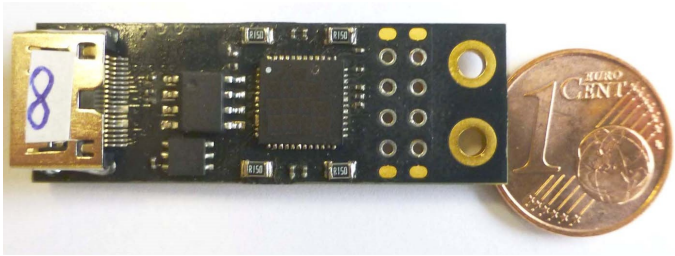

Figure 10.10: Top view of our prototype electronics, with an European cent coin ($\varnothing 16.25\ mm$) for reference. All secondary chips, like the temperature sensor, the EEPROM and the motion controller are placed on this side.

All resistors and capacitors are as small as reasonably possible. In fact we use the 0201 package size, which defines components of 0.6 mm length, 0.3 mm width and 0.2 mm height.
For implementing our circuit design on a PCB of that width, we decided to use a 8 multilayer PCB with 4 planes and 4 layers used for signals. The detailed layer buildup can be seen in figure 10.11.

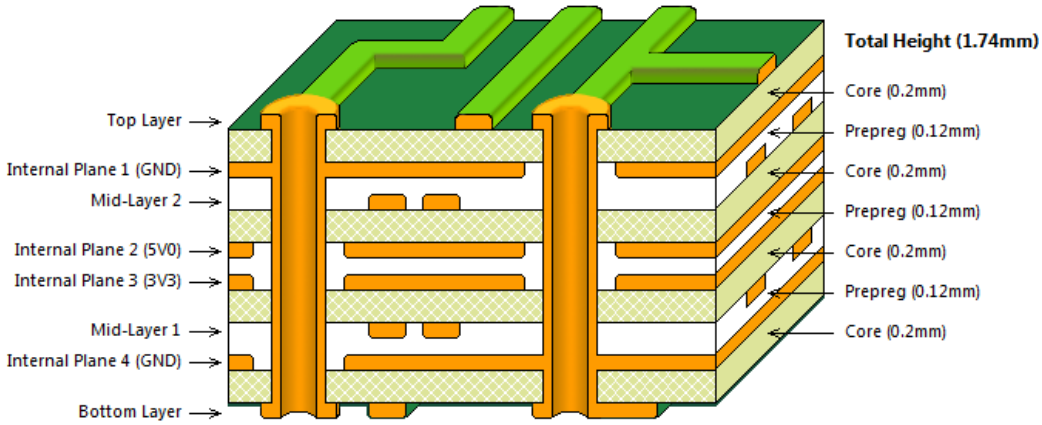

Figure 10.11: Layer buildup sequence of the positioners PCB.

Top and bottom layer, are only used to contact the components, all signals are further directed through vias in the better shielded inner layers. The remaining area on top and bottom are flooded with a hatched shield pattern which reduces the incoming as well as the outgoing EMI best possible. In addition to the shield, the following ground layer provides further shielding for the inner signal layers. To reduce crosstalk and other interferences between signal layers, they are individually encapsulated between ground and DC voltage supply.

10.5.2 Facing EMI

Due to our long term experience with EMI inflicted malfunction on the *Wendelstein Observatory*, we worried about EMI immunity early on. As a matter of fact, the peak of mount Wendelstein is not only an observatory, it further hosts among other smaller a high-power radio and TV VHF-antenna of 55 m height and up to 100 kW transmission power. This makes the *Wendelstein Observatory* a very EMI contaminated place, with field strengths up to 30 $\frac{V}{m}$ over the frequency range from 30 MHz to 300 MHz.

EMI immunity of a single positioner: According to the frequency range, we have to face EMI with wavelengths from $\lambda = 10$ m down to $\lambda = 1$ m. Taking into account the size of an individual positioner and its PCB (<5 cm), we should not encounter direct EMI effects on a single positioner as the coupling antenna is smaller than $\frac{\lambda}{20}$. So, even the minimization of our PCB is more forced by the mechanics, it also helps to reach EMI immunity. Which is further enhanced by the 8 layer design, as presented in figure 10.11. Nevertheless, we calculated the effects of the EMI field at *Wendelstein Observatory* in first order approximation. Even when in reality higher order effects play a role, the following estimation provides a good guess of the EMI impact on a single positioner. Due to the overall thickness of the PCB and its components, the worst effective coupling antenna would be shorter than 5 mm. In reality the electric field will cause a dV between a signal and its reference layer which are always adjoining layers and hence even closer. This leads to an effective dipole length of less than 0.5 mm. Keeping in mind the EMI wavelength range of $\lambda \in [1\ m,\ 10\ m]$, we use the following approximation to get a well educated guess for the introduced difference voltage:

$$dV \;=\; \vec{E} \;\cdot\; l \;=\; 30\,\frac{V}{m} \;\cdot\; 5 \cdot 10^{-4}\,m \;=\; 15\,mV \qquad (10.5.2.1)$$

Compared with the reading $\Delta_{max} V_{GPIO} = 400\ mV$ level tolerances of our digital 3.3 V logic, this 15 mV offset is negligible. Even the dV over the whole PCB is less than 150 mV and can therefore be ignored.

EMI immunity of an array of positioners: While a single positioner is rather immune to EMI, a whole array might behave differently. In the end there is especially one part that may be affected by EMI, which is the field bus system, that handles the communication layer between individual positioners. Due to the need for electrical conductors, a connection board just behind the positioners, is the most vulnerable part of the array and can provide possible antennas for EMI.

In addition to the systematic reasons for the *CAN-BUS* its EMI robust difference signal logic is another advantage. Every *CAN-BUS* receiver has an internal layer of error handling which checks received messages for their validity. In case just one positioner gets an invalid message, the transmitter repeats its message until all attached *CAN* receiver agree on the validity.[45]

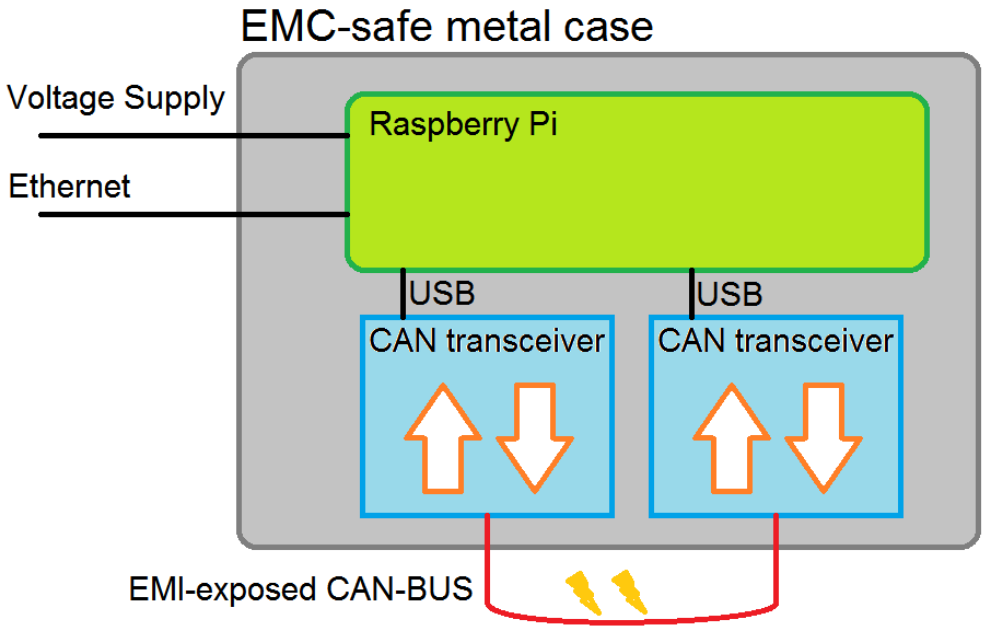

Figure 10.12: Block diagram of the *CAN-BUS* test setup at *Wendelstein Observatory*.

Nevertheless, we performed several *CAN* test runs of several days duration each, to measure possible communication delays caused by EMI. The test was performed at the *Wendelstein Observatory*, using a *Raspberry Pi*® microcomputer[46], which controlled two *USB to CAN-BUS converters*, as it can be seen in block diagram 10.12. All components were placed within an EMI shielded metal box, so only the *CAN* transmitting cable was exposed to the external EMI. During the test period, we send an identical test message from one *CAN* note to the other every 500 ms. After receiving the periodical, initial message, the receiving converter replies immediately with a different message.

[45]Note, that the number of participants does not have to be known for the validity check of a *CAN* message.

[46]Raspberry Pi is a trademark of the Raspberry Pi Foundation.

Both the sent and the received messages were compared and locked with a timestamp. We tested the *CAN* transmission through the two different types of cables defined in figure 10.5.

Cable:	1		2
Style: Conductor: Shield:	twisted-pairs 4 conductor shielded		ribbon cable 10 conductor unshielded
Wire:	Signal:	Wire:	Signal:
1 2 3 4	CAN-High *CAN* Low *CAN* GND NC	1 2 3 4-10	CAN-High *CAN* Low *CAN* GND NC
Testcycles:	995472		995366
On time:	994035		994081
Delayed:	1437 ≈ 0.1%		1282 ≈ 0.1%

Table 10.5: Cable details for the *CAN* EMI test. The twisted pair cable has the following conductor pairs: 1&2, 3&4

Figure 10.13 shows plot of a small part of the log file. Due to operating system effects, the typical dT of two transmissions is 520 ms. Furthermore, polling based effects cause a readout scatter of ± 10 ms. The scatter is large compared to the worst case transmission time of roughly 0.3 ms. Consequently we can assume more delayed transmissions, to be impacted by EMI. The results presented in the lower part of table 10.5, show that the *CAN-BUS* proved to be a very EMI robust communication layer which is only effected by very seldom and minor communication delays.
The data contains obvious operating system effects, like a file buffer, which periodically occur every 24 hours after starting the measurement. Taking them into account, the worst delay for a single transmission was in the order of 10 ms, which could be caused by another random operating system task or interrupt.

In the end we present an early working prototype that withstands even very strong EMI fields, like present at the *Wendelstein Observatory*. Without a complete positioner array, there is not much EMI testing left that can be done so far until we can expose such an array to a dedicated test in an EMI laboratory.

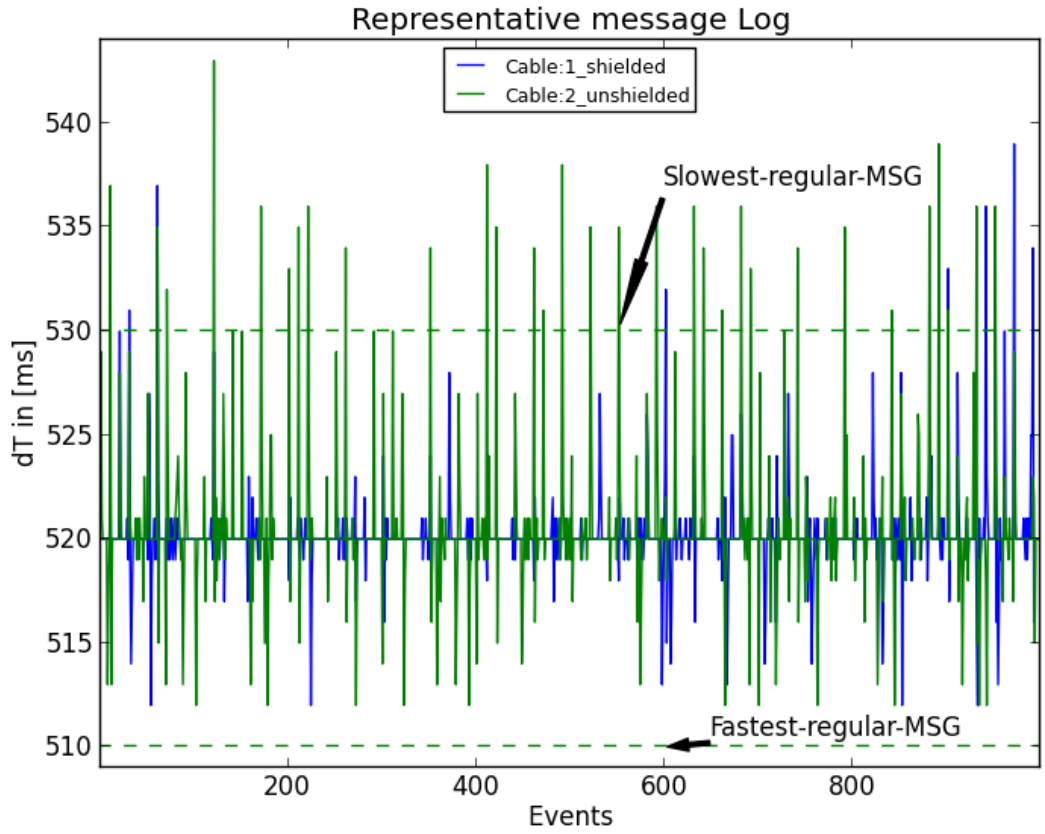

Figure 10.13: Representative difference time diagram of 1000 transmissions($\approx$ 0.1%).

10.6 Positioning precision measurement

Even our design positions without iteration or a metrology system, we choose a optical test set up, presented in figure 10.14, to precisely measure our pointing accuracy.

The first existing prototype of our positioner was a challenging task to manufacture. Due to the prototype status all mechanical parts were manufactured using manually controlled milling and turning machines. The requested tolerances down to 50 μm and below, were more or less achievable. For example the length of the prototypes Φ-stages deviate slightly from its intended value. To measure the positioning accuracy and the mentioned machining discrepancy we set up the optical test, shown in figure 10.14.

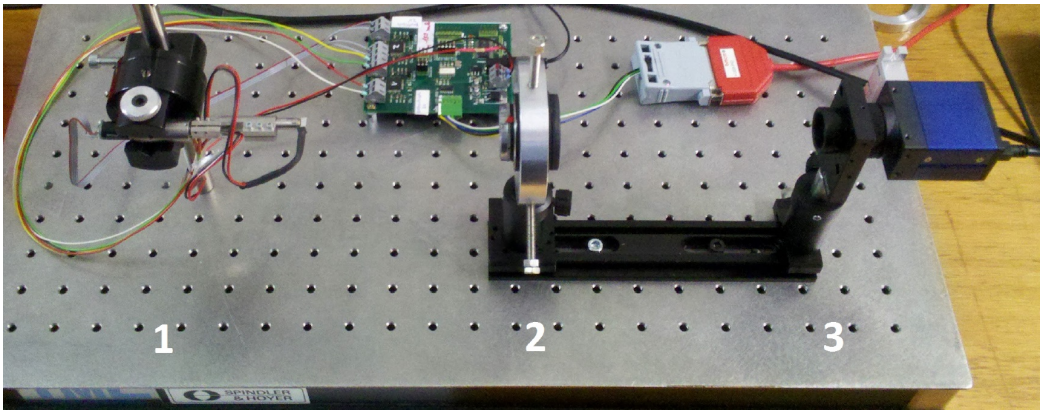

Figure 10.14: Optical prototype test bench, with the following components: (1) positioner on universal mount, (2) optical zoom and (3) CCD camera. Taken from **Degwert 2014**[16].

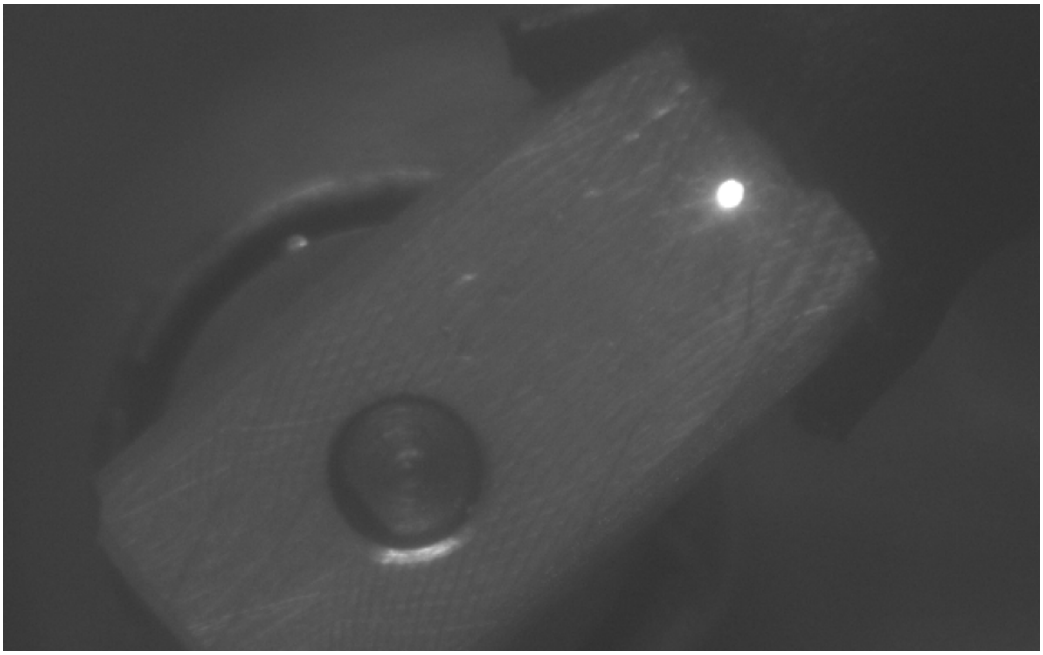

Figure 10.15: CCD image of the Φ-stage with illuminated test point. Taken from **Degwert 2014**[16].

As shown in figure 10.15, we replace the fiber with a small LED, which is exposed through a 200 μm pinhole. This results in a big and bright spot on the CCD images. To get a precise measurement of the center of this spot, we fit a 2 dimensional Gaussian function, which allows to measure the

center with an accuracy of less then a pixel. The according code is part of the *FITSTOOLS* library, developed by **Gössl et al. 2002**[32]. While testing the stability of the algorithm under different light conditions, the center of the light point was stable to 3.8 % with $1\sigma = 1.8$ % of a pixel. Since the algorithm is stable well below our desired resolution we neglect its readout error for the following measurements. The optical zoom of the system allows us to switch between different optical resolutions. To measure global characteristics like the radius of the arm or the eccentricity of the movement we choose a resolution of 18 $\frac{\mu m}{pixel}$ to fit the whole patrol disc on a single CCD image. For all other measurements, like the positioning accuracy, we reconfigured the optics to 4 $\frac{\mu m}{pixel}$. On the one side it turns out that our manually manufactured prototype's eccentric radius deviates from its designed 4.325 mm value. In reality we measure it to be only 4.27 mm with standard deviation of $\sigma = 4.4\ \mu m$. On the other side, the centric radius also deviated from 4.325 mm to 4.43 mm with $\sigma = 7.2\ \mu m$. Adding those values up, one gets an effective maximum radius for the fiber/LED position of 8.7 mm which is pretty close to the desired value of 8.65 mm. So we come to the conclusion that the patrol disc size fits the designed value quite well. **Degwert 2014**[16]
Since we now know our real arm lengths $r_{centric}$ and $r_{eccentric}$, we can implement the coordinate transformation presented in section 10.4. The results are step commands that lead as close as possible towards the desired target position, assuming an equidistant step size. During our measurements we realized that this assumption is not valid.
Indeed the mean size of a step usually fits the theoretical equidistant step size rather well, except some sporadic but significant deviations. As a result, our absolute positions deviate randomly from their targets. This effect is caused by smallest manufacturing tolerances of the steppers and the gear boxes. We could prove the manufacture's information, that the system is periodical after two full rotations. In addition we can see, that it does not make a difference if we just increment by a single step or if we arrive from a distant position with full speed. The motion controller's logic always realizes an adjustable, smooth acceleration and deceleration.
As a result of these random deviations, we achieve an absolute positioning accuracy with a mean value of 22 μm with $\sigma = 15\ \mu m$. Unfortunately we have sporadic positions, where we measure deviations of up to 43 μm, which is worse than our goal of 25 μm absolute positioning accuracy. Unlike the absolute precision, the repeatability is measured with a set of four randomly distributed target positions[47]. Each target is pointed at once for reference.

[47]The absolute accuracy is measured at 10 randomly picked positions, distributed over the

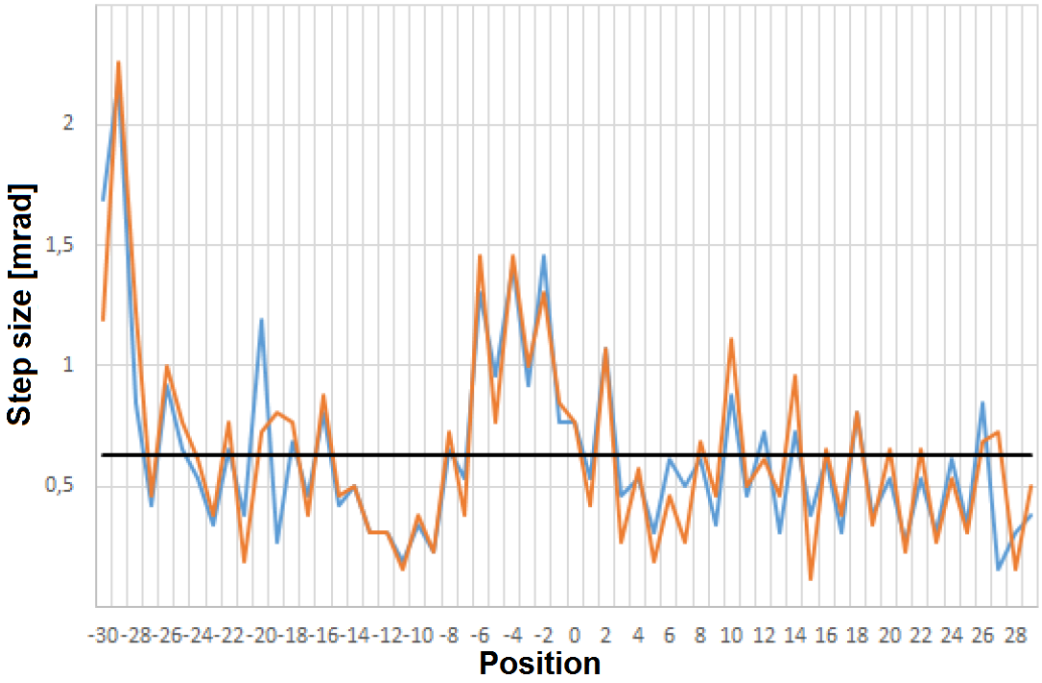

Figure 10.16: Step size diagram, showing the step size in mrad on the y axis plotted against the step number on the x axis. Blue: step size with single step increment. Orange: step size with 2π plus one step increment. Black: theoretical step size. Taken from **Degwert 2014**[16].

Afterwards the positioner is commanded far away and back to these spots. The relative precision proved to be 7 μm with $\sigma = 4$ μm and a maximum deviation of 16 μm. If we now take this random relative positioning error into account, we see that our absolute accuracy is not as good as it seemed earlier. Nevertheless we plan to implement a correction algorithm, that corrects for the constant manufacturing deviations. Therefore an automatic calibration test bench could be used to measure every individual stepper and gear box position. For example our current test bench could be automated by a script to command the positioner, the camera and analyses algorithm. Measuring these $20 * 500 + 20 * 512 = 20240$ positions could be automatically done within $\approx$ 34 minutes [48] per positioner. The algorithm which predicts the local deviation from the target position remains to be tested.

whole patrol disc.

[48] We assume a measuring speed of $1 \frac{position}{100\ ms}$, with 50 ms exposure time. The measurement of every possible position ($102.4 \cdot 10^6$), would even with a high sampling rate of $1 \frac{position}{100\ ms}$ take more than 118 days per positioner. Furthermore such an amount of data can not nearly be stored and processed within a single positioner unit.

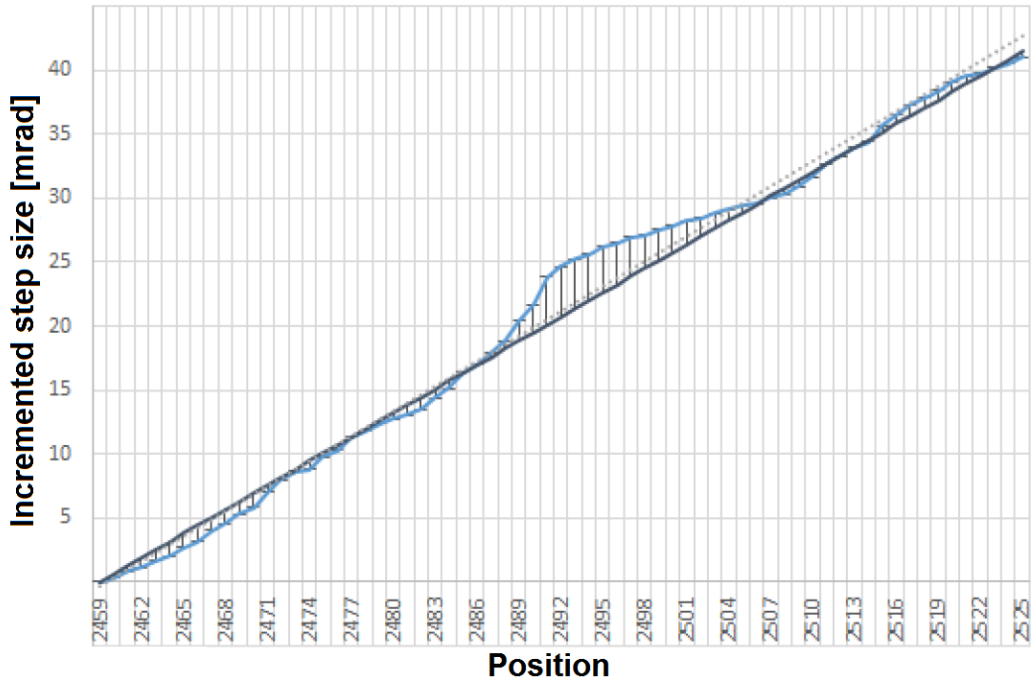

Figure 10.17: Integrated step sizes, showing the steps sum in mrad on the y axis plotted against the step number on the x axis. Blue: step integral. Black: theoretical integral, assuming uniform and equidistant steps.
Taken from **Degwert 2014**[16].

The algorithm's approach is to simply integrate the individual steps until they approach the target the best possible way. This could significantly improve the absolute accuracy with the disadvantage of the additional work and time effort for an automated test bench. A plot of the integrated steps from an exemplary region is shown in figure 10.17.

10.7 Summary

As already shown in table 10.1 we more or less reached all of our design drivers as summarized in table 10.6. While developing, building and testing the prototype, our design proved to be flexible and well scaled. For example, we initially assumed the arm radii to be accurate enough, while we realized during the tests that this is not true. This could be fixed by a minor software change within our microcontroller, which will also allow us to correct for the

	Request:	Status:
1	Center to center distance of two neighbouring units should not exceed 15 mm.	done
2	Absolute positioning accuracy goal: 25 μm	22 μm ($\sigma = 15$ μm) $dxy_{max} = 43$ μm
3	Relative positioning accuracy goal: 10 μm	7 μm ($\sigma = 4$ μm) $dxy_{max} = 16$ μm
4	Filling factor of the focal plane: 100 %	done
5	A control electronics, which is directly attached to every single positioner unit.	done
6	The design should be self locking, so we motor power can be shut down after reaching target.	done
7	Provide a referencing system that is good enough, to position the fiber in the expected accuracy, without using a meterology system.	Mechanical reference needed

Table 10.6: Table of design drivers and there current status.

stepper and gear box tolerances. The following list shows the major tasks that left to be done in the future:

(1) We need to build a set of at least seven positioners for collision tests.

(2) The next version needs to be equipped with a fiber fixture.

(3) A full array of positioners needs to pass an EMI test.

(4) The mechanical reference point needs to be implemented in the design.

(5) Test the calibration algorithm as proposed in the end of section 10.6, in combination with an automated test bench.

Finally our design's 15 mm pitch is comparable to other $\Theta - \Phi$ or $R - \Theta$ positioners and more important, we do neither need an iteration procedure nor an external metrology system to reach our target positions. In addition we utilized contemporary technologies like the *CAN-BUS* and proved to be able to develop smallest size control electronics, which are cost and energy efficient. Both will have influence also on other system parts or projects and will improve instrument performance and reliability in the future.

Update 2016: The *Universitäts-Sternwarte München* was partner in the *4MOST*-consortium from the official Kick-off into the early design phase. We left *4MOST*, due to a reorientation of our instrumentation group towards the MICADO project, which started 2015. Hence further investigations towards our fiber positioner solution have been stopped.

Chapter 11

SCS2: An active mirror control

The following chapter contains a detailed version of the published paper:

Upgrade of the HET segment control system, utilizing state-of-the-art, decentralized and embedded system controllers. [37]

I especially want to point out the contributions from Josef Richter, Herman Kriel[49] and the local staff of the Hobby-Eberly-Telescope.

> *"The Hobby-Eberly Telescope (HET) [11.1] is an innovative large telescope, located in West Texas at the McDonald Observatory. The HET operates with a fixed segmented primary and has a tracker, which moves the four-mirror corrector and prime focus instrument package to track the sidereal and non-sidereal motions of objects. We have completed a major multi-year upgrade of the HET that has substantially increased the pupil size to 10 meters and the field of view to 22 arcminutes by replacing the corrector, tracker, and prime focus instrument package. The new wide field HET will feed the revolutionary integral field spectrograph called VIRUS, in support of the Hobby-Eberly Telescope Dark Energy Experiment (HETDEX), a new low resolution spectrograph (LRS2), an upgraded high resolution spectrograph (HRS2), and later the Habitable Zone Planet Finder (HPF)."*[41]

Important note: Most of the content of the following chapter is similar or equal with the content of Häuser et al. [37]. Such content will hence not be cited any more until the end of this chapter.

[49] Herman Kriel is facility manager of the HET observatory.

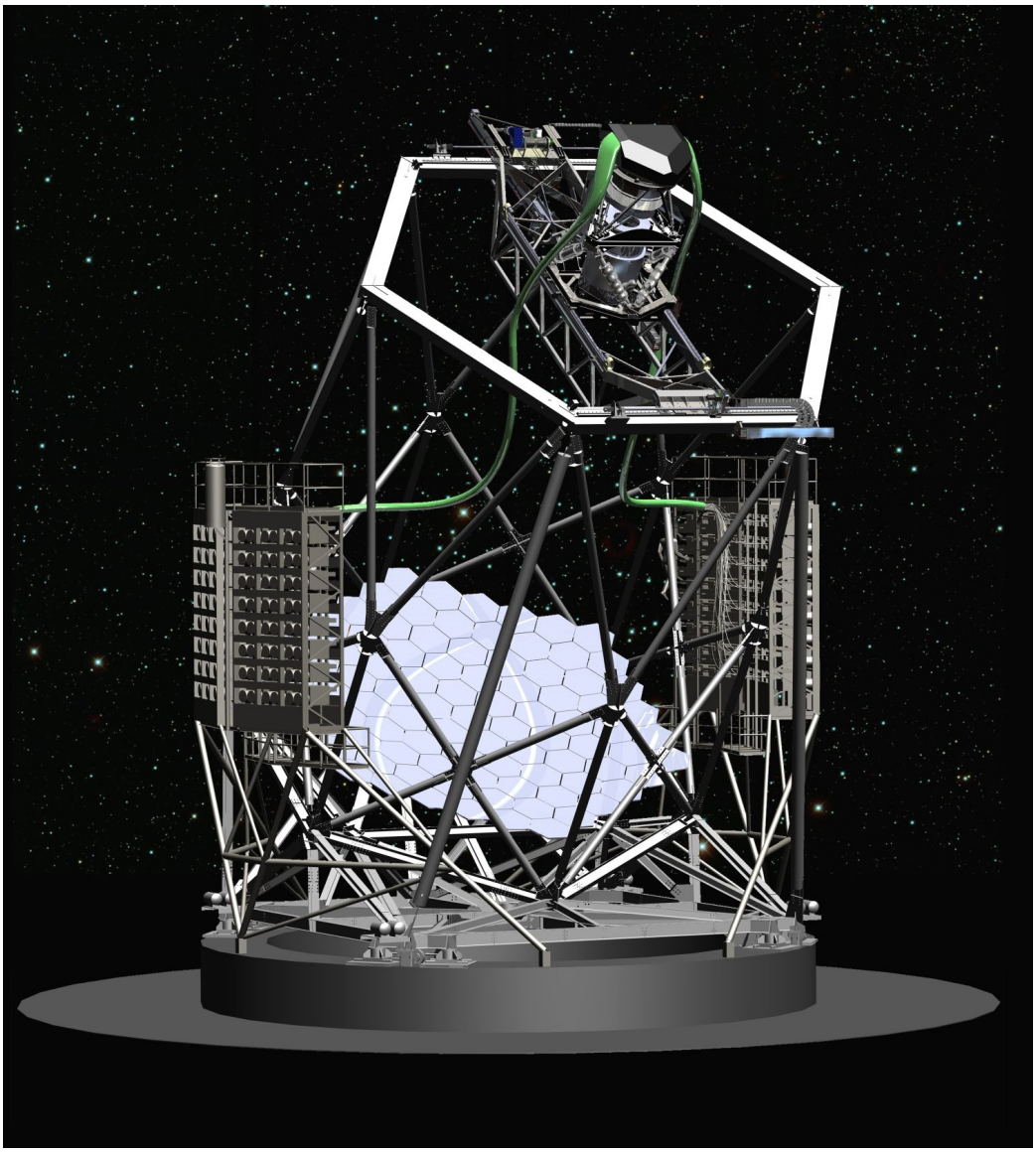

Figure 11.1: Current *HET*design including hardware changes due to the wide-field corrector update and the additional VIRUS-spectrograph enclosures to both sides of the primary.
Details on the wide-field upgrade can be found in Hill et al. 2016 (*Deployment of the Hobby-Eberly Telescope wide-field upgrade.*) [42]
Details on VIRUS can be found in Hill at al. 2016 (*VIRUS: first deployment of the massively replicated fiber integral field spectrograph for the upgraded Hobby-Eberly Telescope.*) [43]

11.1 Abstract

Together with the ongoing major instrument upgrade of the Hobby-Eberly Telescope (*HET*) we present the planned upgrade of the *HET* Segment Control System (SCS) to SCS2. Because *HET*'s primary mirror is segmented into 91 individual 1-meter hexagonal mirrors the SCS is essential to align and maintain the mirror throughout an entire night of observations. SCS2 will complete tip, tilt and piston corrections of each mirror segment at a significantly higher rate than the original SCS. The new motion control hardware will further increase the system's reliability. The initial optical measurements of this array are performed by the Mirror Alignment Recovery System (MARS) and the *HET* Extra Focal Instrument (HEFI).

Once the segments are optically aligned, the inductive edge sensors give sub-micron precision feedback of each segment's positions relative to its adjacent segments. These sensors are part of the Segment Alignment Maintenance System (SAMS) and are responsible for providing information about positional changes due to external influences, such as steep temperature changes and mechanical stress, and for making compensatory calculations while tracking the telescope on sky. SCS2 will use the optical alignment systems and SAMS inputs to command corrections of every segment in a closed loop. The correction period will be roughly 30 seconds mostly due to the measurement and averaging process of the SAMS algorithm.

The segment actuators will be controlled by the custom developed *HET* Segment MOtion COntroller (SMOCO). It is a direct descendant of the embedded, CAN-based system and instrument control tool-kit, developed by the University Observatory Munich. To preserve the existing *HET* hardware layout, each SMOCO will control two adjacent mirror segments. Unlike the original SCS motor controllers, SMOCO is able to drive all six axes of its two segments at the same time.

SCS2 will continue to allow for sub-arcsecond precision in tip and tilt as well as sub-micro meter precision in piston. These estimations are based on the current performance of the segment support mechanics. SMOCO's smart motion control allows for on-the-fly correction of the move targets. Since SMOCO uses state-of-the-art motion control electronics and embedded decentralized controllers we expect about 1 kW reduction of waste heat emission as well as less maintenance time.

11.2 Introduction

Due to *HET*'s 91 individual 1 m hexagonal mirrors with each three actuators, a system is required which controls all 273 axes to align the segments relative to the adjacent segments and to the general surface of the primary sphere. In general, the alignment is maintained by feedback loops between a diagnostic subsystem and the segment control subsystem. Movement of the individual segment is completed by stepper-motor driven actuators on three axes I, J, and K. The diagnostic subsystems currently being used at *HET* are the Segment Alignment Maintenance System (SAMS), Mirror Alignment Recovery System (MARS), and the *HET* Extra Focal Instrument (HEFI).

Each diagnostic system can be given so called *move authority* over the Segment Control System (SCS). *Move authority* is a SCS software term that designates which diagnostic subsystem has the authority to command SCS moves. The SAMS subsystem is made up of inductive edge sensors, which measure relative shear and gap between adjacent segments. The control software calculates tip, tilt, and piston moves for each mirror that will minimize sensor errors relative to initial reference values.

MARS and HEFI are subsystems that give additional optical feedback on the alignment of the primary, rather than SAMS electro-mechanical feedback. The optical feedback loop is used during the daily calibration of the telescope before the actual science operation to gain optimal starting values for the SAMS's electronic feedback loop which runs throughout the whole night to keep the segments aligned.[83]
In *HET* terms, the segment control system consists of its diagnostic subsystems which give feedback on the segments current positions and the actual SCS which actuates the segments. While the *HET* has been heavily upgraded and is back in science mode to pursue the Hobby-Eberly Telescope Dark Energy Experiment (HETDEX) and its other projects, some facility systems, like SCS, also need a major overhaul.

The main reasons for this overhaul are that the vendor of the motion controllers (Diamond Motion) is no longer in business and their hardware therefore no longer available. Given those two facts it was rather clear that the SCS will have to be replaced by a new system. Given the need for a redesign we took the opportunity to solve several of the old SCS's weak points. Within the following chapters, those weaknesses will be addressed while the advantages of the new SCS2 will be pointed out.[40]

The following bottom up system design overview from the individual segment all the way to the high level software serves the reader as a guideline for the upcoming chapters.

SCS2 design overview:

- **Segment topology:** To establish context for the segment motion, the mechanical layout of an individual, 1 m hexagonal mirror and its three actuators is explained. (Section: 11.3.1)
- **Actuator: functionality** Each mirror axis is actuated by a stepper motor-gearbox assembly, the moment of which is transmitted to the mirror segment through the mechanical advantage of a lever. (Section: 11.3.2)
- **Controller:** Each segment has its own CPU and motion controller to handle all three motor drivers; hence, movements are executed simultaneously to every segment. (Section: 11.4.1)
- **CAN Bus:** Each CPU is an active node on a single CAN bus network which is hosted by a commercially available CAN/Ethernet bridge. (Section: 11.4.2)
- **SMOCO:** A set of four controllers is implemented on a single SMOCO board which is the main component of SCS2. To operate the entire array of mirrors, 23 SMOCOs are connected via a 19" rack backplane. (Section: 11.4.3)
- **CAVE:** All SMOCOs are connected via a 19" rack backplane within the Common Actuator Vectorization Entity. CAVE further houses the power supplies, the CAN bus and the cabling bulkhead. (Section: 11.4.4)
- **Power supplies:** SCS2 has three separate power networks. 1. $V_{logic} = 12VDC$: CPU and communication, 2. $V_{sensor} = 24VDC$: Hall Effect sensor and 3. $V_{Axes} = 24VDC$: Stepper motor (Section: 11.4.5)
- **Control software:** Due to the modular *HET*software design, only minor parts of the high level software have to be changed. In addition, an interface code which translates high level commands into the according CAN messages is needed. (Section: 11.5.3)

11.3 Mechanics

While the actual mechanics of the initial SCS system still performs on a good level and proven to be maintainable, the SCS2 upgrade does not aim to replace this crucial part of the system.

11.3.1 Segment topology

In order to keep 91 individual segments aligned on the primary sphere, correctional tip, tilt and piston motions are executed by three linear actuators, labelled I, J, and K, located at 120-degree intervals. They are placed on the vertices of an equilateral triangle in the segment support as can be seen in figure 11.2. Tip and tilt rotations are piston free. Consequently, we get the following instructions to execute the smallest possible tip, tilt and piston movements as shown in table 11.1.

Axes		I	J	K	Units
Δtip	=	+2	-1	-1	± 0.024 arcseconds
$\Delta tilt$	=	0	-1	+1	± 0.014 arcseconds
$\Delta piston$	=	+1	+1	+1	± 0.018 microns

Table 11.1: Instruction table for tip, tilt and piston steps.
Tip and tilt movements are designed to be piston free.

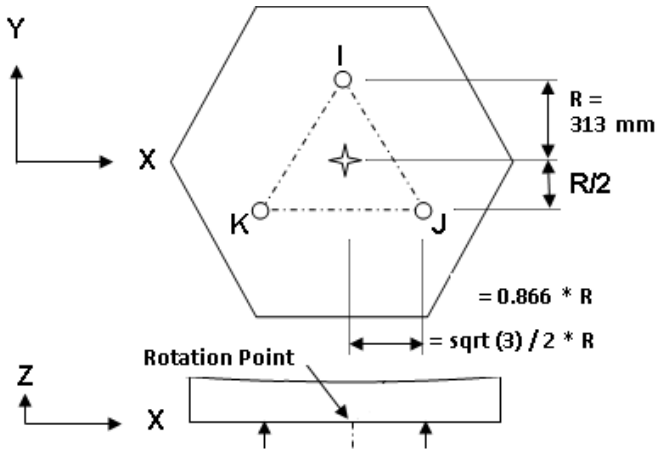

Figure 11.2: HET mirror segment design schematic. The upper sketch shows the actuator location and geometrical placement as a top view of a single segment. The lower part illustrates the support and rotation point of all non-piston motions.

11.3.2 Actuator functionality

After the *HET* staff de-constructed the existing actuators, it was found that crucial parts like the stepper-motor/gearbox assembly are long-term commercially available parts. Therefore, it has been decided to keep the working motor-gearbox configuration to minimize the functional risk of the update.

Each linear actuator consists of a 2-phase stepper motor (24 V 24 steps/rev.), a gearbox (485:1) and a 40.0000 turns/inch drive screw. Figure 11.3 shows the functional scheme of the actuator.

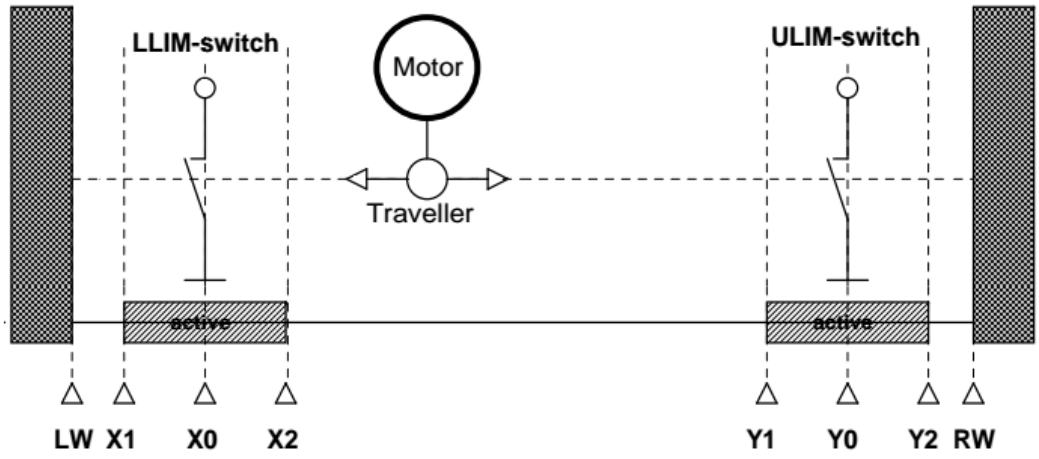

Figure 11.3: Functional actuator schematic. X/Y0 locate the nominal switch positions, while X/Y1 and 2 indicate the activity range of those hall effect switches. Finally LW and RW indicate the ultimate mechanical limits which the actuator should never hit. The functional travel range is between X0 and Y0.

Each actuator operates over a range of 480,000 actuator steps. The upper and lower limits of travel are detected via hall-effect sensors in the actuator housing. On the original SCS setup, these hall-effect sensors drove a high-impedance, 5V TTL input on the controller.

In this configuration they were highly susceptible to electro-magnetic interference (EMI) which caused random false-triggering. SCS2 uses the same hall-effect sensors to drive a 5 mA closed-current loop at 24V. This not only solves the EMI contamination but also allows the detection of broken wires. To avoid internal EMI, the motor signals and the sensor signals are routed on separate and shielded cables as can be seen in figure 11.4.

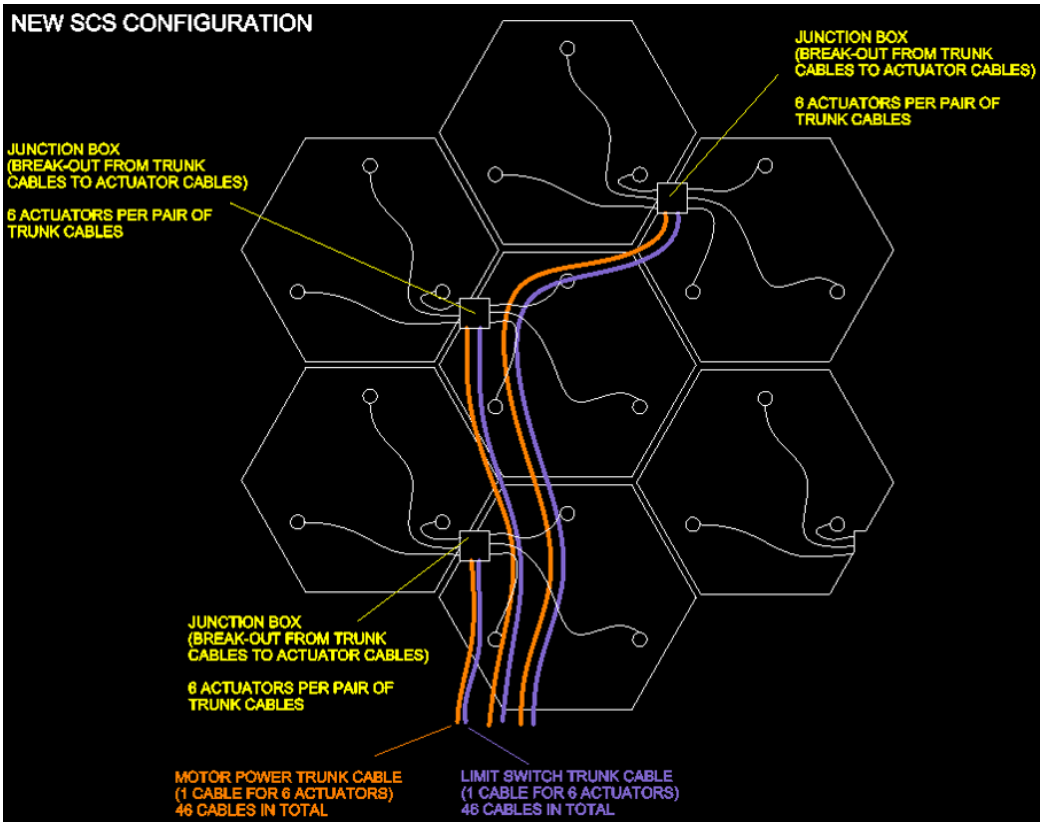

Figure 11.4: Motor and limit switch cabling schematic. The white hexagons represent the *HET* main mirror segments viewed from behind. The small white junction boxes replace the former SCS controllers and only split the common motor and switch cables into individual axes.

11.4 Electronics

In contrast to the reliable mechanical design of the old segment control system, the electronic part of the system has never really reached the expectations and was inconvenient ever since installation. Therefore, we decided to redesign the whole controlling hardware and used the USM DECANIC system as the platform as explained in subsection 11.4.2. The newly designed controller is based on the circuit design as described in section 10.5. The reuse of this well tested hardware allowed us to rapidly produce a first prototype. In contrast to a distributed instrument control design, the *HET* staff did explicitly request a remote controller design to allow for easy maintenance. Therefore the PCB design has been refitted on a 19-inch compatible standard PCB from factor of 100 mm x 160 mm.

11.4.1 Controller

A significant limitation of the old SCS design is the commercial motor controller. Though state-of-the-art when they were initially implemented, they were never specifically designed for the *HET* SCS application. Being a proprietary commercial product they have the following weaknesses:

(I) They can only handle 2 axes per controller. This results in the artificial coupling of two neighbouring segments to segment pairs, each controlled by three boards

(II) The source code and according motion control was not available to the *HET* staff, so troubleshooting and error handling is difficult to impossible.

(III) They can only actuate one axis at a time, which caused the segments to be in suboptimal positions while moving. Additionally, it increased the reconfiguration time for the correction feedback loop.

(IV) The positions were transmitted via a daisy-chained RS232 network leading to long ($\approx 10s$) communication delays.

(V) Failed or incomplete moves are not or are insufficiently reported.

(VI) In order for the controllers to be functional with the hall-effect sensors, they need to be located directly behind the mirrors. This forces the emission of nearly 1.0 kW of waste heat just behind the segmented primary mirror. Additionally, it makes in-situ maintenance difficult and time-consuming.

Throughout the remaining part of this section, these weaknesses will be addressed, while the new system will be presented in detail.
In contrast to the old controllers which were arranged in triplets to control a segment pairs, the new architecture allows a more intuitive understanding of the system and structure. Each segment now has a unique ID, according to its position in the primary. The ID is fixed to the cable harness, connecting the actuators in the mirror truss with the SCS2 assembly. Hence the new controllers can be swapped without keeping track of changes. The segment controller reads this ID and hence knows which segment it is connected to. Using this direct segment to controller affiliation allows them to individually communicate via *CAN* with the high level SCS2 script. Figure 11.5 shows a functional block diagram of one segment CPU.

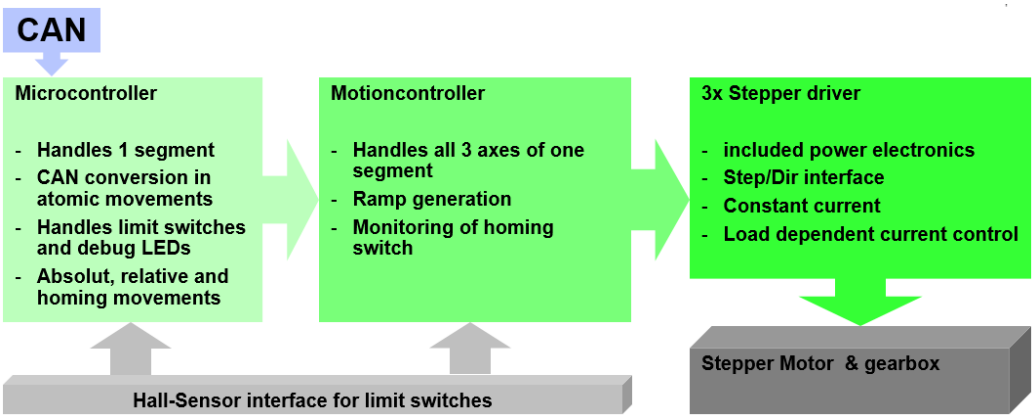

Figure 11.5: CPU block schematic. Three green shaded boxes represent the main semiconductor chips (micro-controller, motion-controller and stepper driver) and lists their responsibilities. External interfaces like the switches and the axes them self are indicated by grey shades.

In the *HET* application each CPU handles all three axes of one segment. Further the full source code of the CPU is available to *HET*, so troubleshooting and maintainability is ensured. By design, the new SCS2 system is able to drive all three axes at once and if needed simultaneously. Hence the SCS weaknesses number (I), (II) and (III) are inherently solved by the SCS2.

11.4.2 CAN Bus

SCS2 relies on the new decentralized CAN-based instrument control toolkit (DECANIC), developed by the University Observatory Munich (USM/LMU). Using the state-of-the-art CAN bus allows much faster communication than the outdated RS232. SCS2 is able to transmit worst case commands (longest possible message) within 0.4 ms. Given this, the communication time for the full array of all 273 axes is typically less than 100 ms. Compared to the nearly 10 s communication time required by the RS232 network, this is roughly a factor of 100x better which allows for a fast feedback loop on the mirror control. The CAN bus allows the CPU to report on the status of each axis and furthermore offers enough communication bandwidth for sophisticated error reports. This allows the high-level computer and the operator to maintain full knowledge over the entire array status. Given these improvements, the CAN bus approach perfectly addresses the old SCS weaknesses (IV) and (V).

11.4.3 SMOCO - Segment MOtion COntroller

The Segment Motion Controller (SMOCO) acronym represents the actual PCB on which we place four individual segment CPUs. The PCB has a standard form factor of 10cm x 16cm and is shaped to fit into a standard 19-inch rack assembly. Use of state-of-the-art components made it possible to fit the functionality of 12 axes of motion onto this small footprint. Figure 11.6 shows the first three SMOCOs just after manufacturing.

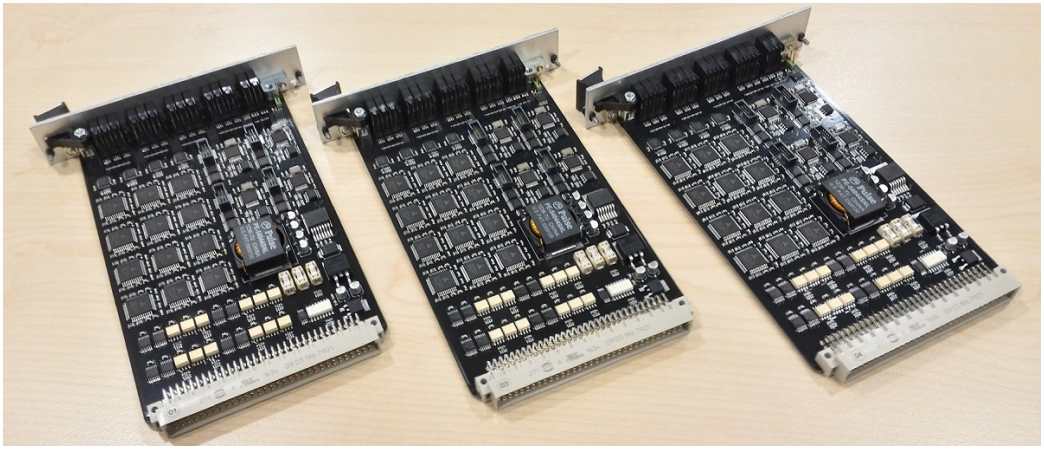

Figure 11.6: Final SMOCO PCBs after manufacturing.

SMOCO characteristics:

- Input circuitry for 2 hall effect sensors per axis
- 3 step, on-PCB power supply
- nominal $\approx$ 1 W waste heat per SMOCO
- 4 segment motion control (12 axes total)
- Front panel status LED interface (Figure 11.7)

Most of the SMOCO logic and its embedded motion-control-circuitry are directly taken from the USM DECANIC system. At its heart, the system is a micro-controller based CPU capable of interfacing various extension modules such as stepper driver, digital I/O, and resolver circuitry. This design fits onto a very small footprint, which can either be located next to the controlled hardware or fit into a control cabinet, requiring minimal space. In either configuration, its energy efficiency (nominal of 1W of waste

heat per SMOCO) allows to operate the individual controllers with little or no cooling required. While all of SMOCOs data and status is available via CAN bus, some of the functional parameters are displayed bye LEDs at the front plate of each SMOCO as can be seen in figure 11.7.

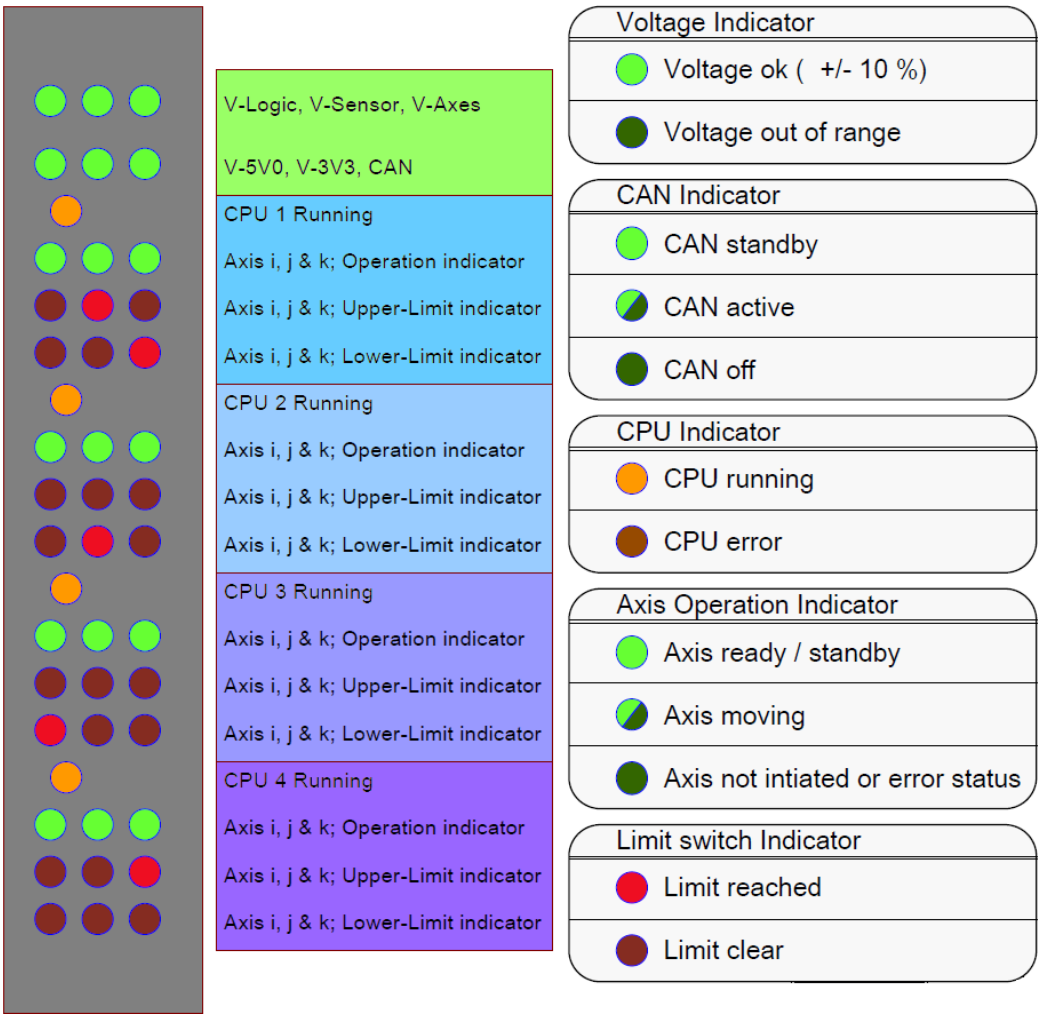

Figure 11.7: SMOCO front panel status LED

Due to SMOCOs modular hardware and low-level software design, the system is scaled to the nearly 300 axes, as required for *HET* SCS2. So each SMOCO handles 4 segments, which leads to a total of 23 identical SMOCOs, all located in a common rack called CAVE (ref. 11.4.4) and connected via CAN bus.

11.4.4 CAVE - Common Actuator Vectorization Entity

While the old SCS controllers needed to be located directly behind their associated mirror segments, the SCS2 SMOCO is designed to handle the actuators remotely. Consequently, all SMOCOs are located within the Common Actuator Vectorization Entity (CAVE). CAVE is designed to fit into a 19-inch rack. Conveniently, HET has a 19-inch rack in an insulated, co-rotating cabinet placed on the structure behind the main mirror known to the *HET* team as the IGLOO. It contains the network, power and cooling systems required to support CAVE and its embedded SMOCOs. Placing SCS2 inside the IGLOO was a request from the technical staff to ease maintenance and improve optical seeing by eliminate waste heat from SCS2 released under the primary mirror.
Extensive measurements revealed that the old SCS controllers released upwards of 1.000 W of waste heat directly into the optical path of the telescope. In comparison, all of the SCS2 SMOCOs release approximately 30W in worst-case scenarios. Additionally, this heat is released into the insulated and temperature-controller IGLOO where it can be exhausted outside of the dome away from the optical path. This is a huge advantage over the old SCS and solves the aforementioned weakness (VI). Figure 11.8 presents the CAVE assembly at its full footprint for the final solution for all 273 axes needed for SCS2.

11.4.5 Power supplies

As mentioned in 11.4.4, the waste heat dissipation was a critical driver for SCS2. The by far largest amount of waste heat is produced by the power supplies. Hence they are also located in the isolated IGLOO cabinet, where the it can be directly cooled. The SCS2 power supply system consists out of three separate power supply systems, which are all tied to a single DC ground to avoid floating voltage levels. This ground level is used as a star point within the ground scheme to minimize electromagnetic interference.

1. First and foremost is the 24 V_{dc} power supply system for the actuator stepper motors. This system consists of multiple 24 V_{dc} supplies run in parallel banks to provide the capability of delivering a minimum of 70 A required to move all axes simultaneously.

2. The second system is a single 24 V_{dc} supply which drive the closed current loops for the hall-effect limit sensors within the actuators. In contrast to the SCS 5 V TTL signals, SCS2 uses 24 V closed-current

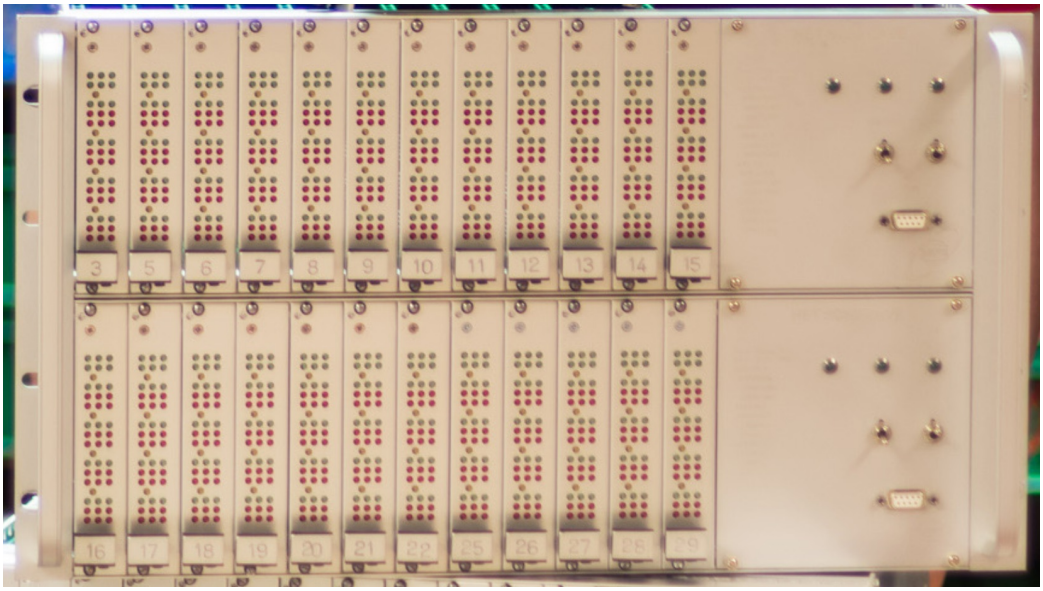

Figure 11.8: Front view of the CAVE assembly as it can be reached during maintenance. 1 of the 24 SMOCOs is an in-situ spare for quick replacements.

loops at 5 mA to compensate for the long (up to 15m) cable lengths from CAVE to the actuators. This leads to a worst-case consumption of 3A but solves the EMI-induced limit switch triggering problems of the old SCS.

3. The third is a 12 V_{dc} logic power supply that is utilized to power the CPUs and associated circuitry. The actual voltages used on the SMOCO PCB are 5 V for CAN communication and 3.3 V for the micro-controller. Still the 12 V_{dc} is used as an industry standard voltage to drive the whole SMOCO array within the CAVE. As mentioned in 11.4.3, each SMOCO contains an on-board DC-to-DC supply to provide the appropriate voltage levels internally. To limit the amount of heat generated on the SMOCOs themselves, this conversion is separated into three further stages. The incoming 12 V_{dc} are first step-down converted towards 7 V_{dc} using a so called buck converter circuit. This is state-of-the-art due to the high efficiency and the resulting minimal waste heat dissipation. However, efficiency here is bought by a rather noisy voltage level. So the second and third conversions from 7 V_{dc} to 5 V_{dc} and 3.3 V_{dc} are handled by classical linear stages which directly convert the excessive voltage into waste heat. This can be accepted due to the low voltage drop which leads to a negligible amount of wasted energy overall, which is based on the high efficiency of first stage. Hence

the design combines minimal waste heat and stable on-board voltage levels at minimal additional cost of three nested power supplies instead of two parallel once.

11.5 Software

The software of the *HET* SCS2 project is separated into three different parts.

1. The low-level software which is coded in C and runs on a Cortex M0 architecture inside the micro-controller (11.5.1).

2. The CAN layer between the low level micro-controller CPUs and the hosting high level software (11.5.2).

3. The high-level control software as an interface to the remaining *HET* software environment (11.5.3).

11.5.1 Low-Level - SMOCO CPU

The low-level, c-based software allows for a comprehensive set of commands. Relative and absolute movement commands and designated homing procedures are implemented on the lowest level of the architecture. By implementing all logic on the micro-controller, which handles an individual axis, the communication between the host computer and the nodes is almost human readable. The code runs as a Real Time Operating System (RTOS) on SMOCOs micro-controller (CPU) and starts an individual thread per axis to handle.

Three axes are operated more or less simultaneously and have access to the on board buses and resources based on mutual exclusion called mutex. This is a vital part of the RTOS and handles conflicting interrupts and hardware requests. Following is an excerpt of the functional commands embedded in the instruction set of the SMOCO CPU shown in table 11.2.

11.5.2 Communication layer - CAN Bus

The CAN bus is the communication back bone of the DECANIC system and proven to be EMI robust and capable of handling larger arrays of smart instrument control nodes.[36] A basic principle of the CAN bus topology is the fact that every connected node receives every message transmitted via the network. Each node has to acknowledge the information which consequently

Instruction set excerpt			
1	set absolute target	9	set $Axis_{Initialised}$
2	set relative target	10	set $Vmax_{Positioning}$
3	request axis status	11	set $Vmax_{Homing}$
4	request limit status	12	set $X_{Position}$
5	move to target	13	abort move
6	move to lower limit	14	axis power On/OFF
7	move to upper limit	15	reset CPU
8	start homing process	16	emergency stop

Table 11.2: Instruction set table for the micro-controller resident low-level software. Details can be found in appendix *SMOCO CPU firmware documentation*.

decreases the chance of an individual node misinterpreting the information. To avoid crowding the nodes with parsing unimportant information, a CAN message is built up of two parts.
First the so called message-ID, which is either 11-Bits (standard mode) or in our case 29-Bits (extended mode) long. Both modes are industrial standard and supported by almost all available CAN bus products. DECANIC uses the message-ID as a 29-Bit field in which several informations are encoded.

28	27	26	19	18	15	14	13	12	11	10	9	8	7	6	5	4	3	2	1	0	Bit Nr.	remark:
x	x	x																			28 . . 26	selects 8 possible prioritys
																					25 . . 20	Unassigned ID space
			x																		19	select ALL nodes
				x																	18	select ALL axis
																					17 and 16	Unassigned ID space
					x	x	x	x	x	x											15 . . 10	possible commands
											x	x									9 and 8	selects motor axis[0..2]
													x	x	x	x	x	x	x	x	7 . . 0	selects CAN node number

Figure 11.9: 29-Bit CAN message-ID bit mapping of SCS2.

DECANIC allows a master-slave allocation which is software implemented. Each participating CAN node can in theory behave like a bus master. In practice slave messages will always start with at least one recessive bit. Table 11.3 provides further information on the detailed use of the proprietary sub fields in the message ID.

In addition to this custom section, the message-ID also contains several bit fields in which security checks, bit stuffing information and many more

CAN message ID sub structures	
1	Priority bits allow emergency messages to be transmitted instantaneous on the network and also allow the host to keep bus control over the slave CPU nodes. 8 Priority levels are implemented.
2	Bit 19 flags if a message is designated to all CPUs at once.
3	Bit 18 flags if a message is designated to all axes on the CPU.
4	Command bits allow for 64 individual commands as listed in the instruction set excerpt.
5	Bit 9 and 8 address the axis on the CPU which is affected by the command.
6	Finally Bits 7 until 0 open an address space for up to 255 nodes. In SCS2 one ID reflects the according mirror segment CPU.
7	Bits 25 until 20 and 17 until 16 are so far unassigned ID space.

Table 11.3: Table of the SCS2 CAN message ID substructure.

CAN specific content is implemented. All of this is CAN standard and can be found in the according documentation.[60]

The second part of a CAN message are the optional data bits. It is noteworthy that a CAN message does not have to contain data bits at all. In some cases, receiving a command via the message-ID without any additional data is just fine. SCS2 makes use of this fact to provide acknowledgement information towards the host, by returning the command just with changed priority. Another example would be the host command to start all axes movements and initiate travel to their individual target positions.
While the positions have to be transmitted individually and with the target position as data bits, the move trigger can be sent to all nodes at once with a single command without any optional data. This reduces the number of messages that need to be transmitted and it saves energy, since only one message needs to be parsed by all nodes and limits bus crowding to a minimum.
In the SCS2 design, the CAN network resides only within within the CAVE assembly. It is accessed via the already mentioned CAN/Ethernet bridge, and the hosting computer need only open an Ethernet-based port connection.

11.5.3 High-Level - SCS2 control software

The high level SCS2 software is almost identical to the old SCS software. As can be seen in figure 11.10, SCS controls the mirror array via a RS232 bus, which has very slow baud rate. Therefore SCS actuators are distributed on 10 banks with serial RS232 communication. The SCS software communicates via an individual Bank Control Demon (BCD) per communication bank, in which each old controller only handled two axes at a time, so three controllers shared authority over two segments. The following figures show the software structure from the old SCS 11.10 via a coexisting phase 11.12 towards the final SCS2 structure 11.11. Everything from the BCDs to the actuators is redesigned for SCS2, but the supporting software structure is almost not affected. The SAMS and MARS diagnostic subsystems communicate in the same manner as in SCS, so the systems precision stays the same. However, the significant reduction in communication time and the ability to move all axes at once reduces the control loop execution time by almost a factor of two. The GUI interface does not need to be changed, which further reduced the upgrade costs in terms of man power and risks.

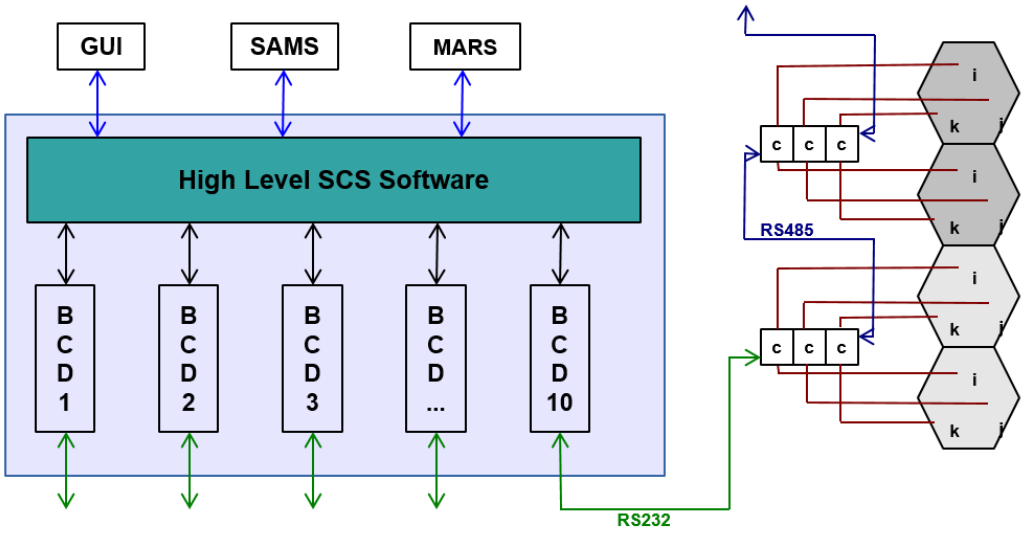

Figure 11.10: Block schematic of the original SCS software.

In contrast to the old SCS design as shown in figure 11.10, diagram 11.12 points out the different approach of SCS2, to have all controllers on one single bus. As already mentioned, this allows the system to trigger various kinds of commands all via one single interface.
During SCS2 system integration, SCS2 and SCS software run together. The

high-level software is updated while SCS2 hardware is installed to insure updated segments are disengaged from SCS BCDs and engaged in the CAN demon. This coexisting set up of both systems can be seen in figure 11.11.

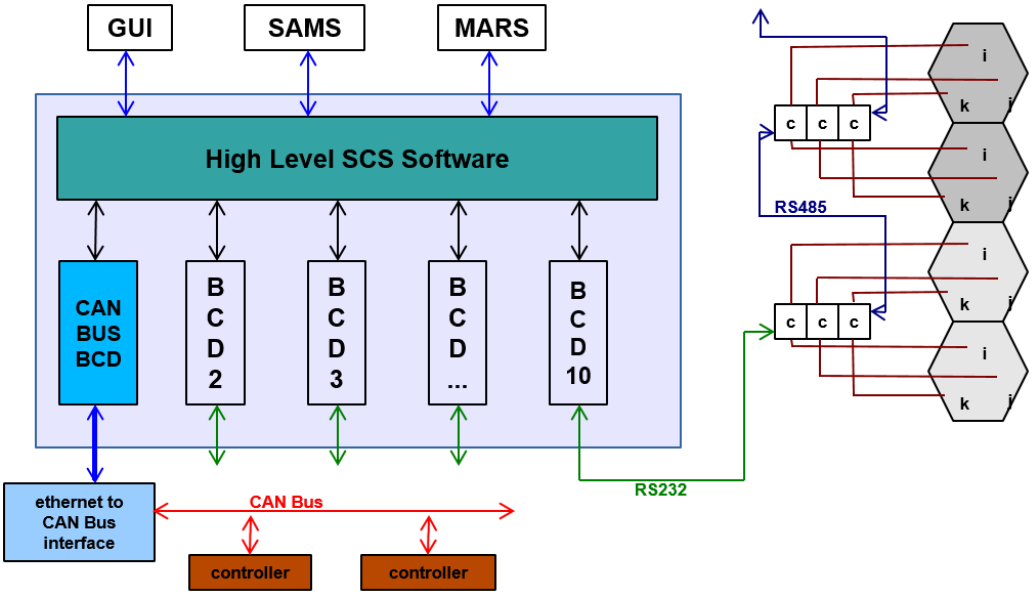

Figure 11.11: Block schematic of the coexisting SCS and SCS2 software.

Being able to integrate the new system in small steps, like one segment pair at a time, has the advantage of not causing any telescope downtime.

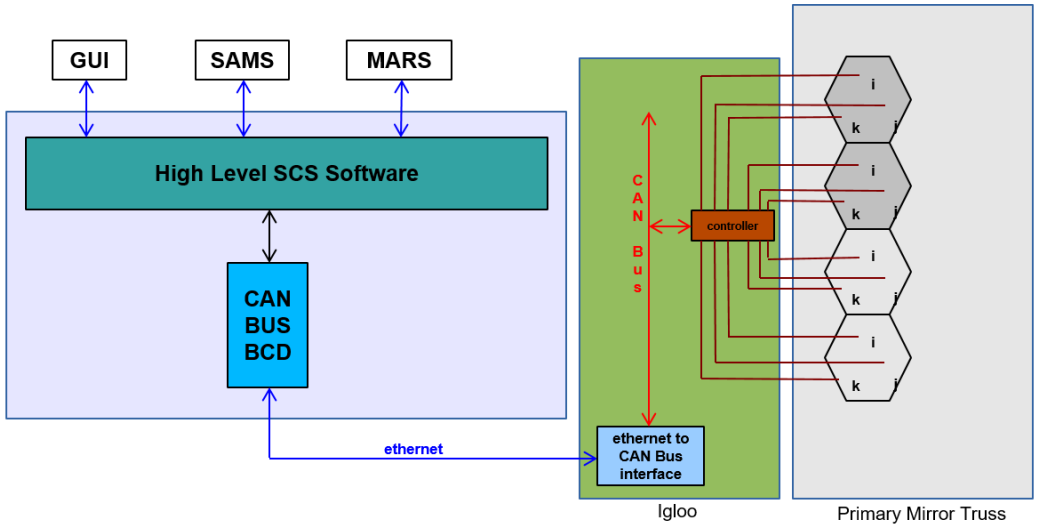

Figure 11.12: Block schematic of the SCS2 software.

As the comparison of figure 11.10 and figure 11.12 shows, only minor parts of the high-level software had to be redesigned. Mainly, this entails a library which converts the high-level commands into the SMOCOs CAN instruction set commands. In *HET* terms, this code is called CAN BUS Bank Control Daemon (BCD).

11.6 Diagnostic Subsystems

While the earlier sections provided detailed information on the new SCS2 system, does the following shed light the needed diagnostic sub systems. As explained above is the primary shape measured through out the whole night in an endless loop. To do so, a non optical position measurement system is required. This is called Segment Alignment Maintenance System (SAMS) [11.6.1]. During telescope initialisation absolute optical verification of the system is done by two independent systems. The so called Mirror Alignment Recovery System (MARS) [11.6.2] and the *HET* Extra Focal Instrument (HEFI) [11.6.3]. As MARS and HEFI both need to access the center of curvature they are mounted on the same optical bench. This configuration is shown in the layout 11.13.

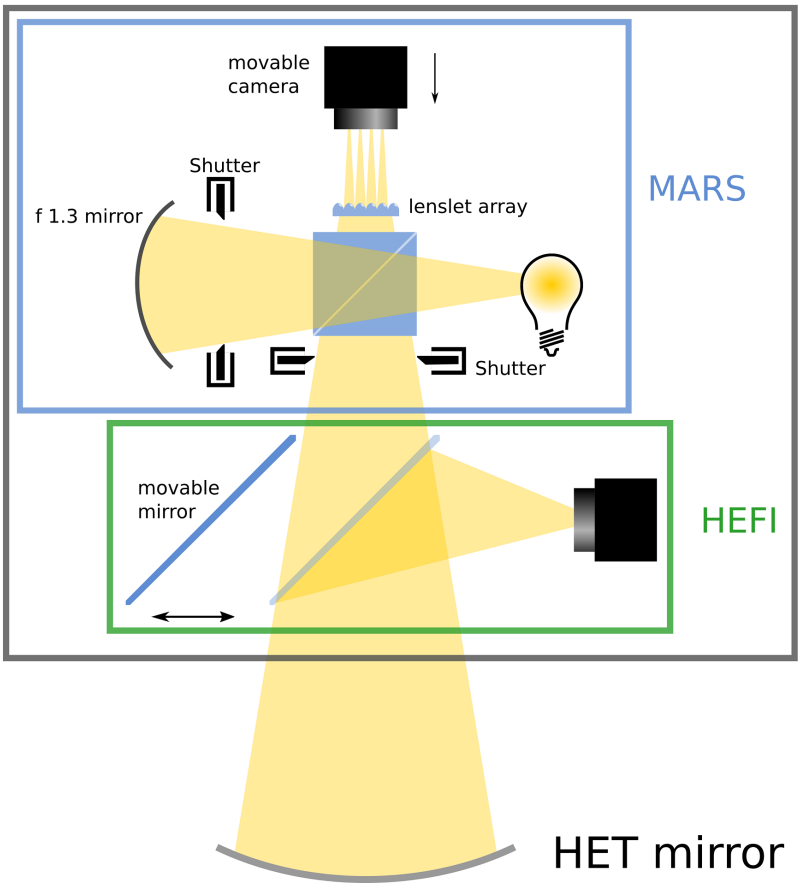

Figure 11.13: Optical layout of MARS and HEFI. Detailed information are given in subsection 11.6.2 and 11.6.3. Credit: H. Kellermann

Diagram 11.14 provides an functional overview of the location of the MARS and HEFI system which need to be in the center of curvature of the primary shape. Since the center is outside of the dome MARS and HEFI had to be installed in the so called Center of Curvature Alignment Sensor (CCAS) tower.

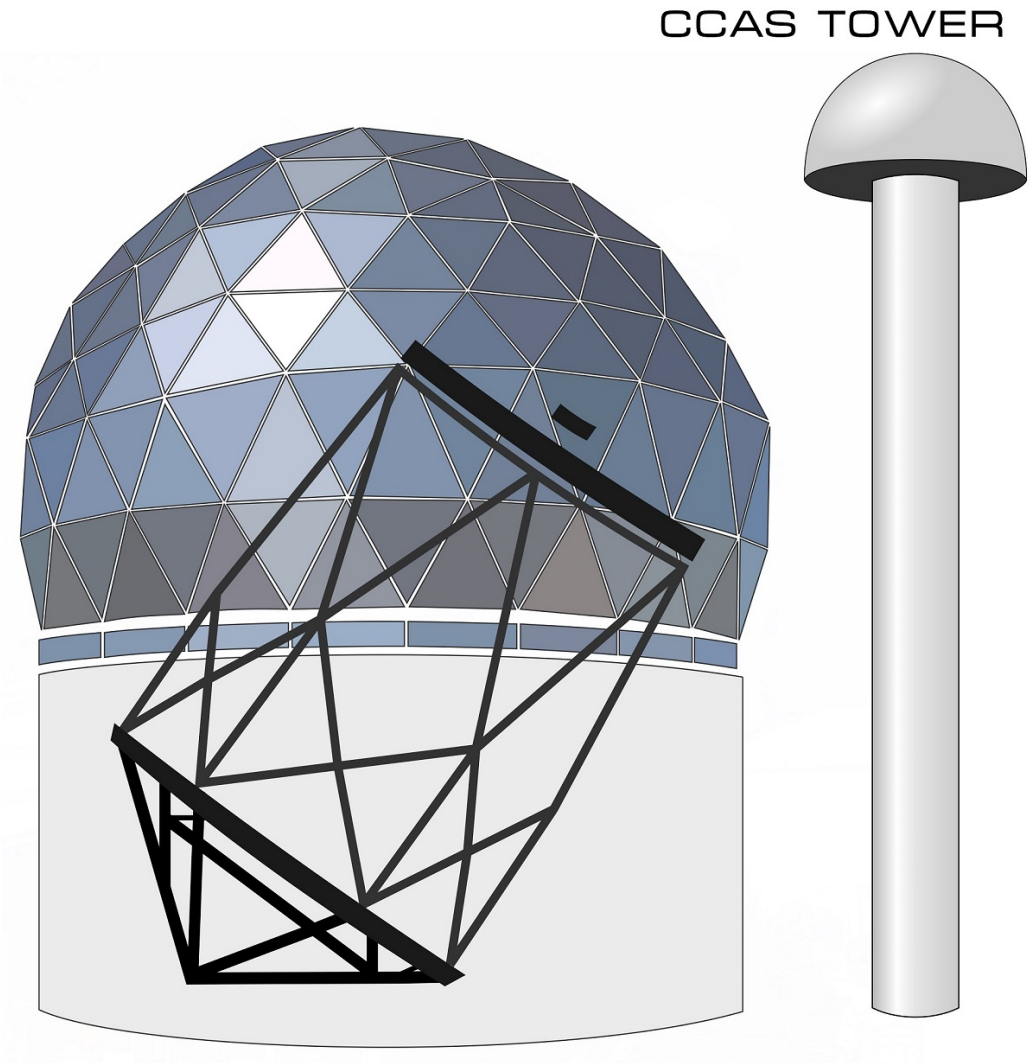

Figure 11.14: Diagram of the *HET* and the Center of Curvature Alignment Sensor (CCAS) tower. CCAS tower is the location of the both absolute optical measurement systems. Credit: H. Kellermann

11.6.1 SAMS - Segment Alignment Maintenance

The SAMS is the prime source of position information for the SCS2. As a vital diagnostic sub system it has already been part of the initial SCS and has not been changed due to the SCS2 upgrade. Its purpose is to feed SCS and SCS2 with relative motion information between neighbouring mirror segments.

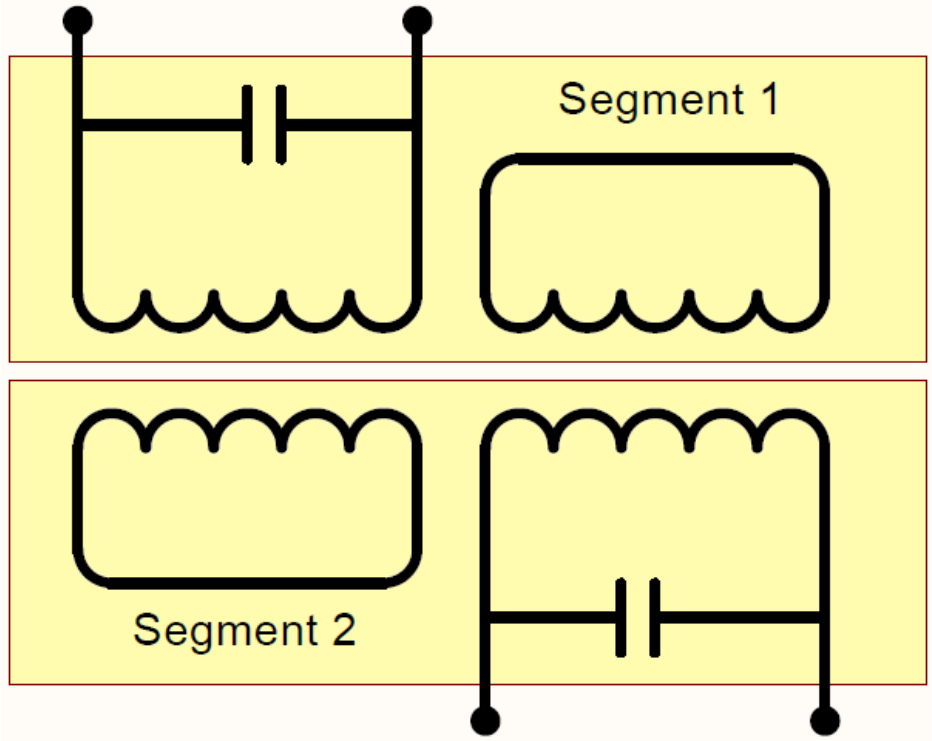

Figure 11.15: SAMS functional principle: Each segment has an actively driven resonant circuit which is mounted in close proximity to the a passive counterpart on the neighbouring segment.

As it can be seen in the functional scheme 11.15 does a pair of SAMS rely on close proximity of the neighbouring sensors. Each segment has an actively driven resonant circuit which is mounted in close proximity to the a passive counterpart on the neighbouring segment.
Relative motion between the segments leads to a detectable misstuning of both resonance frequencies. This can be evaluated and converted into a 2-dimensional drift information which is needed to correct for the relative movement. As the SAMS is a pure relative position feedback system an absolute calibration is further needed.

Picture 11.16 shows an edge sensor pair located on the backside of two prime mirror segments.

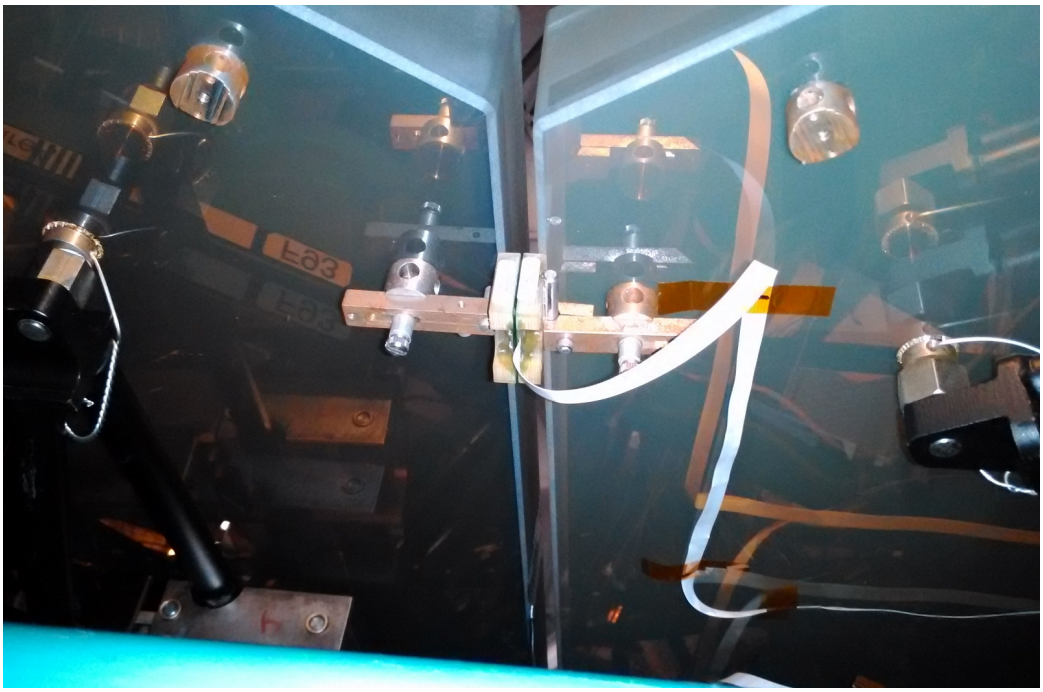

Figure 11.16: In situ picture of SAMS pair.

11.6.2 MARS - Mirror Alignment Recovery

The Mirror Alignment Recovery System is an absolute shape measurement system for *HET*'s prime mirror. MARS compares the real pointing of the mirror segments with a nominal pointing, defined by a scaled reference mirror. The system is illuminated from a light source integrated on the optical bench and coupled via a beamsplitter. Both light paths are regulated via shutters. So the reference mirror and the actual prime mirror segments can be measured individually or simultaneous.
The configuration of the optical elements and the according light paths can be seen in figure 11.17.

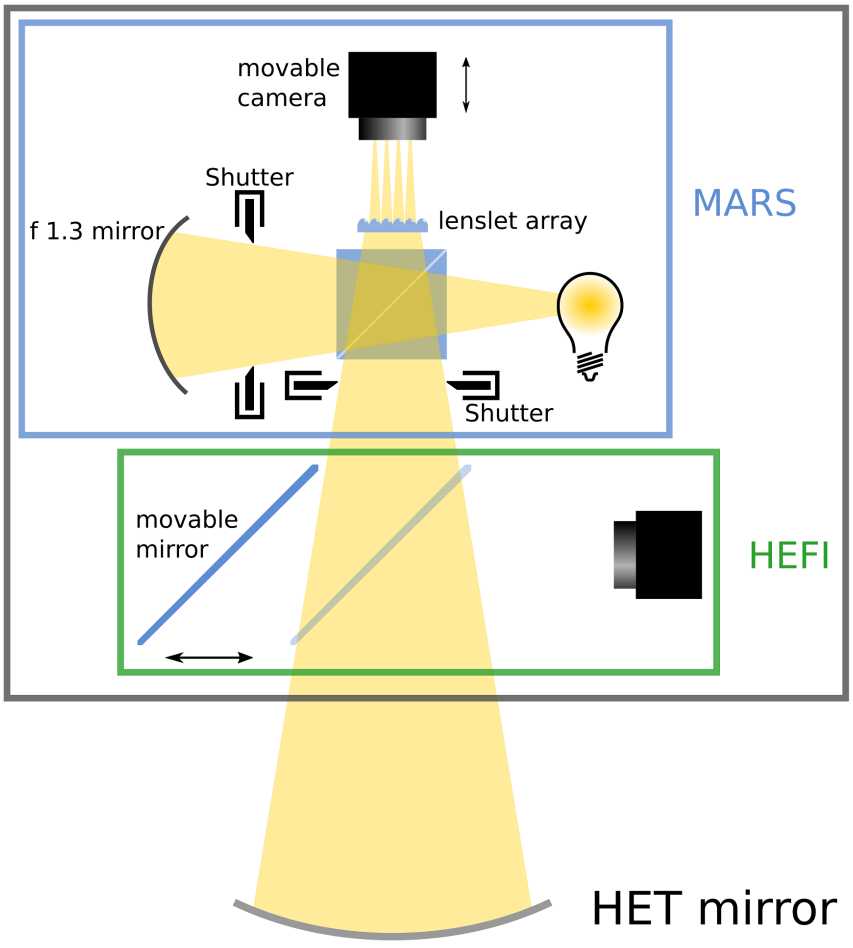

Figure 11.17: Optical layout of MARS. MARS images the prime mirror segment via a lenslet array and compares it with a scaled reference mirror made out of a single piece of glass. Credit: H. Kellermann

Segment pointings are measured by the focus position of the mirror segments imaged via the lenslet array. To ensure a best focused image the MARS camera is mounted moveable. The system starts with a focus series to measure and optimize the PSF of the segments. A defocused (left) and a focused (right) picture can be compared in figure 11.18. It can easily been seen that this are images of the real primary because the shading of the tracker is visible on both (darker lower right corner).

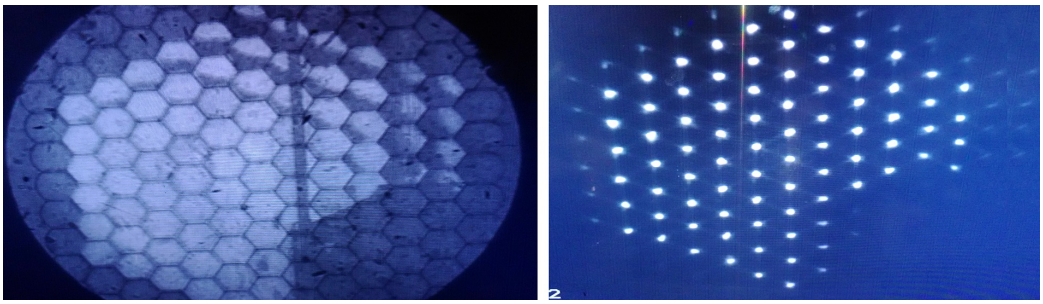

Figure 11.18: Defocused (left) and focused (right) MARS image.

Next, both shutters are opened to image the focused primary and the reference mirror at the same time when the camera has found the focus position.

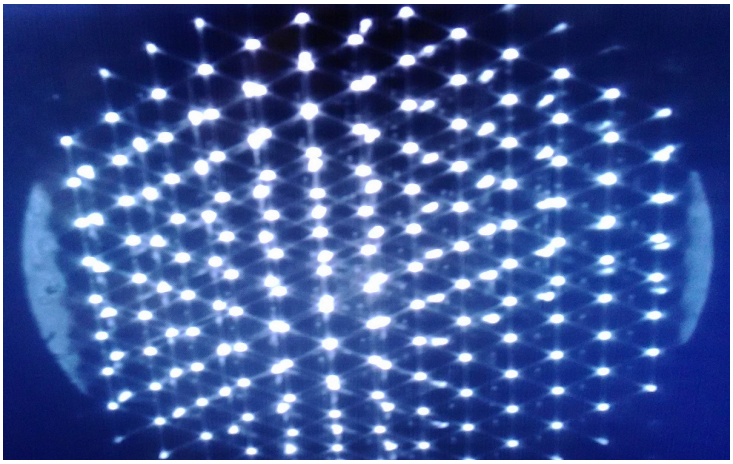

Figure 11.19: Focused overlay MARS image of prime and reference mirror.

This results in an overlay of both segment locations. The desired reference position and the usually slightly deviated actual position are shown in picture 11.19. The system can now differ between both signals by closing and opening the according shutter to measure the deviation of each segment and send the resulting corrections to the SMOCO motion controller.

11.6.3 HEFI - HET Extra Focal Instrument

The last diagnostic sub system is called *HET* Extra Focal Instrument (HEFI). It allows coarse absolute measurements with an excessive field of view to allow the measurement of all mechanically possible segment orientations. Further it provides information on the quality of the current segment configuration. The draft 11.20 shows the HEFI light path and the optical arrangement.

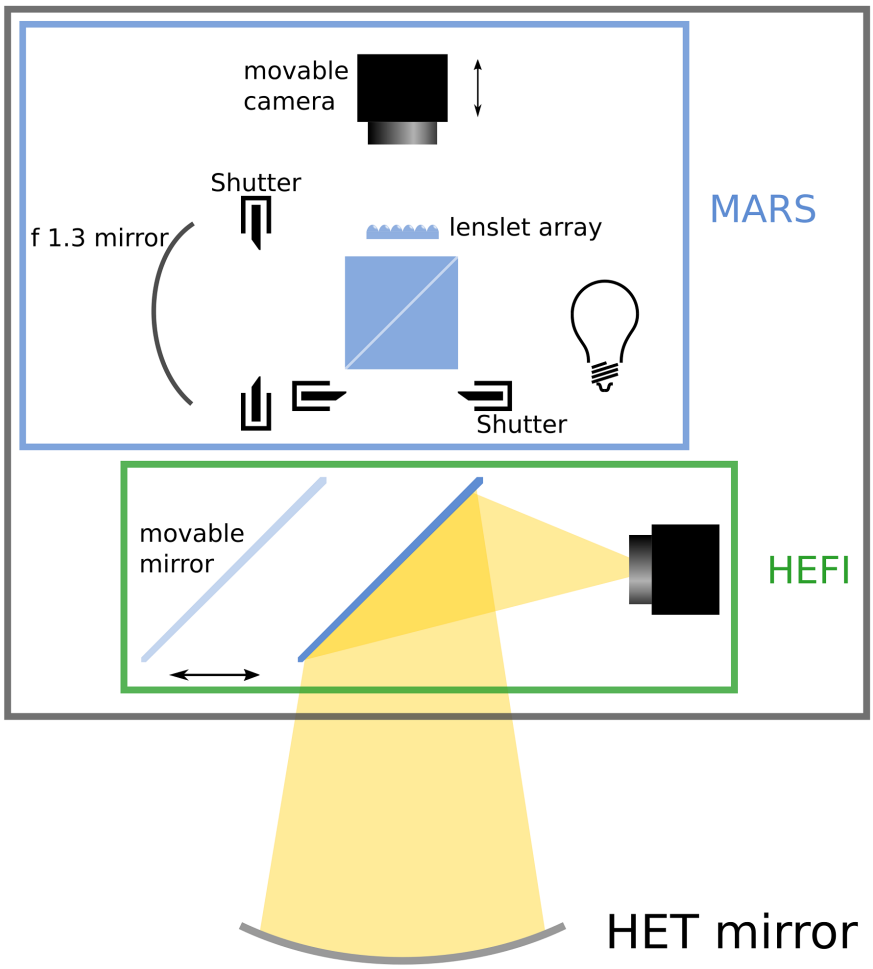

Figure 11.20: Optical layout of HEFI. HEFI images the prime mirror segments directly via a moveable mirror. Credit: H. Kellermann

Due to HEFI's large field of view all possible mirror directions can be seen. This allows for a coarse correction of the individual segments, so the MARS can take over and fine align the segments.

Once all mirrors are in position, HEFI can check the quality of the reached alignment by measuring the PSF of the prime focus (11.21).

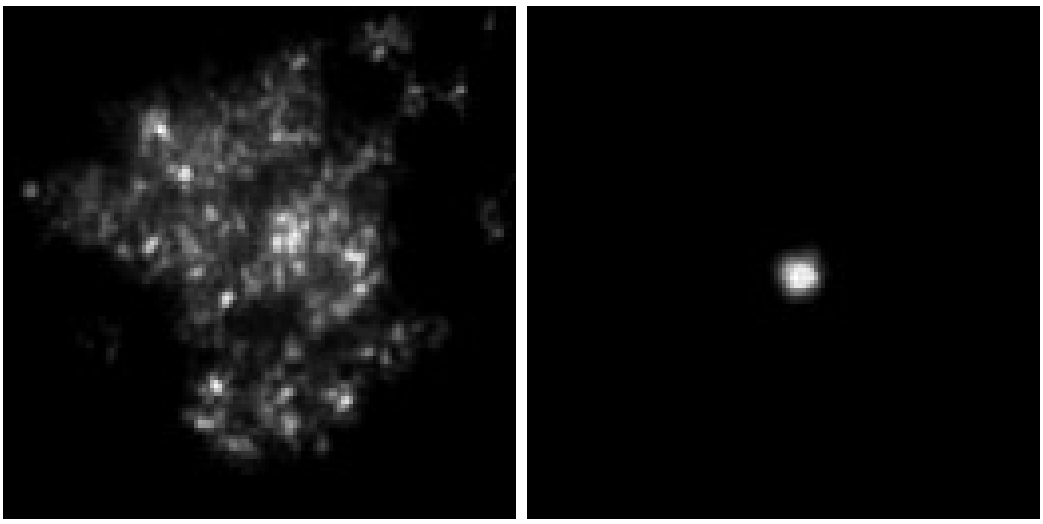

Figure 11.21: HEFI images before (left) and after (right) aligning process.

11.7 Summary

The upgrade of the SCS towards SCS2 will allow the *HET*to maintain its main mirror shape better than before and reduce the amount of time needed to execute corrections on the mirrors' positions significantly.

As already investigated by Racine et al. [70] dome and especially mirror seeing can largely contribute to the overall seeing of the facility. While the *HET* dome design allows for very good airflow, its mirror seeing might have been affected by the large amount of waste heat from those old controllers. The amount of waste heat emitted into the optical beam will be reduced by at least 1000 W. Therefore, we expect the local seeing to improve and hope to gain overall facility efficiency.

The following system diagram 11.22 illustrates the full picture of the SCS upgrade: SCS2

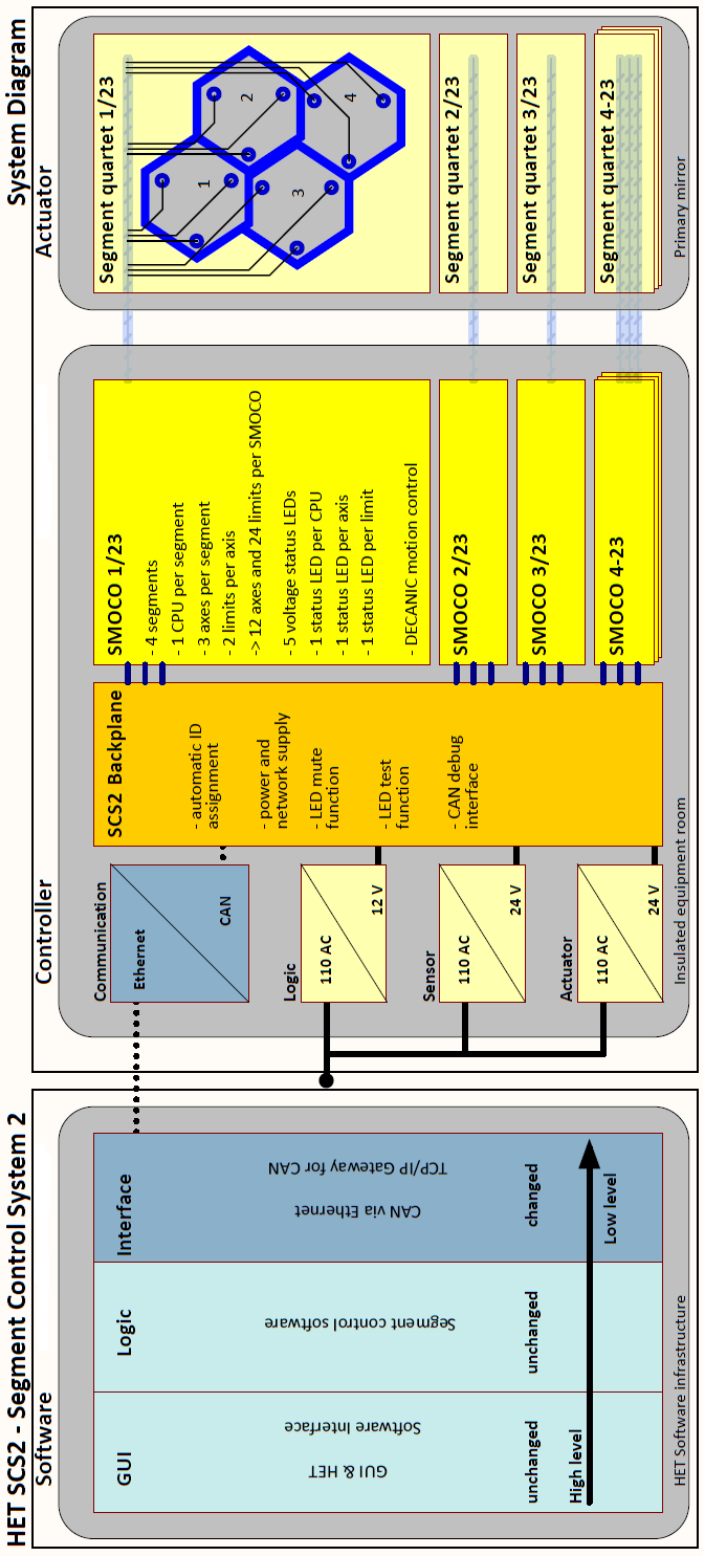

Figure 11.22: Detailed SCS2 system diagram.

11.7.1 Integration

Given the fact that the *HET* staff is busy bringing the *HET* back into full scientific mode, the preparations for the SCS2 upgrade had not highest priority. Still, running the required cabling into the mirror truss has started with low priority in late 2016. We were able to start swapping mirror segments from SCS to SCS2 during the daytime in early 2017 for further proof of concept.

As the individual segments of the mirror are periodically swapped and recoated, the glass and segment support pairs are moved to different locations in the array. While out of the array, the segment supports are realigned according to their next position. This alignment is done within the *HET* mirror lab. Therefore SCS2 has a small lab-based offspring, only consisting of one SMOCO board. Once the alignment has been reached, the high-level software reads the actuators positions from the mirror lab SMOCO board and assigns the according segment CPU within the CAVE set up with those positions from the mirror lab alignment. Afterwards, the overall mirror shape is fine-tuned by the regular system calibration in the beginning of the night, using the MARS and HEFI diagnostic sub-system as explained in section 11.6.

11.7.2 Project Status

SCS2 officially started in December 2015. While the need for a overhaul of the SCS has been obvious for a longer period of time and other opportunities have been researched in detail in 2015, it became clear that a cooperation of the University observatory Munich, the Max-Planck-Institut for extraterrestrial physics and the University of Texas at Austin with its *HET* staff is the most promising solution. Buying a complete system from a regular vendor would be extremely costly. A fair comparison between both options included not only the hardware costs but also the cost in terms of man power and a detailed risk analysis. After a quick and intense design phase in early 2016, the project has been externally reviewed by an international committee. Based on the experts' review results and experience, the *HET* board of directors approved the upgrade in May 2016.

By May 2016, prototype SMOCO boards have been manufactured and have fulfilled expectations. As already mentioned, most of the electrical circuitry has been used for instrumentation at the Mount Wendelstein observatory close to Munich. This was an early proof of concept. Afterwards a minor series of SMOCO has been professionally produced in Autumn and passed last quality checks in late 2016.

During the first half of 2017 a full set of 55 SMOCOs has been automatically manufactured by the electronics workshop of MPE. Afterwards each board was flashed and tested following an extensive test protocol which can be found in appendix *SMOCO Commissioning-Check-List*. Finally two completed CAVE assemblies where shipped to *HET* in August 2017. Alongside the final production of the SMOCOs, the prototype was used to confirm SMOCOs software and functional parameters by using a real size test stand at *HET* and finally real primary mirror segments. Beginning in autumn 2017, *HET* staff started to implement the new SCS2 cabling harness into HETs truss.

In parallel to the infrastructural cabling update, the *HET* staff began to adapt the existing high-level SCS software to account for the increase operations speed of SCS2. Finally after an extended high-level software testing phase, on June the 5th 2019 the *HET* for the first time operated using SCS2. For a brief transition phase SCS and SCS2 coexist, while every day more and more segments are connected with the new SCS2 system.

On the 14th of June 2019, we where informed by the *HET* staff about that the SCS2 now operates the *HET* active mirror control. Onwards the performance, we got the following statement:

> *"As expected, the improvement in performance is quite noticeable compared to the old system. This was especially so during the transition, with part of the mirror on the old controllers; it was obvious how much longer the old controllers were taking to complete a movegroup. The difference is visually apparent and impressive."*
>
> Chris Robison - SCS2 responsible *HET* Software Engineer

List of Figures

List of Tables

Bibliography

[1] Miles - the catalogue, 2019–. [Online; accessed 27.05.2019].

[2] Jennifer K. Adelman-McCarthy, Marcel A. Agüeros, Sahar S. Allam, Kurt S. J. Anderson, Scott F. Anderson, James Annis, Neta A. Bahcall, Ivan K. Baldry, J. C. Barentine, Andreas Berlind, Mariangela Bernardi, Michael R. Blanton, William N. Boroski, Howard J. Brewington, Jarle Brinchmann, J. Brinkmann, Robert J. Brunner, Tamás Budavári, Larry N. Carey, Michael A. Carr, Francisco J. Castander, A. J. Connolly, István Csabai, Paul C. Czarapata, Julianne J. Dalcanton, Mamoru Doi, Feng Dong, Daniel J. Eisenstein, Michael L. Evans, Xiaohui Fan, Douglas P. Finkbeiner, Scott D. Friedman, Joshua A. Frieman, Masataka Fukugita, Bruce Gillespie, Karl Glazebrook, Jim Gray, Eva K. Grebel, James E. Gunn, Vijay K. Gurbani, Ernst de Haas, Patrick B. Hall, Frederick H. Harris, Michael Harvanek, Suzanne L. Hawley, Jeffrey Hayes, John S. Hendry, Gregory S. Hennessy, Robert B. Hindsley, Christopher M. Hirata, Craig J. Hogan, David W. Hogg, Donald J. Holmgren, Jon A. Holtzman, Shin-ichi Ichikawa, Željko Ivezić, Sebastian Jester, David E. Johnston, Anders M. Jorgensen, Mario Jurić, Stephen M. Kent, S. J. Kleinman, G. R. Knapp, Alexei Yu. Kniazev, Richard G. Kron, Jurek Krzesinski, Nikolay Kuropatkin, Donald Q. Lamb, Hubert Lampeitl, Brian C. Lee, R. French Leger, Huan Lin, Daniel C. Long, Jon Loveday, Robert H. Lupton, Bruce Margon, David Martínez-Delgado, Rachel Mandelbaum, Takahiko Matsubara, Peregrine M. McGehee, Timothy A. McKay, Avery Meiksin, Jeffrey A. Munn, Reiko Nakajima, Thomas Nash, Jr. Neilsen, Eric H., Heidi Jo Newberg, Peter R. Newman, Robert C. Nichol, Tom Nicinski, Maria Nieto- Santisteban, Atsuko Nitta, William O'Mullane, Sadanori Okamura, Russell Owen, Nikhil Padmanabhan, George Pauls, Jr. Peoples, John, Jeffrey R. Pier, Adrian C. Pope, Dimitri Pourbaix, Thomas R. Quinn, Gordon T. Richards, Michael W. Richmond, Constance M. Rockosi, David J. Schlegel, Donald P. Schneider, Joshua Schroeder, Ryan Scranton, Uroš Seljak, Erin Sheldon, Kazu Shimasaku, J. Allyn Smith, Vernesa Smolčić, Stephanie A. Snedden, Chris Stoughton, Michael A. Strauss, Mark SubbaRao, Alexander S. Szalay, István Szapudi, Paula Szkody, Max Tegmark, Aniruddha R. Thakar, Douglas L. Tucker, Alan Uomoto, Daniel E. Vanden Berk, Jan Vandenberg, Michael S. Vogeley, Wolfgang Voges, Nicole P. Vogt, Lucianne M. Walkowicz, David H. Weinberg, Andrew A. West, Simon D. M. White, Yongzhong Xu, Brian Yanny, D. R. Yocum, Donald G. York, Idit Zehavi, Stefano Zibetti, and Daniel B. Zucker. The Fourth Data Release of the Sloan Digital Sky Survey. *The Astrophysical Journal Supplement Series*, 162:38–48, January 2006.

[3] Christopher P. Ahn, Rachael Alexandroff, Carlos Allende Prieto, Friedrich Anders, Scott F. Anderson, Timothy Anderton, Brett H. Andrews, Éric Aubourg, Stephen Bailey, Fabienne A. Bastien, Julian E. Bautista, Timothy C. Beers, Alessandra

Beifiori, Chad F. Bender, Andreas A. Berlind, Florian Beutler, Vaishali Bhardwaj, Jonathan C. Bird, Dmitry Bizyaev, Cullen H. Blake, Michael R. Blanton, Michael Blomqvist, John J. Bochanski, Adam S. Bolton, Arnaud Borde, Jo Bovy, Alaina Shelden Bradley, W. N. Brandt, Dorothée Brauer, J. Brinkmann, Joel R. Brownstein, Nicolás G. Busca, William Carithers, Joleen K. Carlberg, Aurelio R. Carnero, Michael A. Carr, Cristina Chiappini, S. Drew Chojnowski, Chia-Hsun Chuang, Johan Comparat, Justin R. Crepp, Stefano Cristiani, Rupert A. C. Croft, Antonio J. Cuesta, Katia Cunha, Luiz N. da Costa, Kyle S. Dawson, Nathan De Lee, Janice D. R. Dean, Timothée Delubac, Rohit Deshpande, Saurav Dhital, Anne Ealet, Garrett L. Ebelke, Edward M. Edmondson, Daniel J. Eisenstein, Courtney R. Epstein, Stephanie Escoffier, Massimiliano Esposito, Michael L. Evans, D. Fabbian, Xiaohui Fan, Ginevra Favole, Bruno Femenía Castellá, Emma Fernández Alvar, Diane Feuillet, Nurten Filiz Ak, Hayley Finley, Scott W. Fleming, Andreu Font-Ribera, Peter M. Frinchaboy, J. G. Galbraith-Frew, D. A. García-Hernández, Ana E. García Pérez, Jian Ge, R. Génova-Santos, Bruce A. Gillespie, Léo Girardi, Jonay I. González Hernández, III Gott, J. Richard, James E. Gunn, Hong Guo, Samuel Halverson, Paul Harding, David W. Harris, Sten Hasselquist, Suzanne L. Hawley, Michael Hayden, Frederick R. Hearty, Artemio Herrero Davó, Shirley Ho, David W. Hogg, Jon A. Holtzman, Klaus Honscheid, Joseph Huehnerhoff, Inese I. Ivans, Kelly M. Jackson, Peng Jiang, Jennifer A. Johnson, K. Kinemuchi, David Kirkby, Mark A. Klaene, Jean-Paul Kneib, Lars Koesterke, Ting-Wen Lan, Dustin Lang, Jean-Marc Le Goff, Alexie Leauthaud, Khee-Gan Lee, Young Sun Lee, Daniel C. Long, Craig P. Loomis, Sara Lucatello, Robert H. Lupton, Bo Ma, III Mack, Claude E., Suvrath Mahadevan, Marcio A. G. Maia, Steven R. Majewski, Elena Malanushenko, Viktor Malanushenko, A. Manchado, Marc Manera, Claudia Maraston, Daniel Margala, Sarah L. Martell, Karen L. Masters, Cameron K. McBride, Ian D. McGreer, Richard G. McMahon, Brice Ménard, Sz. Mészáros, Jordi Miralda-Escudé, Hironao Miyatake, Antonio D. Montero-Dorta, Francesco Montesano, Surhud More, Heather L. Morrison, Demitri Muna, Jeffrey A. Munn, Adam D. Myers, Duy Cuong Nguyen, Robert C. Nichol, David L. Nidever, Pasquier Noterdaeme, Sebastián E. Nuza, Julia E. O'Connell, Robert W. O'Connell, Ross O'Connell, Matthew D. Olmstead, Daniel J. Oravetz, Russell Owen, Nikhil Padmanabhan, Nathalie Palanque-Delabrouille, Kaike Pan, John K. Parejko, Prachi Parihar, Isabelle Pâris, Joshua Pepper, Will J. Percival, Ignasi Pérez-Ràfols, Hélio Dotto Perottoni, Patrick Petitjean, Matthew M. Pieri, M. H. Pinsonneault, Francisco Prada, Adrian M. Price-Whelan, M. Jordan Raddick, Mubdi Rahman, Rafael Rebolo, Beth A. Reid, Jonathan C. Richards, Rogério Riffel, Annie C. Robin, H. J. Rocha- Pinto, Constance M. Rockosi, Natalie A. Roe, Ashley J. Ross, Nicholas P. Ross, Graziano Rossi, Arpita Roy, J. A. Rubiño-Martin, Cristiano G. Sabiu, Ariel G. Sánchez, Basílio Santiago, Conor Sayres, Ricardo P. Schiavon, David J. Schlegel, Katharine J. Schlesinger, Sarah J. Schmidt, Donald P. Schneider, Mathias Schultheis, Kris Sellgren, Hee-Jong Seo, Yue Shen, Matthew Shetrone, Yiping Shu, Audrey E. Simmons, M. F. Skrutskie, Anže Slosar, Verne V. Smith, Stephanie A. Snedden, Jennifer S. Sobeck, Flavia Sobreira, Keivan G. Stassun, Matthias Steinmetz, Michael A. Strauss, Alina Streblyanska, Nao Suzuki, Molly E. C. Swanson, Ryan C. Terrien, Aniruddha R. Thakar, Daniel Thomas, Benjamin A. Thompson, Jeremy L. Tinker, Rita Tojeiro, Nicholas W. Troup, Jan Vandenberg, Mariana Vargas Magaña, Matteo Viel, Nicole P. Vogt, David A. Wake, Benjamin A. Weaver, David H. Weinberg, Benjamin J. Weiner, Martin White, Simon D. M. White, John C. Wilson, John P. Wisniewski, W. M. Wood-Vasey, Christophe Yèche, Donald G. York, O. Zamora,

Gail Zasowski, Idit Zehavi, Gong-Bo Zhao, Zheng Zheng, and Guangtun Zhu. The Tenth Data Release of the Sloan Digital Sky Survey: First Spectroscopic Data from the SDSS-III Apache Point Observatory Galactic Evolution Experiment. *The Astrophysical Journal Supplement Series*, 211:17, April 2014.

[4] L. G. Althaus, M. M. Miller Bertolami, and A. H. Córsico. New evolutionary sequences for extremely low-mass white dwarfs. Homogeneous mass and age determinations and asteroseismic prospects. *Astronomy and Astrophysics*, 557:A19, September 2013.

[5] K. A. Boshkayev, J. A. Rueda, B. A. Zhami, Z. A. Kalymova, and G. S. Balgymbekov. Equilibrium structure of white dwarfs at finite temperatures. In *International Journal of Modern Physics Conference Series*, volume 41 of *International Journal of Modern Physics Conference Series*, page 1660129, March 2016.

[6] M. R. Burleigh, E. Hogan, P. D. Dobbie, R. Napiwotzki, and P. F. L. Maxted. A near-infrared spectroscopic detection of the brown dwarf in the post common envelope binary WD0137-349. *Monthly Notices of the Royal Astronomical Society*, 373:L55–L59, November 2006.

[7] Adam Burrows, W. B. Hubbard, J. I. Lunine, and James Liebert. The theory of brown dwarfs and extrasolar giant planets. *Reviews of Modern Physics*, 73:719–765, July 2001.

[8] Annie. J. Cannon. The Henry Draper extension. *Annals of Harvard College Observatory*, 100:1–226, Jan 1936.

[9] S. L. Casewell, M. R. Burleigh, G. A. Wynn, R. D. Alexander, R. Napiwotzki, K. A. Lawrie, P. D. Dobbie, R. F. Jameson, and S. T. Hodgkin. WD0837+185: The Formation and Evolution of an Extreme Mass-ratio White-dwarf-Brown-dwarf Binary in Praesepe. *The Astrophysical Journal Letters*, 759:L34, November 2012.

[10] G. Chabrier, I. Baraffe, F. Allard, and P. H. Hauschildt. Review on low-mass stars and brown dwarfs. *ArXiv Astrophysics e-prints*, September 2005.

[11] T. S. Chonis, G. J. Hill, H. Lee, S. E. Tuttle, and B. L. Vattiat. LRS2: the new facility low resolution integral field spectrograph for the Hobby-Eberly telescope. In *Ground-based and Airborne Instrumentation for Astronomy V*, volume 9147 of *Society of Photo-Optical Instrumentation Engineers (SPIE) Conference Series*, page 91470A, July 2014.

[12] Taylor Steven Chonis. *The Development of Replicated Optical Integral Field Spectrographs and their Application to the Study of Lyman-alpha Emission at Moderate Redshifts*. PhD thesis, The University of Texas at Austin, January 2015.

[13] B. Coşkunoğlu, S. Ak, S. Bilir, S. Karaali, E. Yaz, G. Gilmore, G. M. Seabroke, O. Bienaymé, J. Bland-Hawthorn, R. Campbell, K. C. Freeman, B. Gibson, E. K. Grebel, U. Munari, J. F. Navarro, Q. A. Parker, A. Siebert, A. Siviero, M. Steinmetz, F. G. Watson, R. F. G. Wyse, and T. Zwitter. Local stellar kinematics from RAVE data - I. Local standard of rest. *Monthly Notices of the Royal Astronomical Society*, 412:1237–1245, April 2011.

[14] The Scipy community. Documentation: scipy.interpolate.CubicSpline. https://docs.scipy.org/doc/scipy-0.18.1/reference/generated/scipy.interpolate.CubicSpline.html, 2018. [Online; accessed 24-May-2018].

[15] R. S. de Jong, S. Barden, O. Bellido-Tirado, J. Brynnel, C. Chiappini, É. Depagne, R. Haynes, D. Johl, D. P. Phillips, O. Schnurr, A. D. Schwope, J. Walcher, S. M. Bauer, G. Cescutti, M.-R. L. Cioni, F. Dionies, H. Enke, D. M. Haynes, A. Kelz, F. S. Kitaura, G. Lamer, I. Minchev, V. Müller, S. E. Nuza, J.-C. Olaya, T. Piffl, E. Popow, A. Saviauk, M. Steinmetz, U. Ural, M. Valentini, R. Winkler, L. Wisotzki, W. R. Ansorge, M. Banerji, E. Gonzalez Solares, M. Irwin, R. C. Kennicutt, D. M. P. King, R. McMahon, S. Koposov, I. R. Parry, X. Sun, N. A. Walton, G. Finger, O. Iwert, M. Krumpe, J.-L. Lizon, V. Mainieri, J.-P. Amans, P. Bonifacio, M. Cohen, P. François, P. Jagourel, S. B. Mignot, F. Royer, P. Sartoretti, R. Bender, H.-J. Hess, F. Lang-Bardl, B. Muschielok, J. Schlichter, H. Böhringer, T. Boller, A. Bongiorno, M. Brusa, T. Dwelly, A. Merloni, K. Nandra, M. Salvato, J. H. Pragt, R. Navarro, G. Gerlofsma, R. Roelfsema, G. B. Dalton, K. F. Middleton, I. A. Tosh, C. Boeche, E. Caffau, N. Christlieb, E. K. Grebel, C. J. Hansen, A. Koch, H.-G. Ludwig, H. Mandel, A. Quirrenbach, L. Sbordone, W. Seifert, G. Thimm, A. Helmi, S. C. trager, T. Bensby, S. Feltzing, G. Ruchti, B. Edvardsson, A. Korn, K. Lind, W. Boland, M. Colless, G. Frost, J. Gilbert, P. Gillingham, J. Lawrence, N. Legg, W. Saunders, A. Sheinis, S. Driver, A. Robotham, R. Bacon, P. Caillier, J. Kosmalski, F. Laurent, and J. Richard. 4MOST: 4-metre Multi-Object Spectroscopic Telescope. In *Ground-based and Airborne Instrumentation for Astronomy V*, volume 9147 of *Society of Photo-Optical Instrumentation Engineers (SPIE) Conference Series*, page 91470M, July 2014.

[16] A. Degwert. Genauigkeitsbestimmung eines Präzisions Glasfaserpositionierers. Bachelorthesis, Ludwig-Maximilians-Universität München, 2014.

[17] Wolfgang Demtroeder. *Experimentalphysik I.* Springer Verlag, 2008.

[18] Wolfgang Demtroeder. *Experimentalphysik 4.* 2009.

[19] Kerry Ann Deutsch. *Behavior of the atomic oxygen 5577 Angstrom emission intensity at mid- latitudes: A climatological view.* PhD thesis, UNIVERSITY OF WASHINGTON, January 2000.

[20] P. D. Dobbie, M. R. Burleigh, A. J. Levan, M. A. Barstow, R. Napiwotzki, J. B. Holberg, I. Hubeny, and S. B. Howell. A near-infrared spectroscopic search for very-low-mass cool companions to notable DA white dwarfs. *Monthly Notices of the Royal Astronomical Society*, 357:1049–1058, March 2005.

[21] P. P. Eggleton and A. A. Tokovinin. A catalogue of multiplicity among bright stellar systems. *Monthly Notices of the Royal Astronomical Society*, 389:869–879, September 2008.

[22] ESO. ESO-MIDAS. https://www.eso.org/sci/software/esomidas/, 2018. [Online; accessed 24-April-2018].

[23] Arno Riffeser et al. mupipe - Task Index . http://www.usm.uni-muenchen.de/people/arri/mupipe/, 2018. [Online; accessed 24-April-2018].

[24] Claus Goessl et al. Image Reduction with FITSTools. http://www.usm.uni-muenchen.de/people/cag/fitstools.html, 2018. [Online; accessed 24-April-2018].

[25] Prasanth Nair et al. Julian dates from proleptic gregorian and julian calendars. version 1.4, 2018–. [Online; accessed 04.12.2018].

[26] R. E. Falcon, D. E. Winget, M. H. Montgomery, and K. A. Williams. A Gravitational Redshift Determination of the Mean Mass of White Dwarfs: DBA and DB Stars. *The Astrophysical Journal*, 757:116, October 2012.

[27] J. Farihi, S. G. Parsons, and B. T. Gänsicke. A circumbinary debris disk in a polluted white dwarf system. *Nature Astronomy*, 1:0032, March 2017.

[28] Benjamin J. Fulton, Erik A. Petigura, Sarah Blunt, and Evan Sinukoff. RadVel: The Radial Velocity Modeling Toolkit. *Publications of the Astronomical Society of the Pacific*, 130:044504, April 2018.

[29] Gaia Collaboration, A. G. A. Brown, A. Vallenari, T. Prusti, J. H. J. de Bruijne, C. Babusiaux, C. A. L. Bailer-Jones, M. Biermann, D. W. Evans, L. Eyer, F. Jansen, C. Jordi, S. A. Klioner, U. Lammers, L. Lindegren, X. Luri, F. Mignard, C. Panem, D. Pourbaix, S. Randich, P. Sartoretti, H. I. Siddiqui, C. Soubiran, F. van Leeuwen, N. A. Walton, F. Arenou, U. Bastian, M. Cropper, R. Drimmel, D. Katz, M. G. Lattanzi, J. Bakker, C. Cacciari, J. Castañeda, L. Chaoul, N. Cheek, F. De Angeli, C. Fabricius, R. Guerra, B. Holl, E. Masana, R. Messineo, N. Mowlavi, K. Nienartowicz, P. Panuzzo, J. Portell, M. Riello, G. M. Seabroke, P. Tanga, F. Thévenin, G. Gracia-Abril, G. Comoretto, M. Garcia-Reinaldos, D. Teyssier, M. Altmann, R. Andrae, M. Audard, I. Bellas-Velidis, K. Benson, J. Berthier, R. Blomme, P. Burgess, G. Busso, B. Carry, A. Cellino, G. Clementini, M. Clotet, O. Creevey, M. Davidson, J. De Ridder, L. Delchambre, A. Dell'Oro, C. Ducourant, J. Fernández-Hernández, M. Fouesneau, Y. Frémat, L. Galluccio, M. García-Torres, J. González-Núñez, J. J. González-Vidal, E. Gosset, L. P. Guy, J. L. Halbwachs, N. C. Hambly, D. L. Harrison, J. Hernández, D. Hestroffer, S. T. Hodgkin, A. Hutton, G. Jasniewicz, A. Jean-Antoine-Piccolo, S. Jordan, A. J. Korn, A. Krone-Martins, A. C. Lanzafame, T. Lebzelter, W. Löffler, M. Manteiga, P. M. Marrese, J. M. Martín-Fleitas, A. Moitinho, A. Mora, K. Muinonen, J. Osinde, E. Pancino, T. Pauwels, J. M. Petit, A. Recio-Blanco, P. J. Richards, L. Rimoldini, A. C. Robin, L. M. Sarro, C. Siopis, M. Smith, A. Sozzetti, M. Süveges, J. Torra, W. van Reeven, U. Abbas, A. Abreu Aramburu, S. Accart, C. Aerts, G. Altavilla, M. A. Álvarez, R. Alvarez, J. Alves, R. I. Anderson, A. H. Andrei, E. Anglada Varela, E. Antiche, T. Antoja, B. Arcay, T. L. Astraatmadja, N. Bach, S. G. Baker, L. Balaguer-Núñez, P. Balm, C. Barache, C. Barata, D. Barbato, F. Barblan, P. S. Barklem, D. Barrado, M. Barros, M. A. Barstow, S. Bartholomé Muñoz, J. L. Bassilana, U. Becciani, M. Bellazzini, A. Berihuete, S. Bertone, L. Bianchi, O. Bienaymé, S. Blanco-Cuaresma, T. Boch, C. Boeche, A. Bombrun, R. Borrachero, D. Bossini, S. Bouquillon, G. Bourda, A. Bragaglia, L. Bramante, M. A. Breddels, A. Bressan, N. Brouillet, T. Brüsemeister, E. Brugaletta, B. Bucciarelli, A. Burlacu, D. Busonero, A. G. Butkevich, R. Buzzi, E. Caffau, R. Cancelliere, G. Cannizzaro, T. Cantat-Gaudin, R. Carballo, T. Carlucci, J. M. Carrasco, L. Casamiquela, M. Castellani, A. Castro-Ginard, P. Charlot, L. Chemin, A. Chiavassa, G. Cocozza, G. Costigan, S. Cowell, F. Crifo, M. Crosta, C. Crowley, J. Cuypers, C. Dafonte, Y. Damerdji, A. Dapergolas, P. David, M. David, P. de Laverny, F. De Luise, R. De March, D. de Martino, R. de Souza, A. de Torres, J. Debosscher, E. del Pozo, M. Delbo, A. Delgado, H. E. Delgado, P. Di Matteo, S. Diakite, C. Diener, E. Distefano, C. Dolding, P. Drazinos, J. Durán, B. Edvardsson, H. Enke, K. Eriksson, P. Esquej, G. Eynard Bontemps, C. Fabre, M. Fabrizio, S. Faigler, A. J. Falcão, M. Farràs Casas, L. Federici, G. Fedorets, P. Fernique, F. Figueras, F. Filippi, K. Findeisen, A. Fonti, E. Fraile, M. Fraser, B. Frézouls, M. Gai, S. Galleti, D. Garabato, F. García-Sedano, A. Garofalo, N. Garralda, A. Gavel, P. Gavras, J. Gerssen,

R. Geyer, P. Giacobbe, G. Gilmore, S. Girona, G. Giuffrida, F. Glass, M. Gomes, M. Granvik, A. Gueguen, A. Guerrier, J. Guiraud, R. Gutiérrez-Sánchez, R. Haigron, D. Hatzidimitriou, M. Hauser, M. Haywood, U. Heiter, A. Helmi, J. Heu, T. Hilger, D. Hobbs, W. Hofmann, G. Holland, H. E. Huckle, A. Hypki, V. Icardi, K. Janßen, G. Jevardat de Fombelle, P. G. Jonker, Á. L. Juhász, F. Julbe, A. Karampelas, A. Kewley, J. Klar, A. Kochoska, R. Kohley, K. Kolenberg, M. Kontizas, E. Kontizas, S. E. Koposov, G. Kordopatis, Z. Kostrzewa-Rutkowska, P. Koubsky, S. Lambert, A. F. Lanza, Y. Lasne, J. B. Lavigne, Y. Le Fustec, C. Le Poncin-Lafitte, Y. Lebreton, S. Leccia, N. Leclerc, I. Lecoeur-Taibi, H. Lenhardt, F. Leroux, S. Liao, E. Licata, H. E. P. Lindstrøm, T. A. Lister, E. Livanou, A. Lobel, M. López, S. Managau, R. G. Mann, G. Mantelet, O. Marchal, J. M. Marchant, M. Marconi, S. Marinoni, G. Marschalkó, D. J. Marshall, M. Martino, G. Marton, N. Gaia Data Release 2. Summary of the contents and survey properties. *Astronomy & Astrophysics*, 616:A1, August 2018.

[30] Gaia Collaboration, T. Prusti, J. H. J. de Bruijne, A. G. A. Brown, A. Vallenari, C. Babusiaux, C. A. L. Bailer-Jones, U. Bastian, M. Biermann, D. W. Evans, L. Eyer, F. Jansen, C. Jordi, S. A. Klioner, U. Lammers, L. Lindegren, X. Luri, F. Mignard, D. J. Milligan, C. Panem, V. Poinsignon, D. Pourbaix, S. Randich, G. Sarri, P. Sartoretti, H. I. Siddiqui, C. Soubiran, V. Valette, F. van Leeuwen, N. A. Walton, C. Aerts, F. Arenou, M. Cropper, R. Drimmel, E. Høg, D. Katz, M. G. Lattanzi, W. O'Mullane, E. K. Grebel, A. D. Holland, C. Huc, X. Passot, L. Bramante, C. Cacciari, J. Castañeda, L. Chaoul, N. Cheek, F. De Angeli, C. Fabricius, R. Guerra, J. Hernández, A. Jean-Antoine-Piccolo, E. Masana, R. Messineo, N. Mowlavi, K. Nienartowicz, D. Ordóñez- Blanco, P. Panuzzo, J. Portell, P. J. Richards, M. Riello, G. M. Seabroke, P. Tanga, F. Thévenin, J. Torra, S. G. Els, G. Gracia- Abril, G. Comoretto, M. Garcia-Reinaldos, T. Lock, E. Mercier, M. Altmann, R. Andrae, T. L. Astraatmadja, I. Bellas-Velidis, K. Benson, J. Berthier, R. Blomme, G. Busso, B. Carry, A. Cellino, G. Clementini, S. Cowell, O. Creevey, J. Cuypers, M. Davidson, J. De Ridder, A. de Torres, L. Delchambre, A. Dell'Oro, C. Ducourant, Y. Frémat, M. García-Torres, E. Gosset, J. L. Halbwachs, N. C. Hambly, D. L. Harrison, M. Hauser, D. Hestroffer, S. T. Hodgkin, H. E. Huckle, A. Hutton, G. Jasniewicz, S. Jordan, M. Kontizas, A. J. Korn, A. C. Lanzafame, M. Manteiga, A. Moitinho, K. Muinonen, J. Osinde, E. Pancino, T. Pauwels, J. M. Petit, A. Recio-Blanco, A. C. Robin, L. M. Sarro, C. Siopis, M. Smith, K. W. Smith, A. Sozzetti, W. Thuillot, W. van Reeven, Y. Viala, U. Abbas, A. Abreu Aramburu, S. Accart, J. J. Aguado, P. M. Allan, W. Allasia, G. Altavilla, M. A. Álvarez, J. Alves, R. I. Anderson, A. H. Andrei, E. Anglada Varela, E. Antiche, T. Antoja, S. Antón, B. Arcay, A. Atzei, L. Ayache, N. Bach, S. G. Baker, L. Balaguer-Núñez, C. Barache, C. Barata, A. Barbier, F. Barblan, M. Baroni, D. Barrado y Navascués, M. Barros, M. A. Barstow, U. Becciani, M. Bellazzini, G. Bellei, A. Bello García, V. Belokurov, P. Bendjoya, A. Berihuete, L. Bianchi, O. Bienaymé, F. Billebaud, N. Blagorodnova, S. Blanco-Cuaresma, T. Boch, A. Bombrun, R. Borrachero, S. Bouquillon, G. Bourda, H. Bouy, A. Bragaglia, M. A. Breddels, N. Brouillet, T. Brüsemeister, B. Bucciarelli, F. Budnik, P. Burgess, R. Burgon, A. Burlacu, D. Busonero, R. Buzzi, E. Caffau, J. Cambras, H. Campbell, R. Cancelliere, T. Cantat-Gaudin, T. Carlucci, J. M. Carrasco, M. Castellani, P. Charlot, J. Charnas, P. Charvet, F. Chassat, A. Chiavassa, M. Clotet, G. Cocozza, R. S. Collins, P. Collins, G. Costigan, F. Crifo, N. J. G. Cross, M. Crosta, C. Crowley, C. Dafonte, Y. Damerdji, A. Dapergolas, P. David, M. David, P. De Cat, F. de Felice, P. de Laverny, F. De Luise, R. De March, D. de Martino,

R. de Souza, J. Debosscher, E. del Pozo, M. Delbo, A. Delgado, H. E. Delgado, F. di Marco, P. Di Matteo, S. Diakite, E. Distefano, C. Dolding, S. Dos Anjos, P. Drazinos, J. Durán, Y. Dzigan, E. Ecale, B. Edvardsson, H. Enke, M. Erdmann, D. Escolar, M. Espina, N. W. Evans, G. Eynard Bontemps, C. Fabre, M. Fabrizio, S. Faigler, A. J. Falcão, M. Farràs Casas, F. Faye, L. Federici, G. Fedorets, J. Fernández-Hernández, P. Fernique, A. Fienga, F. Figueras, F. Filippi, K. Findeisen, A. Fonti, M. Fouesneau, E. Fraile, M. Fraser, J. Fuchs, R. Furnell, M. Gai, S. Galleti, L. Galluccio, D. Garabato, F. García-Sedano, P. Garé, A. Garofalo, N. Garralda, P. Gavras, J. Gerssen, R. Geyer, G. Gilmore, S. Girona, G. Giuffrida, M. Gomes, A. González-Marcos, J. González-Núñez, J. J. González-Vidal, M. Granvik, A. Guerrier, P. Guillout, J. Guiraud, A. Gúrpide, R. Gutiérrez-Sánchez, L. P. Guy, R. Haigron, D. Hatzidimitriou, M. Haywood, U. Heiter, A. Helmi, D. Hobbs, W. Hofmann, B. Holl, G. Holland, J. A. S. Hunt, A. Hypki, V. Icardi, M. Irwin, G. Jevardat de Fombelle, P. Jofré, P. G. Jonker, A. Jorissen, F. Julbe, A. Karampelas, A. Kochoska, R. Kohley, K. Kolenberg, E. Kontizas, S. E. Koposov, G. Kordopatis, P. Koubsky, A. Kowalczyk, A. Krone-Martins, M. Kudryashova, I. Kull, R. K. Bachchan, F. Lacoste-Seris, A. F. Lanza, J. B. Lavigne, C. Le Poncin-Lafitte, Y. Lebreton, T. Lebzelter,. The Gaia mission. *Astronomy & Astrophysics*, 595:A1, November 2016.

[31] J. Girven, B. T. Gänsicke, D. Steeghs, and D. Koester. DA white dwarfs in Sloan Digital Sky Survey Data Release 7 and a search for infrared excess emission. *Monthly Notices of the Royal Astronomical Society*, 417:1210–1235, October 2011.

[32] C. A. Gössl and A. Riffeser. Image reduction pipeline for the detection of variable sources in highly crowded fields. *Astronomy and Astrophysics*, 381:1095–1109, January 2002.

[33] C. A. Gössl and A. Riffeser. Image reduction pipeline for the detection of variable sources in highly crowded fields. *Astronomy and Astrophysics*, 381:1095–1109, January 2002.

[34] D.J. Griffiths. *Introduction to Quantum Mechanics*. Pearson international edition. Pearson Prentice Hall, 2005.

[35] M. Haeuser. Stellar classification of Pan-Planets extrasolar planet candidates, utilizing the 11 m HET and development of a hardware control system for the *HETDEX* project. Masterthesis, Ludwig-Maximilians-Universität München, 2013.

[36] M. Haeuser, F. Lang-Bardl, J. Richter, H.-J. Hess, A. Degwert, A. Karasz, R. Kosyra, U. Hopp, and R. Bender. Presenting a high accuracy Theta-Phi-style fiber-positioner prototype with a 15-mm pitch. In *Ground-based and Airborne Instrumentation for Astronomy V*, volume 9147, page 91476V, July 2014.

[37] Marco Haeuser, Josef Richter, Herman Kriel, Amanda Turbyfill, Brent Buetow, and Michael Ward. Upgrade of the het segment control system, utilizing state-of-the-art, decentralized and embedded system controllers, 2016.

[38] David M. Henry, Eli Atad-Ettedgui, Mark M. Casali, Richard J. Bennett, Alan Bridger, Derek J. Ives, R. G. Rae, and Timothy G. Hawarden. Wide-field camera for the United Kingdom Infrared Telescope. In *Proc. SPIE Vol. 4008, p. 1325-1333, Optical and IR Telescope Instrumentation and Detectors, Masanori Iye; Alan F. Moorwood; Eds.*, volume 4008, pages 1325–1333, August 2000.

[39] Ronald W. Hilditch. *An Introduction to Close Binary Stars*. 2001.

[40] G. J. Hill, N. Drory, J. Good, H. Lee, B. Vattiat, H. Kriel, R. Bryant, L. Elliot, M. Landriau, R. Leck, D. Perry, J. Ramsey, R. Savage, R. D. Allen, G. Damm, D. L. DePoy, J. Fowler, K. Gebhardt, M. Haeuser, P. MacQueen, J. L. Marshall, J. Martin, T. Prochaska, L. W. Ramsey, J.-P. Rheault, M. Shetrone, E. Schroeder Mrozinski, S. E. Tuttle, M. E. Cornell, J. Booth, and W. Moreira. Deployment of the Hobby-Eberly Telescope wide field upgrade. In *Ground-based and Airborne Telescopes V*, volume 9145, page 914506, July 2014.

[41] Gary J. Hill, Niv Drory, John M. Good, Hanshin Lee, Brian L. Vattiat, Herman Kriel, Jason Ramsey, Randy Bryant, Linda Elliot, Jim Fowler, Marco Haeuser, Martin Landiau, Ron Leck, Stephen Odewahn, Dave Perry, Richard Savage, Emily Schroeder Mrozinski, Matthew Shetrone, D. L. DePoy, Travis Prochaska, J. L. Marshall, George Damm, Karl Gebhardt, Phillip J. MacQueen, Jerry Martin, Taft Armandroff, and Lawrence W. Ramsey. Deployment of the hobby-eberly telescope wide-field upgrade, 2016.

[42] Gary J. Hill, Niv Drory, John M. Good, Hanshin Lee, Brian L. Vattiat, Herman Kriel, Jason Ramsey, Randy Bryant, Linda Elliot, Jim Fowler, Marco Haeuser, Martin Landiau, Ron Leck, Stephen Odewahn, Dave Perry, Richard Savage, Emily Schroeder Mrozinski, Matthew Shetrone, D. L. DePoy, Travis Prochaska, J. L. Marshall, George Damm, Karl Gebhardt, Phillip J. MacQueen, Jerry Martin, Taft Armandroff, and Lawrence W. Ramsey. Deployment of the hobby-eberly telescope wide-field upgrade, 2016.

[43] Gary J. Hill, Sarah E. Tuttle, Brian L. Vattiat, Hanshin Lee, Niv Drory, Andreas Kelz, Jason Ramsey, D. L. DePoy, J. L. Marshall, Karl Gebhardt, Taylor Chonis, Gavin Dalton, Daniel Farrow, John M. Good, Dionne M. Haynes, Briana L. Indahl, Thomas Jahn, Hermanus Kriel, Francesco Montesano, Harald Nicklas, Eva Noyola, Travis Prochaska, Richard D. Allen, Guillermo Blanc, Maximilian H. Fabricius, Martin Landriau, Phillip J. MacQueen, M. M. Roth, R. D. Savage, Jan M. Snigula, and Heiko Anwad. Virus: first deployment of the massively replicated fiber integral field spectrograph for the upgraded hobby-eberly telescope, 2016.

[44] Paul Hirst, Mark Casali, Andy Adamson, Derek Ives, and Tom Kerr. The UKIRT wide-field camera (WFCAM): commissioning and performance on the telescope. In *Ground-based and Airborne Instrumentation for Astronomy. Edited by McLean, Ian S.; Iye, Masanori. Proceedings of the SPIE, Volume 6269, id. 62690Y (2006).*, volume 6269, June 2006.

[45] R. N. Hook, S. Maisala, T. Oittinen, M. Ullgren, K. Vasko, V. Savolainen, J. Lindroos, M. Anttila, O. Solin, P. M. Møller, K. Banse, and M. Peron. PyMidas–A Python Interface to ESO-MIDAS. In *Astronomical Data Analysis Software and Systems XV ASP Conference Series, Vol. 351, Proceedings of the Conference Held 2-5 October 2005 in San Lorenzo de El Escorial, Spain. Edited by Carlos Gabriel, Christophe Arviset, Daniel Ponz, and Enrique Solano. San Francisco: Astronomical Society of the Pacific, 2006., p.343*, volume 351, page 343, July 2006.

[46] Ulrich Hopp. Wendelstein Observatory. http://www.wendelstein-observatorium.de:8002/wst_en.html, 2018. [Online; accessed 05-April-2018].

[47] Y. Huang, X.-W. Liu, H.-B. Yuan, M.-S. Xiang, Z.-Y. Huo, B.-Q. Chen, Y. Zhang, and Y.-H. Hou. Determination of the local standard of rest using the LSS-GAC DR1. *Monthly Notices of the Royal Astronomical Society*, 449:162–174, May 2015.

[48] Briana Indahl. Mc Donald Observatory. https://speakerdeck.com/brianalane/introduction-to-the-lrs2-cure-based-reduction-pipeline, 2018. [Online; accessed 11-April-2018].

[49] Eric Jones, Travis Oliphant, Pearu Peterson, et al. SciPy: Open source scientific tools for Python, 2001–. [Online; accessed 28.11.2018].

[50] S. O. Kepler, S. J. Kleinman, A. Nitta, D. Koester, B. G. Castanheira, O. Giovannini, A. F. M. Costa, and L. Althaus. White dwarf mass distribution in the SDSS. *Monthly Notices of the Royal Astronomical Society*, 375:1315–1324, March 2007.

[51] J. Davy Kirkpatrick, I. Neill Reid, James Liebert, Roc M. Cutri, Brant Nelson, Charles A. Beichman, Conard C. Dahn, David G. Monet, John E. Gizis, and Michael F. Skrutskie. Dwarfs Cooler than "M": The Definition of Spectral Type "L" Using Discoveries from the 2 Micron All-Sky Survey (2MASS). *The Astrophysical Journal*, 519:802–833, July 1999.

[52] Ralf Koehler. *Constraining Cosmology with Lyman-alpha Emitters a Study Using HETDEX Parameters*. PhD thesis, Ludwig-Maximilians-Universitaet Muenchen, January 2009.

[53] D. Koester. White dwarf spectra and atmosphere models. *Memorie della Societa Astronomica Italiana*, 81:921–931, January 2010.

[54] D. Koester and G. Chanmugam. REVIEW: Physics of white dwarf stars. *Reports on Progress in Physics*, 53:837–915, July 1990.

[55] G. Kovács, S. Hodgkin, B. Sipőcz, D. Pinfield, D. Barrado, J. Birkby, M. Cappetta, P. Cruz, J. Koppenhoefer, E. L. Martín, F. Murgas, B. Nefs, R. Saglia, and J. Zendejas. A sensitivity analysis of the WFCAM Transit Survey for short-period giant planets around M dwarfs. *Monthly Notices of the Royal Astronomical Society*, 433:889–906, August 2013.

[56] S. S. Kumar. On planets and black dwarfs. *Icarus*, 6:136–137, 1967.

[57] F. Lang-Bardl, R. Bender, C. Goessl, F. Grupp, H.-J. Hess, J. Kaminski, K. Hodapp, U. Hopp, S. Jacobson, H. Kravcar, A. Monna, W. Mitsch, J. Schlichter, and M. Wegner. The Wendelstein three channel imager (3KK): alignment, commissioning, and first results. In *Ground-based and Airborne Instrumentation for Astronomy VI*, volume 9908 of *procspie*, page 990844, August 2016.

[58] F. Lang-Bardl, R. Bender, F. Grupp, M. Haeuser, H.-J. Hess, V. Junk, R. Kosyra, B. Muschielok, J. Richter, J. Schlichter, and C. Schwab. A fibre positioner solution for the 4MOST instrument. In *Society of Photo-Optical Instrumentation Engineers (SPIE) Conference Series*, volume 8446 of *Society of Photo-Optical Instrumentation Engineers (SPIE) Conference Series*, September 2012.

[59] F. Lang-Bardl, K. Hodapp, S. Jacobson, R. Bender, C. Gössl, M. Fabricius, F. Grupp, U. Hopp, and W. Mitsch. 3kk: the Optical-NIR Multi-Channel Nasmyth Imager for the Wendelstein Fraunhofer Telescope. In *Ground-based and Airborne Instrumentation for Astronomy III*, volume 7735 of *procspie*, page 77353Q, July 2010.

[60] W. Lawrenz and N. Obermöller. *Controller-Area-Network: CAN ; Grundlagen, Design, Anwendungen, Testtechnik*. VDE-Verlag, 2011.

[61] S. P. Littlefair, S. L. Casewell, S. G. Parsons, V. S. Dhillon, T. R. Marsh, B. T. Gänsicke, S. Bloemen, S. Catalan, P. Irawati, L. K. Hardy, M. Mcallister, M. C. P. Bours, A. Richichi, M. R. Burleigh, B. Burningham, E. Breedt, and P. Kerry. The substellar companion in the eclipsing white dwarf binary SDSS J141126.20+200911.1. *Monthly Notices of the Royal Astronomical Society*, 445:2106–2115, December 2014.

[62] Mc Donald Observatory.
Electronic Spectrograph Number 2 (ES2)/ Users' Manual
. http://www.as.utexas.edu/mcdonald/facilities/2.1m/es2_manual.pdf (Users' Manual).

[63] Ross McLure. UDS: The Ultra Deep Survey. http://candels-collaboration.blogspot.de/2012/07/uds-ultra-deep-survey.html, 2018. [Online; accessed 24-April-2018].

[64] T. Nakajima, B. R. Oppenheimer, S. R. Kulkarni, D. A. Golimowski, K. Matthews, and S. T. Durrance. Discovery of a cool brown dwarf. *Nature*, 378:463–465, November 1995.

[65] J. Nordhaus, D. S. Spiegel, L. Ibgui, J. Goodman, and A. Burrows. Tides and tidal engulfment in post-main-sequence binaries: period gaps for planets and brown dwarfs around white dwarfs. *Monthly Notices of the Royal Astronomical Society*, 408:631–641, October 2010.

[66] Christian Obermeier. Searching for hot jupiter transits around cool stars. September 2016.

[67] S. G. Parsons, J. J. Hermes, T. R. Marsh, B. T. Gänsicke, P.-E. Tremblay, S. P. Littlefair, D. I. Sahman, R. P. Ashley, M. Green, S. Rattanasoon, V. S. Dhillon, M. R. Burleigh, S. L. Casewell, D. A. H. Buckley, I. P. Braker, P. Irawati, E. Dennihy, P. Rodríguez-Gil, D. E. Winget, K. I. Winget, K. J. Bell, and M. Kilic. Two white dwarfs in ultrashort binaries with detached, eclipsing, likely sub-stellar companions detected by K2. *Monthly Notices of the Royal Astronomical Society*, 471:976–986, October 2017.

[68] E.-M. Pauli, R. Napiwotzki, U. Heber, M. Altmann, and M. Odenkirchen. 3D kinematics of white dwarfs from the SPY project. II. *Astronomy and Astrophysics*, 447:173–184, February 2006.

[69] Michael Perryman. *The Exoplanet Handbook*. 2011.

[70] R. Racine, D. Salmon, D. Cowley, and J. Sovka. Mirror, dome, and natural seeing at CFHT. *Astronomical Society of the Pacific*, 103:1020–1032, September 1991.

[71] D. Raghavan, H. A. McAlister, T. J. Henry, D. W. Latham, G. W. Marcy, B. D. Mason, D. R. Gies, R. J. White, and T. A. ten Brummelaar. A Survey of Stellar Families: Multiplicity of Solar-type Stars. *The Astrophysical Journal Supplement Series*, 190:1–42, September 2010.

[72] R. Rebolo, E. L. Martin, and A. Magazzu. Spectroscopy of a brown dwarf candidate in the Alpha Persei open cluster. *The Astrophysical Journal Letters*, 389:L83–L86, April 1992.

[73] B. Röck, A. Vazdekis, E. Ricciardelli, R. F. Peletier, J. H. Knapen, and J. Falcón-Barroso. MILES extended: Stellar population synthesis models from the optical to the infrared. *Astronomy & Astrophysics*, 589:A73, May 2016.

[74] Y. H. Ryu, A. Udalski, J. C. Yee, M. D. Albrow, S. J. Chung, A. Gould, C. Han, K. H. Hwang, Y. K. Jung, I. G. Shin, W. Zhu, S. M. Cha, D. J. Kim, H. W. Kim, S. L. Kim, C. U. Lee, Y. Lee, B. G. Park, R. W. Pogge, KMTNet Collaboration, P. Pietrukowicz, S. Kozłowski, R. Poleski, J. Skowron, P. Mróz, M. K. Szymański, I. Soszyński, M. Pawlak, K. Ulaczyk, and The OGLE Collaboration. OGLE-2016-BLG-0693LB: Probing the Brown Dwarf Desert with Microlensing. *The Astronomical Journal*, 154, December 2017.

[75] T. O. B. Schmidt, R. Neuhäuser, A. Seifahrt, N. Vogt, A. Bedalov, Ch. Helling, S. Witte, and P. H. Hauschildt. Direct evidence of a sub-stellar companion around CT Chamaeleontis. *Astronomy and Astrophysics*, 491:311–320, November 2008.

[76] R. Sharples, R. Bender, R. Bennett, K. Burch, P. Carter, M. Casali, P. Clark, R. Content, R. Davies, R. Davies, M. Dubbeldam, G. Finger, R. Genzel, R. Haefner, A. Hess, M. Kissler-Patig, K. Laidlaw, M. Lehnert, I. Lewis, A. Moorwood, B. Muschielok, N. Foester Schreiber, J. Pirard, S. Ramsay Howat, P. Rees, J. Richter, D. Robertson, I. Robson, R. Saglia, M. Tecza, N. Thatte, S. Todd, and M. Wegner. Surveying the High-Redshift Universe with KMOS. *The Messenger*, 122:2–5, December 2005.

[77] A. Shimono, N. Tamura, H. Sugai, and H. Karoji. The system software development for Prime Focus Spectrogrsph on Subaru Telescope. *ArXiv e-prints*, October 2012.

[78] J. H. Silber, C. Schenk, E. Anderssen, C. Bebek, F. Becker, R. Besuner, M. Cepeda, J. Edelstein, H. Heetderks, P. Jelinsky, T. Johnson, A. Karcher, P. Perry, R. Post, M. Sholl, K. Wilson, and Z. Zhou. Design and performance of an R-Theta fiber positioner for the BigBOSS instrument. In *Society of Photo-Optical Instrumentation Engineers (SPIE) Conference Series*, volume 8450 of *Society of Photo-Optical Instrumentation Engineers (SPIE) Conference Series*, September 2014.

[79] E. M. Sion, J. L. Greenstein, J. D. Landstreet, J. Liebert, H. L. Shipman, and G. A. Wegner. A proposed new white dwarf spectral classification system. *The Astrophysical Journal*, 269:253–257, June 1983.

[80] B. Sipócz, G. Kovács, D. Pinfield, and S. Hodgkin. The WFCAM Transit Survey. In *Detection and Dynamics of Transiting Exoplanets, St. Michel l'Observatoire, France, Edited by F. Bouchy; R. DÃaz; C. Moutou; EPJ Web of Conferences, Volume 11, id.06003*, volume 11, February 2011.

[81] M. F. Skrutskie, R. M. Cutri, R. Stiening, M. D. Weinberg, S. Schneider, J. M. Carpenter, C. Beichman, R. Capps, T. Chester, J. Elias, J. Huchra, J. Liebert, C. Lonsdale, D. G. Monet, S. Price, P. Seitzer, T. Jarrett, J. D. Kirkpatrick, J. E. Gizis, E. Howard, T. Evans, J. Fowler, L. Fullmer, R. Hurt, R. Light, E. L. Kopan, K. A. Marsh, H. L. McCallon, R. Tam, S. Van Dyk, and S. Wheelock. The Two Micron All Sky Survey (2MASS). *The Astrophysical Journal*, 131:1163–1183, February 2006.

[82] J. M. Snigula, N. Drory, M. Fabricius, M. Landriau, F. Montesano, G. J. Hill, K. Gebhardt, and M. E. Cornell. Cure-WISE: HETDEX Data Reduction with Astro-WISE. In *Astronomical Data Analysis Software and Systems XXIII*, volume 485, page 447, May 2014.

[83] M. A. Stallcup and J. L. Lindner. Analysis and verification of Hobby-Eberly Telescope 1-m mirror deflections due to edge sensor loading. In A. E. Hatheway, editor, *Optomechanical Design and Engineering 2001*, volume 4444, pages 102–106, November 2001.

[84] Keivan G. Stassun, Kaitlin M. Kratter, Aleks Scholz, and Trent J. Dupuy. Correcting for Activity Effects on the Temperatures, Radii, and Estimated Masses of Low-Mass Stars and Brown Dwarfs. *arXiv e-prints*, page arXiv:1209.1756, Sep 2012.

[85] P. R. Steele, M. R. Burleigh, P. D. Dobbie, R. F. Jameson, M. A. Barstow, and R. P. Satterthwaite. White dwarfs in the UKIRT Infrared Deep Sky Survey Large Area Survey: the substellar companion fraction. *Monthly Notices of the Royal Astronomical Society*, 416:2768–2791, October 2011.

[86] P. R. Steele, R. P. Saglia, M. R. Burleigh, T. R. Marsh, B. T. Gänsicke, K. Lawrie, M. Cappetta, J. Girven, and R. Napiwotzki. NLTT 5306: the shortest period detached white dwarf+brown dwarf binary. *Monthly Notices of the Royal Astronomical Society*, 429:3492–3500, March 2013.

[87] B. Vattiat, G. J. Hill, H. Lee, W. Moreira, N. Drory, J. Ramsey, L. Elliot, M. Landriau, D. M. Perry, R. Savage, H. Kriel, M. Häuser, and F. Mangold. Design, alignment, and deployment of the Hobby Eberly Telescope prime focus instrument package. In *Ground-based and Airborne Instrumentation for Astronomy V*, volume 9147 of *Society of Photo-Optical Instrumentation Engineers (SPIE) Conference Series*, page 91474J, July 2014.

[88] Alexander von Boetticher, Amaury H. M. J. Triaud, Didier Queloz, Sam Gill, Monika Lendl, Laetitia Delrez, David R. Anderson, Andrew Collier Cameron, Francesca Faedi, Michaël Gillon, Yilen Gómez Maqueo Chew, Leslie Hebb, Coel Hellier, Emmanuël Jehin, Pierre F. L. Maxted, David V. Martin, Francesco Pepe, Don Pollacco, Damien Ségransan, Barry Smalley, Stéphane Udry, and Richard West. The EBLM project. III. A Saturn-size low-mass star at the hydrogen- burning limit. *Astronomy and Astrophysics*, 604, August 2017.

[89] M. Wang, Y. Zhao, and A. Luo. LAMOST fiber unit positional precision passive detection exploiting the technique of template matching. In *Society of Photo-Optical Instrumentation Engineers (SPIE) Conference Series*, volume 8450 of *Society of Photo-Optical Instrumentation Engineers (SPIE) Conference Series*, September 2012.

[90] William F. Welsh, Jerome A. Orosz, Joshua A. Carter, and Daniel C. Fabrycky. Recent Kepler Results On Circumbinary Planets. In Nader Haghighipour, editor, *Formation, Detection, and Characterization of Extrasolar Habitable Planets*, volume 293 of *IAU Symposium*, pages 125–132, April 2014.

[91] A. Whitworth, M. R. Bate, Å. Nordlund, B. Reipurth, and H. Zinnecker. The Formation of Brown Dwarfs: Theory. *Protostars and Planets V*, pages 459–476, 2007.

[92] Paul A. Wiegert and Matt J. Holman. The Stability of Planets in the Alpha Centauri System. *The Astrophysical Journal*, 113:1445–1450, April 1997.

[93] J. T. Wright and J. D. Eastman. Barycentric Corrections at 1 cm s^{-1} for Precise Doppler Velocities. *Publications of the Astronomical Society of the Pacific*, 126:838, September 2014.

List of appendices

Appendix A

Science Justification

Based on the work of our former colleague Paul Steele, we study and characterize several binary systems consisting of a white dwarf (WD) with a brown dwarf (BD) companion. The complete sample has a magnitude range of $8.4 < i < 17$ and contains 14 objects. All systems have already been visited with HET HRS at least once.
The detection and study of BD mass companions to WDs is of great importance in the analysis of high mass ratio binary formation and evolution. Two distinct populations are thought to be the outcome of stellar evolution; wide pairs where the secondary has migrated outwards due to the mass loss of the WDs progenitor and close systems in which the secondary has survived a stage of common envelope evolution and may eventually lead to the formation of a cataclysmic variable (CV) (Farihi et al. 2006 [ApJ 646, 480-492]; Nordhaus et al. 2010 [MNRAS 408, 631-641]).

Our approach to efficiently follow up these candidates is to use the ES2 cassegrain spectrometer on the Otto Struve 2.08m telescope to obtain radial-velocity (RV) data. Assuming typical *Balmer*-lines of WDs, the ES2 instrument will provide us with measured line-widths of about 40 pixels, allowing us to measure the centroid of the line with an accuracy of $\frac{\Delta\lambda[\text{Å}]}{\sqrt{N}} = \frac{1.4\text{Å}}{\sqrt{40}} = 0.22\text{Å}$ for the higher resolving grating 25. The obtained spectra will allow us to measure RVs with uncertainties of $\Delta\nu_{H_\beta} = 15.3\frac{km}{s}$ & $\Delta\nu_{H_\gamma} = 15.1\frac{km}{s}$, which leads to a combined uncertainty of $\Delta\nu_{H_\beta \& H_\gamma} \approx 10.7\frac{km}{s}$. Based on our already published pioneer target *NLTT 5306* (Steele et al. 2013 [MNRAS 429, 3492]), we expect this accuracy to be sufficient for our analysis. Hence, we apply for observation time at the Otto Struve 2.08m telescope to obtain the needed RV data for at least and preferably more than one full period, using the ES2 cassegrain spectrometer. Detailed stellar characterization for the WDs will be done with the HET HRS data and is in progress.

We already gained practical experience with the TI1 detector during the granted observing time in July in which we observed planetary candidates of the Pan-Planets survey. We further targeted a peculiar white dwarf system and measured low resolution spectra with grating 22. The 20 minute exposure, shown in figure B, is an early result our new and automated reduction pipeline (complete analysis ongoing). The gained S/N is a proof of concept for our observation plan, hence we are confident to reach the estimated accuracy. In order to optimize our observation efficiency, we use the already measured light curves for our objects to determine the optimal time slots for their observations and record the maximum RV amplitude. The light curve of our object *SDSS070433* (Mag_g: 16.5) is shown in figure A and indicates a periodic occultation with a best fitting period of 4.6 days.
Once reasonable RV data and characterisation is obtained, we will further follow up our objects in NIR at different telescope facilities in order to characterize the BD companion in more detail. We will subtract the best fitting theoretical WD spectra from the measured spectra and hence be left with the spectral contribution of the BD. This method has already been used by our former colleague (P. Steele et al. 2012, [MNRAS 429, 3492-3500]). Running this extensive analysis on the whole sample will allow us to shed some light on those very rare but scientifically exciting binary systems.

Since the observations are relevant for the PhD thesis of Marco Haeuser, the members are kindly asked to recognize the importance of graduate education at UT Austin and other institutions by adjusting rankings for dissertation proposals as appropriate.

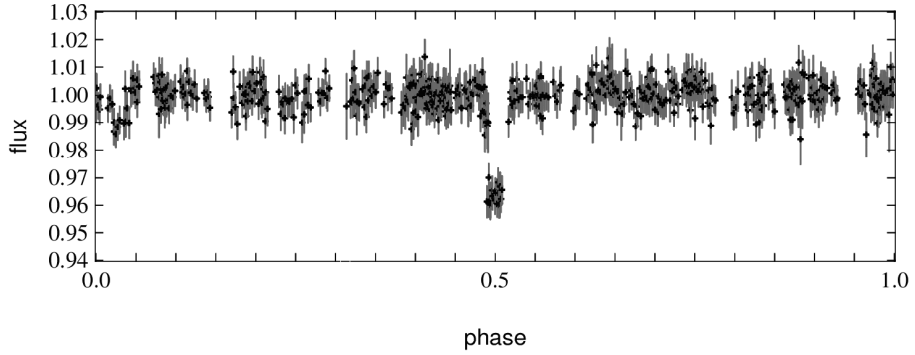

Figure A: Light curve of our prime target *SDSS070433* (Mag_g: 16.0), folded in the best fitting period of 4.66 days. The steep decrease of the occultation is symptomatic of a white dwarf as the host star.

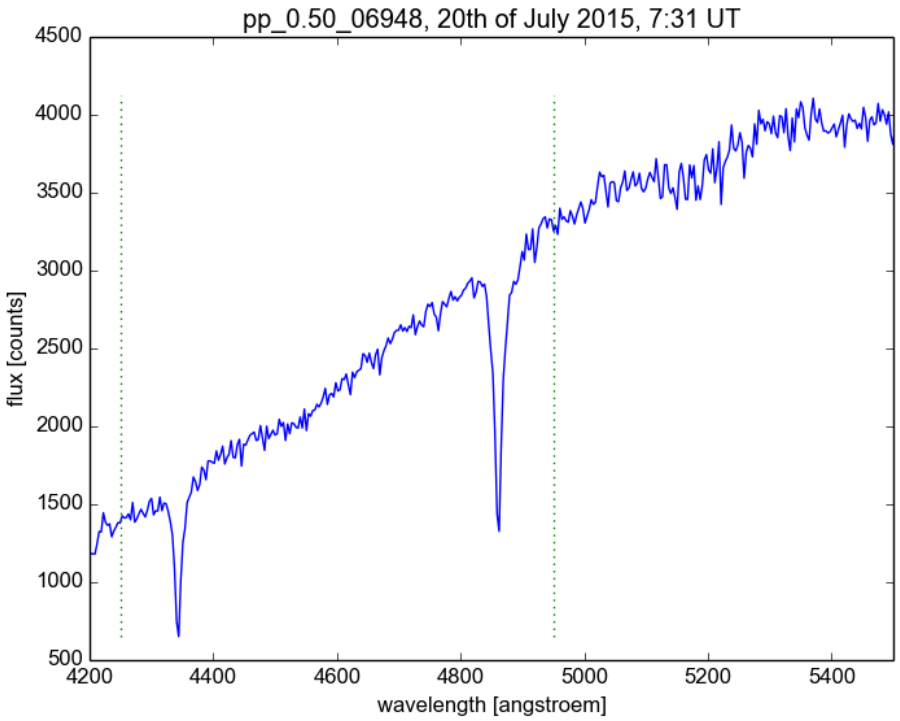

Figure B: Spectrum of our object of interest and white dwarf candidate *pp_0.50_06948* with clearly visible absorption lines H_β at 4861Å & H_γ at 4341Å. Changing to grating 25 should leave us with an observable range of about 700 Å (green dotes) which is enough to still cover both *Balmer*-lines. [Target: *pp_0.50_06948*, Mag_g: 14.5, Date: 07-20-2015, Exposure-time: 20 minutes, Detector: TI1, Grating: 22]

Description of Observations & Justification of Exposure Times

We request two runs of 6 consecutive nights in visitor mode at the Otto Struve 2.08m telescope, using the ES2 cassegrain spectrometer to observe in total 10 white dwarf - brown dwarf binary targets.

While the first run we will focus on our first two primary targets *WDC68* and *WDC39*, which are both in the same sky region and further gather data for our other 3 objects of interest. The 2nd run will give us additional time to take care of the other five targets (6 - 10), with a focus on 19d_1_09358 and WDC21.

#	Name	RA	DEC	Mag_g
1	WDC68	16:48:21.95	+12:46:17.00	11.1
2	SDSS171537	17:15:37.96	+03:23:48.82	17.0
3	WDC39	17:27:23.65	+03:11:53.50	09.2
4	SDSS193144	19:31:44.04	+36:17:26.40	14.0
5	SDSS193252	19:32:52.87	+36:05:33.80	16.0
6	SDSS193354	19:33:54.51	+36:53:11.30	16.0
7	SDSS193455	19:34:55.75	+36:39:50.50	15.0
8	19d_1_09358	19:35:56.40	+36:17:47.00	15.3
9	SDSS193704	19:37:04.46	+36:27:30.30	16.0
10	WDC21	21:38:23.46	+04:16:50.20	08.4

We will take measurements for a significant part of the rotation period of our targets. The request for 6 consecutive nights is based on the variability periods of our targets and accounts one night for weather loss. In the case more time is available, we would gratefully request more nights, to trace more than one period for better statistics, but two runs of 6 days is our baseline request to be able to get reasonable results.

Due to the brightness range of our targets ($8.4 < g < 17.0$), we will take several exposure per night with integration times between 10 minutes and 60 minutes which should provide us with enough S/N and at the same time give us enough temporary resolution. All exposures will be done with the Ti1 detector and grating 25. Within this setup we will find two *Balmer*-lines (Hβ at 4861 Å and Hγ at 4341 Å) providing us with two measurements and hence improve our resulting radial velocity.

Based on our previous experience, we will use slit positions 5 = 1,6 arcsec which is suitable for the expected seeing conditions. For optimal performance, we will take argon, bias, dark and flat calibration exposures in every night.

Adding 30 minutes per night for observation of flux and spectroscopic standards, we will be able to observe up to almost 6 hours per night in case we get our preferred timeslot, which is detailed on the next page.

Description & Justification of Special Constraints

Depending on the assigned observation time, we would lose about 70% of the night in April and still lose some 30% in May, so we could not really make reasonable use of those nights. The perfect time slot for our first run would be from the 1st till the 10th of June. Any other dark time after the 1st of June till the end of this trimester (31st of July) would allow us to use almost all of the night and would therefore be perfect. Based on our experience dark time would really be needed for our fainter objects, but we could still work with grey time and any moon separation that is larger than 80°.
In addition to the already mentioned circumstances, we ask you to not assign us with any dates between then 23rd of June until the 4th of July, due to the presence of our observers at the SPIE conference in Edinburgh, were they will give a talk to present their latest results.

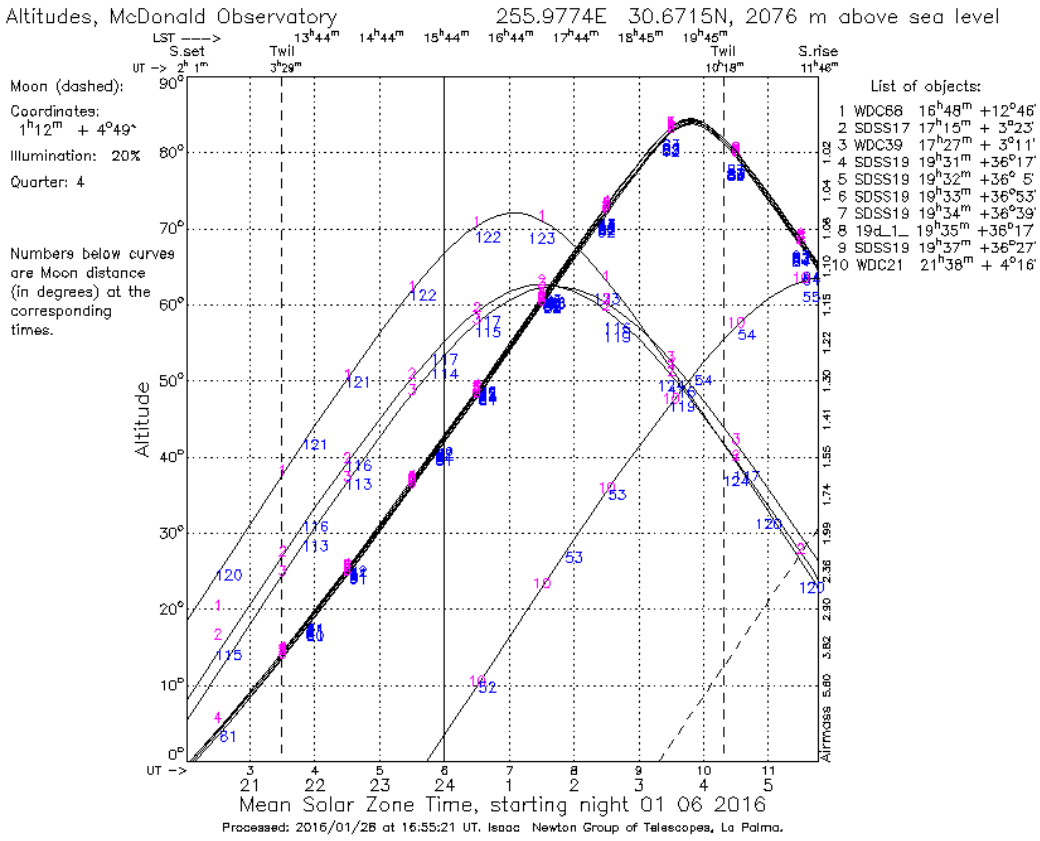

Figure C: Airmass and moon distance on the 1st of June for the McDonald observatory.

Results from Previous Observing Time at McDonald

This is our third proposal seeking time for the Otto Struve 2.08m telescope. Our last observation run in January lasted 6 days, which we lost almost completely to bad weather. We could only observe 1,5 nights out of all 6 and even the this nights did not deliver the estimated signal to noise ratio due to unstable conditions.
In contrast to the last one, was our first observing run in July 2015 for Pan-Planets highly successful. We could prove that our stellar characterization method, SED fitting, works very reliably across all stellar types. The obtained spectra confirmed the characterization of the targets and allowed us to select the best-suited targets for high resolution follow-up, which is ongoing right now. The reconnaissance spectra taken with the HIRES instrument on the Keck telescope further confirmed the best-fitting stellar type of the ES2 data for our high-priority targets. The corresponding project paper *Pan-Planets: Searching for Hot Jupiters around Cool Dwarfs* (Obermeier et al. 2015| arXiv:1512.07259) which includes the ES2 spectra, has been published in December 2015.

In addition to the originally granted observing time of our first proposal, we gratefully were granted three extra observation nights (31th August till 2nd September) in the summer trimester 2015 in which we could already partly test our observing tactic for this proposal. Those nights allowed us to take one night of low-res spectra and two nights of high-res spectra. Unfortunately we lost time due to clouds so we could not record every target in both resolutions but were still able to complete most of our project. The data analyses of the gained spectra is still ongoing. The planed reconnaissance observation runs, which we apply for in this proposal, will allow us to complete our detailed radial-velocity analyses of these white dwarf - brown dwarf binaries.
Marco Haeuser has been co-observer on several observing runs on the 2.7m Harlan J. Smith telescope using VIRUS-W to address questions on the dark matter distribution within dwarf galaxies. Additionally he was the single observer on our last observing run at the Otto Struve 2.08m telescope and has more than 16 nights of experience with the ES2 spectrograph on the Otto Struve 2.08m telescope and in total more than 20 nights with the telescopes altogether. He is therefore well trained in operating the telescope facility as well as the ES2 instrument.
Furthermore our group extensively used the HET with HRS to characterize white dwarf binary systems and published the according pioneer target *NLTT 5306* (Steele et al. 2013 [MNRAS 429, 3492]) for this larger study.

Appendix B

The *ES2* data reduction is mostly automated and executed by the *Python* -script *82-es2-pipe.py* . Table A provides an overview of the reduction steps, while the following sections describe the pipeline in detail.

ES2 data reduction

#	Step:	Prefix:	Code:	Options:	Reference file:
1	Bias	b	biasredux	-b	masterbias.fits
2	Bias offset	ob	subtractfits	-c	
3	Extract slit	eob	extractfits	-r	
4	Flatfield	feob	dividefits	-f	masterflat.fits
5	Cosmics	cfeob	cosmicfits	-c -k	
6	Rotation	rcfeob	pymidas		
7	Rebinning	rrcfeob	multrebin	-1 -2 -c -i -w	

Table A: Overview of the *ES2* data reduction pipeline.

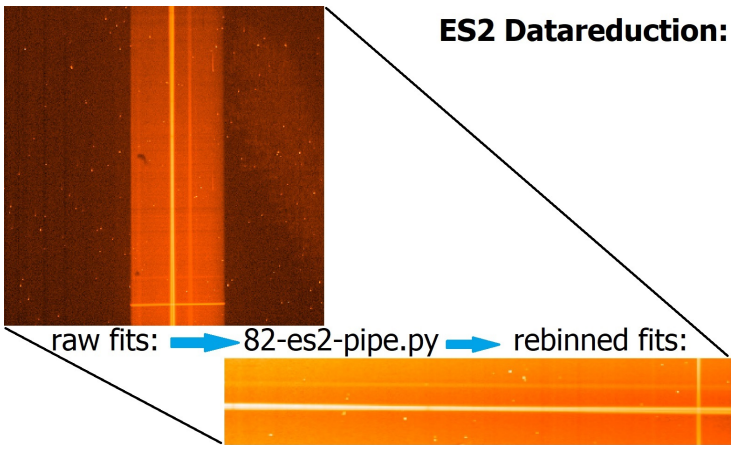

Figure D: *ES2* pipeline. Left: Raw fits file as observed by the *ES2*-spectrograph. Bottom: Final fits file, ready for spectral data extraction.

Bias

ES2 data reduction Bias reduction

#	Step:	Prefix:	Code:	Options:	Reference file:
1	Bias	b	biasredux	-b	masterbias.fits
			masterbias	-b	

Problem: The *ES2* CCD readout electronics adds a small systematic bias, based on which readout channel of the electronics is used. The effect is a caused by smallest variations in the manufacturing process of CCDs, which could to systematic error within the data.

Solution: Five bias exposures with zero exposure time are taken once a night. These files are normalized and combined by a median, to one masterbias.fits file, using the *masterbias* code, written by Arno Riffeser.

Masterbias options Code by: Arno Riffeser[23]

#	Option:	Value:	Meaning:
1	-r	409:2;2:399	Overscan region [x1:y1;x2:y2] [px]

Afterwards this masterbias.fits is subtracted pixel by pixel from each file, using the *biasredux* code.

Biasredux options Code by: Arno Riffeser[23]

#	Option:	Value:	Meaning:
1	-b	masterbias.fits	Name of reference file

Bias offset

ES2 data reduction Bias offset reduction

#	Step:	Prefix:	Code:	Options:	Reference file:
2	Bias offset	ob	subtractfits	-c	

Problem: In addition to the signal variations mentioned in section 11.7.2, the readout process also adds an overall offset to the real signal. The offset is a little bit different for each single file, because it is sensitive to all kinds of external influences, like the temperature of the detector and the readout electronic itself, as well as to small variations in the power supply.

Solution: To correct for all this variations, we subtract a constant correction value, which is individually calculated for every file. The *ES2* provides files with a designated overscan region, that is declared in the fits header. This region contains several thousand pixel and is big enough to provide us with a good estimate for the overall readout offset. Hence, we readout the overscan region[50] and compute the median of all of these pixel to gain an accurate offset. This median assessment is based on the assumption, that a sample size of over 2000 pixel is large enough so that outliers are suppressed well enough and no further sigma clipping is needed. The subtraction of the offset value is executed using the *subtractfits* code, written by Claus Gössl.

Subtractfits options Code by: Claus Gössl[33] [24]

#	Option:	Value:	Meaning:
1	-c	File depending	Constant subtraction value

[50]The overscan region is roughly 5 pixels smaller in any directions, to avoid any boundary effects.

Slit extraction and dark current

ES2 data reduction Slit region extraction

#	Step:	Prefix:	Code:	Options:	Reference file:
3	Extract slit	eob	extractfits	-r	

Problem: While *ES2* is a simple, slit instrument its CCD is a regular, squarish, scientific detector. In consequence, the light of the measured sky region passes through the slit and only illuminates the central part of the CCD. The not illuminated region is used to measure the accumulating dark current which is caused by minor leak current, leading to an artificial signal. It turns out, that the CCD cooling for both detectors is sufficient, so that the dark current is even for longest exposures negligible and therefore not corrected.

Solution: Based on the different sizes of the detectors, the slit illuminates different regions of the according detectors. Since the remaining unilluminated region is further unused we cut those regions from the fits files to be left with smaller and more handy files. The detailed regions and detector sizes are shown in table B. To extract those regions, we use the *extractfits* code, written by Claus Gössl.

Detector:	Detector size:	x_{min}	x_{max}	y_{min}	y_{max}
CC1	512 x 512	218	367	0	512
TI1	400 x 400	168	289	0	400

Table B: *ES2* detector sizes and slit regions, which are used to automatically extract spectra from fits files. For Details on the detector setup please see 3.1.

Extractfits options Code by: Claus Gössl[33] [24]

#	Option:	Value:	Meaning:
1	-r	see table B	Extraction region

Flatfield correction

ES2 data reduction Flatfield correction

#	Step:	Prefix:	Code:	Options:	Reference file:
4	Flatfield	feob	dividefits	-p -m	masterflat.fits
			masterflat	-c -o	

Problem: Due to the diffraction of the entrance optics, the illumination of a detector is never uniform for all locations. Typically border sections of the field of view (FoV) see a reduced illumination. In the case of spectroscopy this may lead to a systematic underestimation of the flux of wavelengths measured at such detector boarder regions.

Solution: To correct for such illumination effects we use observation of a dedicated flatfield lamp. The *ES2*-spectrograph features a quartz incandescent lamp[51] for such calibrations.[62] Based on practical experience of the observatory staff members, we used a series of five 0.1 *s* exposures, to calibrate for the flatfield.
In order to correct the scientific files, each nights set of flatfield exposures are merged into a so called *"masterflat.fits"*. First the input files are normalized and afterwards the masterflat is created by calculating the weighted average of each pixel. All this is done using the *masterflat* code, written by Arno Riffeser.

Masterflat options Code by: Arno Riffeser[23]

#	Option:	Value:	Meaning:
1	-c	1	Scale output with median
2	-o	masterflat.fits	Output file name

Once the masterflat for a night is calculated, all remaining exposures are corrected using the *dividefits* code, written by Claus Gössl.

Dividefits options Code by: Claus Gössl[33] [24]

#	Option:	Value:	Meaning:
1	-m	n/a	Use median values

[51] Details on the lamp can be found in the *ES2* user manual: *Electronic Spectrograph Number 2 (ES2) - Users' Manual* by Mc Donald Observatory 2003 [62]

Cosmic correction

ES2 data reduction Cosmic correction

#	Step:	Prefix:	Code:	Options:	Reference file:
5	Cosmic	cfeob	cosmicfits	-c -k	

Problem: All objects on Earth are constantly hit by cosmic particles. These particles either origin outside Earth's atmosphere or are generated when high energetic particles hit Earth's atmosphere. Such particles are also referred to as cosmic rays. The radioactive decay within the detector itself is a further source of irradiation. When such a particle hits a CCD it causes charges to transfer inside the detector and hence mimic photonic flux. Due to the kinetic energy involved, such signals exceed photonic signals by far and hence destroy the measurement for the affected pixels.

Solution: As the likelihood for such impacts is a function of altitude and exposure time, one can only try to minimize the exposure time. For most photometric or astrometric application one simply takes multiple short exposures of the object and combines the images, neglecting obvious outliers. For many spectroscopic applications this works fine. In our case this is more critical as the targets orbital periods are in the order of several hours until few days. Combining this with the faintness of the targets we choose exposure times of up to 1 hour. Taking individual exposures would cause additional overhead and smear our radial velocity signal.
To account for cosmic rays we rather use a code called *cosmicfits*. The code scans the fits files for the characteristic signature of locally restricted groups of outliers and replaces them by interpolated values. As the code was initially written for imager exposures, a relative high kappa-sigma clipping value of 5 σ was chosen to clip cosmics, but to ignore actual spectral emission lines.[52] Consequently some minor cosmics may still show up in the final data, but as they always cause strong positive outliers, they can easily be flagged and avoided during spectral extraction.

Cosmicfits options Code by: Claus Gössl[33] [24]

#	Option:	Value:	Meaning:
1	-c	1.5	Clipped region multiplier
2	-k	5.0	Kappa threshold

[52]This mostly was critical for exposures of spectral calibration lamps.

Spectral rotation

ES2 data reduction Spectral rotation

#	Step:	Prefix:	Code:	Options:	Reference file:
6	Rotation	rcfeob	pymidas		

Problem: The 2.1 m Otto Struve Telescope can be used with all kinds of instruments, of which most are facility instruments. Typically such old fashioned telescopes with a German-mount only feature one Cassegrain focus, which is for only one instrument at a time. Therefore the *ES2*-spectrograph commonly gets dismounted after each observation run.
As described in section 3.1 also the detector including its cooled mount can be switched. All this makes a reproducible alignment of the sky-slit-grism-detector axis almost impossible.

Solution: In order to account for alignment uncertainties, the measured spectra need to be rotated in a fashion which parallelize the dispersion-axis and the desired detector-axis (x or y). In a first order we correct by a 90° offset between the detector-axis and the nominal axis which our spectral extraction software desires.
Furthermore we also measure the actual misalignment α which results from the instrumental mounting process. The misalignment is stable over a whole observation run. Finally the combined rotational correction $90° + \alpha$ is executed within one step, using the python implementation of the well known ESO-MIDAS data reduction software.

pymidas Code by: ESO [22] [45]

#	Option:	Value:	Meaning:
1	INDISK	cfeob*.fits	Input filename
2	REBIN	$90° + \alpha$	Rotation angle
3	OUTDIS	rcfeob*.fits	Output filename

Appendix C

As discussed in chapter 6, use flux-normalized spectra to measure our targets radial velocity. In order to do so, we first discuss four ideas, on how to fit such spectral continuum to later normalize our data.

1. *Black-body radiation*:
   The simplest idea is to assume *Black-body radiation* and hence fit a *Planck-curve* to the continuum. As discussed this will not work, as the continuum is rather dominated by the throughput, than by its *Black-body radiation*.

2. *Black-body radiation* + instrument throughput:
   In case we combine our knowledge about the *Black-body radiation* and the throughput we already improved our approach, but many unstable instrument and observational effects like atmospheric dispersion[53] might still render this fitting method pointless. Consequently we shall find a way of fitting the continuum nicely without pre-assuming its characteristics imperfectly.

3. Polynomials:
   The simplest, reasonable mathematical approach without any pre-assumptions is to apply a smart polynomial fit, which iteratively improves it self be identifying outliers. Therefore the algorithm naively fits all data points and further calculates the standard deviation σ for this fit. Now, all data point which deviate further than a given σ-threshold [54] are clipped from the dataset and the next iteration is started. After a while this σ-clipping algorithm removed all outliers and absorption

[53] Atmospheric dispersion: As Earth's atmosphere consists of many different layers of different densities, temperatures and Refractive indices it actually disperses the targets light, just like a prism. This effect is actually the reason, why the sun seams bright and white during daytime, but appears even redder the closer it gets to the horizon.

[54] typically 2.0 or 3.0 σ work nice for a σ-threshold for spectral continuum clipping

line data points from its sample and remains with a reasonable polynomial fit. For science cases like stellar characterization of main sequence stars, like done by Haeuser in 2013 [35] this approach is suitable.

However, the implicit reduction to polynomial functions lead to several boundary effects and tends to still fail especially for very wide and deep absorption lines. In our case, the WDs *Balmer-lines* are wide enough to be partly be approximated by a polynomial fit, so we can never be sure our measurements will not be affected by the normalization. Hence, we need to improve even further.

4. Cubic splines:
   In contrast to the last approach we now only try to fit the continuum for minor segments with cubic polynomials and merge them to a continuous curve. This approach allows us to find a nice continuum function, which is not affected by the wide absorption lines. The following section 6.1 will hence discuss this approach in detail, while section 6.2 provides an independent quality check for this solution.

As we now motivated the cubic spline approach, we can now focus on the algorithm itself. To do so we assume a known set of interpolation points as discussed in section 6.1.

In order to calculate a proper fit, we use step wise defined spline functions. As shown in figure E, we need to find at-least a function which is continuous in it self and also which has a continuous first order derivative.

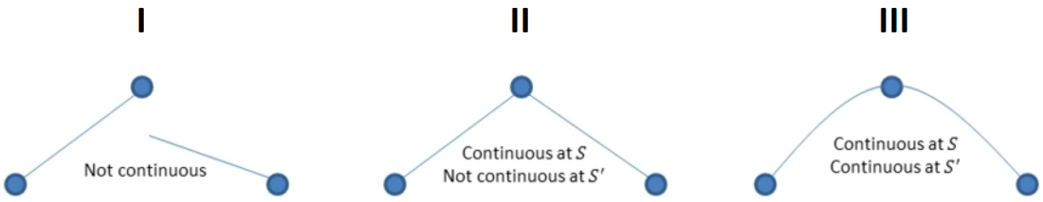

Figure E: Options for piecewise defined functions:
Case I: Non-continuous functions; obviously insufficient
Case II: Continuous functions which connect properly; still insufficient
Case III: Continuous functions with matched derivatives, which meet all data points smoothly

Furthermore, we even require a continuous second order derivative to find a smooth solution without non-physical features. Taking this into account we find that we need at least third order polynomials to piecewise approximate the data points. Otherwise we will not be able to calculate a meaningful second order derivative.

So we can note the following conditions for our fractional cubic spline S_Δ:

1. Piecewise definition:
$$S_{\Delta j,j+1}\left(x_j, y_j; x_{j+1}, y_{j+1}\right) \text{ is defined within } [j, j+1]$$
2. Third order polynomial definition:
$$S_{\Delta j,j+1} \;=\; ax^3 \;+\; bx^2 \;+\; cx \;+\; d$$
3. Continuous splines:
$$S_{\Delta j,j+1} \;=\; S_{\Delta j+1,j+2} \text{ at } (x_{j+1}, y_{j+1})$$
4. Continuous first order derivative:
$$S'_{\Delta j,j+1} \;=\; S'_{\Delta j+1,j+2} \text{ at } (x_{j+1}, y_{j+1})$$
5. Continuous second order derivative:
$$S''_{\Delta j,j+1} \;=\; S''_{\Delta j+1,j+2} \text{ at } (x_{j+1}, y_{j+1})$$

When combing all those requirements we end up with a large but solvable system of equations. The details on the computational implementation are as usual left to standard libraries which is in our case *pythons SciPy* module [14].

For the given example from section 6.1, the resulting cubic spline function is plotted as red line within the following figure F and meets all our requirements and fits the spectra very nicely.

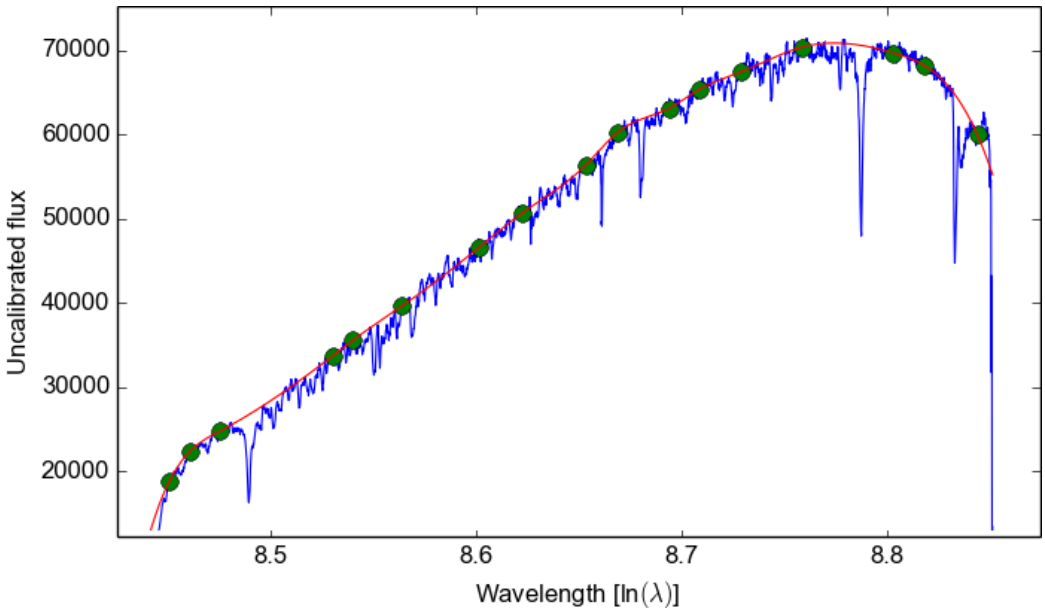

Figure F: Random, cubic spline fitted *LRS2* spectrum, showing target SDSS193144. The blue continuum is probed at 17 minor wavelength bands which are marked with green circles. Based on this new data points, the algorithm calculates the red cubic spline, which meets all those abstract data points nicely.

Appendix D

SMOCO CPU firmware documentation.

The following figures show the frozen interface documentation for the SCS2 SMOCO CPU firmware.
Date: 16 March 2017

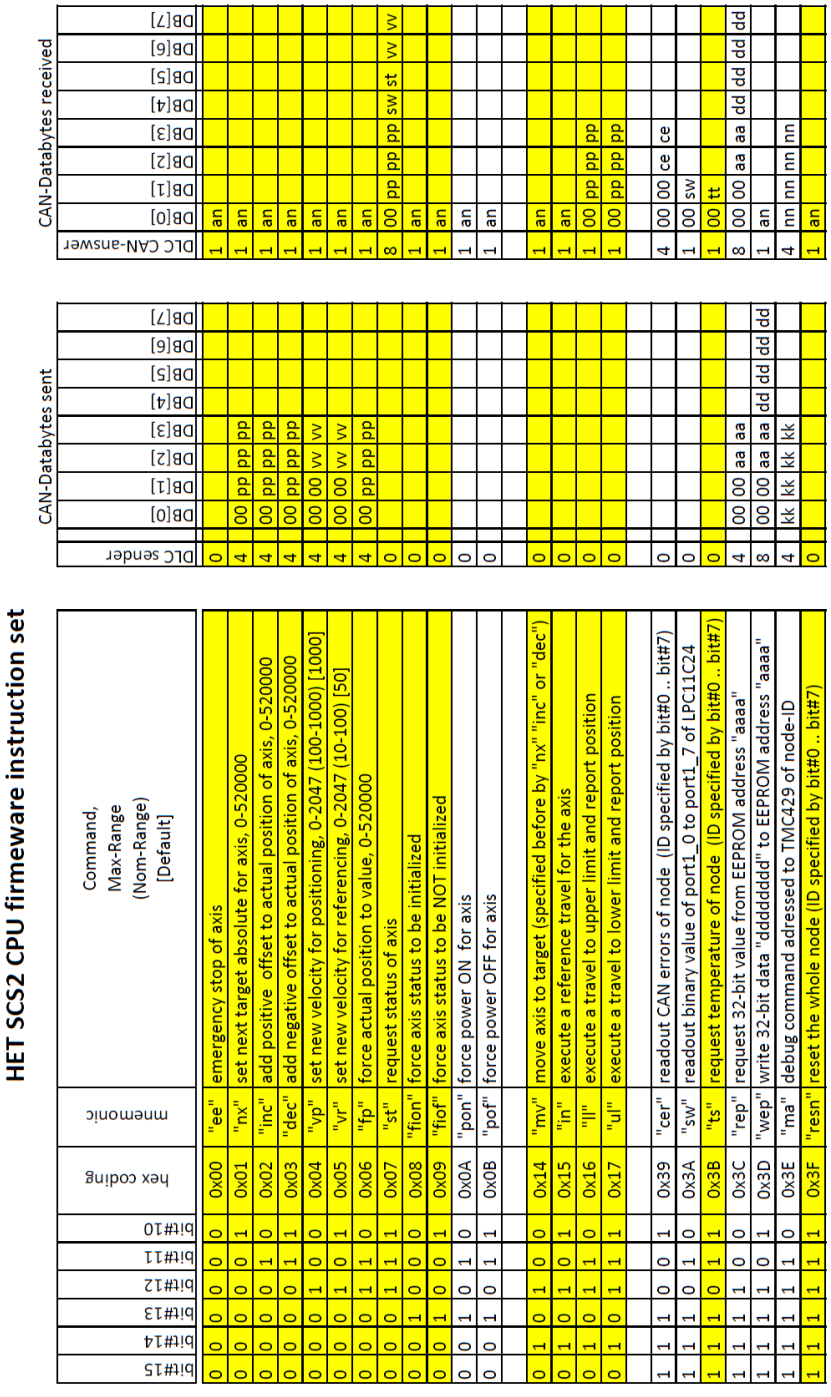

Figure G: SMOCO CPU firmware instruction set.

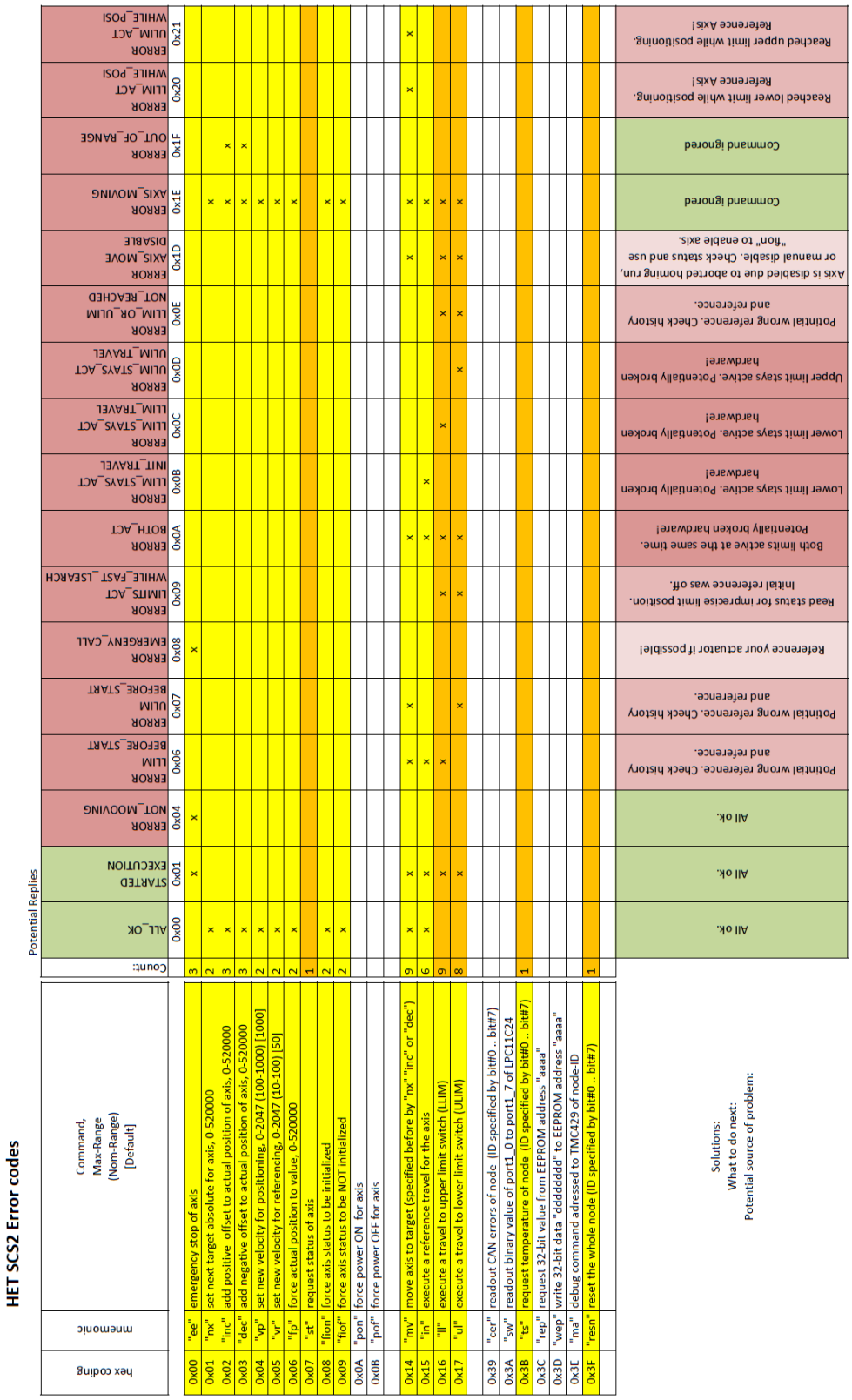
HET SCS2 Error codes
Potential Replies
hex coding
mnemonic
Command,
Max-Range
(Non-Range)
[Default]
Count:
ALL_OK
STARTED EXECUTION
ERROR NOT_MOOVING
ERROR LLIM BEFORE_START
ERROR ULIM BEFORE_START
ERROR EMERGENY_CALL
ERROR LIMITS_ACT WHILE_FAST_SEARCH
ERROR BOTH_ACT
ERROR LLIM_STAYS_ACT INIT_TRAVEL
ERROR LLIM_STAYS_ACT LLIM_TRAVEL
ERROR ULIM_STAYS_ACT ULIM_TRAVEL
ERROR LLIM_OR_ULIM NOT_REACHED
ERROR AXIS_MOVE DISABLE
ERROR AXIS_MOVING
ERROR OUT_OF_RANGE
ERROR LLIM_ACT WHILE_POSI
ERROR ULIM_ACT WHILE_POSI
0x00 "ea" emergency stop of axis 3 x x
0x01 "nx" set next target absolute for axis, 0-520000 2 x x
0x02 "inc" add positive offset to actual position of axis, 0-520000 3 x x
0x03 "dec" add negative offset to actual position of axis, 0-520000 3 x x
0x04 "vp" set new velocity for positioning, 0-2047 (100-1000) [1000] 2 x x
0x05 "vr" set new velocity for referencing, 0-2047 (10-100) [50] 2 x x
0x06 "fp" force actual position to value, 0-520000 2 x x
0x07 "st" request status of axis 1 x
0x08 "fion" force axis status to be initialized 2 x x
0x09 "fiof" force axis status to be NOT initialized 2 x x
0x0A "pon" force power ON for axis
0x0B "pof" force power OFF for axis
0x14 "mv" move axis to target (specified before by "nx" "inc" or "dec") 9 x x x

Appendix E

SMOCO

Commissioning-Check-List

Author:
Marco Haeuser (mhaeuser@astro.as.utexas.edu / mhaeuser@usm.lmu.de)

1.0 Introduction

This document is meant to help the technical staff to verify the functionality of a single SMOCO board. This is either needed for new populated SMOCO boards or after any repair work done on SMOCO boards. It further can be used as a full functional check list to verify an individual SMOCO board.

1.0.1 Document details

Version:	1.0
Date:	17th of November 2016
Note:	Steps 1 till 9 are hardware related and rather well defined. We need further test steps to also check key functionality of the SMOCO software in combination with actual actuator hardware. *Input from HET staff is welcome here.*

1.0.2 Required hard- & software

Prior to the actual testing of a SMOCO board, this section lists all hard- and software parts needed for the following check list.

1.0.2.1 Hardware

Supplies:

- 110V/230V AC power
- Ethernet connection

Equipment:

- SMOCO board to be tested
- Working SMOCO test device (SMOCO mirror lab test stand)
- Hall-sensor simulator or real actuators
- Either motor test assembly or real actuators
- ULink adapter to code micro-controller and ethernet connection
- Computer with needed software
- Technical clean ice-spray to verify temperature readings (optional)
- PCAN adapter to additionally monitor CAN-Bus (optional)

1.0.2.2 Software

- Latest version of micro controller code
- μ-Vision software to flash micro controller
- P-CAN software to monitor and optionally send CAN messages (optional but very helpful for debug)
- Custom, terminal based SCS2 command software to drop and receive commands via the ethernet/CAN bridge

1.1 Commissioning check list

Step 1.1.0 is meant to ensure the test devices functionality. Given the commissioning of several SMOCOs in a row, this step has only to be executed once and hence start over with step 1.1.1.

This check list is just a commissioning advice and does not cover detailed sources of errors or further repair steps. SMOCO boards which have failed at any level should not be further tested and be marked and separated for debugging and repair by a trained technician. In doubt contact author for further advice. [mhaeuser@astro.as.utexas.edu]

1.1.0 Initialize SMOCO test device

Goal: Making sure the SMOCO test device is ready and functional for further testing.

To-do-list:

1. Connect the test device with proper AC power.
2. Turn on test device, using the ON/Off button.
   If this fails, check internal circuit breaker and fuses.
3. Check the three supply voltages V-Axes(24VDC), V-Sensor (24VDC) and V-Logic (12VDC) using the according LED's.
   Measure at the power supplies if in doubt of function.
   Warning:
   Be aware of dangerous AC power, when working on the supplies!
4. Connect working ethernet to test device.
5. Connect CAN-Bus of test device with P-CAN Adapter.
6. Send some random CAN messages via the Ethernet connection and verify there correct appearance via PCAN.
7. Turn test device off.

Status after check: All basic functions of the test device should now be tested. Power, ethernet and CAN should be connected and the test device should be off. **Do not proceed with SMOCO commissioning if this tests has not been passed!**

1.1.1 Power Test

Goal: Test SMOCO basic on board power supply and connectivity.

To-do-list:

1. Insert SMOCO testee into test device. Check mechanically for proper connection.
2. Turn on test device.
3. Set LED-Mute switch at test device to "not mute".
4. Check all 5 power LEDs on testee. V-Axes usually is a little bit dimmer then the other 4 but should be clearly active.
5. If one of those LEDs is not showing expected behaviour, stop testing, repeat with 11.7.2 and/or mark SMOCO for repair and debugging.

Status after check: Test device on; SMOCO inserted
LED-Mute = "not mute"; SMOCO power LEDs active.

1.1.2 LED Test

Goal: Test SMOCO connectivity and functionality of LED-Mute and LED-Test to ensure all SMOCO LEDs are working.

To-do-list:

1. Check LED-Mute is set to "not mute" and do not push LED-Test.
   Power LEDs should be active. V-Axes and CAN LED usually are a little dimmer then the others.
2. Push LED-Test button.
   All LEDs should now be active and be equally bright.
3. Release LED-Test button and toggle LED-Mute.
   All LEDs should now be off. This is the nominal behaviour for operations.
4. Push LED-Test button.
   Independent of the LED-Mute button all LEDs should be active. If not, individual LEDs might have failed and need repair. (unlikely)
5. Release LED-Test and set LED-Mute to "not-mute".

Status after check: Test device on; SMOCO inserted
LED-Mute = "not mute".

1.1.3 Flashing the segment controller

Goal: Flash all segment controller (micro controller) with the latest software.

To-do-list:

1. Connect U-Link adapter with the first segment controller, using the mini-pinheader.
2. Compile and download the latest segment controller code, which is approved for operation.
3. Check for the validity message of the download and disconnect the U-Link adapter.
4. Repeat steps 1 till 3 for remaining controllers.

Status after check: Test device on; SMOCO inserted.
4 coded segment controllers.

1.1.4 Segment controller test

Goal: Verify basic activity of all segment controller.

To-do-list:

1. Reset of the whole test device using the ON/OFF switch.
2. CPU running LEDs should now be active with a 50% duty cycle, displaying the CPUs clock rate at 12 MHz.
3. Push LED-Test button to see the brightness difference between the 50% duty cycle and 100% while LED-Test.

Status after check: Test device on; SMOCO inserted.

1.1.5 CAN bus and segment ID assignment test

Goal: Verify CAN connectivity and segment ID assignment.

To-do-list:

1. Activate the CAN message logging of P-CAN software.
2. Perform a power cycle of test device and read logged CAN welcome messages.
3. Each controller should send his own welcome message including his ID.
4. While message arrival can alternate, all IDs have to be transmitted.
   (0xXXXX XXDC, 0xXXXX XXDD, 0xXXXX XXDE, 0xXXXX XXDF)
   If 4 welcome messages appear but do show different IDs, check correct wiring of ID-Bit2 till ID-Bit6 within the test device.
   Mirror lab test device has been assigned with the SMOCO IDs:
   (0d220 [0xDC] till 0d223 [0xDF])

Status after check: Test device on; SMOCO inserted.
4 segment CPUs flashed, running and communicating.

1.1.6 Temperature sensor tests

Goal: Verify temperature sensor functionality and validity.

To-do-list:

1. Refresh the CAN message logging of P-CAN software.
2. Read temperatures of all CPUs by sending CAN message 0x0008 ECXX.
3. Each CPU should reply with 0x1008 ECXX while XX is the according ID and the data bytes contain the temperature values in unites of 1 degree Celsius, encoded as signed 8-bit data.
4. Resend temperature request automatic once per 1 second and use technical clean ice-spray to significantly alter temperature readings and check correct bit flip of signed 8-bit data.
   ($+1°$ Celsius =0x01, $0°$ Celsius =0x00, $-1°$ Celsius =0xFF)
5. Stop resending temperature request.

Status after check: Test device on; SMOCO inserted
Temperature sensors working fine.

1.1.7 Flashing EEProm

Goal: Flashing EEProm and verify readability of the data.

To-do-list:

1. Refresh the CAN message logging of P-CAN software.
2. Send preconfigured EEProm data using the commands 0x0000 F4XX.
   Each EEProm should be loaded separately, even sending the data to all at the same time should be possible. This is considered to be nice to have but not baseline.
3. Read EEProm data using 0x008 F0XX and verify the correctness.

Status after check: Test device on; SMOCO inserted
EEProm flashed and working fine.

1.1.8 Motioncontroller Test

Goal: Verify communication and status of segment motioncontroller.

To-do-list:

1. Refresh the CAN message logging of P-CAN software.
2. Request motioncontroller software revision using command 0x0008 F8XX.
3. Each motioncontroller should reply with the command 0x1008 F8XX and data 0x0042 9101.

Status after check: Test device on; SMOCO inserted
Motioncontroller working.

1.1.9 Hall-sensor Test

Goal: Verify correct readability of hall-sensor states.

To-do-list:

1. Connect the hall-sensor simulator to the test device.
2. Manually make a connection between GND and the first hall-sensor channel.
3. Check the SMOCO front LED status. LED should be toggling between active and passive according to the manual connection.
4. Do the same check for all other sensor channels.
5. Refresh the CAN message logging of P-CAN software.
6. Request frequently hall-sensor status using command 0x0008 E8XX.
7. Manually make a connection between GND and the first hall-sensor channel.
8. Check the replies for consistency with the shortened hall-sensor channels.
9. Optionally repeat the tests with a real actuator.

Status after check: Test device on; SMOCO inserted
Hall-sensors working.

1.1.10 Motor Test

Goal: Verify drive functionality.

To-do-list:

1. Connect the motor test stand.
2. Verify the correctness of the flashed motor parameter in the EEProm to meet the specifications of the test stand motors. If not correct, update parameters.
3. Use scripted command sequence (TBD) to initialize all axes, activate their power, set new target positions and send a global movement trigger.
4. All axes should be starting and finishing movement almost at once.

Status after check: Test device on; SMOCO inserted
Motordrives working.

Acknowledgments

This Ph.D. thesis has been like a roller coaster ride, which I took together with great colleagues, good friends, excellent supervisors and my family.

The journey lead me halfway around the globe and finally back home. It started with the trust and support which I got early on from my great colleagues at USM. My special thanks goes to Achim, who lead me for many years with vision and experience; Josef with whom I collaborated on so many projects, we truly became friends.

On a larger scope, my technological developments have always been guided from great supervisors and colleagues like Florian Lang-Bardl and Maximilian Fabricius alike. Both paved my road to success with their experience and leadership skills. I especially like to thank Ulrich Hopp, who not only supported me as an astronomical observer at Mount Wendelstein, but also provided me with important feedback on most of my work.

Aside my home-base at the USM, Garching and especially the MPE have become my second home institute. Here I could focus myself towards astrophysics itself and had some of the best co-workers I could have asked for. Even we never worked directly together, Matthias Kluge has become a real friend. Hanna Kellermann; she always offered her expertise on optics and her support also had an important impact on my projects and this thesis. Furthermore, I especially like to thank Christian Obermeier who supported me on various occasions and with which I had some of my nicest observation runs in Texas.Also I like to thank Prof. Roberto Saglia for his guidance and support for all those years.

The journey of this Thesis lead me to so many places I could not have imagined before, but one destination truly became a pattern over all these years. It already began with my master studies in which I spend a term abroad and studied at the University of Texas in Austin. Gary Hill, which finally became my 2nd referee for this thesis, early on trusted me with the development of my own subsystems for the *HET* which also became my second home facility. I like to thank him and the whole *HET* staff, from which I especially like to point out Herman Kriel for their support and trust they put in me.

One of the most important persons for this thesis, is my fellow student Alexander Arth. He most likely had the most impact on this work, as we passed all our academic steps simultaneously. I will miss the days when we taught students together or fought over the details of our theses, all to come too the best possible solution. Thank you!

It remains obvious that aside of this great professional support, I could not have achieved this without my family in general and my siblings as well as my father in special. Furthermore I like to thank my closest friends Markus, Richard, Wolfgang and Markus, they cheered me up when I needed it and brought me back to Earth when I lost myself. Just like Ralph and Alexander I could not have done this work without all of you.

I would like to address my final words towards two professors. Without the early support from Harald Lesch, I could not have finished my Bachelor and Master studies in just 9 terms. He paved my road into professional Astronomy and opened the door to my professional passion: Help building the largest telescopes and instruments on Earth to gaze as deep into the universe as humans can ever do.

My doctoral advisor Ralf Bender finally enabled me to live my passion and ultimately is responsible for my success. I deeply thank you for your trust and support during this long journey.

Instrument acknowledgments:

- ***3KK* data:** *This paper contains data obtained at the Wendelstein Observatory of the Ludwig-Maximilians University Munich.*

- ***ES2*-spectrograph data:** *This thesis includes data taken at The McDonald Observatory of The University of Texas at Austin.*

- ***LRS2*-spectrograph data:** *The Hobby-Eberly Telescope (HET) is a joint project of the University of Texas at Austin, the Pennsylvania State University, Stanford University, Ludwig-Maximilians-Universität München, and Georg-August-Universität Göttingen. The HET is named in honor of its principal benefactors, William P. Hobby and Robert E. Eberly.*

Tools and survey data acknowledgments:

- ***2Mass* data:** *This publication makes use of data products from the Two Micron All Sky Survey, which is a joint project of the University of Massachusetts and the Infrared Processing and Analysis Center/California Institute of Technology, funded by the National Aeronautics and Space Administration and the National Science Foundation.*

- ***IRSA* finder charts:** *This research has made use of the NASA/ IPAC Infrared Science Archive, which is operated by the Jet Propulsion Laboratory, California Institute of Technology, under contract with the National Aeronautics and Space Administration.*

- ***UKIRT WFCAM* data:** *UKIRT is owned by the University of Hawaii (UH) and operated by the UH Institute for Astronomy; operations are enabled through the cooperation of the East Asian Observatory. When the data reported here were acquired, UKIRT was supported by NASA and operated under an agreement among the University of Hawaii, the University of Arizona, and Lockheed Martin Advanced Technology Center; operations were enabled through the cooperation of the East Asian Observatory.*

- ***SDSS* data:** *Funding for the Sloan Digital Sky Survey IV has been provided by the Alfred P. Sloan Foundation, the U.S. Department of Energy Office of Science, and the Participating Institutions. SDSS-IV acknowledges support and resources from the Center for High-Performance Computing at the University of Utah. The SDSS web site is www.sdss.org.*

  SDSS-IV is managed by the Astrophysical Research Consortium for the Participating Institutions of the SDSS Collaboration including the Brazilian Participation Group, the Carnegie Institution for Science, Carnegie Mellon University, the Chilean Participation Group, the French Participation Group, Harvard-Smithsonian Center for Astrophysics, Instituto de Astrofísica de Canarias, The Johns Hopkins University, Kavli Institute for the Physics and Mathematics of the Universe (IPMU) / University of Tokyo, the Korean Participation Group, Lawrence Berkeley National Laboratory, Leibniz Institut für Astrophysik Potsdam (AIP), Max-Planck-Institut für Astronomie (MPIA Heidelberg), Max-Planck-Institut für Astrophysik (MPA Garching), Max-Planck-Institut für Extraterrestrische Physik (MPE), National Astronomical Observatories of China, New Mexico State University, New York University, University of Notre Dame, Observatário Nacional / MCTI, The Ohio State University, Pennsylvania State University, Shanghai Astronomical Observatory, United Kingdom Participation Group, Universidad Nacional Autónoma de México, University of Arizona, University of Colorado Boulder, University of Oxford, University of Portsmouth, University of Utah, University of Virginia, University of Washington, University of Wisconsin, Vanderbilt University, and Yale University.

- ***Gaia* data:** *This work has made use of data from the European Space Agency (ESA) mission Gaia (`https://www.cosmos.esa.int/gaia`), processed by the Gaia Data Processing and Analysis Consortium (DPAC, `https://www.cosmos.esa.int/web/gaia/dpac/consortium`). Funding for the DPAC has been provided by national institutions, in particular the institutions participating in the Gaia Multilateral Agreement.*

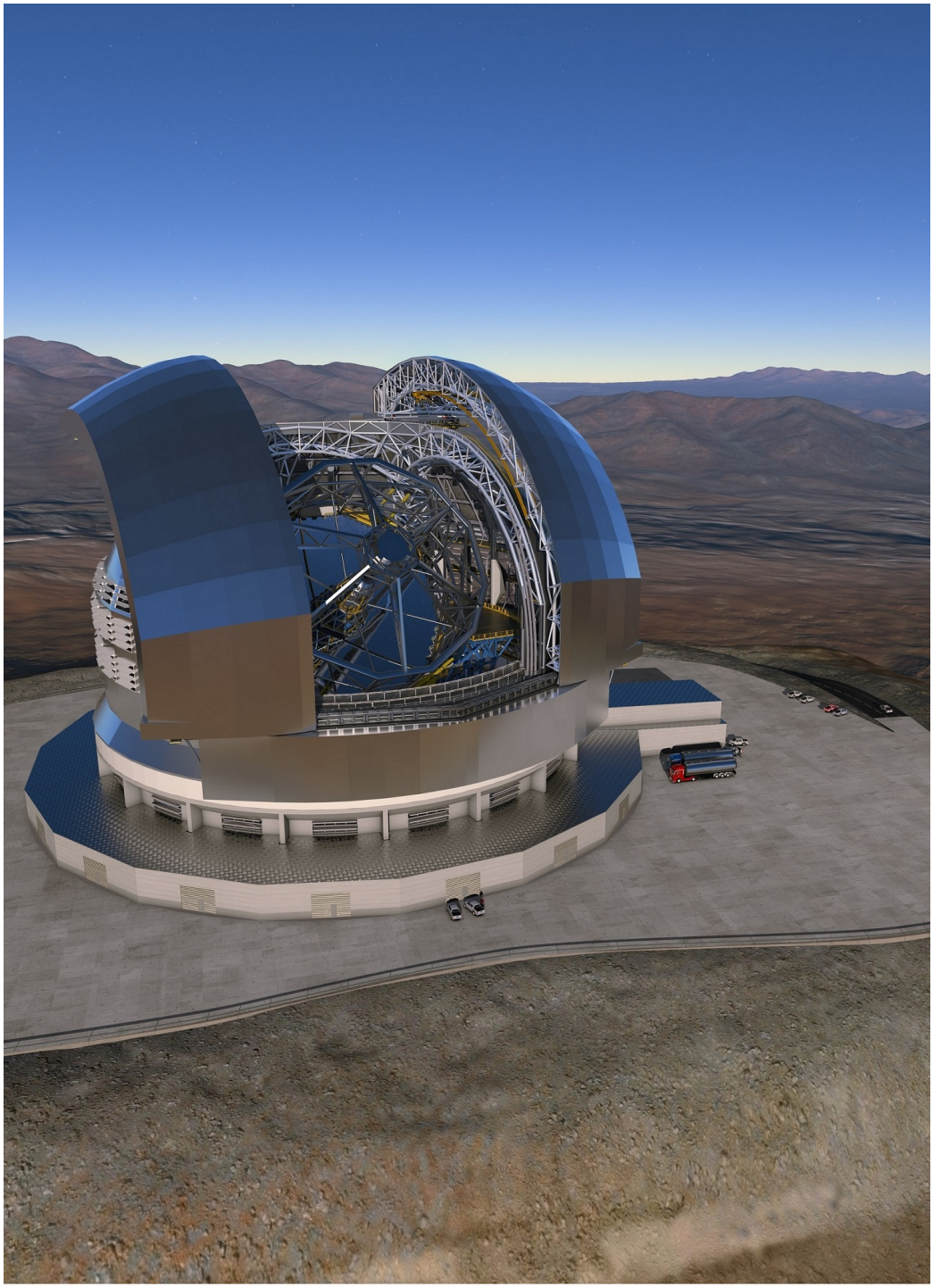

Next step: 39m ELT - under construction at Cerro Armazones, Chile

Credit: ESO

"We're still pioneers, we barely begun. Our greatest accomplishments cannot be behind us, cause our destiny lies above us."

Joseph A. Cooper